IJCESEN

International

Journal of

Computational and

Experimental

Science and

ENgineering

Founder-Editor-in-Chief : Prof.Dr. İskender AKKURT

dergipark.org.tr/en/pub/ijcesen

Indexing/Abstracting Databases

ULAKBİM
TR DİZİN

INDEX COPERNICUS
INTERNATIONAL

ASOS
indeks

ISIFI
INTERNATIONAL SERVICES FOR IMPACT FACTOR AND INDEXING

GENERAL IMPACT FACTOR
Universal Digital Object Information

Google Scholar

ISI ISI ISI ISI ISI ISI ISI ISI
INTERNATIONAL
Scientific Indexing

DRJI

publons

Cosmos

sis

J-Gate

WorldCat®

ESJI
www.ESJIndex.org
Eurasian
Scientific
Journal
Index

JIF JIFACTOR

CiteFactor
Academic Scientific Journals

Academic
Resource
Index
ResearchBib

Scientific Journal
Impact Factor

TOGETHER WE REACH THE GOAL

Table of Contents

Prenatal Attachment and Related Factors in Adolescent Pregnant Women

Zehra İncedal SONKAYA[1], Gülseren DAĞLAR[2], Demet ÇAKIR[3]*, Aysun Tekeli TAŞKÖMÜR[4]

[1]Amasya University, Sabuncuoğlu Şerefeddin Vocational School of Health Services, Health Care Services Department, Amasya-Turkey, **Email:** zehra.incedal@amasya.edu.tr - **ORCID:** 0000-0002-5446-9707

[2]Sivas Cumhuriyet University, Faculty of Health Sciences, Midwifery Department, Sivas-Turkey, **Email:** gulserendaglar@gmail.com - **ORCID:** 0000-0001-7159-5011

[3]Tokat Gaziosmanpaşa University, Faculty of Health Sciences, Midwifery Department, Tokat-Turkey, ***Corresponding Email:** zehra.incedal@amasya.edu.tr - **ORCID:** 0000-0003-4794-516X

[4]Amasya University, School of Medicine, Department of Obstetrics and Gynecology, Amasya-Turkey, **Email:** dr.isoon77@hotmail.com - **ORCID:** 0000-0001-7839-6963

Abstract:

The aim of this study was to determine the level of prenatal attachment and related factors in adolescent pregnant women. The study is cross-sectional descriptive type. The sample consisted of 34 adolescent pregnant women who applied to obstetrics outpatient clinics in a Training and Research Hospital. The data were collected between June 2018-June 2019. The Personal Information Form was collected using the Prenatal Attachment Inventory (PAI), Marriage Life Scale (MLS) and Health Practices in Pregnancy Scale (HPPS). The mean scores obtained from the scales are PAI 38.38±11.47; MLS is 32.74±8.16 and HPPS is 94.93±10.87. A significant negative correlation was found between PAI and HPPS mean score, and a positive and strong relationship between PAI and MLS score mean. While the mean score of PAI and MLS in adolescent pregnants is below the average level, HPPS is above the average. Prenatal attachment level was found to be low in those who are secondary school graduates, married for 2 years, whose first pregnancy and gender of the baby were male, and who evaluated the relationship with their husband at a moderate level. Prenatal attachment increases as satisfaction with marriage increases, while prenatal attachment decreases as health practices during pregnancy increase. Midwives should especially evaluate the prenatal attachment level and related factors of adolescent pregnants, and perform applications to increase prenatal attachment.

1. Introduction

Pregnancy is an important process in a woman's life during which normal physiological changes occur. Physical and mental changes accompanying pregnancy can make it difficult to adapt to these new roles and responsibilities, and therefore, more anxiety, stress and anxiety may be experienced during pregnancy [1]. According to World Health Organization (WHO), the age group of 10-19 years is defined as adolescents and those 15-24 years of age are defined as youth [2]. Adolescence refers to the transition from childhood to adulthood. Marriages under 19 years, before an adolescent is physiologically and psychologically ready to shoulder the responsibilities of marriage and parenthood, are defined as early marriages and also prevent child's social development [3].

The adaptation of adolescents to pregnancy and risky situations that may develop during pregnancy is affected by one's own internal dynamics (thoughts, emotions, desires, fears) and environmental factors [4].

Particular reasons such as limited access to health services in adolescence, insufficient knowledge of reproductive health, cultural pressure, and difficulty in making their own decisions cause adolescent pregnancies to be at high risk and increase maternal mortality rate; besides, depression and post-traumatic stress disorders are common [3].

Furthermore, it was determined that adolescent mothers cannot adequately meet the physical and psychological needs of their babies compared to adult mothers, babies of adolescent mothers have more nutritional disorders, growth and developmental retardation, cognitive dysfunctions and suffer from low learning capacity, exhibit higher behavioral problems in childhood and higher potential to commit crimes [5]. It is thought that all these negativities are caused by insufficient attachment during pregnancy [4]. Attachment develops depending on the nature of the real relationship and turns into great love over time. Although the most intense attachment is experienced in the postpartum period, it is known that the attachment process truly begins in the prenatal period. Attachment is very important for the adoption of the maternal role and the continuity of parenting. Previous reports stated that mother-infant attachment during pregnancy is affected by the family's income level, planned pregnancy and feeling fetal movements; however, the effects of maternal age and physical symptoms of pregnancy are still not fully known [6, 7].

On the other hand, while increasing depression rates decrease attachment, positive health behaviors increase attachment [7] and negative health behaviors affect attachment negatively. Inadequate health practices during pregnancy lead to maternal bleeding, invasive delivery, preterm delivery, congenital anomalies and miscarriages in the fetus, and low birth weight in newborns [8].

Quality and adequate prenatal care provided to adolescent pregnant women would be effective in improving health practices during pregnancy and increasing prenatal attachment. "Satisfaction in marriage" refers to one's perception of the degree to which their needs in the marital relationship were being met and is also defined as the happiness felt from the marital relationship [9].

Mood changes in the adolescent age group may negatively affect their marriage and harmony between couples. Spouses need to support each other for satisfaction in marriage, so late prenatal attachment occurs in marriages with a lack of spousal support and weak family bonds [10].

Based on the above-mentioned information, it is believed that satisfaction in marriage and health practices can be effective among adolescent pregnant women as in other pregnant women. Midwives should determine the factors that may affect prenatal attachment in adolescent pregnant women, give care with a holistic perspective, and determine the possible risks in advance. Therefore, the current study examines prenatal attachment in adolescent pregnant women and related factors.

2. Material and Methods

2.1. Sample and Population

Adolescent pregnant women who attended the maternity clinic of a Research and Training Hospital between June 2018 and June 2019 participated in the study. The population of this study consists of adolescent pregnant women who visited this Research and Training Hospital between the stated dates for follow-up. A total of 44 adolescent pregnant women applied to the hospital where the study was conducted in 2017. While determining the sample size, Vural Batik and Kalkan's study and G*Power 3.1 were used (11). While calculating the sample size, the effect size (d=0.63), 1-β=0.95 and the margin of error were taken as 5%, and accordingly, we determined that the study could be conducted with 34 adolescent pregnant women. Pregnant women aged 19 and under, with a healthy pregnancy period, at 24-40 weeks of pregnancy, who were not diagnosed with psychiatric illness, and who agreed to participate in the study were included in the study. Data were gathered with face-to-face interviews by the researcher. The interviews were carried out in a convenient room of the hospital before or after the follow-up visits. The interview duration was an average of 20 minutes.

2.2. Ethical Permission

The study was conducted under the Principles of the Declaration of Helsinki. Before the study, ethical approval was obtained from Sivas Cumhuriyet University Non-Interventional Clinical Research Ethics Committee (dated 30.04.2018 and numbered 04/31) and the research permission was obtained from the Provincial Health Directorate (dated 04.12.2018 and numbered E. 11853). Also, the participants were informed about the nature of the study and they provided written informed consents.

2.3. Data Collection Tools

Data was collected using "Personal Information Sheet", "Marital life scale", "Prenatal Attachment Inventory", and "Health Practices in Pregnancy Questionnaire".

I.Personal Information Sheet was created by the authors based on a literature survey and consists of items related to the sociodemographic and obstetric characteristics of pregnant women [6, 11].

II. Prenatal Attachment Inventory (PAI) was developed by Muller to reveal the thoughts and feelings experienced by women during pregnancy

and to determine their prenatal attachment level [12]. The inventory consists of 21 items assessed by using a four-point Likert scale (1 = never, 2 = rarely, 3 = often, and 4 = always). The highest and lowest scores that can be obtained from the scale were 84 and 21, respectively. Higher scores indicate higher prenatal attachment. The validity and reliability studies for the Turkish version of the inventory were carried out in a previous study and the Cronbach's Alpha reliability coefficient was calculated as 0.84 [6]. However, in the current study, Cronbach's Alpha was found to be 0.90.

III. Marital life scale (MLS) was developed by Tezer to measure the overall satisfaction in the marital relationship [13]. MLS consists of 10 items assessed with a five-point Likert scale. Comprising: Strongly disagree (1); Disagree (2); Undecided (3); Agree (4); and Strongly agree [5]. The lowest and highest scores that can be obtained from the scale were 10 and 50, respectively. Higher scores indicate higher satisfaction in marriage. The Cronbach's Alpha reliability coefficient of the scale was calculated as 0.85, whereas, in the current study, it was found to be 0.78 [13].

IV. Health Practices in Pregnancy Questionnaire (HPQ) was developed by Lindgreen to evaluate health practices during pregnancy that may affect pregnancy outcomes [14]. HPQ consists of 33 items. Health practices during pregnancy were defined as balance of rest and exercise, safety measures, nutrition, avoiding the use of harmful substances, obtaining health care, and obtaining information. The items 1-16 were rated on a five-point Likert scale (always = 5, often = 4, sometimes = 3, rarely = 2, never = 1). The items 17-33 were scored 1 to 5 through five answer choices. Ten items of the scale (6, 7, 21, 22, 23, 24, 25, 26, 32, and 33) were reverse-coded. A score that can be obtained from the scale varies from 33 to 165. Higher scores indicate higher quality health behaviors during pregnancy. However, it was calculated as 0.62 in our study.

2.4. Analysis of the Data

The data were analyzed using Statistical Package for Social Sciences (SPSS 21.0). While analyzing the data, the descriptive statistical methods (mean, standard deviation minimum and maximum values, and percentages) were used and also chi-square test was performed to examine the relationships between the categorical variables. As stated by Demir et al., Shapiro-Wilk's test was used to examine if the variables are homogeneously distributed since the sample size is 34 [15]. After determining the variables were homogeneously distributed, the

independent sample t-test was used for comparison of two independent groups and One Way ANOVA was conducted for comparing more than two independent groups. Pearson Correlation analysis was used to examine the relationships between the scales. To identify which group is significantly different from other groups, the Tukey test was used when the homogeneity assumption was met and Tamhane's T2 test was used when the homogeneity assumption was not met. p<0.05 was accepted as statistically significant.

3. Results and Discussions

The mean age of the adolescent pregnant women was 18.07±0.76. We determined that 55.9% of the participants were "high school" graduates, almost all of them were married, 82.4% were not spouse's kin, 76.5% were married for 1 year or less, 97.1% were unemployed, 88.2% were not smokers, and 61.8% of them perceived their income as equal to their expenditure. A total of 52.9% of pregnant women's husbands were "primary school" graduates and 50.0% of them were "workers" (Table 1).

Table 1: Distribution of Pregnant Adolescents' Sociodemographic Characteristics

Sociodemographic Characteristics		n	%
Mean age	18.07±0.76 (min-max: 17-19)		
Education	Primary school	15	44.1
	High school	**19**	**55.9**
Marital Status	Married	**33**	**97.1**
	Single	1	2.9
Spouse's kin	Yes	6	17.6
	No	**28**	**82.4**
Marriage Duration	1 Year and Less	**26**	**76.5**
	2-3 Years*	8	23.5
Employment	Unemployed	**33**	**97.1**
	Employed	1	2.9
Spouse's Education	Primary school	**18**	**52.9**
	High school and above	16	47.1
Spouse's Occupation	Public servant	4	11.8
	Worker	**17**	**50.0**
	Farmer	5	14.7
	Storekeeper	5	14.7
	Self-employment	3	8.8
Income Perception	Income is Less Than Expenses	10	29.4
	Income is Equal to Expenses	**21**	**61.8**
	Income is Higher Than Expenses	3	8.8
Smoking	Never Used	**30**	**88.2**
	Still Using	4	11.8
Total		34	100.0

*6 pregnant women have been married for 2 years and 2 pregnant women for 3 years

The mean pregnancy weak of the adolescent pregnant women was 26.50±9.94. We determined that 82.4% of the participants had their first pregnancy, 50.0% of them prefer a baby "boy", 94.1% were willing to become pregnant, and 73.5% had a planned pregnancy. Moreover, 85.3% of the pregnant women felt "joy and happiness" when they

learned pregnancy and 82.4% defined their relationship with their spouse as "very good" (Table 2).

Table 2: *Distribution of Pregnant Adolescents' Obstetrical Characteristics*

Obstetrical Characteristics		n	%
Mean Pregnancy Week	26.50±9.94 (min-max: 25–40)		
Number of pregnancies	First Pregnancy	28	82.4
	Second or Third Pregnancy *	6	17.6
Number of children alive	No children alive	31	91.2
	One or Two Children**	3	8.8
Pregnancy after assisted reproduction	Yes	3	8.8
	No	31	91.2
Gender of the baby	Girl	14	41.2
	Boy	10	29.4
	Not yet known	10	29.4
Gender Preference	Girl	16	47.1
	Boy	17	50.0
	Does not matter	1	2.9
Willingness to Become Pregnant	Yes	32	94.1
	No	2	5.9
Planned Pregnancy	Yes	25	73.5
	No	9	26.5
Emotions Felt When They Learned Pregnancy	Joy and Happiness	29	85.3
	Fear and Anxiety	5	14.7
Relationship with Spouse	Very good	28	82.4
	Good	3	8.8
	Very Bad	3	8.8
Total		34	100

*Third pregnancy of 1 pregnant and the second pregnancy of 5 pregnant women; **1 woman had 2 living children and 2 women had 2 living children.

Table 3: *Mean scores of Prenatal Attachment Inventory, Marital life scale, and Health Practices in Pregnancy Questionnaire*

Scales	The highest and lowest scores that can be obtained from the scale	Min-Max	Mean ± SS
Prenatal ttachment Inventory	21 - 84	21-67	38.79±11.66
Marital life scale	10 - 50	12-44	32.62±8.38
Health Practices in Pregnancy Questionnaire	33 - 165	69-114	94.03±10.94

Mean scores of the adolescent pregnant women for PAI, MLS, and HPQ were 38.79±11.66, 32.62±8.38, and 94.03±10.94, respectively (Table 3). Significant differences were found in the adolescent pregnant women's MLS scores according to smoking status, gender of the baby, and emotions felt when they learned pregnancy. Furthermore, the PAI scores significantly differ according to gender, being spouse's kin, willingness to become pregnant, and emotions felt when they learned pregnancy. Moreover, significant differences were obtained in the HPQ scores according to the number of pregnancies and pregnancy after assisted reproduction (p<0.05) (Table 4). MLS scores were

higher in those who never smoked, whose baby was male, and those who felt joy and happiness when they learned pregnancy. Furthermore, PAI scores were higher in those aged 18 years, spouse's kin, willing to become pregnant, and those who felt joy and happiness when they learned pregnancy. Moreover, higher HPQ scores were observed in pregnant women in their first pregnancy and became pregnant after assisted reproduction. On the other hand, no significant differences were found in the mean scores of MLS, PAI, and HPQ according to education and relationship with their spouse (p>0.05).

Table 4: *Comparison of the Adolescent Pregnant Women's MLS, PAI, and HPQ scores with Their Sociodemographic and Obstetric Characteristics*

Sociodemographic and Obstetric Characteristics	n	MLS	PAI	HPQ
Age				
17	9	**35.44±8.15**	36.00±8.88	90.89±11.94
18	14	31.29±8.35	**44.64±12.10**	92.21±9.09
19	11	32.00±8.82	33.64±10.55	98.91±11.56
F* / p		0.706/0.501	3.573/0.040	1.731/0.194
Education				
Primary School	15	**32.73±9.22**	38.13±12.60	92.87±11.50
High School	19	32.53±7.91	**39.32±11.19**	94.95±10.70
t** / p		0.070/0.944	0.289/0.774	0.545/0.590
Spouse's Kin				
Yes	6	30.67±8.98	49.50±10.48	90.50±10.89
No	28	**33.04±8.36**	36.50±10.73	**94.79±11.00**
t** / p		-0.622/0.538	2.703/0.011	-0.867/0.392
Smoking				
Never Used	30	36.00±3.74	39.28±12.11	99.20±4.55
Still Using	4	30.92±8.88	36.80±9.85	92.84±10.89
t** / p		**-2.063/0.047**	0.399/0.692	-1.058/0.298
Number of Pregnancies				
First Pregnancy	28	32.57±8.03	37.96±11.90	**96.25±9.38**
Second or Third Pregnancy	6	32.83±10.70	**42.67±10.53**	83.67±12.58
t** / p		-0.068/0.946	-0.893/0.379	**2.811/0.008**
Pregnancy after assisted reproduction				
Yes	3	30.33±11.59	**48.67±20.79**	**95.26±10.31**
No	31	**32.84±8.23**	37.84±10.50	81.33±10.69
t** / p		-0.489/0.628	1.568/0.127	**2.227/0.033**
Gender of the Baby*				
Girl	14	28.50±8.84	37.71±12.31	94.86±10.12
Boy	10	**36.40±2.27**	35.40±7.77	**99.00±8.64**
Not yet known	10	34.60±9.62	**43.70±13.35**	87.90±12.08
F* / p		**3.427/0.045**	1.400/0.262	2.953/0.067
Willingness to Become Pregnant				
Yes	32	**32.72±8.39**	**56.50±14.84**	**94.41±11.03**
No	2	31.00±11.31	37.69±10.78	88.00±9.89
t** / p		0.277/0.783	2.360/0.025	0.799/0.430
Emotions Felt When They Learned Pregnancy				
Joy and Happiness	25	**34.17±7.80**	**51.60±10.99**	94.76±10.86
Fear and Anxiety	9	23.60±5.81	36.59±10.43	89.80±11.64
t** /p		**2.878/0.007**	**2.951/0.006**	0.934/0.357
Relationship with Spouse				
Very Good	28	**33.36±8.56**	**42.00±21.65**	95.36±11.14
Goof	3	33.00±2.00	38.50±10.85	86.00±9.53
Very Bad	3	25.33±8.73	38.33±13.01	89.67±7.57
F*/ p		1.265/0.296	0.118/0.889	1.273/0.294

MLS: Marital Life Scale; PAI: Prenatal Attachment Inventory; HPQ: Health Practices in Pregnancy Questionnaire *One Way ANOVA; **Independent Sample T-test;

An examination of the mean scores of MLS, PAI, and HPQ indicated that a strong positive correlation exists between PAI and MLS scores (r=0.873; p=0.025) and a weak negative correlation exists between PAI and HPQ scores (r=-0.423; p=0.005) (Figure 1). The adolescent pregnant women perceived higher overall satisfaction of marriage as their prenatal attachment increases and accordingly, the increase in prenatal attachment leads to higher satisfaction in marriage. However, prenatal attachment increases as the health practices in pregnancy decrease and health practices in pregnancy increase as the prenatal attachment decreases.
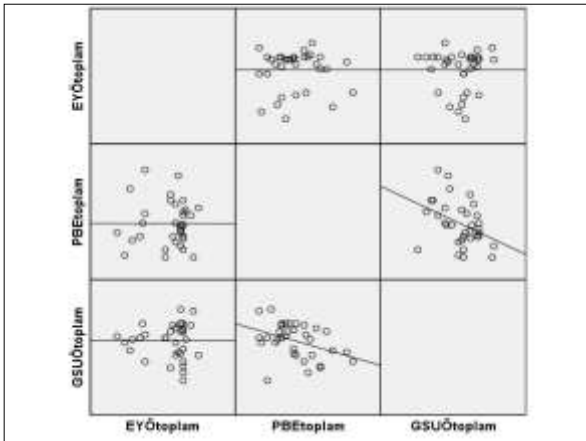
***Figure 1:** The relationship curves for MLS, PAI, and HPQ*

The results of the current study which aimed at examining the level of prenatal attachment experienced by adolescent pregnant women and related factors are discussed using the recent research literature. We found that the adolescent pregnant women's perceived overall satisfaction of marriage increases as their prenatal attachment increases; however, prenatal attachment increases as health practices in pregnancy decrease. According to a literature survey on prenatal attachment, studies on mother-infant attachment in Turkey generally focused on adult pregnant women and few studies have examined factors affecting the level of prenatal attachment experienced by adolescent pregnant women [16-19]. The present study is very important since it examined both the level of mother-infant attachment and the relation of mother-infant attachment to marital harmony and health practices in pregnancy. With this study, our purpose was to draw attention to adolescent pregnancies, to evaluate the level of mother-infant attachment and its related factors, as well as to be aware of the importance of care and practices targeting these factors. Our findings draw attention to the potential risks in adolescent pregnant women and also the importance of general health practices and satisfaction in

marriage on prenatal attachment. We found that the mean PAI score of adolescent pregnant women was 38.79±11.66. Considering that the lowest and highest scores that can be obtained from the scale were 21 and 84, respectively, the levels of prenatal attachment experienced by adolescent pregnant women were below average. Previous studies found that the PAI mean scores were 64.67±6.61 in pregnant women 20 years of age or younger; 62,50±9,67 in pregnant women 19 years of age or younger [18, 20]. The lower PAI scores obtained in our study than these reports can be explained by the mean participant age was lower and the duration of the marriage in our study was higher than these studies, as well as the regional differences [18]. A similar PAI mean score (44.7±14.08) with our study was obtained by the study of Eyüpoğlu and Eyüpoğlu examining adolescent pregnant women with pregnancy complications [19]. Adolescent pregnancies are defined as high risk and may negatively affect mother-infant attachment [2].

We found that those aged 18 years, were spouse's kin, willing to become pregnant, and felt joy and happiness when she'd learned she was pregnant had higher PAI scores. A majority of the pregnant women who participated in our study stated that their relationship with their spouse was very good (82.4%) and they planned to become pregnant (73.5%). It may be argued that these factors helped women to feel happy as well as to increase relationships with their spouses and the level of prenatal attachment. Consistent with our results, Alan Dikmen and Çankaya found that those willing to become pregnant had significantly higher PAI scores [16]. Also, Ulu and Bayraktar determined a significant relationship between the level of prenatal attachment experienced by pregnant women and their relationship with their spouses [21]. On the other hand, Badem and Zeyneloğlu found that the PAI scores significantly differ according to the age and emotions felt when they've learned pregnancy [18]. They also determined that those aged 19 years and younger felt happiness when they've learned pregnancy had higher prenatal attachment compared to those aged 20 years and above and felt sadness when they've learned pregnancy. These results suggest that willingness to become pregnant might be effective on willing and enthusiastic to be a mother and mother-infant attachment can be affected by many factors including age. In our study, the mean MLS score of adolescent pregnant women was calculated as 32.62±8.38. Considering that the highest and lowest scores that can be obtained from the scale were 50 and 10, respectively, the participants' mean score was found to be above the average scale score. This was a desirable and important finding as it indicates adolescent pregnant

women had good marital harmony. The fact that only a limited number of studies examined adolescent pregnant women using MLS limits the opportunity to discuss the data, therefore, the results were also evaluated using the reports on adult pregnant women [22]. Accordingly, Yıldız and Baytemir calculated the mean MLS scores as 37.95±8.08 and Ulu and Bayraktar found to be 38.64±8.49 in adult pregnant women. The mean MLS scores of adult pregnant women were found to be higher than the mean score calculated in our study [21, 23]. Marriage is a union between spouses who have a sense of responsibility towards each other, support each other socially, have open communication, and can develop problem-solving skills. It can be argued that individuals who have not yet completed their own identity and personality development and have not formed value judgments cannot build a healthy marriage union and cannot get satisfaction from marriage. Because, in marriages made at a young age, individuals may be more likely to make mistakes when choosing a life partner and this may lead to an increased risk of divorce; so, spouses may exhibit negative attitudes towards each other. From this point of view, the higher MLS scores in adult women than adolescents are considered expected results. Aslan et al. determined that women who married before the age of 18 had lower marital harmony than those who married after the age of 18 [16]. Instead of satisfaction in marriage, other terms such as marital harmony, quality of marriage, marital success, marital happiness are also used in the literature [24]. The relationship between marital adjustment and marital satisfaction allows these two concepts to be used synonymously [25]. We found that adolescent pregnant women who never smoked, carrying a boy, and felt joy and happiness when learned pregnancy had higher MLS scores. Consistent with our results, Haylı et al. found that a baby of the desired gender and Yanıkkerem et al. determined that planned pregnancy and not smoking positively affect marital harmony [26, 27]. Furthermore, in a previous study, a significant correlation was found between the marital harmony of adult women who had a 1–4-month-old baby and having a desired gender of baby [28]. Having planned and a desired number of children, experiencing desired pregnancies, proper birth preparedness before and during pregnancy might increase the attachment of both mother and father to the baby as well as help increase marital satisfaction.

We found that the mean HPQ score of adolescent pregnant women was 94.03±10.94, and those in their first pregnancy and became pregnant after assisted reproduction had higher HPQ scores. However, we determined that the age of women did not affect HPQ scores. In previous studies using HPQ, Sis

Çelik and Aksoy Derya calculated the mean HPQ score as 114.43±17.90 in adult pregnant women; Beyaz et al., calculated as 105.85±10.17 in women who had their first pregnancy before 18 years old; Hadian et al. calculated as 135.29±9.08 in adolescent pregnant women [29-31]. Accordingly, the mean HPQ score found in our study was below the mean scores found in the previous studies. Probably, this difference in the mean HPQ scores lies in the socio-cultural differences, adolescent pregnancies, and pregnant women's lack of knowledge in general health practices. Consistent with our findings, some previous reports obtained a significant correlation between number of pregnancies and HPQ scores and found that HPQ scores decrease as the number of pregnancies increases [29, 30]. These results point out that the workload caused by having more children might negatively affect the individual health practices of adolescent pregnant women.

While describing factors affecting prenatal attachment, readiness to become a mother, spouse support for building and maintaining a love relationship between mother and fetus, and health practices during pregnancy are important [17]. The correlation analysis conducted to determine relationships between the scales revealed that adolescent pregnant women perceived overall satisfaction in marriage increase as their prenatal attachment increases. On the other hand, prenatal attachment increase as their perceived overall satisfaction in marriage increases. Previous studies showed that marital harmony and social support increase prenatal attachment [32]; pregnant women who experienced dating prior to marriage and who were emotionally and physically supported exhibit higher marital harmony and prenatal attachment [17]; a moderate positive correlation exists between mother's satisfaction in marriage and mother-baby attachment and mother's satisfaction in marriage increases as mother-baby attachment increases [28]. Ulu and Bayraktar also emphasized that pregnant women's satisfaction in marriage increases as their prenatal attachment increases [21]. These previous reports support our research findings. Therefore, it can be argued that higher harmony with spouse during pregnancy increases marital harmony, provides psychological relief in the expectant mother, enables more effective adaptation of the role of motherhood, and thus increases prenatal attachment. Moreover, when a pregnant woman has positive attitudes towards her unborn baby, she might exhibit more warm and responsive behaviors towards her baby and spouse, adopt a parental role better, and thus have higher satisfaction in marriage as well as higher marital harmony. Positive health behaviors include not smoking, not using alcohol, receiving health care before birth and involving in

health care practices, healthy eating, regular sleep, and exercising. Previous research showed that women with higher prenatal attachment try to develop positive health behaviors and positive health behaviors increase as prenatal attachment increases [7, 31]. Badem and Zeyneloğlu found that prenatal attachment levels of pregnant women who developed positive health behaviors during pregnancy were higher than those who did not develop positive health behaviors [18]. However, our findings surprisingly suggest that prenatal attachment increases as health practices in pregnancy decrease and health practices in pregnancy increase as prenatal attachment decreases. Furthermore, we found that pregnant women who did not smoke and did not use alcohol during pregnancy had a higher prenatal attachment. In this regard, while the presence of a positive relationship between health practices during pregnancy and prenatal attachment is expected, the negative relationship determined in our study is a thought-provoking result. The underlying reasons for this contradiction may be different health practices other than smoking and alcohol use. Hadian et al. obtained a weak positive correlation between maternal-fetal attachment in adolescent pregnant women and HPQ scores [31]. Our finding that indicating increased positive health behaviors resulted in lower prenatal attachment suggests that adolescents do not attach much importance to their own health and do not pay more attention to protecting the health of their babies.

4. Conclusions

Our results showed that the mean PAI score of the adolescent pregnant women was below the average inventory score whereas, their mean MLS and HPQ scores were above the average. We found that the participants who were high school graduates, carrying a boy, had a moderate spouse relationship displayed lower levels of prenatal attachment. Also, the satisfaction in marriage increases as prenatal attachment increases, on the other hand, the health practices in pregnancy increase as prenatal attachment decreases. In this regard, it is important to ensure that midwives and nurses evaluate prenatal attachment, marital harmony, and health practices during pregnancy while receiving histories of pregnant women, especially adolescent pregnant women. Also, they should determine factors that may affect prenatal attachment and provide education and counseling to adolescent pregnant women, who are a risky group in terms of prenatal attachment and evaluate pregnant women from a holistic perspective. To prevent adolescent pregnancies, it is important to detect early pregnancy

if a pregnancy has occurred. Also, a mother's physical and mental health should be protected by regular physical and psychological follow-ups in the postpartum period. Furthermore, studies evaluating the effectiveness of evidence-based practices regarding prenatal attachment are needed.

Author Statements:

- **Ethical approval:** The conducted research is not related to either human or animal use.
- **Conflict of interest:** The authors declare that they have no known competing financial interests or personal relationships that could have appeared to influence the work reported in this paper
- **Acknowledgement:** The authors declare that they have nobody or no-company to acknowledge.
- **Author contributions:** The authors declare that they have equal right on this paper.
- **Funding information:** The authors declare that there is no funding to be acknowledged.
- **Data availability statement:** The data that support the findings of this study are available on request from the corresponding author. The data are not publicly available due to privacy or ethical restrictions.

References

[1] Arslan, S., Okçu, G., Coşkun, M.A., Temiz, F. (2019). Women's perception of pregnancy and the affecting factors. *Journal of Health Science and Profession*. 6(1):179-192. DOI: 10.17681/hsp.432333

[2] World Health Organization (2021, Jun 14). Adolescent health, 2021. https://www.who.int/southeastasia/health-topics/adolescent-health; Accessed Date: 10 Aug 2021.

[3] Kabir, R., Ghosh, S., Shawly, A. (2019). Causes of early marriage and its effect on reproductive health of young mothers in Bangladesh. *American Journal of Applied Sciences*. 16(9):289-297. DOI: 10.3844/ajassp.2019.289.297

[4] Keramat, A., Malary, M., Moosazadeh, M., Bagherian, N., Raiabi-Shakib, M.R. (2021). Factors influencing stress, anxiety, and depression among Iraian pregnant women: the role of sexual distress and genital self-image. *BMC Pregnancy and Childbirth*. 21:87. DOI:10.1186/s12884-021-03575-1

[5] Kara Uzun, A., & Şimşek Orhon, F. (2013). Influences of adolescent pregnancy on maternal and infant health. *Ankara Üniversitesi Tıp Fakültesi Mecmuası*. 66(1):19-23. DOI: 10.1501/Tipfak_0000000836

[6] Yılmaz, D.S., & Kızılkaya Beji, N. (2013). Turkish version of prenatal attachment inventory: A study of

reliability and validity. *Journal of Anatolia Nursing and Health Sciences*. 16(2):103-109.

[7] Karakaş, M. N., & Dağlı Şahin, F. (2019). The importance of attachment in infant and influencing factors. *Turkish Archives of Pediatrics*. 54(2):76-81. DOI: 10.14744/TurkPediatriArs.2018.80269

[8] Balkaya Akdolun, N., Vural, G., Eroğlu, K. (2014). Investigating problems related to the health of mothers and their babies resulting from risk factors determined during pregnancy. *Journal of Duzce University Health Sciences Institute*. 1(1):6-16.

[9] Yedirir, S., & Hamarta, E. (2015). Emotional expression and spousal support as predictors of marital satisfaction: The case of Turkey. *Educational Sciences: Theory and Practice*. 15(6):1549-1558. DOI: 10.12738/estp.2015.6.2822

[10] Dakin, J., & Wampler, R. (2007). Money doesn't buy happiness, but it helps: marital satisfaction, psychological distress, and demographic differences between low- and middle-income clinic couples. *The American Journal of Family Therapy*. 36:300-311. DOI: 10.1080/01926180701647512

[11] Vural Batık, M., & Kalkan, M. (2017). Perceived marital problem-solving skills and marital satisfaction. *Journal of the Human and Social Science Researches*, 6(5):2630-2646.

[12] Muller, M.E. (1993). Development of the prenatal attachment inventory. *Western J Nurs Res*. 15(2):199-211. DOI: 10.1177/019394599301500205

[13] Tezer, E. (1996). Satisfaction from marital relationship: Marital Life Scale. *Turkish Psychological Counseling and Guidance Journal*. 2(7):1-7.

[14] Lindgren, K. (2005). Testing the Health Practices in Pregnancy Questionnaire-II. *Journal of Obstetric, Gynecologic, and Neonatal Nursing: JOGNN*. 34(4):465–472. DOI: 10.1177/0884217505276308

[15] Demir, E., Saatçioğlu, Ö., İmrol, F. (2016). Examination of educational researches published in international journals in terms of normality assumptions. *Curr Res Educ*. 2(3):130-149.

[16] Alan Dikmen, H., & Çankaya, S. (2018). Effects of maternal obesity on prenatal attachment. *Acıbadem University Health Sciences Journal*. 9(2):118-123. DOI: 10.31067/0.2018.1

[17] Küçükkaya, B., Kahyaoğlu Süt, H., Öz, S., Altan Sarıkaya, N. (2020). The relationship between dyadic adjustment and prenatal attachment in pregnancy. *Acıbadem University Health Sciences Journal*. 11(1):102-110. DOI:10.31067/0.2020.246

[18] Badem, A., & Zeyneloğlu, S. (2021). Determination of prenatal attachment levels of pregnant women and affecting factors. *Kırşehir Ahi Evran University Journal of Health Sciences*. 1(1):37-47.

[19] Eyüpoğlu, D., & Eyüpoğlu, M. (2020). Prenatal attachment, anxiety and depression in pregnant adolescents and the emotional availability of their parents. *Anatolian Journal of Psychiatry*. 21(2):124-132. DOI:10.5455/apd.56516

[20] Dağlar, G., & Nur, N. (2018). Level of mother-baby bonding and influencing factors during pregnancy and postpartum period. *Psychiatria Danubina*. 30(4):433-440. DOI: 10.24869/psyd.2018.433

[21] Ulu, P.G., & Bayraktar, S. (2018). Investigation of variables related to prenatal bonding levels in pregnant women. *Yeni Symposium*. 56(2):1-9. DOI: 10.5455/NYS.20180629015333

[22] Tekin, H.H., & Karakuş, Ö. (2019). The relationship between childhood trauma, emotion regulation difficulties and marital satisfaction in pregnant adolescents. *Turkish Journal of Family Medicine and Primary Care*. 13(4):500-507. DOI:10.21763/tjfmpc.519969

[23] Yıldız, M. A., & Baytemir, K. A. (2016). Mediation role of self-esteem in the relationship between marital satisfaction and life satisfaction in married individuals. *Inonu University Journal of the Faculty of Education*. 17(1):67-80. DOI: 10.17679/iuefd.17181627

[24] Fincham, F. D., & Bradbury, T. N. (1987). The assessment of marital quality: A reevaluation. *Journal of Marriage and the Family*. 797-809. DOI: 10.2307/351973

[25] Erbil, D. D., & Hazer, O. (2018) Examination of married and working individuals' marital adjustment. *International Journal of Eurasian Education and Culture*. 3(5):99-116. DOI: 388/810

[26] Haylı, R.G., Durmuş, E., Kış, A. (2017). Investigating the marital satisfaction in terms of gender: A meta-analysis study. *International Journal of Human Sciences*. 14(4):3328-3342. doi:10.14687/jhs.v14i4.4830

[27] Yanikkerem, E., Goker, A., Ustgorul, S., Karakus, A. (2016). Evaluation of sexual functions and marital adjustment of pregnant women in Turkey. *Int J Impot Res*. 28(5):176–183. DOI: 10.1038/ijir.2016.26

[28] Durualp, E., Kaytez, N., Aykanat Girgin, B. (2017). An analysis of the relation between marital satisfaction and maternal bonding. *Anatolian Journal of Psychiatry*. 18(2):129-138.

[29] Sis Çelik, D., & Aksoy Derya, Y. (2019). Determining the self-care agency and the health practice levels of the pregnant women and the effective factors. *Gümüşhane University Journal of Health Sciences*. 8(1):111-119.

[30] Beyaz, E., Gökçeoğlu, S., Özdemir, N. (2020). Determination the health practice levels of pregnant women in the Muş City Center. *Van Health Sciences Journal*. 13(2):9-16.

[31] Hadian, T., Moosavi, S., Meedya, S., Mohammad-Alizadeh-Charandabi, S., Mohammadi, E., Mirghafourvand, M. (2021). Relationship of health practices with depression and maternal-fetal attachment in adolescent pregnant women: A prospective study. *Archives of Psychiatric Nursing*. 35(5):465–471. DOI: 10.1016/j.apnu.2021.06.011

[32] Özcan, N., Boyacıoğlu, N., Dikeç, G., Dinç, H., Enginkaya, S., Tomruk, N. (2018). Prenatal and postnatal attachment among turkish mothers diagnosed with a mental health disorder. *Journal Issues in Mental Health Nursing*. 39(9):795-801. DOI:10.1080/01612840.2018.1455773

Research Article
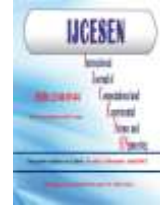
Computation of Neutron Coefficients for B₂O₃ reinforced Composite

Bekir ORUNCAK*

Afyonkocatepe University, Afyonkarahisar-Turkey
* **Corresponding Author** : **Email:** boruncak@aku.edu.tr - **ORCID:** 0000-0001-9823-5665

Abstract:

Radiation is an important phenome and is used in different area since its discovery. Although there are different types of radiation, neutron is one of the most interesting types as it is an uncharged particle. This character made neutron is more dangerous radiation types than others and thus protection from neutron effect requires more care. In this paper neutron attenuation coefficients of B_2O_3 reinforced composite have been investigated using Phy-X/PSD software.

1. Introduction

Radiation is an important phenome and has been used in many different fields such as medical science, energy sector etc. Although there are different types of radiation, neutron is one of the most interesting types as it is an uncharged particle. This character made neutron is more dangerous radiation types than others and thus protection from neutron effect requires more care. There are many different works were report in this field including lead and led based materials [1-5]. As the neutron interaction with material are mainly through (n,p) reaction, this leads to use low atomic number materials as shielding materials to be protected from neutron [6-20]. As the neutron uncharged particle, it has weak interaction processes with a medium and this results deep penetrate into materials. Thus boron is one of the main material for this purposes [21-36]. The neutron interaction with matter is expressed with the neutron cross section (σ_t) and it can be expressed as in equation 1.

$$\sigma_t = \sigma_s + \sigma_a \qquad (1)$$

here σ_s is the scattering while σ_a is the absorption of neutrons.

The attenuation for neutron is expressed the fast neutron effective removal cross section (FNRCS) which express neutron shielding properties. It is given using equation 2.

$$\Sigma_R = \Sigma_i \rho_i (\frac{\Sigma_R}{\rho})_i \qquad (2)$$

In this paper neutron attenuation coefficients of B_2O_3 reinforced composite have been investigated using Phy-X/PSD.

2. Materials and Methods

The neutron attenuation coefficients are obtained in terms of FNRCS. The materials used for this work is Al_2O_3 composite where B_2O_3 were used in different rate of 45, 50, 55, 60, 65, 70 (mol%). The addition of B_2O_3 in composite is to see whether is it possible to increase neutron shielding properties. When B_2O_3 rate is changed in composite the Average molecular weight (g/mol) of composite and thus density for composite changed. These results were shown in Figure 1 and Figure 2 respectively where it is seen that both quantities have been increased linearly with the increasing B_2O_3 rate in composite. The parameters have been obtained for six different types materials using Phy-X/PSD online code which is a free online platform [37].

3. Results and Discussions

The calculations result of FNRCS of six different types of composites where B_2O_3 have been used, are shown Fig. 3 where it is seen that the FNRCS increased with the increasing B_2O_3 rate. This is

interesting and expected results as boron is well known element for neutron absorption. The relation between Neutron attenuation coefficients and Average molecular weight is displayed in Fig. 4 where it is clearly seen that over 97% correlation has been obtained between two parameters.
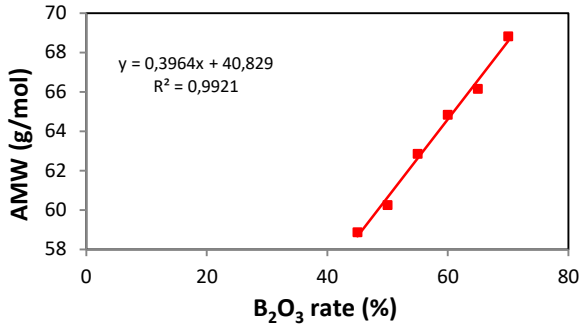
Figure 1. *Average molecular weight (g/mol) as a function of B2O3 rate in composite*
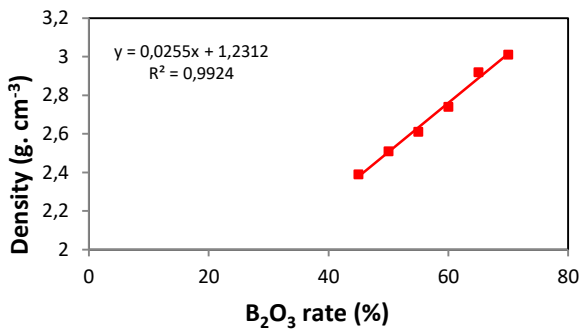
Figure 2. *Correlation between B_2O_3 rate and density of composite materials*
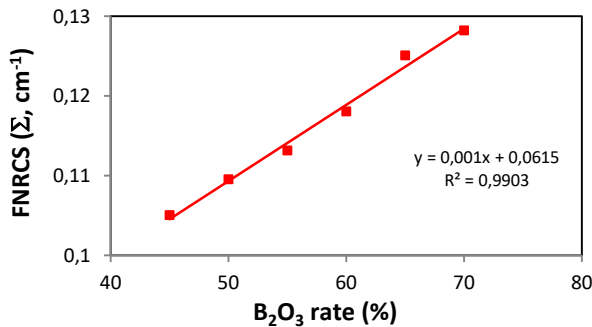
Figure 3. *The FNRCS as a function of B_2O_3 rate in composite*
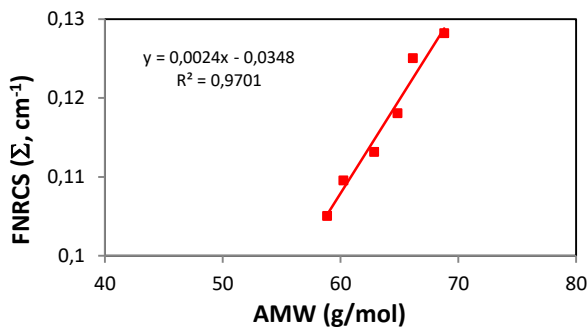
Figure 4. *Correlation between Neutron attenuation coefficients and Average molecular weight*

Author Statements:

- **Ethical approval:** The conducted research is not related to either human or animal use.
- **Conflict of interest:** The author declares that there is NO known competing financial interests or personal relationships that could have appeared to influence the work reported in this paper
- **Acknowledgement:** The author declare that there is NO nobody or no-company to be acknowledged.
- **Author contributions:** The author declare that all works done by himself.
- **Funding information:** The author declares that there is no funding to be acknowledged.
- **Data availability statement:** The data that support the findings of this study are available on request from the corresponding author. The data are not publicly available due to privacy or ethical restrictions.

References

[1] Waheed, F. , İmamoğlu, M. , Karpuz, N. & Ovalıoğlu, H. (2022). Simulation of Neutrons Shielding Properties for Some Medical Materials . *International Journal of Computational and Experimental Science and Engineering*. 8 (1); 5-8 . DOI: 10.22399/ijcesen.1032359

[2] Aljawhara H. Almuqrin, M.I. Sayyed, Ashok Kumar, B.O. El-bashir, I. Akkurt (2021). Optical, mechanical properties and gamma ray shielding behavior of TeO2-Bi2O3-PbO-MgO-B2O3 glasses using FLUKA simulation code. *Optical Materials* 113:110900 DOI: 10.1016/j.optmat.2021.110900

[3] Al-Obaidi S., H. Akyıldırım, K. Gunoglu, I. Akkurt. (2020) *Acta Physica Polonica A* 137; 551 DOI: 10.12693/APhysPolA.137.551

[4] Iskender Akkurt, Parisa Boodaghi Malidarreh & Roya Boodaghi Malidarre (2021). Simulation and Prediction the Attenuation Behavior of the KNN-LMN Based Lead Free Ceramics by FLUKA Code and Artificial Neural Network (ANN) - Based Algorithm, *Environmental Technology* DOI: 10.1080/09593330.2021.2008017

[5] Tan, T., Zhao, Y., Zhao, X., Chang, L. & Ren, S. (2022). Mechanical properties of sandstone under hydro-mechanical coupling. *Applied Rheology*, 32(1); 8-21. https://doi.org/10.1515/arh-2022-0120

[6] V. P. Singh, N. M. Badiger, (2016). Photon interaction with semiconductor and scintillation detectors, *Nucl Sci Tech* 27:72. DOI 10.1007/s41365-016-0076-8.

[7] Huseyin Ozan Tekin, Baris Cavli, Elif Ebru Altunsoy, Tugba Manici, Ceren Ozturk, Hakki Muammer Karakas (2018). An Investigation on Radiation Protection and Shielding Properties of 16 Slice Computed Tomography (CT) Facilities. *International Journal of Computational and*

Experimental Science and Engineering 4(2);37 – 40. https://doi.org/10.22399/ijcesen.408231

[8] Iskender Akkurt (2007). Effective Atomic Numbers for Fe–Mn Alloy Using Transmission Experiment *Chinese Phys. Lett.* 24; 2812. DOI: 10.1088/0256-307X/24/10/027

[9]Şen Baykal, D , Tekin, H , Çakırlı Mutlu, R.(2021). An Investigation on Radiation Shielding Properties of Borosilicate Glass Systems. *International Journal of Computational and Experimental Science and Engineering*,7(2);99-108 DOI: 10.22399/ijcesen.960151

[10]R., Boodaghi Malidarre, R. Khabaz, M. R. Benam, and V. Zanganeh, (2019). A Feasibility Study to Reduce the Contamination of Photoneutrons and Photons in Organs/Tissues during Radiotherapy. *Iran. J. Med. Phys.* 17; 366-373. http://doi.org 10.22038/ijmp.2019.40879.1579.

[11]Salima, B., Seloua, D., Djamel, F. & Samir, M. (2022). Structure of pumpkin pectin and its effect on its technological properties. *Applied Rheology*, 32(1), 34-55. https://doi.org/10.1515/arh-2022-0124

[12] Akkurt, I Basyigit C., Kilincarslan S., Beycioglu A. (2010). Prediction of photon attenuation coefficients of heavy concrete by fuzzy logic. *Journal of Franklin Institute-Engineering and Applied Mathematics.* 347(9);1589-1597. DOI: 10.1016/j.jfranklin.2010.06.002

[13]Günay, O. , Gündoğdu, Ö. , Demir, M. , Abuqbeitah, M. , Yaşar, D. , Aközcan, S. , Kapdan, E. & Yarar, O. (2019). Determination of the Radiation Dose Level in Different Slice Computerized Tomography. *International Journal of Computational and Experimental Science and Engineering,* 5(3); 119-123 . DOI: 10.22399/ijcesen.595645

[14] Hakan AKYILDIRIM (2019). Calculation of Fast Neutron Shielding Parameters for Some Essential Carbohydrates. *Erzincan University Journal of Science and Technology*, 12(2);1141-1148, DOI: 10.18185/erzifbed.587514

[15]Iskender Akkurt, Roya Boodaghi Malidarre. (2022). Physical, structural, and mechanical properties of the concrete by FLUKA code and phy-X/PSD software. *Radiation Physics and Chemistry* 193; 109958. DOI: 10.1016/j.radphyschem.2021.109958

[16]Tekin, Huseyin Ozan, ALMisned, Ghada, Susoy, Gulfem, Zakaly, Hesham M. H., Issa, Shams A. M., Kilic, Gokhan, Rammah, Yasser Saad, Lakshminarayana, Gandham and Ene, Antoaneta. (2022). A detailed investigation on highly dense CuZr bulk metallic glasses for shielding purposes. *Open Chemistry*, 20(1);69-80. DOI: /10.1515/chem-2022-0127

[17]Hamdy A. Awad, Ibrahim Abu El-Leil, Aleksey V Nastavkin, Abdellah Tolba, Mostafa Kamel , R. M. El-Wardany , Abdalla Rabie, Antoaneta Ene , H.O. Tekin, Shams A.M. Issa, Hesham M.H. Zakaly. (2022). Statistical Analysis on the Radiological Assessment and Geochemical studies of Granitic Rocks in the North of Um Taghir Area, Eastern Desert, Egypt. *Open Chemistry*, 20(1): https://doi.org/ 10.1515/chem-2022-0131

[18]Zarkooshi, A. , Latıf, K. H. & Hawı, F. (2021). Estimating the Concentrations of Natural Isotopes of 238 U and 232Th and Radiation Dose Rates for Wasit Province-Iraq by Gr-460 system . *International Journal of Computational and Experimental Science and Engineering*, 7(3):128-132 . DOI: 10.22399/ijcesen.891935

[19]Kadir Gunoglu, İskender Akkurt (2021). Radiation shielding properties of concrete containing magnetite. *Progress in Nuclear Energy* 137;103776. DOI: 10.1016/j.pnucene.2021.103776

[20]Demir, N., Tarim, U.A., Popovici, MA. et al. (2013) Investigation of mass attenuation coefficients of water, concrete and bakelite at different energies using the FLUKA Monte Carlo code. *J Radioanal Nucl Chem* 298; 1303–1307. DOI: 10.1007/s10967-013-2494-y

[21]I. Akkurt, H. Akyıldırım, F. Karipçin, B. Mavi, (2012). Chemical corrosion on gamma-ray attenuation properties of barite concrete. *Journal of Saudi Chemical Society*.16(2);199-202. https://doi.org/10.1016/j.jscs.2011.01.003.

[22]E.E. Altunsoy, H.O. Tekin, A. Mesbahi, I. Akkurt. (2020) MCNPX Simulation for Radiation Dose Absorption of Anatomical Regions and Some Organs. *Acta Physica Polonica A* 137(4);561. DOI: 10.12693/APhysPolA.137.561

[23]Sarihan, Mucize. (2021). Simulation of gamma-ray shielding properties for materials of medical interest. *Open Chemistry*, 20(1);81-87. DOI: 10.1515/chem-2021-0118

[24]Ural, A. & Kilimci, Z. H. (2021). The Prediction of Chiral Metamaterial Resonance using Convolutional Neural Networks and Conventional Machine Learning Algorithms. *International Journal of Computational and Experimental Science and Engineering*, 7(3),156-163. DOI: 10.22399/ijcesen.973726

[25]Tekin, Huseyin Ozan, ALMisned, Ghada, Zakaly, Hesham M. H., Zamil, Abdallah, Khoucheich, Dalia, Bilal, Ghaida, Al-Sammarraie, Lubna, Issa, Shams A. M., Al-Buriahi, Mohammed Sultan and Ene, Antoaneta. (2022). Gamma, neutron, and heavy charged ion shielding properties of Er3+-doped and Sm3+-doped zinc borate glasses. *Open Chemistry*, 20(1);130-145. https://doi.org/10.1515/chem-2022-0128

[26] Kaplan, M. F. (1989). Concrete Radiation Shielding. Longman Scientific and Technology, *Longman Group UK Limited, Essex,* London.

[27]Gökçe, C. O. , Durusu, V. & Unal, R. (2023). Disturbance Rejection Performance Comparison of PSO and ZN Methods for Various Disturbance Frequencies. *International Journal of Computational and Experimental Science and Engineering*, 9(1);17-19 . DOI: 10.22399/ijcesen.1202255

[28]Malidarre, R. B., Ozan Tekin, H., Gunoglu, K. & Akyıldırım, H. (2023). Assessment of Gamma Ray Shielding Properties for Skin. *International Journal of Computational and Experimental Science and Engineering*, 9(1);6-10. DOI: 10.22399/ijcesen.1247867

[29]El Sayed Y, El-Adawy A, El-KheshKhany N, (2006). Effect of rare earth (Pr2O3, Nd2O3, Sm2O3, Eu2O3, Gd2O3 and Er2O3) on the acoustic properties of glass belonging to bismuth–borate system, *Solid State Commun*. 139; 108–113. https://doi.org/10.1016/j.ssc.2006.05.022

[30]Caymaz, T. , Çalışkan, S. & Botsalı, A. R. (2022). Evaluation of Ergonomic Conditions using Fuzzy Logic in a Metal Processing Plant. *International Journal of Computational and Experimental Science and Engineering*, 8(1);19-24. DOI: 10.22399/ijcesen.932994

[31]Arbouz, H. (2022). Modeling of a Tandem Solar Cell Structure Based on CZTS and CZTSe Absorber Materials . *International Journal of Computational and Experimental Science and Engineering ,*, 8(1); 14-18. DOI: 10.22399/ijcesen.843038

[32]Zhang R, WilsonVL, Hou A, MengG (2015) Source of lead pollution, its influence on public health and the countermeasures. *Int J Health Anim Sci Food Saf* 2;18–31

[33]Blizard, E.P., Abbott, L.S. (1962). Reactor Handbook, vol. III, Part B, Shielding, *John Wiley and Sons, Inc*.

[34]Chilton, A.B., Shultis, J.K., Faw, R.E. (1984). Principles of Radiation Shielding, *Prentice-Hall,* Englewood Cliffs.

[35]Woods, J. (1982). Computational Methods in Reactor Shielding, *Pergamon Press Inc.,* New York.

[36]Schmidt, F.A.R. (1969). Analytical Radiation Shielding Calculations for Concrete – Formulas and Parameters, *Nuclear Engineering and Design*, 10; 308-324. DOI: 10.1016/0029-5493(69)90067-3

[37]Erdem Şakar, Özgür Fırat Özpolat, Bünyamin Alım, M.I. Sayyed, Murat Kurudirek. (2020). Phy-X / PSD: Development of a user friendly online software for calculation of parameters relevant to radiation shielding and dosimetry. *Radiation Physics and Chemistry* 166;108496 https://doi.org/10.1016/j.radphyschem.2019.108496

The Effect of Parametric Design on the Reconstruction of Cultures within the Context of Jakobson's Communication Model

Rıza Fatih MENDİLCİOĞLU*

Baskent University, Faculty of Art, Design and Architecture, Interior Architecture and Environmental Design Department, 06790, Ankara-Turkey
* **Corresponding Author** : **Email:** rizafatih@gmail.com - **ORCID:** 0000-0003-0094-2826

Abstract:

The aim of this study is to examine the effect of parametric design on cultural architectural works within the framework of Roman Jakobson's model of communication. The study will focus on how the use of parametric design is handled as a source of form in contemporary architecture, how it affects the way cultural buildings are perceived and how they communicate their cultural significance. In addition, the other aim of the research is to examine how social culture and architecture, which are both means of communication, can be re-established in a contemporary way through parametric design. Within the framework of Jakobson's communication model, the relationship between the five functions of communication and architecture will be analysed, and then the relation between this relationship and parametric design will be established. In this context, the cultural impact of parametric design will also be examined around four of the five basic functions of Jakobson's communication model, and how parametric design contributes to the process of cultural communication and message creation will be discussed.

The research methodology includes a literature review on parametric design, cultural constructs and Jakobson's communication model. In addition, a case study approach will be used to examine the impact of parametric design on the cultural architectures of societies. In this context, "Sunac Guangzhou Theatre" from China, which reconsiders its ancient culture shaped by geography with western culture through contemporary architecture, will be taken as a sample building. The use of parametric design tools will be analysed in the creation of the design concept and cultural quality of the building.

In the conclusion and evaluation section, the evaluation of the cultural impact of parametric design through Jakobson's communication model will be evaluated through a table, and the positive contributions of parametric design to the cultural visions of societies in contemporary form will be summarized.

1. Introduction

The use of computational design in architecture has become intertwined with the design and production process, merging digital information and production knowledge in the last decade of the 20th century. Parametric design, one of the methods of computational design, stands out among other digital design methods, particularly among architects who reject the notion of architecture solely based on function and aim to rebuild the relationship between architecture and meaning through forms. In parametric design, data related to the building, such as environmental and cultural factors, can be used as a source of form. Along with digital architecture, designers have gained the ability to create complex and curved forms such as topological forms and isomorphic surfaces more easily through parametric design, as well as the ability to associate them with other forms and change them independently of the design process. Today, the possibilities of form offered by parametric design, which are beyond the usual, make up a significant part of the architectural designs of developing countries, particularly China, the United Arab Emirates, and other countries that sustain their economic development with their cultural change. Parametric design is utilized in the designs of buildings that represent the cultures of these countries. In this study, the opportunities provided by parametric design in rethinking culture and representing it through architecture, the relationships between form-culture and form-

meaning, and how cultural and environmental information is utilized in parametric design will be examined in the context of Jakobson's communication theory. The architectural form-culture relationships, geometry-meaning relationships, and how cultural and environmental information is utilized in parametric design will be investigated through the analysis of a contemporary cultural structure designed using parametric design methods. The study will focus on the Sunac Guangzhou Grand Theatre in China, which tries to reconnect with its ancient culture that has been separated due to political reasons, but now is rebuilding its cultural connections with the influence of economic power. The study will use a descriptive survey model and will discuss qualitative research methods based on the analysis of Jakobson's communication model functions in the meaning analysis of the structure. In the discussion and conclusion section, the cultural and architectural effects of addressing the relationships between meaning-form and culture-form through the opportunities provided by parametric design in the design of cultural structures will be discussed.

2. Material and Methods

2.1 Architecture As A Sign And Communication Tool

Architectural design involves recording processes that are encrypted in different forms such as plans and sections. The architect uses diagrams, iconic visual indicators, signs, symbols, codes, qualitative and quantitative indicators in these recording processes. The codes of architectural components are typological. These codes are directly related to the function and geometry of the architectural component and represent the most prominent but only a part of architectural coding. In the design phase, both the function and geometry of the architectural component are articulated by the architect. In order to decipher the codes, it is necessary to find and recognize the codes that the architectural component harbors in order to be able to understand and evaluate the meaning of the architectural component. In order to decipher cultural and historical codes of an architectural component, one must know the social and cultural codes of the society to which it belongs, just as in deciphering a text.

According to Eco; conveying the function carried by a formal property of an architectural component is a cultural datum [1]. These formal properties explain how a door, a staircase, or a column is a sign. For example, after an individual acquires an image of a dwelling space (house, cave, hollow, etc.), they can convey the structure of the shelter to others using

visual indicators. Thus, architectural coding creates a visual code and becomes the subject of communicative relationships [1]. When it comes to the relationship between culture and architecture, another deciphering process may be required, along with Eco's method, in order to decode cultural images. Because the cultures of societies are complex and deep, the same goes for the symbolic representation in architecture. Therefore, as proposed by Jakobson, it may be necessary to reveal the interrelated multi-layered functions to decipher a communicative phenomenon.

Linguistics researcher Roman Jakobson proposed a coding and decoding model by examining each component of the communication process in his book "Closing statement: Linguistics and Poetics" written in 1960. According to this model, the correct use of each component allows for proper understanding and effective communication. Jakobson's communication theory is based on the coding and decoding process. The coding process is the process in which the message sender conveys their meaning, while the decoding process is the process in which the message receiver extracts meaning. These two processes take place on five components referred to as source, message, channel, receiver, and code.

Drawing from the claim that the architectural design process shows similarities to the communication process, it can be concluded that designers design their designs to convey a specific message and that this message is conveyed from the source (designer), code (language), message (design), channel (architectural language), to the receiver (user). Feedback is the use and interpretation of the architectural work.

According to Leach, Jakobson's communication model can provide an important framework for the use and interpretation of language in architecture by emphasizing the symbolic nature of architecture and the differences between different architectural languages [2]. In this context, Jakobson's communication diagram is an approach to defining and understanding the functions of language and communication. This diagram can also be used in fields such as architecture and design, and can be used to analyze and evaluate designs according to communication objectives.

Essentially, considering the direction of communication for an object is also defining its primary function, i.e., an architectural object can be perceived as a communication that refers only to function (message) and physical structure (channel). In other words, this interaction can be defined as an example within the primary function of the object in communication. Jakobson divides the functions of language into five different categories: referential,

expressive, aesthetic, phatic, and metalingual [3]. These categories represent the different aspects and purposes of language. If these functions are examined from an architectural perspective, they can be applied as follows:

Function of Expression: The linguistic expression of a building's architectural use, material choices, and layout plan, which aims to define the architectural use of expression, the design and appearance of the building, the use of interior spaces, and how people feel in the building. It carries the lines of a particular style.

Aesthetic Function: It includes the use of aesthetic elements such as color, texture, geometry, form, and rhythm, which are also related to the cultures of societies in architecture.

Semiotic Function: Directly related to culture, the purpose of a building, its social and cultural meanings, symbolic values, or aesthetic goals are expressed through the appearance, form, material, color, and so on of the building.

Metalinguistic Function: Derived from history, an architectural object that was used in a cultural context in the past can be used with a new understanding. This can be defined as a reference to the source of the code. When architecture is designed to achieve a specific purpose or create a specific effect, the metalinguistic function becomes important. For example, a building's design can influence people's thoughts and behavior. It can determine the size, design, interior spaces, and how the building's appearance should be perceived and how people should feel in the building.

Injunction Function: Architectural objects and environmental objects can limit people's behavior. Especially complementary objects such as stairs and railings can serve a warning and control function on functions.

The work of Christian Norberg Schultz's language system-architecture research and Preziosi's perception and space relation research continued with Eco's efforts to interpret architecture in the 1970s. In his book "Logic der Baukunst," Schultz examined architecture through the fundamental philosophy of language, associating the components of architecture with the facts of syntax and semantics. However, such attempts have been limited to the reuse of clichés and have not been able to create a more complex syntax.

After the unsuccessful attempts of the 1970s and 1980s, it became apparent that architectural semiotics could not be reduced to either syntax or semantics. During this period, theorists and architects such as Peter Eisenman and Charles Jenks, who were at the forefront of using computer algorithms-logic and architecture triangle, worked on the use and interpretation of semiotic systems in architecture. The inclusion of computers in the design process in the "digital era of architecture" has enabled the creation of more complex and curved forms, and the concept of "form" has started to emerge in architecture, breaking away from the purely functionalist understanding.

2.2 Parametric Design as a Cultural Recreation Tool

Greg Lynn's book "The Folding in Architecture" published in 1993 has been a turning point for digital design beyond a digital design understanding that only includes CAD tools. Based on Leibniz's mathematics, Lynn argues that there is nothing in the universe, including architecture, that cannot be digitized. However, Lynn is not interested in "Modular" digitization or the deconstructivist focus on the breaking of form with predetermined and selected forms for the world or architecture. Instead, "the fold is chasing heterogeneity and differentiation. The fold allows unrelated elements to constantly blend together [4].

Lynn's philosophy focuses on topological forms that can be forgotten due to the difficulty of their production in the past and can be reshaped at any moment. The Baroque connotation added to Deleuze's metaphor of "fold" has directed architectural practice towards a paradigm where structures are transformed into a complex with multiple layers that symbolizes a higher level of reality, containing different meanings and moving away from both the post-modernist understanding of the 80s and the complex deconstructionist discourse of the 90s. While Baudrillard describes this paradigm as "cultural hyperreality", Greg Lynn has pointed out that "digital architecture is more concerned with the production of virtual representations than any other discipline [5].

In the early days of digital architecture, the most important problem designers faced was the difficulty of controlling the unlimited geometric structure inherent in topological forms. While this "limitlessness" develops the creativity of the designer in the production of conceptual forms, it has caused difficulties in the practical implementation of design in a discipline such as architecture where there are limitations. The most important of these difficulties have been the association of topological forms that coincide with the needs of architectural design with different geometries. In response to these problems, designers have developed the parametric design method based on parametric algorithms, which are easy to use and enable the production of unlimited geometries, and see architectural knowledge as a source of form. Parametric design is a digital design understanding

based on the relationships between models. Based on the tool to generate a geometry in variable forms, it relies on constraints. As a tool for controlling geometric relationships, parametric design enables the creation and modification of elements that constitute a design by differentiating them. The basis of parametric design tools is numerical algorithms. Thus, it increases the control of the designer on the design geometry and allows the evaluation of certain conditions by the designer. The geometry of the design is determined, designed, associated with different geometries and modified through interfaces called "schemas" with the help of code that can perform algorithmic calculations. These schemas perform an interface function where any geometric form can be created, manipulated, and associated with other geometries (Figure 1). "Thinking of parametric design logic as a new form of digital design, thinking promises to continue to influence future developments in theories and technologies of design media [6].
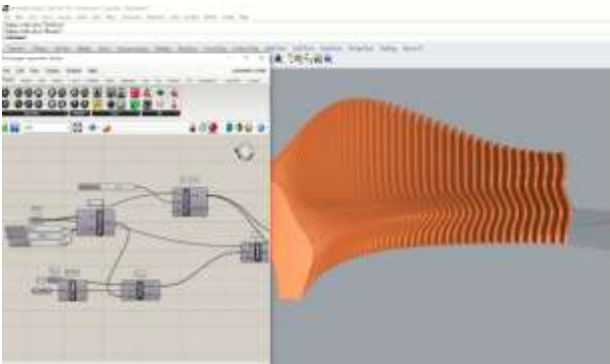
Figure 1. Parametric design geometries are created In the scheme, the forms can be related to each other, simultaneously can be manipulated.

Certain computer software is often used as parametric design tools. The most important of these are Rhino-Grasshopper and Revit-Dynamo. In addition to these, programs specific to the needs and characteristics of the project can be written codes. The common features of all these programs are that they allow design criteria such as light, topography and wind to be handled as codable geometric forms. Desired forms can be created in schemes with the help of codes according to certain desired characters.

Parametric Design Has Adaptatiton Ability
Parametric design brings flexibility and also creates the concept of "adaptation" in design. In a parametric design scheme, one or more basic form particles that will constitute the design are taken into account. These form particles replicate and differentiate according to the algorithm written, ultimately

creating the main form. As a result, the designs created can adapt to another design or become a part of it by modifying their data. In parametric design, the concept of "adaptation" can regulate not only the design geometry but also the relationships of the structure with its environment. For instance, creating a local pattern that represents a culture parametrically can provide "cultural adaptation" to the structure, and shaping its facade according to sunlight, wind, and topography can provide "environmental adaptation." Environmental adaptation can enhance the sustainability of the structure. For example, using the angles of the sun's rays and other information as the source of the form can solve the issue of openness in buildings and increase the utilization of natural light.

The identity of parametric design is formed by the designer's approach to geometries and the ability to relate them to each other. In the scheme, non-Euclidean, topological forms can be associated with each other, replicated through iteration and differentiated to create the main form (continuous differentiation and differentiation). Along with these operations, various rotating and advancing variations of the same form can be derived. (Figure 2). All of these elements form the formal character of parametric design and ensure its formal harmony.
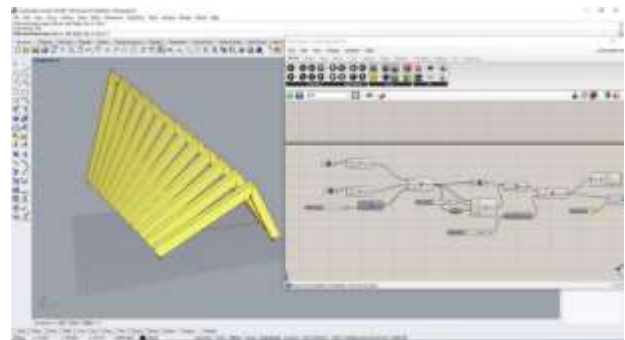
Figure.2: Same as Continious Differentiation and iteration methods reproduction and reproduction of the form with different variables. Reference:Author's Design.

Parametric Design Uses Data(s) As the Source of Form
In architecture, one of the most important components of design is having tectonic knowledge, which includes the mathematical and three-dimensional morphology of a structure. "Parametric design implies the ability (knowledge as well as digital skills) to mediate tectonic knowledge [7]. The source, representation, metaphorical or any geometric structure can be a source of knowledge, which can be processed into a parametric schema and form. In a performative and form-generating parametric schema, shapes that are compatible with forces that affect the structure such as the angle of the sun, wind direction, and topography can be

created. These forces can shape the design and material and production systems can be coded to be compatible with the design (Figure 3).

In his article Patrik Schumacher defines parametric design as "a design paradigm beyond a formal style that can utilize purely environmental effects to create all tectonic textures from environmentally adaptive façade geometries to light-controlled apertures" [8]. A specific cultural pattern, form, or geometry that represents a culture can be taken as the source of the form, modified, transformed, and presented with a new understanding.

With the increasing density of communication in the post-Fordist knowledge society, social communications have become more complex and intensified. The post-Fordist knowledge society demands that individuals communicate as much as possible with the outside world. This communication system, consisting of various social relationships, becomes stages of the social knowledge system where the morphology of spaces is redefined. Social communication and social memory change and develop simultaneously. The concentration and complexity of social communication along with knowledge lead to the densification and complexity of social memory.

Parametric design is based on "data" exchange. Each data representing social memory can be approached in the form of algorithms. The form-generating qualities (rules) of parametric software such as differentiation and adaptation have now begun to separate and relate urban and architectural subsystems to represent each other. Over time, the urban memory that has been layered uncontrollably due to increased information density can be reconsidered and transformed into refined design geometry. A specific cultural pattern, form, or geometry that represents a culture can be taken as the source of the form, modified, transformed, and presented with a new understanding. Likewise, through parametric design, the representational geometry that forms the structure of a museum as a space of memory can be metaphorically recreated, and the relationship between culture and structure can be established in this way.

Relation Between Culture and Architecture can be established through the use of information as a source of form through parametric design. This can strengthen the cultural qualities of a structure. The "Abu Dhabi Louvre Museum" located in Abu Dhabi can be considered as an important example in this regard. The roof of the structure has been reconsidered in a contemporary form through parametric design, utilizing the traditional component of Arab architecture, the "Mashrabiya" (Figure 3).

Figure 3*: The roof of the Louvre in Abu dhabi parametric mashrabiya It is designed by reconsidering it through algorithms.*

In this section, the current cultural architecture of a society trying to recreate its cultural structure in a contemporary way will be examined in the context of the possibilities provided by parametric design. The consequences of using cultural memory and environmental data as a source of form in cultural structures will be discussed. In the framework of the examination, the "Guangzhou Sunac Grand Theater" from China, which reinterprets its ancient culture in a contemporary way with economic power, will be taken as an example.

In the analysis, the museum, designed with a parametric design approach, will be examined as a cultural communication object, and its architectural components and represented cultural phenomena will be analyzed. The methods of analyzing the functions that make up Roman Jakobson's communication model will be used as the analysis method. In this context, the plan scheme, main geometry, relationship with the surroundings and topography, material, and structural structure of the building will be discussed with the methods stated, and the possibilities provided by parametric design in establishing form-culture and form-meaning relationships will be examined.

3. Case study: Sunac Guangzhou Grand Theatre

In 1949, with Mao's Cultural Revolution, China weakened its ties with its past, restricted its relations with the West, and began to rebuild its culture with the revival of its economy and renewed relations with the West in the early 21st century. In this context, Western-style museums, art galleries, theaters, and opera houses began to be built, especially in Beijing and Guangzhou, which were redesigned as the country's gateway to the West, and these structures were mostly designed by Western architects such as Zaha Hadid, Patrik Schumacher, and Perkins+Will. China attached great importance to theater structures, which have an important place

in its culture, and more than 400 theaters have been built in just the last decade of the 21st century [9]. In the design of theaters, not only elements of Western culture, but also elements from traditional Chinese theater designs and symbols representing Chinese culture were used, and parametric design was mainly preferred due to its use of local culture and associated topographic elements as form sources, as well as its iconic form and size understanding. Sunac Guangzhou Grand Theater can be considered as one of the most important examples of these theater structures both culturally and symbolically (Figure 4).

Figure 4. Sunac Guangzhou Grand Theater. Reference: Steven Chilton Architects.

In this study, the Sunac Guangzhou Grand Theater, which takes on cultural symbols and architectural elements of traditional Chinese theater through parametric design, will be investigated as an example. The cultural symbols that form the source of the theater's design will be analyzed in the context of Jakobson's communication model, and the contribution of parametric design to societies that recreate their cultures through architecture and the ability of parametric design to transmit local culture will be examined. One of the most important features of Guangzhou, where the theater is located, is that it is the center of silk production and the starting point of the Silk Road. Moreover, the city, which is also the birthplace of the myth of the "phoenix" bird, which has an important place in Chinese culture, was also one of the important centers of traditional Chinese theater culture in the past, which was restricted during the Mao era. Silk fabric and phoenix bird images were used as form sources in the design of the exterior shell of the structure. The fluidity of silk fabric was digitized through parametric design algorithms, combined with the shape resembling the wings of the phoenix bird, and refined again through parametric algorithms to reach the final geometry (Figure 5). The use of the image of the phoenix, which can be reborn from its own ashes in mythology, alongside the image of silk

Figure 5. Sunac Guangzhou Grand Theather's form source is a silk fabric and phoenix created with parametric design tools. Reference: Dezeen.com

fabric, symbolizes the traditional Chinese theater, which was once restricted but has been revived in a contemporary form. According to Ahuja, each fold in the outer shell is designed to symbolize the Guangzhou valley, where silk is processed [10].
The folded shell hangs down at one end of the structure and is finished with another folded entrance. This curved entrance is also a reference to the iconic curved curtains of traditional Chinese theater that were once banned, and it is intended to highlight the main entrance of the theater (Figure 6).

Figure 6. The entrance of the building is decorated with the curtains of traditional Chinese theatre symbolises. Reference: Steven Chilton Architects.

The outer shell of the building, which provides its curved geometry, is made of perforated aluminum to support its flexibility and curved form, and it is painted in red, representing Chinese culture and art (Figure 7). Artist Honfei has drawn phoenix (Fenghuang) patterns on the surface. According to Ahuja, Fenghuang represents virtue and grace, and strengthens the purpose of the building [10]. The building's floor plan is designed with the theater hall at the center, surrounded by other spaces around it. The circular traditional Chinese theater scheme is used in the design of the hall, while other spaces are designed in accordance with the geometry of the building through parametric algorithms (Figure 8). If Sunac Guangzhou Grand Theater's cultural communication features are considered through Jakobson's communication model:

Figure 7. Facade, *is made of perforated aluminum to support its flexibility and curved form, and it is painted in red, representing Chinese culture and art. Reference: Steven Chilton Architects.*

Figure 8. *Circular plan diagram of the building designed by parametric algorithms. Reference: Steven Chilton Architects.*

Metalingual Function: Updating and reusing an architectural form used in the past, recreating traditional Chinese theater through parametric algorithms.

Expressive Function: Designed through parametric design. The floor plan is circular and two-story like traditional Chinese theaters. The structure is made of steel and concrete, with a red anodized aluminum shell decorated with Phoenix bird figures.

Semiotic Function: The sources of the curved geometry of the façade include silk fabric, an important symbol in Chinese culture, the wings of the Phoenix bird, the elevations of Guangzhou Valley, and the shape of the unified shell becoming the form of the theater curtain opening at the entrance.

Aesthetic Function: The soft, hyperbolic, and curved shell geometry created through parametric algorithms, the use of red color in both interior and exterior spaces.

4. Conclusions

In this study, the impact of parametric design on cultural structures in contemporary architecture has been examined in the context of Jacobson's communication model. Architects and thinkers who opposed the post-modernist approach to design, which was based solely on function, searched for ways to give meaning back to architecture and approached architecture as a sign and communication tool. The ability of parametric design to use cultural symbols as a source of form has made it a frequently used tool in the cultural structures of societies that recreate their culture through architecture, especially in the contemporary era. When the iconic form approach is added to the qualities of parametric design, it has become one of the leading architectural styles of countries that want to present their cultural development along with their economic power, such as China and the UAE. Based on the assertion that architecture is a communication tool, the qualities of parametric design were analyzed through the example of Sunac Guangzhou Grand Theater. Four of the five functions proposed by Jacobson's communication model were used, and the results were presented in a table (Table 1).

Table 1. *Analysis of the structure according to the Jakobson model of communication*

Metalungial function	Expressive function	Semiotic function	Aesthetic function
Recreation of traditional Chinese theatre through parametric algorithms.	-It was designed by means of parametric design. -The plan scheme is circular and two-storeyed, as in traditional Chinese theatres.	-The form sources of the curved geometry of the façade; silk fabric representing silk, which has an important place in Chinese culture, the wings of the phoenix, the elevations of the Guangzhou valley, -The transformation of the monolithic shell into the opening of the theatre curtain at the entrance.	-Soft, hyperbolic and curved shell geometry generated by parametric algorithms -Use of red colours in interiors and exteriors
Updating of Ancient Culture	Rebirth of a forgotten culture.	Iconicisation of ancient but restricted culture with forgotten geometries.	Presentation of the new face of contemporary China with its past culture.

From a narrative perspective, the structure represents a contemporary expression of bringing together multiple cultural elements that are beginning to fade away or be forgotten, while the curved surfaces

created through parametric algorithms depict China's new architectural and aesthetic understanding. The iconic appearance of the structure reinforces its symbolic aspect and sanctifies ancient cultural images. The redesign of traditional Chinese theater in a contemporary form, which had an important place in China's culture in the past but was restricted during the Mao era, constitutes the superordinate function of the structure. The result of this study shows that parametric design has a significant impact on cultural structures in architecture. Examples like the Sunac Guangzhou Grand Theatre provide important clues on how parametric design can be utilized in the reconstruction of culture. When examined in the context of Jakobson's communication model, the study shows that architectural practices play a significant role in the reconstruction of culture in cultural structures.

Author Statements:

References

[1] Eco, U. (1973*).* Function and Sign: Semiotics of Architecture ", Structures Implicit and Explicit (ed.J. Bryan and R. Sauer), *Philadelphia, Publ. of the raduate School of Fine Arts, Universty of Pennsylvania,* 2;131.

[2]Leach, N. (1997). Rethinking Architecture: *A Reader in Cultural Theory.* Routledge.

[3]Jakobson, R. (1960). Linguistics and Poetics, İçinde T. Sebeok, (Yay.)., Style in Language, *Cambridge, MA: M.I.T. Press.*

[4]Şentürk, L.(2006). Deleuze ve Mekan. *Doxa.10/ V.3.*İstanbul.

[5]Lynn, G. (1999) Animate Form. *Princeton Architectural Press:* New York.

[6]Burry, M. (2011). Scripting Cultures: *Architectural Design and Programming*. NY: Wiley.

[7]Oxman, Rivka. Oxman, Robert (2014) Theories of The Digital In Architecture.*TJ Int.Limited.* Cornwall

[8]Schumacher, P.(2009). Parametricism: *A New Global Style for Architecture and Urban Design. Architectural Design*. 79(4);15.

[9]Xue,C. & Zhang,L.&Sun,C&Talamini,C (2021). Cultural Megastructures And Chinese Cities In The 21st Century: The Case Of Grand Theater. *Architecture Asia.* 4(10-10):5-6.

[10]Ahuja, A.(2020). A swirling Edifice: Steven Chilton Architects Unveil the Sunac Guangzhou Grand Theatre. Stirworld. *https://www.stirworld.com/see-news-a-swirling-edifice-steven-chilton-architects-unveil-the-sunac-guangzhou-grand-theatre*
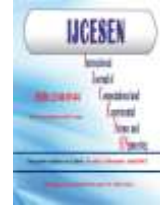
Using Machine Learning to Detect Different Eye Diseases from OCT Images

Şükrü AYKAT[1]*, Sibel SENAN[2]

[1] Mardin Artuklu University, Department of Computer Technologies, 47510, Mardin-Turkey
* **Corresponding Author** : **Email:** sukruaykat@gmail.com - **ORCID :** 0000-0003-1738-3696

[2] Istanbul University-Cerrahpasa, Department of Computer Engineering, 34320, Istanbul-Turkey
Email: ssenan@iuc.edu.tr - **ORCID :** 0000-0001-6773-0428

Abstract:

Diseases or damage to the retina that cause adverse effects are one of the most common reasons people lose their sight at an early age. Today, machine learning techniques, which give high accuracy results in a short time, have been used for disease detection in the biomedical field. Optical coherence tomography is an advanced tool for the analysis, detection and treatment of retinal diseases by imaging the retinal layers. The aim of this study is to detect eight retinal diseases that can occur in the eye and cause permanent damage as a result, using machine learning from eye tomography images. For this purpose, hyperparameter settings were applied to six deep learning models, training was performed on the OCT-C8 dataset and performance analyzes were made. The performance of these hyperparameter-tuned models was also compared with previous eye disease detection studies in the literature, and it was seen that the classification success of the hyperparameter-tuned DenseNet121 model presented in this study was higher than the success of the other models discussed. The fine-tuned DenseNet121 classifier achieved 97.79% accuracy, 97.69% sensitivity, and 97.79% precision for the OCT-C8 dataset.

1. Introduction

One of the five sense organs, which has a very important place in human life, is the eye. The retina, on the other hand, is an important layer of the eye consisting of color and light-sensitive cells and nerve fibers that provide vision directly related to the brain. In order to make sense of the perceived visual signals, it is transferred to the brain to complete the visual event [1]. Diseases that occur in the retina often cause blindness and severe vision loss. Early detection of the disease is of great importance in order to avoid incurable eye damage caused by these diseases [2]. Many imaging modalities are used to evaluate and monitor retinal abnormalities. Optical coherence tomography (OCT) and Fundus imaging are widely used.

Recently, artificial intelligence has taken an important place in disease detection and diagnosis in the biomedical field. Artificial intelligence applications provide great convenience in disease diagnosis by performing classification processes that take a long time and are tiring for experts [3], [4].

Machine learning is a subfield of artificial intelligence designed to mimic human intelligence by learning from data [5]. Deep learning, on the other hand, is a subset of machine learning based on artificial neural networks architecture. In general, artificial neural networks consist of input layer, several hidden layers and output layers. Techniques based on machine learning have shown success in many industries, including finance, pattern recognition, entertainment, biomedical and medical applications. Liu et al. [6] in estimation of stock price, Sarkar et al. [7] and Tripathi in the recommendation system of music and Sharma [8] in diagnosis of brain tumor and skin cancer used machine learning methods. In the literature, machine learning models trained with retinal images obtained from different imaging techniques have achieved a high success rate in the diagnosis of retinal diseases.

Kermany et al. [1] applied the transfer learning model to a dataset of OCT images. The model's success in classifying diabetic macular edema and age-related macular degeneration demonstrated comparable performance to ophthalmologists.

Islam et al. [9] examined how to use deep transfer learning using OCT images to detect diabetic retinopathy. In their study, they explored how to optimize the models by retraining existing deep learning models. The proposed method outperformed existing methods in terms of accuracy and training time. Tayal et al. [10] presented a deep learning framework for the classification of four different retinal diseases. In their study, multiple eye deformity estimation was performed using three different convolutional neural network models. Noise removal, retinal layer removal and brightness enhancement preprocesses were applied to OCT images. With this study, classification accuracy was 96.5%, sensitivity 96% and specificity 98.6%. Lu et al. [11] developed a new intelligent model for retinal disease detection based on deep learning from OCT images. In the proposed system, sensitivity was 94%, specificity was 97.3%, and average accuracy was 95.9%. In the presented study, Subramanian et al. The OCT-C8 dataset [12], which is openly published on Kaggle and consists of 8 different classes, was used by [13]. These classes include central serous retinopathy (CSR), age-related macular degeneration (AMD), choroidal neovascularization (CNV), diabetic macular edema (DME), diabeticretinopathy (DR), drusen and macular hole (MH) diseases and their normal appearance. Six different deep learning models with hyperparameter tuning were applied on the dataset. The performances of the models discussed are compared with each other and with other studies in the literature, and the results are presented. The materials and methods used in this study are described in Section 2. The performances of the machine learning models discussed in Section 3 are examined. The general results of the study are given in Section 4.

2. Material and Methods

2.1 Dataset

The OCT-C8 dataset [12] consists of 8 classes as Normal, CSR, DME, DR, AMD, CNV, DRUSEN, and MH. This dataset is divided into three sections, Training, Validation, and Testing. The distributions are shown in Table 1. The OCT-C8 dataset, which was created from images collected from various sources such as Open-ICPSR and Kaggle, was subjected to data preprocessing. As preprocessing, cropping, filling, horizontal rotation and image enhancement techniques were used. The number of samples in the data set reached 24,000 images after image augmentation [13]. Sample images from the dataset are shown in Figure 1.

Table 1. OCT-C8 dataset distribution

Classes	Number of	Train	Validation	Test
AMD	3.000	2.300	350	350
CNV	3.000	2.300	350	350
CSR	3.000	2.300	350	350
DME	3.000	2.300	350	350
DR	3.000	2.300	350	350
DRUSEN	3.000	2.300	350	350
MH	3.000	2.300	350	350
Normal	3.000	2.300	350	350
Total	**24.000**	**18.400**	**2.800**	**2.800**
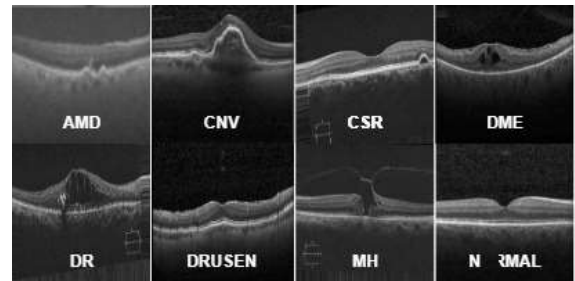
Figure 1. *Sample images of the OCT-C8 dataset*

2.2 Convolutional Neural Network (CNN)

CNN is one of the most widely used deep learning architectures for efficient training through multiple layers [14]. Figure 2 depicts the overall architecture of the CNN. The Convolutional, pooling, and fully connected layers are the basic layers of the CNN architecture. In the convolution layer, a filter is moved on the
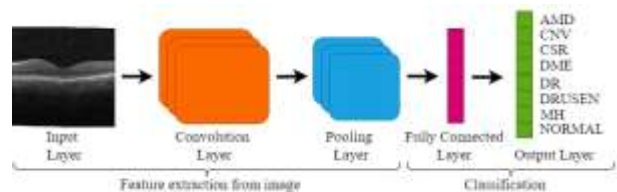
Figure 2. *General architecture of convolutional neural network*

given input variables by a user-specified number of steps. As a result of the convolution layer, feature maps are formed and used as the input of the next layer. The pooling layer is used to reduce the size of a feature. The output size of the layer is smaller than the previous layer. The output of the pooling layer is given to the fully connected layer as one-dimensional input [15].

2.3 DenseNet121

DenseNet121 algorithm proposed by Huang et al. [16] is the current architecture of CNN used for visual object recognition with fewer parameters. DenseNet combines previous layer output with subsequent layers with combined point attributes.

2.4 EfficientNetV2S

Tan and Le [17] proposed a convolutional neural network called EfficientNet in May 2019. The authors used a multidimensional hybrid model method to improve both accuracy and speed of the model. EfficientNet improves accuracy and provides speed by balancing network width, depth and resolution with integrated scaling. EfficientNet is seven models modified from the most basic model B0 to B7 in terms of channels, layers and resolution.

2.5 InceptionV3

Inception network is a pre-trained ESA model introduced by Google in 2014 [18]. This network consists of 22 layers with filters of different sizes used for maximum pooling and extracting features at various scales. Small filters are used to save time in calculations. In 2015, Google released the 48-layer InceptionV3 [19] to reduce parameters in the Inception model.

2.6 MobileNet

MobileNet is a new type of convolutional neural network. With its high efficiency and low power consumption features, MobileNet provides a high accuracy in image classification and recognition. MobileNet optimizes the standard convolution layer and divides the standard convolution process into two parts. These are deep convolution and point convolution. Deep convolution applies a single convolution kernel to the single input channel of each feature map for convolution computation. Point convolution is a standard convolution with a 1x1 convolution kernel [20].

2.7 VGG16

VGG16 is a neural network based model with approximately 138 million parameters and 16 layers. ReLU activation at the end of each convolution layer and maximum pooling at the end of all blocks are used to minimize dimensions [21]. It is among the best image classification models of neural networks.

2.8 Xception

It is a CNN architecture introduced by Chollet [22], which consists entirely of deeply separated convolution layers. In order to reduce the size of the problem in the Xception model, 1×1 convolution and deeply separable convolutions, which are a combination of deep convolution and point convolution, are used. There are approximately 23 million parameters in the Xception architecture.

2.9 Proposed Hyperparameter Tuned Model
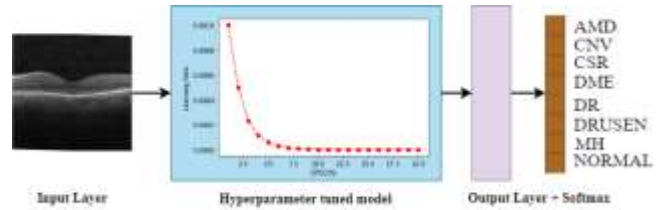
***Figure 3.** Proposed hyperparameter tuned model architecture*

In this study, convolutional neural network models DenseNet121, EfficientNetV2S, InceptionV3, MobileNet, VGG16 and Xception were used. The architecture of the proposed hyperparameter tuned model is shown in Figure 3. The OCT images applied to the input layer of the models are 224x224x3 in size. Before training on the data set, these models were hyperparameter tuned.

Model trainings were conducted during 20 epochs. While the learning rate was 0.001 at the beginning of the training, the learning rate was halved as the number of epochs increased. The reason we do this is that if the learning rate is too small at the beginning, it may get stuck at the optimum local value and cause the optimum global value to never be reached. In the last layer, OCT images were classified using the softmax function.

3. Results and Discussions

3.1 Confusion Matrix

The confusion matrix is used to measure the performance of a model. As seen in Table 2, in the confusion matrix, the rows show the actual sample numbers in the test set, and the columns show the sample numbers predicted by the model.

***Table 2.** Confusion Matrix*

		Predicted Class	
		correct	**incorrect**
Actual Class	correct	True Positive - [TP]	False Negative - [FN]
	incorrect	False Positive - [FP]	True Negative - [TN]

Accuracy

It is the ratio of the number of correct and incorrect samples found to be correct to the total number of samples.

Accuracy = (TP+TN) / (TP+TN+FP+FN)   (1)

Sensitivity

It is the rate at which samples in the real class are guessed correctly.

Sensitivity = (TP) / (TP+FN)   (2)

Precision

It is the ratio of the number of correctly predicted samples to the number of samples that are actually correct.

Precision = (TP) / (TP+FP)   (3)

The accuracy, sensitivity and precision metric values of the CNN learning models are shown in Table 3. Compared to other learning models used in this study, the DenseNet121 model has the best performance with an overall accuracy rate of 97.79%. Among the ESA learning models, the lowest performing models were VGG16 with an overall accuracy of 96.14%.

Table 3. *Performance metric values of hyperparameter-tuned deep learning models*

Models	Accuracy (%)	Precision (%)	Sensitivity (%)
DenseNet121	**97.79**	**97.79**	**97.69**
EfficientNetV2S	97.57	97.57	97.57
InceptionV3	97.71	97.71	97.60
MobileNet	96.36	96.42	96.32
VGG16	96.14	96.24	96.04
Xception	97.39	97.38	97.30

The resulting confusion matrix for the DenseNet121 model is shown in Figure 4. The diagonal elements of the confusion matrix represent the correct classifications. The remaining items are misclassifications. The rows show the predicted classes, the columns the actual classes. Accuracy, precision, and sensitivity class criteria are determined using the confusion matrix. Table 4 shows the comparison of the best performing hyperparameter tuned DenseNet121 model in our study with the performance of other studies in the literature. When Table 4 is examined, it is seen that our model is classified with the highest
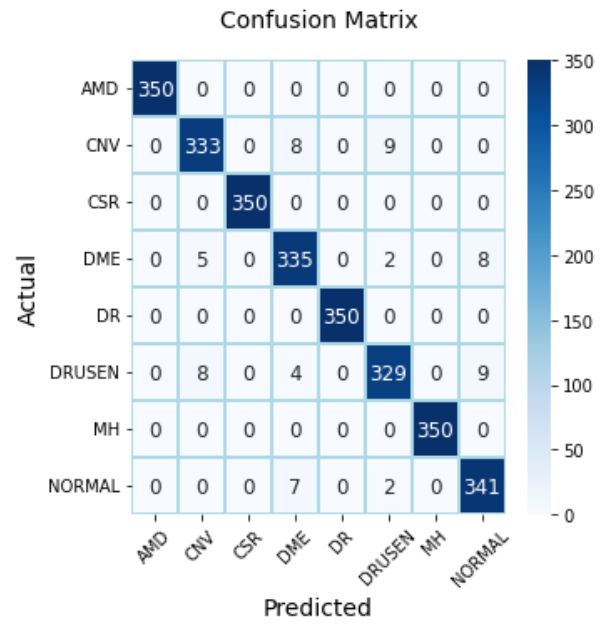
Figure 4. *Confusion matrix of the DenseNet121 model*

Table 4. *Comparison results of Hyperparameter tuned DenseNet121 model with performances of other studies*

Study	Model	Number of Classes	Accuracy (%)
Kermany et al. [1]	InceptionV3	4	96.60
Islam et al. [9]	DenseNet 201	4	98.66
Tayal et al. [10]	DL-CNN	4	96.54
Lu et al. [11]	ResNet	4	95.90
Subramanian et al. [13]	VGG16	8	97.21
Hyperparameter-Tuned DenseNet121		*8*	*97.79*

performance of 8-class data. At the same time, our model performed better than most models that classify 4-class data. The high success of our proposed model is the result of changing the hyperparameter setting of existing deep learning models.

4. Conclusions

In this period when retinal diseases increase and negatively affect human life, we propose new results in deep learning models to classify retinal patients into eight classes using OCT images. Six hyperparameter-tuned deep learning models were used to classify AMD, CSR, CNV, DR, DME, DRUSEN, and MH patients and healthy individuals. It has been observed that the hyperparameter tuned deep learning models have good performances on the OCT dataset. The classification success of the hyperparameter tuned DenseNet121 model is 97.79%. This result demonstrates the effectiveness

of the deep learning approach in detecting retinal diseases.

Within the scope of this study, applications can be made that can be used by ophthalmologists in the future and can give ideas to the experts. In addition, mobile applications can be developed to help physicians in the detection of retinal diseases.

Author Statements:

- **Ethical approval:** The conducted research is not related to either human or animal use.
- **Conflict of interest:** The authors declare that they have no known competing financial interests or personal relationships that could have appeared to influence the work reported in this paper
- **Acknowledgement:** The authors declare that they have nobody or no-company to acknowledge.
- **Author contributions:** The authors declare that they have equal right on this paper.
- **Funding information:** The authors declare that there is no funding to be acknowledged.
- **Data availability statement:** The data that support the findings of this study are available on request from the corresponding author. The data are not publicly available due to privacy or ethical restrictions.

References

[1] D. S. Kermany *et al.*, (2018). Identifying Medical Diagnoses and Treatable Diseases by Image-Based Deep Learning. *Cell*, 172(5);1122-1131 doi: 10.1016/J.CELL.2018.02.010.

[2] K. L. Pennington and M. M. DeAngelis (2016). Epidemiology of age-related macular degeneration (AMD): associations with cardiovascular disease phenotypes and lipid factors. *Eye Vis. (London, England)*, 3(1) doi: 10.1186/S40662-016-0063-5.

[3] X. Yang, T. Zhang, C. Xu, S. Yan, M. S. Hossain, and A. Ghoneim, (2016). Deep relative attributes. *IEEE Trans. Multimed.*, 18(9);1832–1842, doi: 10.1109/TMM.2016.2582379.

[4] M. S. Hossain, G. Muhammad, and A. Alamri, (2019). Smart healthcare monitoring: a voice pathology detection paradigm for smart cities, *Multimed. Syst.*, 25(5);565–575, doi: 10.1007/S00530-017-0561-X/FIGURES/9.

[5] I. El Naqa and M. J. Murphy, (2015). What Is Machine Learning?," in Machine Learning in Radiation Oncology: Theory and Applications, *I. El Naqa, R. Li, and M. J. Murphy, Eds. Cham: Springer International Publishing,* pp. 3–11. doi: 10.1007/978-3-319-18305-3_1.

[6] K. Liu, J. Zhou, and D. Dong, (2021). Improving stock price prediction using the long short-term memory model combined with online social networks. *J. Behav. Exp. Financ.*, 30; 100507, doi: 10.1016/J.JBEF.2021.100507.

[7] M. Sarkar, A. Roy, Y. Badr, B. Gaur, and S. Gupta, (2022). An Intelligent Music Recommendation Framework for Multimedia Big Data: *A Journey of Entertainment Industry*, pp. 39–67, doi: 10.1007/978-981-16-3828-2_3.

[8] S. Tripathi and N. Sharma, (2021). Computer-Based Segmentation of Cancerous Tissues in Biomedical Images Using Enhanced Deep Learning Model. 39(5);1208–1222, doi: 10.1080/02564602.2021.1994044.

[9] K. T. Islam, S. Wijewickrema, and S. O'Leary (2019). Identifying diabetic retinopathy from OCT images using deep transfer learning with artificial neural networks. *Proc. - IEEE Symp. Comput. Med. Syst.*, 281–286, doi: 10.1109/CBMS.2019.00066.

[10] A. Tayal, J. Gupta, A. Solanki, K. Bisht, A. Nayyar, and M. Masud, (2022). DL-CNN-based approach with image processing techniques for diagnosis of retinal diseases. *Multimed. Syst.*, 28(4);1417–1438, doi: 10.1007/S00530-021-00769-7/FIGURES/13.

[11] W. Lu, Y. Tong, Y. Yu, Y. Xing, C. Chen, and Y. Shen, (2018). Deep Learning-Based Automated Classification of Multi-Categorical Abnormalities From Optical Coherence Tomography Images. *Transl. Vis. Sci. Technol.*, 7(6);41–41, doi: 10.1167/TVST.7.6.41.

[12] Retinal OCT - C8, (2022). https://www.kaggle.com/datasets/obulisainaren/reti nal-oct-c8/code (accessed May 09, 2023).

[13] M. Subramanian, K. Shanmugavadivel, O. S. Naren, K. Premkumar, and K. Rankish, (2022). Classification of Retinal OCT Images Using Deep Learning, *Int. Conf. Comput. Commun. Informatics, ICCCI* , doi: 10.1109/ICCCI54379.2022.9740985.

[14] Y. LeCun, L. Bottou, Y. Bengio, and P. Haffner, (1998). Gradient-based learning applied to document recognition, *Proc. IEEE*, 86(11);2278–2323, doi: 10.1109/5.726791.

[15] M. M. Islam, T. N. Poly, B. A. Walther, H. C. Yang, and Y. C. Li, (2020). Artificial Intelligence in Ophthalmology: A Meta-Analysis of Deep Learning Models for Retinal Vessels Segmentation, *J. Clin. Med. 9;*(4);1018, doi: 10.3390/JCM9041018.

[16] G. Huang, Z. Liu, L. Van Der Maaten, and K. Q. Weinberger, (2017). Densely Connected Convolutional Networks. *Conf. Comput. Vis. Pattern Recognit.*, pp. 4700–4708, Accessed: Sep. 11, 2022. [Online].: https://github.com/liuzhuang13/DenseNet.

[17] M. Tan and Q. V. Le, (2019). EfficientNet: Rethinking Model Scaling for Convolutional Neural Networks. *36th Int. Conf. Mach. Learn. ICML 2019*, 2019;10691–10700, doi: 10.48550/arxiv.1905.11946.

[18] C. Szegedy et al., (2015). Going deeper with convolutions; Going deeper with convolutions. doi: 10.1109/CVPR.2015.7298594.

[19] C. Szegedy, V. Vanhoucke, S. Ioffe, and J. Shlens, (2016). Rethinking the Inception Architecture for

Computer Vision; Rethinking the Inception Architecture for Computer Vision. *IEEE Conf. Comput. Vis. Pattern Recognit.*, pp. 2818–2826, doi: 10.1109/CVPR.2016.308.

[20] A. G. Howard *et al.*, (2017). MobileNets: Efficient Convolutional Neural Networks for Mobile Vision Applications.

[21] K. Simonyan and A. Zisserman, (2015). VERY DEEP CONVOLUTIONAL NETWORKS FOR LARGE-SCALE IMAGE RECOGNITION. *Comput. Vis. Pattern Recognit.*, 2015, Accessed: Apr. 26, 2022. [Online]. Available: http://www.robots.ox.ac.uk/

[22] F. Chollet, (2017). Xception: Deep Learning with Depthwise Separable Convolutions. doi: 10.1109/CVPR.2017.195.
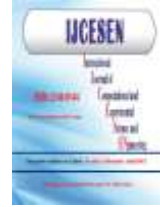
Water Quality Assessment of Simav River (Susurluk Basin/Turkey) According to Seasons and Stations

Nezire Lerzan ÇİÇEK[1*], Salim Serkan GÜÇLÜ[2], Ömer ERDOĞAN[3], Fahrettin KÜÇÜK[4]

[1] Isparta University of Applied Sciences, Faculty of Eğirdir Fisheries, Isparta-Turkey
*Corresponding Author E-mail: lerzancicek@isparta.edu.tr - **ORCID:** 0000-0002-5511-0464

[2] Isparta University of Applied Sciences, Faculty of Eğirdir Fisheries, Isparta-Turkey
E-mail: salimguclu@isparta.edu.tr – **ORCID:** 0000-0002-9256-449X

[3] Isparta University of Applied Sciences, Yalvaç Technical Sciences Vocational School, Environmental Protection Department, Isparta-Turkey
E-mail: omererdogan@isparta.edu.tr **ORCID:** 0000-0002-0196-5854

[4] Isparta University of Applied Sciences, Faculty of Eğirdir Fisheries, 32000 Isparta-Turkey
E-mail: fahrettinkucuk@isparta.edu.tr – **ORCID:** 0000-0002-0470-9063

Abstract:

Susurluk Basin is under intense pressure from domestic, industrial wastes and agricultural activities. In this study, the effect of environmental factors on Simav Stream, one of the important rivers of the Susurluk Basin, was tried to be determined. In this purpose water samples were taken from 13 station seasonally in 2014-2015, and water quality parameters including dissolved oxygen, oxygen saturation, temperature, pH, electrical conductivity, salinty, turbidty, calcium, magnesium, total hardness, nitrite nitrogen, nitrate nitrogen, ammonium nitrogen, phosphate phosphorus, total phosphor, chloride, bicarbonate, carbonate, were determined in this samples. The results were compared with the limit values specified in the national and international quality criteria. According to the Surface Water Quality Regulation (SWQR), the upper parts of the river were less polluted (II. quality) and the middle and lower parts were polluted water (III. quality). As a result of the research, it has been observed that the middle and lower reaches of the Simav Stream are under the pressure of intense agricultural, animal livestock and pollution from domestic and industrial waste waters. It was determined that the pollution pressure started to increase in the upper part as well.

1. Introduction

Water is an essential natural resource essential for sustainable of life. While sea water is about %98 on earth water, approximately %2 fresh water and only 0,036 percent of it is found in lakes and rivers. Nowadays many the fresh water resources are polluted industrial, domestic and agricultural activities. Therefore, these polluted resources are not been suitable for human health and activities (drinking, agricultural etc.). In addition, the increasing contamination of freshwaters with this pollution resources is one the most important of the environmental problems in present-day [1-5].
Water quality which affect utility of water resource is the most important factor more than the amount of water. For this reason, monitoring and

management of freshwater resources in terms of surface water quality and pollution is one of the most important issues. Evaluation of water quality parameters and pollution control are essential for effective water quality management [6-9]. When the water source becomes polluted, it is very difficult to restore water quality even if it is protected from polluting sources. Water pollution affects firstly physicochemical parameters of water. Due to the water pollution, life of aquatic organisms are damaged. Therefore, it is very important to determine the water quality of the river and to take the necessary measures for the protection of water resources [6,10,11]. In recent years, as a result of gradually unplanned urbanization, industrialization and rapid population growth in Turkey, the water pollution has become an important problem. Simav Stream, one of the

important streams of the Susurluk Basin, is one of the main sources used as irrigation water in the region. There are many industrial enterprises/plant (Susurluk Sugar Factory, Oil, Cement, Marble Factories, Meat and Milk Integrated Facilities, chicken farms, fish and chicken processing plants etc.) and agricultural areas in the basin where Bursa, Balıkesir and Kütahya provinces and districts are located [12, 13]. It is known that Simav Stream is under intense pollution pressure. The purpose of in this research; To determine the simav river water quality and how environmental factors affect the stream, to comparing the results (river water quality parameter values) with national and international water quality criteria, is to provide resources for future studies in the river.

2. Material and Methods

2.1 Study area and sampling

The river are poured to Simav Lake after its first sources are taked from Şaphane mountains, east of Simav Lake. The River passes through some settlements and reaches Marmara Sea after passing Karacabey. During this time, it is fed from the excess waters of Uluabat and Kuşgöl lakes and anyway also many the other large and small streams such as Orhaneli Stream, Mustafakemalpaşa Stream, Kocaçay ve Nilüfer Stream. Simav Stream is known as Susurluk River after Balıkesir province. The length of the path followed by this river is 341 km. In this study, total 13 sampling stations were selected on the Simav River. The common features of these points are due to the fact that they are connected with the small streams around them, the fields on which agricultural activities are carried out, and the residential areas (Figure 1, Tablo 1). Water samples were collected seasonally between the dates of May 2014 – February 2015. The names of these places where experimental studies were carried out at the stations briefly denoted as (ST1, ST2, ST3, ST14, ST5, ST6, ST7, ST8, ST9, ST10, ST11, ST12, and ST13 as seen in Table 1).

2.2 Physicochemical analysis

Measurements of dissolved oxygen (DO), oxygen saturation (%) and temperature (T), electrical conductivity (EC, 25 ºC μS/cm) and salinity, pH in water of Simav River were performed in situ. For this purpose was used WTW Oxi 320 meter, YSI EcoSense EC300A, YSI EcoSense pH100A measurement devidaces during the field studies. Water samples, taken from stations have been analyzed within 24 hours after sampling.

***Figure 1.** Simav River and Sampling stations*

***Table 1.** Sampling points and coordinate*

Station No	Sampling points	Location	Latitude Longitude
ST1	Şırla Stream	Simav-Kütahya (Rahimler)	39º 06′ 760″ K 29º 09′ 438″ D
ST2	Kalkan Pond exit	Simav-Kütahya	39º 05′ 286″ K 29º 05′ 642″ D
ST3	Çay Kasabası	Simav-Kütahya	39º 07′ 257″ K 28º 52′ 505″ D
ST4	Binmurt Bridge	Sındırgı-Balıkesir	39º 12′ 167″ K 28º 29′ 436″ D
ST5	Sındırgı Bridge (Çaygören Dam exit)	Sındırgı-Balıkesir	39º 17′ 061″ K 28º 11′ 497″ D
ST6	Cüneyt Bridge	Sındırgı-Balıkesir	39º 13′ 614″ K 28º 07′ 394″ D
ST7	Bigadiç Bridge	Balıkesir	39º 24′ 799″ K 28º 05′ 655″ D
ST8	Mahmudiye Bridge	Kepsut-Balıkesir	39º 36′ 247″ K 28º 05′ 122″ D
ST9	Yıldızköy Bridge	Susurluk-Balıkesir	39º 48′ 973″ K 28º 10′ 714″ D
ST10	Harmanlı Bridge	Karacabey-Bursa	40º 14′ 417″ K 28º 24′ 321″ D
ST11	Hayırlar Bridge (Lake Uluabat exit)	Karacabey-Bursa	40º 17′ 818″ K 28º 27′ 534″ D
ST12	Nilüfer Çayı joint point	Karacabey-Bursa	40º 18′ 382″ K 28º 26′ 891″ D
ST13	Estuary	Estuary	40º 23′ 348″ K 28º 30′ 332″ D

In water samples brought to the laboratory Mg^{+2} (mg/l), Ca^{+2} (mg/l), total hardness (mg /l $CaCO_3$), HCO_3^- (mg/l), CO_3^- (mg/l), Cl^- (mg/l), NH_4-N (mg/l), NO_3^--N (mg/l), NO_2^--N (mg/l), PO_4^{-3}-P (mg/l), $\sum P$ (mg/l) and turbidity (NTU) have been measured. Total hardness ($CaCO_3$) were determined by EDTA titrimetric method and alkalinity (HCO_3 and CO_3 mg/l $CaCO_3$) by titration with acid (Sulfiric acid). Cl^- determine by titrating of $AgNO3$ according to Mohr method. In addition, the amount of the substances, NH_4-N, NO_3^--N, NO_2^--N, PO_4^{-3}-P, $\sum P$, were determined with CECİL CE4003 brand spectrophotometer associated with photometric test kits [14].

3. Results and Discussions

Range (minimum, maximum) and mean values of some water quality parameters of Simav River were given Table 2-4, and Figure 2-4, also seasonal

variatons of these parameters were given Table 5-8. Physichochemical values of Simav River were show change acoocrding to stations and seasonal. Accordingly, in the river the lowest and the highest values; for temperature 6.4-23.4 C^0; for dissolved oxygen 0,3-18,1 mg/l; for pH 7.65-9.3; for electrical conductivity 254-2198 µS/cm; for turbidity 0.3-141.5 NTU; for Ca^{+2} 11.2-80.2 mg/l; for Mg^{+2} 6.8-68.04 mg/l; for total hardness 72.6-304.1; for $NO_3{}^{-}N$ 0,015-3,2 mg/l; for $NO_2{}^{-}$-N 0.008-0.96 mg/l; for NH_4-N 0.01-3.6 mg/l; for $PO_4{}^{-3}$-P 0.02-2.63 mg/l; for $\sum P$ 0.08-6.68 mg/l; for Cl^{-} 8.8-536.9 mg/l; for $HCO_3{}^{-}$ 112,5-530,7 mg/l have been found.

For easy of analysis, the data of the parameters of the Simav River water obtained from experimental measurements, we have, first, divided these parameters into two groups such as Group-1(Table 5-6) and Group-2 (Table 7-8). Due to the stations 2 and 3 (ST2, ST3) river were dried, water samples were not taken in this period.

The pH value of the river water changes very little depending on the stations and seasons, this change maybe expressed with the the width of the river changing from place to place. It is very difficult to determine the direct or indirect effect of pH on water quality [15]. The geological structure of the region is one of the most important factors affecting the pH of the waters, and it is closely related to the dissolved CO_2 in the water. The presence of free CO_2, carbonate and bicarbonate in water can be determined by measuring the pH of the water. As a result of photosynthesis, phytoplankton consume the CO_2 and increase the pH in the environment [16]. Aquatic organisms are tolerant to a certain pH range and can generally develop at pH 6.4-8.6 limit values [17]. pH, which deviates from the value range specified for the development of living things, negatively affects the life of aquatic organisms [7]. In decleration of human use purpose waters of the Turkish Standards Institute [18], the recommended value is 6.5<pH<8.5, while the maximum allowed value is reported as 6.5<pH<9.5 range [18]. During the research, pH values varied between 7.6 and 9.3, and the highest average value was found to be 8.84. pH values were measured seasonally above the upper limit value recommended in Drinking Water Standards (TS266) [18] and Surface Water Quality Regulation (SWQR) [19] in rivers. However, in terms of average values, recommended limit values were not exceeded, and Simav River water has alkaline property along the year (Table 2).

Water temperature changes the concentration of many variables by affecting biological, chemical and physical activities in water. By affecting all vital activities of aquatic organisms, it causes a change in their physiology and affects their distribution in water. Becouse of increase metabolic and respiratory rate of organisms as the temperature in water, dissolved oxygen value is decrease [20, 21]. During our research, the water temperature values at the sampling points changed within normal limits depending on the seasons. The average temperature values were show a change between 9,42-17,63 C^0 in the river. While the lowest temperature (6.4 C^0/November) was measured at the source point, the highest temperature (23 C^0/August) was measured at the point of the stream close to the sea. It was observed that especially at the river bed expanded and the sampling points close to the sea, temperature values were higher than the other sampling points. In [12], reported that the water temperature is high in the sub-region of Simav Stream during the summer months. In similar studies, it was stated that the water temperature increased with the expansion of the river bed and proximity to the sea, and while the water temperature in the river reached the highest value in the summer period and decreased in the winter period [1, 11, 22, 23, 24, 25]. It is stated that the optimal conditions in terms of water temperature are between 7-18°C in trout farming and between 16-26°C in carp farming [26, 27] reported that in the upper basin of the Simav River (from the source point to the Binmurt bridge), there are members of Cyprinidae that prefer the fast-flowing upper reaches of the stream.

Electrical conductivity of the water, EC, shows that the capacity of the ions included by the river water and whether this water allows the current to pass or not. Since conductivity can be considered as an indicator of dissolved substances in water, it is monitoring parameter.

An increase in conductivity in drinking water may indicate that the water is polluted or that sea water is mixed [16, 25]. From the point of view of fisheries, it becomes dangerous especially for fish if the EC value is greater than $^{10}00$ µmhos/cm [1, 8, 28]. Acceptable value for aquatic organisms is 250-500 µmhosx10/cm. The electrical conductivity values in the stream changed according to the stations, and high values were measured in the lower basin during the summer (2198 µmhos/cm in ST11) and autumn (956 µmhos/cm in ST12) periods. It can be said that the climatic conditions, intensive agricultural and livestock activities in the river region, and the pollution load brought to the Simav Stream by other important streams of the basin affect the measurement of high electrical

***Table 2.** Range, mean and S.E. of physicochemical parameters at the stations of the Simav River*

Parameters		Water Temp. (C⁰)	DO (mgl-1)	Oxygen Saturation(%)	pH	E.C (25C⁰ µS/cm)	Salinity	Turbidity
ST1	Range	13,1-6,4	16,5-11,41	153,4-93	9,34-7,65	562-492,4	0,2-0,3	8,55-0,97
	Mean±SE	9,42±1,66	14,10±1,13	129,93±14,06	8,52±0,12	530,35±14,497	0,25±0,028	3,46±1,73
ST2	Range	15,2-6,9	10-18,15	178-82,3	8,74-8,16	607-400,1	0,3-0,2	2,12-1,38
	Mean±SE	10,26±2,52	13,18±2,50	117,37±30,4	8,46±0,16	477,43±65,187	0,2±0,081	2,22±0,51
ST3	Range	14,2-7,2	11,84-5,68	143,6-97,7	8,93-8,59	254,4-267,9	0,1	1,39-0,5
	Mean±SE	10,7±3,5	13,76±1,92	120,65±22,9	8,76±0,17	261,15±6,75	0,1±0,00	0,94±0,44
ST4	Range	22,1-11,8	7,67-11,02	100,9-78,7	9,03-8,62	865-375,4	0,3-0,2	8,08-1,16
	Mean±SE	16,45±2,690	8,79±0,76	89,2±4,54	8,842±0,08	586,87±106,81	0,057±0,041	4,16±1,46
ST5	Range	20,4-8,2	6,96-11,84	100,4-68,8	8,78-8,41	564-356,9	0,3-0,2	13,69-1,7
	Mean±SE	14,45±8,49	8,65±1,15	84,5±9,06	8,535±0,08	476,22±52,288	0,25±0,029	6,1±2,61
ST6	Range	20,3-9,8	6,03-11,23	99-53,4	9,14-7,82	561-379,7	0,3-0,2	3,21-0,35
	Mean±SE	3,8±2,47	8,22±1,23	76,42±9,63	8,575±0,28	457,55±39,309	0,225±0,025	1,82±0,73
ST7	Range	23-11,4	5,54-17,4	203,20-58,2	9,3-8,35	637-390,5	0,3-0,2	14,08-2,34
	Mean±SE	17,15±2,41	10,01±2,79	107,3±33,50	8,775±0,20	520,12±50,95	0,25±0,029	5,96±2,73
ST8	Range	21,1-13,8	5,7-11,7	124-65,3	9,34-8,07	592-438,9	0,4-0,2	12,31-3,04
	Mean±SE	16,4±2,74	8,96±1,27	93,45±12,8	8,565±0,27	594,22±66,75	0,275±0,048	7,80±2,51
ST9	Range	22-10,7	5,71-10,61	95,4-59,1	8,98-7,97	744-435	0,2-0,4	11,51-2,23
	Mean±SE	17,07±2,78	7,45±1,11	76,22±8,64	8,314±0,23	608,5±78,79	0,3±0,058	6,14±2,07
ST10	Range	21,5-12	4,8-11,7	107,7-54,3	8,96-7,84	656-488,7	0,3-0,2	22,07-8,45
	Mean±SE	15,4±2,09	9,11±1,54	86,4±11,72	8,422±0,23	567,42±44,48	0,25±0,029	15,06±3,12
ST11	Range	23,4-12,2	0,32-7,12	66,7-23,4	8,16-7,87	2198-513	1,1-0,4	141,5-17,98
	Mean±SE	15,97±2,58	4,95±1,56	53,8±10,28	8,03±0,06	1309,75±389,49	0,775±0,149	59,68±28,43
ST12	Range	21,6-10,5	0,44-10,57	94,5-10,4	8,65-7,65	956-523	0,5-0,3	22,07-14,38
	Mean±SE	16,82±2,82	4,46±2,47	45,13±20,92	8,017±0,23	826,5±102,42	0,45±0,05	21,25±2,56
ST13	Range	22,7-12,3	21,61-6,64	88,2-28,00	9,1-7,71	924-480	0,5-0,3	7,4-1,64
	Mean±SE	17,63±2,88	11,25±3,50	64,33±12,83	8,471±0,33	752,5±102,95	0,4±0,057	5,83±1,40

***Table 3.** Range, mean and S.E. of physicochemical parameters at the stations of the Simav River*

Parameters		Ca+ (mgl-1)	Mg++ (mgl-1)	Total Hardness (CaCO₃ mgl-1)	Cl- (mgl-1)	HCO-3 (mgl-1)	CO-23 (mgl-1)
ST1	Range	64,16-52,93	45,68-35,02	290,84-261,87	39,93-13,31	268,4-186,05	60-12
	Mean±SE	58,94±2,65	38,4±2,45	280,61±6,40	22,18±6,27	231,5±20,73	27,57±10,94
ST2	Range	80,2-17,64	40,82-10,69	237,59-185,75	35,5-26,63	423,95-213,5	30,1-6
	Mean±SE	38,895±21,14	18,952±10,18	163,02±64,08	29,58±2,95	320,25±60,77	16±7,21
ST3	Range	38,49	17,49	156,94	8,87	152,5-106,75	60-3
	Mean±SE	38,49±0,00	17,49±0,00	156,94±0,00	8,87±0,00	129,62±22,87	31,5±28,5
ST4	Range	65,76-11,23	54,43-16,52	245,36-72,66	35,5-17,75	280,6-155,55	45-9
	Mean±SE	39,29±12,92	35,72±9,301	190,94±39,85	26,62±5,12	232,56±30,15	17,25±9,75
ST5	Range	70,58-22,46	24,3-6,8	183,24-140,17	35,5-8,87	204,35-122	60-6
	Mean±SE	45,71±9,98	17,98±3,83	172,40±10,74	22,18±5,43	167,75±20,72	20,25±13,60
ST6	Range	41,7-11,23	59,29-37,91	235,8-190,41	17,75-8,88	347,7-198,25	15,1-6
	Mean±SE	23,66±6,42	44,22±5,04	212,79±12,92	13,31±1,81	257,72±32,24	5,25±3,54
ST7	Range	56,14-19,25	68,04-23,33	304,13-179,68	22,19-13,31	283,65-179,95	24,1-3
	Mean±SE	38,89±8,24	41,79±9,39	229,21±26,51	19,96±2,21	244,76±22,52	11,25±5,79
ST8	Range	59,35-17,64	49,57-23,33	276,55-181,2	39,94-22,19	314,15-176,9	24,1-9
	Mean±SE	39,29±8,52	33,53±6,17	214,60±22,09	26,62±4,43	273,73±32,62	13,5±5,54
ST9	Range	67,37-28,87	62,21-34,99	293,21-253,75	62,13-31,06	344,65-158,6	15,1-6
	Mean±SE	49,32±7,95	45,19±6,35	280,14±8,94	43,26±6,62	270,68±43,21	5,25±3,54
ST10	Range	48,12-26,66	54,43-40,82	261,95-226,69	102,06-48,81	305-15,25	30,1-9
	Mean±SE	32,33±5,26	48,81±3,36	249,58±7,86	53,25±24,13	250,1±34,06	9±14,28
ST11	Range	56,14-35,28	55,4-43,74	292,13-250,1	536,94-221,88	530,7-280,6	0,00
	Mean±SE	40,5±5,21	50,05±2,87	274,95±8,88	369,425±64,569	420,9±52,04	0,00
ST12	Range	48,12-12,83	43,74-30,13	261,95-136,62	199,68-102,06	396,5-240,95	0,00
	Mean±SE	33,682±7,43	39,607±3,233	221,647±28,65	137,56±23,198	336,26±33,69	0,00
ST13	Range	48,12-19,25	59,29-29,16	260,69-201,43	366-112,5	366-112,3	12,1-6
	Mean±SE	34,887±6,15	43,982±8,560	234,367±13,91	285,08±58,150	285,08±58,15	4,5±2,872

Table 4. *Range, mean and S.E. of physicochemical parameters at the stations of the Simav River*

Parameters		NO$_3$-N (mgl-1)	NO$_2^-$-N (mgl-1)	NH$_4$-N (mgl-1)	PO$_4^{-3}$-P (mgl-1)	∑P (mgl-1)
ST1	Range	0,91-0,12	0,017-0,01	0,12-0,02	0,11-0,02	0,37-0,11
	Mean±SE	0,447±0,18	0,013±0,001	0,07±0,02	0,061±0,021	0,22±0,063
ST2	Range	0,5-0,1	0,063-0,008	0,54-0,13	0,24-0,04	0,35-0,08
	Mean±SE	0,26±0,12	0,026±0,018	0,27±0,135	0,116±0,062	0,18±0,085
ST3	Range	0,5-0,015	0,033-0,014	0,87-0,14	0,07-0,022	0,35-0,08
	Mean±SE	0,25±0,24	0,024±0,009	0,50±0,36	0,046±0,024	0,215±0,135
ST4	Range	1-0,18	0,02-0,01	0,21-0,02	1,57-0,07	1,42-0,17
	Mean±SE	0,49±0,19	0,015±0,002	0,12±0,03	0,565±0,347	0,742±0,259
ST5	Range	0,72-0,15	0,034-0,01	0,13-0,024	0,14-0,02	0,27-0,21
	Mean±SE	0,54±0,13	0,018±0,005	0,06±0,02	0,105±0,040	0,247±0,014
ST6	Range	0,74-0,2	0,017-0,011	0,94-0,025	0,08-0,025	0,24-0,08
	Mean±SE	0,47±0,11	0,014±0,001	0,33±0,20	0,05±0,012	0,138±0,034
ST7	Range	0,15-1,34	0,034-0,028	0,16-0,025	0,39-0,04	0,95-0,39
	Mean±SE	0,85±0,26	0,031±0,0015	0,08±0,03	0,197±0,072	0,6±0,122
ST8	Range	3,2-0,35	0,071-0,032	0,56-0,025	0,75-0,13	1,32-0,46
	Mean±SE	1,2±0,679	0,051±0,011	0,193±0,124	0,36±0,139	0,842±0,202
ST9	Range	1,99-0,35	0,22-0,044	0,38-0,025	1,79-0,25	1,82-0,65
	Mean±SE	1,09±0,42	0,141±0,039	0,19±0,07	0,802±0,338	1,482±0,278
ST10	Range	0,92-0,02	0,13-0,015	3,66-0,04	0,86-0,28	2,2-0,57
	Mean±SE	0,48±0,18	0,063±0,027	1,01±0,88	0,517±0,122	1,277±0,383
ST11	Range	0,68-0,2	0,104-0,073	2,9-0,22	2,63-0,36	6,68-1,65
	Mean±SE	0,32±0,12	0,301±0,219	1,12±0,61	1,367±0,551	3,623±1,091
ST12	Range	0,8-0,2	0,38-0,019	1,86-0,18	1,63-0,25	2,78-0,81
	Mean±SE	0,57±0,13	0,133±0,083	1,067±0,451	0,745±0,306	1,725±0,404
ST13	Range	0,2-0,2	0,1-0,01	1,28-0,11	1,29-0,03	4,55-0,12
	Mean±SE	0,2±0,00	0,056±0,018	0,64±0,30	0,612±0,264	2,41±0,96

Table 5. *The values of the parameters included in Group-1 measured in May and August at 13 stations*

		pH	E.C. (25 ^{0}C μS/cm)	D.O. (mg/l)	Satur. (%)	T (^{0}C)	Salin (ppt)	Turb. (NTU)	Total Hardness (CaCO$_3$ mg/l)
ST1	May	8,8	528	13,14	150,2	11,4	0,2	0,97	261,87
	August	8,23	539	16,5	153,4	13,1	0,3	8,55	290,84
ST2	May	8,74	425,2	18,15	178	15,2	0,3	1,38	185,75
	August	-*	-*	-*	-*	-*	-*	-*	-*
ST3	May	8,93	267,9	15,68	143,6	14,2	0,1	0,5	156,94
	August	-*	-*	-*	-*	-*	-*	-*	-*
ST4	May	9,03	474,1	7,94	89	20	0,2	8,08	72,66
	August	8,62	633	7,67	88,2	22,1	0,3	2,99	216,95
ST5	May	8,78	420	8,85	100	20,4	0,2	1,7	183,24
	August	8,41	564	6,96	68,8	14,6	0,3	4,53	140,17
ST6	May	9,14	417,8	9,25	83	15	0,2	3,21	235,8
	August	7,82	561	6,4	70,3	20,3	0,3	0,78	234,54
ST7	May	9,3	509	17,4	203,2	18,2	0,2	4,28	304,13
	August	8,35	544	5,54	64,3	23	0,3	2,34	179,68
ST8	May	9,34	592	10,04	124	20,8	0,2	3,87	276,55
	August	8,07	581	5,7	65,3	21,1	0,3	12,31	216,11
ST9	May	8,98	515	7,41	86	22	0,2	7,22	253,78
	August	7,97	744	5,71	64,4	21,5	0,4	3,63	288,05
ST10	May	8,62	488,7	11,7	107,7	13,8	0,2	22,07	261,95
	August	7,84	632	4,8	54,3	21,5	0,3	11,4	226,69
ST11	May	8,11	513	7,12	66,7	12,7	0,7	54,92	292,13
	August	7,98	2198	0,32	23,4	23,4	1,1	141,5	280,47
ST12	May	9,25	730	6,23	72	20,3	0,4	22,07	261,95
	August	7,65	944	0,44	10,4	21,6	0,5	26,8	136,62
ST13	May	8,86	707	6,64	73	22,54	0,3	7,4	221,48
	August	7,71	899	2,61	28	22,7	0,5	7,03	260,69

Table 6. *The values of the parameters included in Group-1 measured in May and August at 13 stations*

		pH	E.C. (25 ^{0}C μS/cm)	D.O. (mg/l)	Satur. (%)	T (^{0}C)	Salin (ppt)	Turb. (NTU)	Total Hardness (CaCO$_3$ mg/l)
ST1	November	8,43	562	15,38	123,1	6,4	0,3	2,7	284,58
	February	8,63	492,4	11,41	93	6,8	0,2	1,64	285,18
ST2	November	8,16	607	10,2	82,3	8,7	0,3	2,12	228,67
	February	8,49	400,1	11,2	91,8	6,9	0,2	3,17	237,59
ST3	November	-*	-*	-*	-*	-*	-*	-*	-*
	February	8,59	254,4	11,84	97,7	7,2	0,1	1,39	156,94

	November	8,93	865	8,56	78,7	11,8	0,3	1,16	228,79
ST4	February	8,79	375,4	11,02	100,9	11,9	0,2	4,41	245,36
	November	8,41	564	6,96	68,8	14,6	0,3	4,48	183,1
ST5	February	8,54	356,9	11,84	100,4	8,2	0,2	13,69	183,1
	November	8,54	471,7	6,03	53,4	10,1	0,2	0,35	190,41
ST6	February	8,8	379,7	11,23	99	9,8	0,2	2,97	190,41
	November	8,84	637	5,8	58,2	16	0,3	3,17	211,75
ST7	February	8,61	390,5	11,33	103,5	11,4	0,2	14,08	221,3
	November	8,38	765	8,4	80,8	13,8	0,4	3,04	184,57
ST8	February	8,47	438,9	11,7	103,7	9,9	0,2	12,01	181,2
	November	8	740	6,1	59,1	14,1	0,4	2,23	285,58
ST9	February	8,32	435	10,61	95,4	10,7	0,2	11,51	293,21
	November	8,27	656	9,05	84,5	14,3	0,3	8,45	257,05
ST10	February	8,96	493	10,89	99,1	12	0,2	18,33	252,65
	November	7,87	1707	6,46	66,2	15,6	0,9	17,98	277,1
ST11	February	8,16	821	5,9	58,9	12,2	0,4	24,33	250,1
	November	8,12	956	6,4	65,2	13,6	0,5	14,38	244,01
ST12	February	8,65	523	10,57	94,5	10,5	0,3	21,76	244,01
	November	8	924	7,31	68,3	13	0,5	7,27	253,87
ST13	February	9,1	480	9,43	88,2	12,3	0,3	1,64	201,43

conductivity values in the lower basin. It has been reported that the pollution of Nilüfer Stream increases gradually towards the lower region where it joins with Simav Stream [29]. In the upper river basin, the electrical conductivity values were measured at 561 µmhos/cm and above, and it was measured below this value only in ST2. It is thought that the periodic drying of the second station is effective in measuring this value. In [30] reported that there is an increase in the pollution of the middle part of the stream due to the mixing of wastes from Sındırgı and Bigadiç sewage systems, dairy farms and slaughterhouses into the Simav Stream without any treatment. According to SWQR, the upper and middle course of the river II. in quality class (medium), lower grade III. in the quality class.

Dissolved oxygen, DO, is one of the most important parameters used in monitoring water quality change. The amount of dissolved oxygen in a river is very important especially for the fish living in a river [7, 31]. The amount of dissolved oxygen determined in the water at any time in the water changes depending on the current temperature of the water, the partial pressure of the atmospheric gas on the water surface, the water flow rate, the dissolved salt concentration and biological events. The amount of dissolved oxygen in water decreases with decreasing temperature. While the amount of dissolved oxygen in water increases with photosynthesis and current velocity, it decreases as salt density, temperature, organic matter degradation and respiration activities increase [17,32,33] As seen from Table 5 and 6, the

amount of the DO in river water decreases gradually from May to August in time and increases slowly from November to February in time. It may be due to heavy rainfall in May and December and less rainfall in August and February. The mean dissolved oxygen values of Simav Stream were measured between 4.95-14.10 mg/l (Table 2). Especially in the lower regions of the stream (ST10;ST11; ST12; ST13), it was observed that the dissolved oxygen value decreased very much (respectively 4.8; 0.3; 0.44; 2.61 mg/l) during the summer period. Due to the expansion of the river bed the decrease in the flow rate, weather conditions and increased pollution load are tought to be effective in the decrease of dissolved oxygen in these stations. The river subdivision (ST10, ST11, ST12, ST13) is exposed to agricultural, industrial, and domestic wastes while passing through the settlements where intensive agriculture and livestock are made. At the 10th sampling point (ST10), Kocasu emerged from Lake Uluabat, and at the 12th sampling point (ST12) Nilüfer Stream are join the stream. It was reported that Uluabat Lake was under intense pollution pressure and could not be used as drinking or irrigation water, and also stated that pollutant limits should be introduced on the basis of basin [34]. It is stated that the water quality of the Nilüfer Stream is an open sewer at the exit of the Bursa city center and is heavily polluted due to domestic and industrial discharges in the city center [35]. According to the EC directive declared by the European Union Commission on the purpose of the protection of fish health in fresh waters, a decrease in the dissolved oxygen level below 4 mg/L in the water

poses a threat to Cyprinid species [36]. Dissolved oxygen values should be between 9.20–11.50 mg/L for trout and 5.00–9.00 mg/L for carp [26]. Oxygen below 5mg/l produces harmful effects and sensitivity to low levels varies by species; however, most species experience stress between 2 and 4 mg/L. Fish deaths occur especially at oxygen levels below 2 mg/l [37, 38]. It has been stated that in the lower basin of the river (in the region where Nilüfer Stream mixes), the majority of the species that prefer clean, oxygen-soluble, slow-flowing regions of the rivers have disappeared [27]. According to SWQR (Surface Water Quality Regulation), the upper part of the stream is II. quality (very good), and subgrade III. quality (medium) class.

Turbidity is due to particles dissolved or suspended in water. Since turbidity is inversely proportional to the penetration of light into water, it is an important parameter for aquatic organisms [1, 39]. Excessive turbidity may adversely affect the food sources, spawning areas and gill functions of fish and other aquatic organisms. Simav Stream turbidity values have exceeded the limit values specified in TS266 along the stream. It was observed that turbidity values increased especially in the summer period. The highest turbidity values were measured in the stream sub-region (ST10, ST11, ST12) (Table 2). The decreasing amount of water in the summer period and the amount of suspended matter coming from the side arms and upper region may be effective formed of the high turbidity. The increase in turbidity values have been remarkable after Uluabat Lake outlet waters and the mixing of Nilüfer Stream.

Generally, the hardness for water is understood as the precipitation property of the soap in water. In practice, the hardness of the water is expressed with the amount of Ca^{+2} ve Mg^{+2} ions dissolving in water passing through the soil [40, 41, 42]. One of the water quality parameters that increase the effect of toxic substances in water is total hardness and hard water increases this effect. Therefore, hard water is not suitable for aquaculture [42].
$CaCO_3$ is one of the water quality parameters. Hardness in water is given as $CaCO_3$ equivalent in mg/l unit; soft water (0-50 mg/l $CaCO_3$), medium hard (150-250 mg/l $CaCO_3$), hard water (250-350 mg/l $CaCO_3$), very hard (brackish) water (>350

mg/l $CaCO_3$) classified as [16]. According to the measured data seen in Table 5 and 6, as it is seen that the total hardness values show variations along the river, calculated average values show that the river takes a place among the rivers classified with medium hard. Ca^{+2} and Mg^{+2} are the most found metal ions dissolved in streams and rivers. Among these, calcium is the one much more found than those. These two ions play a vital role on the formation of cobonate salts which are necessary especially for aquatic animals, and for the elimination of the toxic effects of some substances [17, 43, 44, 45, 46,]. The normal the least and maximum amounts of Ca^{+2} and Mg^{+2} are 1-150 and 5-10 mg/l, respectively [47, 48]. In Table 7 and 8, Fig. 3, it is seen that the amount of the value of Ca^{+2} ve Mg^{+2} in Simav Çayı valley do not vary prominently. Mg^{+2} can be derived from igneous and metamorphic rocks and magnesium carbonate (dolomite) in sedimentary rock. Some researchers have suggested that the sources of magnesium are due to the rains bringing magnesium from different regions with volanic, karstic and calcareous structures [13, 50, 49]. In [50] reported that the Simav Stream valley is over volcanic materials. According to the determined calcium and magnesium values, it can be said that the river rock structure has a karstic structure. Chloride anion is found in all of the natural waters, and it is the one of the minerals effecting on the diversity of livings. Since the solubility of chloride salts is high, it is one of the important indicators of healthy water. A water is called very salty water if its chloride concentration is higher than 250 mg/L [51]. Its concentration is usually low but it is high concentrations in polluted waters. The source of chloride in natural water may be domestic, industrial wastes, agricultural activities, as well as it may be of mineral origin. Chloride content may vary according to the distance of freshwater to the sea and the rock structure. The sudden increase in chloride suggests that industrial wastes are mixed with water [11, 32, 40, 49, 52,]. Chloride values of the Simav River water at upper basins are close to each other varying from 8,87-29,58 m/l as seen in Table 7 and 8. It is thought that the lowest value was determined at the 3rd sampling point because the river dries up periodically. The required value of chloride in natural is between 0 and 30 mg/L. So, the chloride concentration value of the river at the mentioned basins may be said that it is suitable. It was observed that the chloride values increased after the Kepsut region.
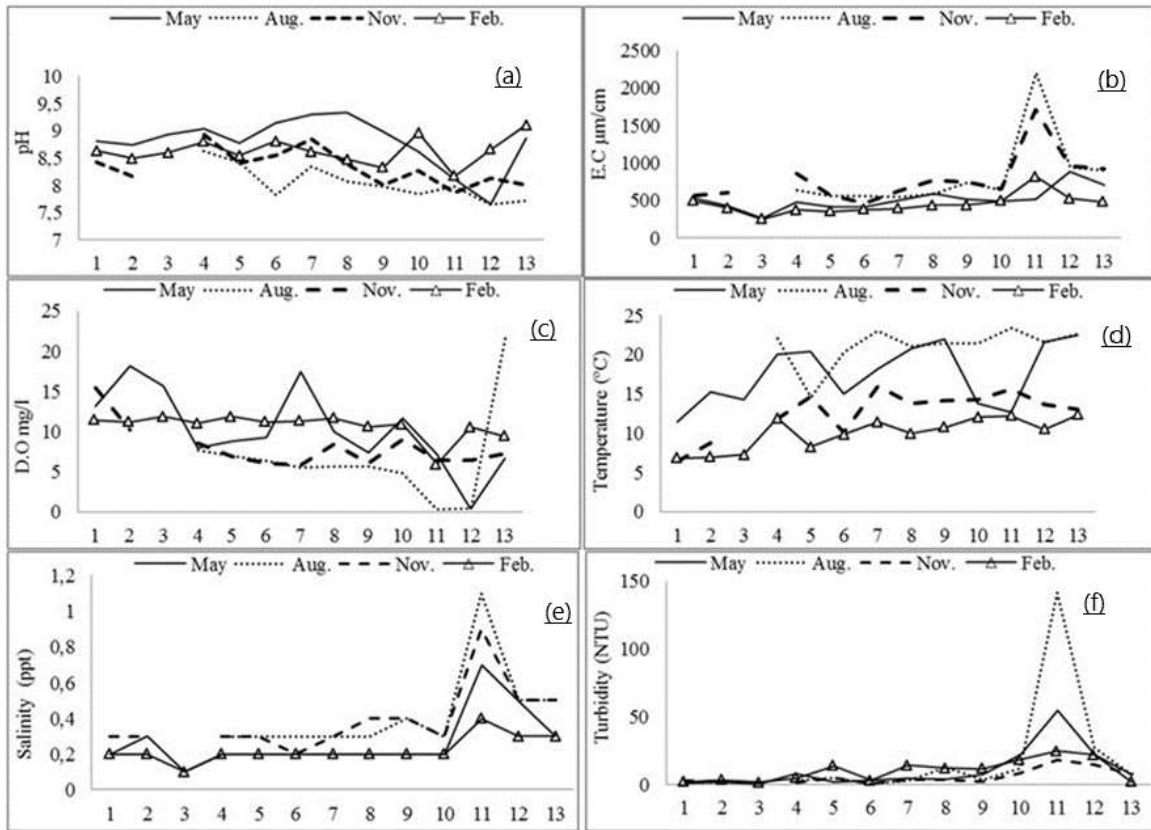
Figure 2. *Variations of water quality parameters the Simav River corresponding to seasonally of of (a) pH, (b) E.C, (c) DO, (d) temperature, (e) salinity and (f) turbidity*

Table 7. *The values of the parameters included in Group-2 measured in May and August at 13 stations*

		NH₄-N (mg/l)	NO₃-N (mg/l)	NO₂-N (mg/l)	PO₄-P (mg/l)	ΣP (mg/l)	Ca (mg/l)	Mg (mg/l)	Cl (mg/l)	HCO₃ (mg/l)	CO₃ (mg/l)
ST1	May	0,05	0,6	0,01	0,11	0,37	56,14	35,02	13,31	186,05	60
	August	0,01	0,91	0,017	0,02	0,28	52,93	45,68	39,93	207,4	12
ST2	May	0,54	0,5	0,063	0,07	0,35	17,64	40,82	26,63	213,5	30
	August	0,27	0,25	0,027	0,12	0,18	51,86	25,27	29,586	320,25	16
ST3	May	0,87	0,5	0,033	0,07	0,35	38,49	17,49	8,87	152,5	60
	August	0,505	0,257	0,023	0,046	0,215	38,49	17,49	8,87	129,625	31,5
ST4	May	0,21	1	0,02	0,49	0,78	56,14	16,52	17,75	213,5	15
	August	0,024	0,59	0,012	0,13	0,6	11,23	54,43	17,75	280,6	9
ST5	May	0,09	0,7	0,01	0,06	0,24	70,58	6,8	35,5	122	60
	August	0,02	0,72	0,034	0,02	0,21	22,46	24,3	8,87	201,3	6
ST6	May	0,94	0,5	0,017	0,08	0,24	41,7	37,91	17,75	228,75	15
	August	0,025	0,45	0,011	0,025	0,11	11,23	59,29	8,88	347,7	0
ST7	May	0,05	1,2	0,028	0,2	0,95	48,12	68,04	22,18	225,7	24
	August	0,025	1,34	0,034	0,04	0,39	19,25	37,91	13,31	253,15	3
ST8	May	0,56	0,35	0,071	0,37	1,32	59,35	36,94	22,19	311,1	24
	August	0,025	0,91	0,032	0,13	0,46	17,64	49,57	22,19	292,8	0
ST9	May	0,13	0,35	0,11	0,56	1,72	52,93	34,99	31,06	247,05	15
	August	0,025	1,64	0,22	0,61	1,74	28,87	62,21	62,13	332,45	0
ST10	May	3,66	0,6	0,083	0,45	1,61	48,12	40,82	102,06	150,25	0
	August	0,04	0,92	0,13	0,48	2,2	27,27	45,68	66,56	271,45	0
ST11	May	0,93	0,2	0,073	0,53	2,6	56,14	43,74	221,88	448,35	0
	August	0,43	0,2	0,96	1,95	6,68	35,29	55,4	536,94	530,7	0
ST12	May	1,83	0,6	0,083	0,45	1,61	48,12	40,82	102,06	366	0
	August	0,18	0,8	0,38	0,65	2,78	12,83	30,13	199,68	396,5	0
ST13	May	1,06	0,2	0,1	0,43	3,31	48,12	29,16	159,75	335,5	6
	August	0,14	0,2	0,06	0,7	4,55	32,08	58,32	181,94	366	0

Table 8. *The values of the parameters included in Group-2 measured in November and February at 13 stations*

		NH₄-N (mg/l)	NO₃-N (mg/l)	NO₂-N (mg/l)	PO₄-P (mg/l)	ΣP (mg/l)	Ca (mg/l)	Mg (mg/l)	Cl (mg/l)	HCO₃ (mg/l)	CO₃ (mg/)l
ST1	November	0,12	0,16	0,014	0,07	0,11	62,56	36,94	22,19	268,4	18,3
	February	0,11	0,04	0,01	0,03	0,12	64,16	35,96	13,31	265,4	20
ST2	November	0,13	0,15	0,008	0,24	0,08	57,74	24,3	26,63	323,3	6
	February	0,14	0,1	0,009	0,04	0,11	80,2	10,69	35,5	423,95	12

	November	0,505	0,2575	0,0235	0,046	0,215	38,49	17,49	8,87	129,625	31,5
ST3	February	0,14	0,015	0,014	0,022	0,08	38,49	17,49	8,87	106,75	3
	November	0,11	0,2	0,011	1,57	1,42	24,06	48,6	35,5	280,6	45
ST4	February	0,15	0,18	0,018	0,07	0,17	65,76	23,33	35,5	155,55	0
	November	0,03	0,6	0,01	0,2	0,27	44,91	20,41	22,19	204,35	15
ST5	February	0,13	0,15	0,021	0,14	0,27	44,91	20,41	22,19	143,35	0
	November	0,26	0,2	0,014	0,055	0,085	20,88	39,85	13,31	256,2	6
ST6	February	0,12	0,74	0,014	0,04	0,12	20,85	39,85	13,31	198,25	0
	November	0,11	0,73	0,028	0,39	0,56	32,08	37,91	22,19	283,65	18
ST7	February	0,16	0,15	0,032	0,16	0,5	56,14	23,33	22,19	179,95	0
	November	0,06	3,2	0,068	0,75	1,03	40,1	24,3	39,94	314,15	21
ST8	February	0,13	0,34	0,034	0,19	0,56	40,1	23,33	22,19	176,9	9
	November	0,38	1,99	0,19	1,79	1,82	48,12	47,63	39,94	344,65	0
ST9	February	0,23	0,39	0,044	0,25	0,65	67,37	35,96	39,94	158,6	6
	November	0,07	0,02	0,015	0,86	0,73	27,27	54,43	48,81	305	6
ST10	February	0,25	0,38	0,025	0,28	0,57	26,66	54,32	53,25	173,85	30
	November	0,22	0,2	0,065	2,63	3,56	35,29	54,43	359,44	423,95	0
ST11	February	2,9	0,68	0,104	0,36	1,65	35,28	46,66	359,44	280,6	0
	November	1,86	0,7	0,05	1,63	1,7	36,89	43,74	146,44	341,6	0
ST12	February	0,4	0,2	0,019	0,25	0,81	36,89	43,74	102,06	240,95	0
	November	1,28	0,2	0,055	1,29	1,66	19,25	59,29	124,25	326,35	0
ST13	February	0,11	0,2	0,01	0,03	0,12	40,1	29,16	88,75	112,5	12
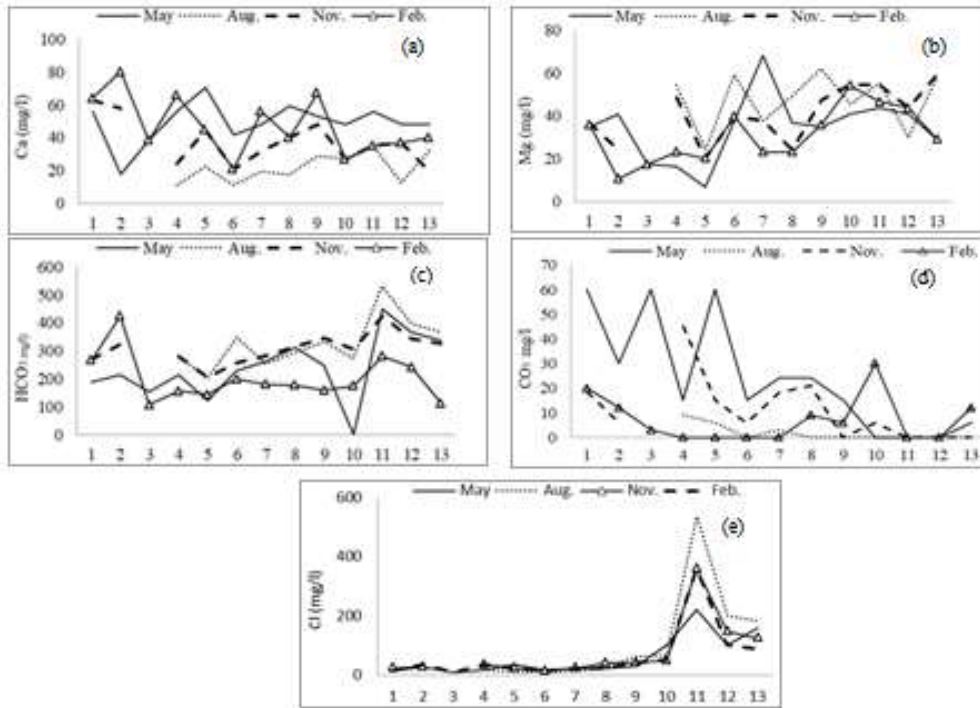
Figure 3. *Variations of water quality parameters the Simav River corresponding to seasonally of (a) Ca, (b) Mg, (c) HCO_3, (d) CO_3, (e) Cl^-*
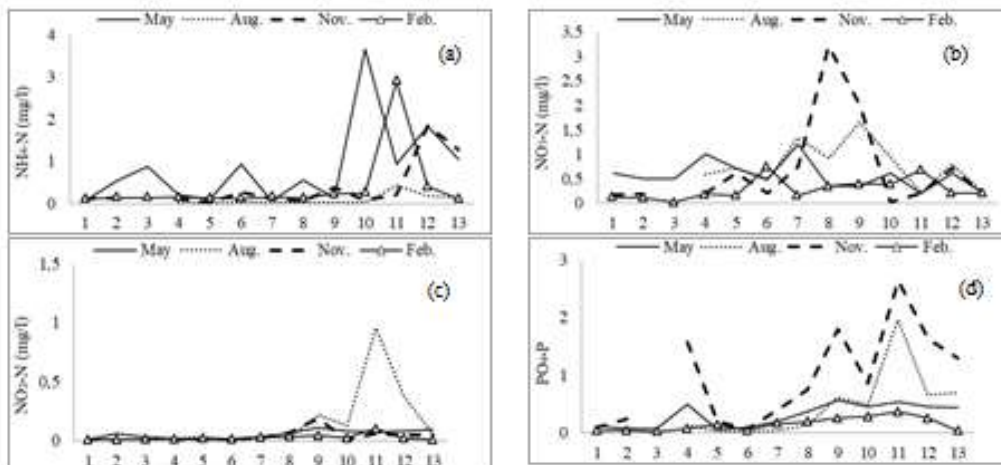
Figure 4. *Variations of water quality parameters the Simav River corresponding to seasonally of (a) NH_4-N, (b) NO_3-N, (c) NO_2-N, (d) PO_4-P*

The highest mean value (369.42 mg/l) was determined at the 11th sampling point (Uluabat Lake outlet) (Table 3, Figure 3).

In [53] stated that chloride creates a pollution load together with some the other parameters in the Lake Uluabat and domestic and agricultural drainage waters pollute the lake. It could be said that especially in Kepsut region and afterwards (ST8, 9, 10, 11, 12, 13), the increase in chloride values was caused by intense domestic and industrial wastes and agricultural activities. The large agricultural lands have been expressed quite close to the stream in the Kepsut region [13]. In this research, it has been observed that the agricultural lands of the region were flooded in the autumn period and the surface waters from these lands mixed with the stream.

Phosphorus is found in natural waters either in the form of dissolved organic phosphorus or in the form of organic phosphorus suspended in water. Therefore, it indirectly affects the development of heterotrophic organisms negatively. Lack of phosphorus limits the growth of autotrophs organisms [44, 17]. Domestic wastes (especially detergents), industrial wastes, sewage water are constitute 91% of the phosphorus source. Agricultural fields, volcanic rocks, meteorites and soil constitute 9% of the phosphorus source. Phosphates mixed with surface waters from these sources creates eutrophication as they cause excessive growth of algae and other aquatic plants. Some researchers sudgested that the amount of phophorous may vary from 0,05 to 0,3 mg/l in stream and river waters [17, 32, 40, 44]. Phosphorus values increased along the river in Kepsut and afterwards. In the upper region of Simav Stream did not show much change at stations, but its value at station 4 (1.57 mg/l PO4-P and 1.42 mg/l total P in autumn) was remarkable (Figure 4). It was detected in the 9th sampling point (1.79 mg/l, 1.82 mg/l) between Kepsut and Susurluk settlements in the central region. It is thought that intensive agricultural activities and direct discharge of domestic wastes into streams in these regions caused an increase in phosphorus values. Phosphorus values were determined above the limit values in the summer and autumn periods seasonally. We can said that due to the decreased in stream flow caused in summer and due to the runoff from agriculturel areas in autumn phosporus values were incresead (Figure 4). It has been reported that phosphorus values increase in the middle region of Simav Stream in summer, and it was a receiving body for domestic and industrial wastewater, especially after Çaygören Dam. For this reason, it have been stated that the water pollution of Simav Stream increases towards the north [30]. The highest phosphorus values of Simav Stream (in summer and autumn) were determined in the river sub-region. It is thought that the reason for this increase as the mixing of the side branches carrying the pollution load into the river and is also caused by the environmental factors mentioned above. According to SWQR (the Surface Water Quality Regulation), the stream III. quality (medium) class. One of the important elements found in natural waters is nitrogen (N) and it is also found in stream and river waters in the form of dissolved gas (N$_2$), inorganic nitrogen (NH$_4$, NO$_2$, NO$_3$) and dissolved or organic compound.

Inorganic nitrogen is only nutritive element taking place among these nitrogen compounds. These nutritive elements are very important for the microorganisms to survay their lives. There are many nitrogen sources are due to the interaction between water and atmosphere, natural decomposition of organic matter, the metabolic by-product of protein catabolism that provides NH4-N, the nitrogen bound by microorganisms from the soil and the biological degradation of domestic, agricultural and industrial wastes. In recent years, the increase in these nitrogenous compounds with human influence affects the distribution and physiology of aquatic organisms. Therefore, nitrogen compounds are one of the important parameters in the determination of water pollution [42, 44, 54, 55, 56]. In natural waters, ammonia is 0.1 mg/l and ammonium compounds are 1 mg/l or less [17,57]. Nitrite, nitrate and ammonium nitrogen levels, which are nitrogen derivatives, showed differences according to stations and seasons in Simav Stream. The values increasing from the upper course of the stream to the lower course were measured. The values increasingly from the upper region of the river to the lower region were measured. The highest nitrate nitrogen (1.99 mg/l, autumn) and nitrite nitrogen (0.96 mg/l, spring) values were determined in the sub-region stream (Table 4). According to SWQR, it was in the I. quality class in terms of NO3-N value. The lower and middle region of the stream heve been in I. quality (good) class according to the average value of NH4-N value, but the middle region, only around Karacabey, and the lower region II. have been determined in the quality class. Seasonally, the highest ammonium nitrogen (3.66 mg/l) was detected in ST10 (in the lower part of the stream) in the spring period (Figure 4). It can be said that it was caused by the increasing domestic and industrial wastes, as well as the intensive livestock

activities. It was emphasized that the discharge of slaughterhouse and factory wastes, sewage water in the river basin to the Simav Stream created intense pollution pressure, and it have been stated that especially the Nitrate values were high [13].

4. Conclusions

In this research, it was aimed to determine the water quality of Simav River which one of the most important river of the Turkey. As a result of rapid population growth, unplanned urbanization and industrialization in Turkey, water pollution has been occurring in recent years. Simav River is under pressure of pollotion from spring point to sea. Especially upper catchment is affected from the agricultural activies and middle/down catchment from the both agriculturel and livestock, endustrial activities. It is thought that, all of thesese man-made activities cause pollution in Simav river. Periodic floods and wastes from the food industry (especially from meat, milk production and industrial facilities) are thought to be effective in the formation of pollution. In the region both the main stream and its tributaries are used for irrigation, and Çaygören Dam Lake on the river is also that purpose. Relatively cleaner areas of the stream have been the sections passing through high mountain areas and low population areas.

In order to increase the quality of Simav Stream and provide its sustainability;

- By raising awareness of the people of the region, excessive use of chemical fertilizers and pesticides in agricultural activities should be prevented.
- In order to prevent the mixing of the rivers due to the flood from the agricultural areas, a flood prevention plan should be prepared and the surrounding people should be informed.
- The industrial facilities in the basin should be inspected frequently, and the facilities whose treatment systems do not work or that operate irregularly should be prevented from continuing their activities.
- The people of the environment, one of the most important livelihoods of which is livestock, should be informed about the sustainability of waters. In addition, other pollution sources (Integrated meat plant, poultry farm etc) should be inspected frequently.
- For the sustainability of the stream, the water quality should be constantly monitored physically, chemically and biologically. Necessary measures should be taken according to the data obtained.

Author Statements:

References

[1] Çiçek, N. L. & Ertan, Ö. O. (2012). Köprüçay Nehri (Antalya)'nın Fiziko-Kimyasal Özelliklerine Göre Su Kalitesinin Belirlenmesi. *Ekoloji,* 21(84): 54-65. DOI: 10.5053/ekoloji.2012.847

[2] Kumar S. K., Babu, S.H., Rao, E., Selvakumar S., Thivya, C., Muralidharan, S., Jeyabal, G. (2017). Evaluation of water quality and hydrogeochemistry of surface and groundwater, Tiruvallur District, Tamil Nadu, India. *Applied Water Science* 7: 2533–2544. DOI 10.1007/s13201-016-0447-7

[3] Mullai, P., Yogeswari, M.K., Oommen, B., Saravanakumar, K. and Kathiresan, K. (2013). Monitoring of water quality parameters in Uppanar River of Cuddalore District, Tamil Nadu State, India. *Journal of Water Sustainability,* 3(4): 179.

[4] Palmer, C. M. (1980). Algae and Water Pollution. *Castle House Publications Ltd.*

[5] Reddy K. H. D. & Lee S. M. (2012). Water Pollution and Treatment Technologies. *Journal Environmental & Analytical Toxicology* 2(4):2-5. DOI:10.4172/2161-0525.1000e103

[6] Gümüş, N. E. (2021). Akarçay Akarsuyu (Afyonkarahisar) Su Kalitesi ve Ağır Metal Kirliliğinin Belirlenmesi. *Journal of Anatolian Environmental and Animal Sciences*, 6(1):120-127. DOI: https://doi.org/10.35229/jaes.839147

[7] Tokatlı, C. (2020). Ergene Nehir Havzası Su Kalitesinin Çok Değişkenli İstatistik Analizler Kullanılarak Değerlendirilmesi. *LimnoFish.* 6(1):38-46. DOI: 10.17216/LimnoFish.524036

[8] Ugwu, A. I. & Wakawa, R. J. (2012). A study of seasonal physicochemical parameters in River Usma. *American Journal of Environmental Science.* 8 (5): 569-576 DOI: https://doi.org/10.3844/ajessp.2012.569.576

[9] Verep, B., Mutlu T., Çakır V., Aydın, G. (2017). Derepazarı Deresinin (Rize-TÜRKİYE) Fiziko-Kimyasal Su Kalitesinin Belirlenmesi ve Bazı Su Kalite Standartlarına Göre Değerlendirilmesi. *Journal of Anatolian Environmental & Animal Sciences.* 2 (1): 19-22.

[10] Jindal, R. & Sharma, C. (2011). Studies on water quality of Sutlej River round Ludhiana with reference to physicochemical parameters. *Environmental Monitoring and Assessment*, 174: 417-425.

[11] Mutlu, E., Yanık, T., Demir, T. (2013). Horohon Deresi (Hafik-Sivas) Su Kalitesi Özelliklerinin Aylık Değişimleri. *Alınteri,* 25(B):45-57.

[12] Gürkan, Ü., Özan-Tekin, S. (2012). Susurluk Çayı (Bursa- Balıkesir)'ndaki Tatlı Su Kefali (*Squalius cephalus* L.)'nin Helmint Faunası. *SDÜ Journal of Science (E-Journal).* 7 (2): 77-85.

[13] Kudun, K. (1994). Simav Çayı'nın Hidrojeokimyası. *Istanbul Technical University, Graduate School of Natural and Applied Sciences, Master Thesis.*

[14] Anonymous (2005) Standart Methods for the Examination of Water and Wastewater. *APHA, AWWA, WEF, Washington*

[15] Lampert W, Sommer U (2007) Limnoecology. *Oxford University Press.*

[16] Anonymous (2011). Çevre Sağlığı, Suların Analiz Parametreleri (850CK0011). *T.C. Milli Eğitim Bakanlığı, Ankara.* http://www.megep.meb.gov.tr/mte_program_modul /moduller_pdf/Sular%C4%B1n%20Analiz%20Para metreleri.pdf

[17] Tanyolaç, J. (2004). Limnoloji. *Hatiboğlu Yayıncılık.*

[18] TS266, (2005). Water intended for human consumption. *Turkish Standardization Institute, ICS 13.060.20.* https://www.resmigazete.gov.tr/eskiler/2005/02/20 050217-3.htm

[19] SWQR., (2021). Surface Water Quality Regulation. *Official Gazette* (RG16/6/2021-31513)

[20] Alas, A., Çil, O. H. S., (2002). An Investigation of Water Quality Parameters at Some Springs Supplying *Drinking Water for Aksaray. Ekoloji,* 11 (42): 40-44.

[21] Reynolds, C.S., 1993. The Ecology of Freshwater Phytoplankton. *Chambridge Univ. Press*

[22] Küçükali, S. (2019). Filyos Nehri'nin Fiziksel Su Kalitesi Parametrelerinin İstatistiksel Olarak İncelenmesi. *Journal of Anatolian Environmental and Animal Sciences.* 4(3):519-524.

[23] Öz, Ü., Ertaş, E., (2016). Arılı Deresi (Rize)'nin fiziko-kimyasal açıdan su kalitesinin tespit edilmesi. *Turkish Journal of Aquatic Sciences.* 31(1): 30-39.

[24] Shrestha, S., Kazama, F., (2007). Assessment of surface water quality using multivariate statistical techniques: A case study of the Fuji river basin, Japan. *Environmental Modelling and Software,* 22: 464-475.

[25] Taşdemir M.,Göksu Z.L., 2001. Asi Nehri'nin (Hatay, Türkiye) Bazı Su Kalite Özellikleri. *E.U. Journal of Fisheries & Aquatic Sciences.* 18(1-2): 55-64.

[26] Çelikkale MS. 1994. İçsu balıkları yetiştiriciliği. *Karadeniz Teknik Üniversitesi, Deniz Bilimleri Fakültesi Yayınları, Trabzon.*

[27] Öztrük, E., Küçük, F. (2017). Simav Çayı'nın Balık Faunası. *Süleyman Demirel Üniversitesi Eğirdir Su Ürünleri Fakültesi Dergisi,* 13(2): 132-152.

[28] Verep, B., Serdar, O., Turan D., Şahin C. (2005). İyidere (Trabzon)'nin Fiziko-Kimyasal Açıdan Su Kalitesinin Belirlenmesi. *Ekoloji.* 14(57):26-35.

[29] Dere, Ş., Dalkıran, N., Karacaoglu, D., Elmacı, A., Dulger, B., Eng˙ın Senturk, E., (2006). Relationships Among Epipelic Diatom Taxa, Bacterial Abundances And Water Quality In a Highly Polluted Stream Catchment, Bursa – Turkey. *Environmental Monitoring and Assessment.* 112: 1–22. DOI: 10.1007/s10661-006-0213-7

[30] Gülüm, A., Akgün, A. (2011). Simav Çayı Aşağı Çığırında (Çaygören Baraj Çıkışı İle Kepsut Boğazı Arasında) Su Kirlenmesi Sorunu ve Çözüm Önerileri. *e-Journal of New World Sciences Academy,* 6(2):31-42.

[31] Boyd, C.E, Lichtkopper, F. (1979). Water Quality Management in Pond Fish Culture. *Auburn University, Alabama Agricultural Experiment Station Press, Auburn, Alabama.*

[32] Cirik, S. Cirik, Ş. (2008). Limnoloji. *Ege Üniversitesi Su Ürünleri Fakültesi Yayınları, İzmir*

[33] Kocataş, A. (2006). Ekoloji ve Çevre Biyolojisi. *Ege Üniversitesi Su Ürünleri Fakültesi Yayınları.*

[34] Katip, A. & Karaer F. (2011). Uluabat Gölü Su Kalitesinin Türk Mevzuatına Ve Uluslararası Kriterlere Göre Değerlendirilmesi. *Uludağ Üniversitesi Mühendislik-Mimarlık Fakültesi Dergisi,* 16 (2):25-34.

[35] Kaynak, A.G. (2002). Bursa şehir merkezinden kaynaklanan atıksular, arıtılmaları ve Nilüfer Çayı'na etkileri, Master Thesis. *Uludağ .Univ. Graduate School of Natural and Applied Sciences, Department of Environmental Engineering, Bursa.*

[36] EC (European Communities). 2006. EC of the European Parliament and of the council of 6 September 2006 on the quality of fresh waters needing protection or improvement in order to support fish life. *Directive 2006/44.*

[37] Mcneil, D. G., Closs, G. P. (2007). Behavioural responses of a south-east Australian floodplain fish community to gradual hypoxia. *Freshwater Biology*, 52: 412–420.

[38] Qadir, A., Malik, R. N., Husain, S. Z., (2008). Spatio-temporal variations in water quality of Nullah Aik-tributary of the river Chenab, Pakistan. *Environ Monit Assess.* 140:43–59. DOI 10.1007/s10661-007-9846-4

[39] Anonymous (2008). Minnesota Pollution Control Agency. *Turbidity: Description, Impact on Water Quality, Sources, Measures. Water Quality/Impaired Waters,*

https://www.pca.state.mn.us/sites/default/files/wq-iw3-21.pdf

[40] Egemen, Ö. (2006). Su Kalitesi (Ders Kitabı). *Ege Üniversitesi Yayınları, Bornova-İzmir.*

[41] Gedik, K., Verep, B., Terzi, E. Fevzioglu, S. (2010) Determination of Water Quality of Fırtına Stream (Rize) in Terms of Physico-Chemical Structure. *Ekoloji,* 19 (76): 25-35.

[42] Göksu, Z. L. (2003) Su Kirliliği. *Çukurova Üniversitesi Su Ürünleri Fakültesi Yayınları, Adana*

[43] Allan, D. J. (1996). Stream Ecology. *Chapman and Hall, London.*

[44] Atay, D., Pulatsü, S., (2000). Su Kirlenmesi ve Kontrolü. *Ankara Üniversitesi Ziraat Fakültesi, Yayın No:1513, Ankara.*

[45] Boyd, C.E. (1990). Water quality in ponds for aquaculture. *Agriculture Experiment Station, Auburn University, Alabama.*

[46] Şener, Ş., Şener, E., Davraz, A. (2017). Evalution of water quality using water quality index (WQI) method and GIS in Aksu River (SW-Turkey). *Sciences of the Total Environment,* 584-585: 131-144.

[47] Şen, B., Yıldız, Ş., Akbulut, A. (1994, Temmuz 5-8). Karamık Gölü Planktonundaki Bacillariophyta Üyeleri ve Su Kalitesinin Değerlendirilmesi. *In: XII. Ulusal Biyoloji Kongresi, Edirne-Turkey,* 166-172.

[48] Taş, B. (2006). Derbent Baraj Gölü (Samsun) Su Kalitesinin İncelenmesi. *Ekoloji,* 15(60):1-6

[49] Güler, Ç. (1997). Su Kalitesi. *Çevre Sağlığı Temel Kaynak Dizisi* No: 43.

[50] Soykan A., (2000). Sındırgı-Bigadiç Depresyonları Arasında Simav Çayı Vadisinin Jeomorfolojisi. *Balıkesir Üniversitesi Sosyal Bilimler Enstitüsü Dergisi,* 3(4):22-41.

[51] Taş, B. (2011). Gaga Gölü (Ordu, Türkiye) Su Kalitesinin İncelenmesi. *Karadeniz Fen Bilimleri Dergisi,* 2(1)3: 43-61.

[52] Kazancı N (2004) Köyceğiz-Dalyan Özel Çevre Koruma Bölgesi Sucul Ekosistemi'nin Hidrobiyolojik yönden incelenmesi. *Türkiye İç Suları Araştırmaları Dizisi: VIII, İmaj Press.*

[53] Bulut, C., Atay, R., Uysal, K., Köse, E., Çınar, Ş. (2010). Uluabat Gölü Yüzey Suyu Kalitesinin Değerlendirilmesi. *İstanbul University Journal of Fisheries & Aquatic Sciences.* 25 (1):9-18.

[54] Barakat, A., Baghdadi, M.E., Rais, J., Aghezzaf, B. and Slassi, M. (2016). Assessment of spatial and seasonal water quality variation of Oum Er Rbia River (Morocco) using multivariate statistical techniques. *International Soil and Water Conservation Research,* 4: 284-292.

[55] Kazancı N., Girgin S., Dügel M., Oğuskurt D., (1998). Burdur Gölü ve Acı Göl'ün Limnolojisi, Çevre Kalitesi ve Biyolojik Çeşitliliği. *Türkiye İç Suları Araştırma Dizisi:III.*

[56] Romano, N. & Zeng, C. (2013). Toxic Effects of Ammonia, Nitrite, and Nitrate to Decapod Crustaceans: A Review on Factors Influencing their Toxicity, Physiological Consequences, and Coping Mechanisms. *Reviews in Fisheries Science,* 21(1):1–21.

[57] Chapman, D., & Kimstach, V. (1996). Selection of water quality variables. In: Chapman D (ed), Water Quality Assessments-A Guide to Use of Biota, Sediments and Water in Environmental Monitoring. *University Press, Cambridge.*
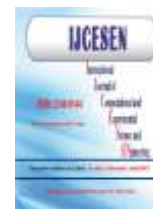
Comparison of The Molecular Docking Properties of Three Potentially Active Agents

Güvenç GÖRGÜLÜ[1]*, Bülent DEDE[2]

[1]*Burdur Mehmet Akif Ersoy University, Faculty of Education, Department of Science Education, Burdur, Türkiye
* **Corresponding Author** : **Email:** guvencgorgulu@mehmetakif.edu.tr - **ORCID:** 0000-0003-4740-7265

[2]Süleyman Demirel University, Faculty of Arts and Science, Department of Chemistry, Isparta, Türkiye
Email: bulentdede@sdu.edu.tr - **ORCID:** 0000-0003-1416-7373

Abstract:

Antineoplastic agents are generally the drugs used to recess or prevent tumor growth which is promoted in many cases by certain factors like vascular endothelial growth factor-2 (VEGFR-2) and cyclooxygenase-2 (COX-2). These two factors seem important in angiogenesis and lymphangiogenesis in fetal, normal and neoplastic tissue. Prevention of VEGF family of proteins and COX-2 enzyme is a good strategy to inhibit the growth of tumor tissue eventually may give rise to recession. In this study, three potentially active and an active ligand were tested for their binding properties to two target molecules mentioned above by molecular docking study. This research is aimed to compare three different molecules according to their binding affinities, binding energies and the nature of bonds formed between the ligand and the target molecules. Showing the 3D structures will localize the fitted ligands on proteins and the possible hydrogen bonds formed were defined. Among the three proposed ligands, Ligand 1 showed the closest results to the commercial product lenalidomide®. All three ligands showed similar ΔG values and fitness scores with lenalidomide® which is an indicator of good fit, proximity and orientation with the target molecule.

1. Introduction

Specific binding modes of ligands to the target molecules are one of the major concerns of pharmacology today. To understand the properties of these couples of ligand protein complexes in term of proximity and orientation would help the researchers to construct a pattern of molecular interaction. A scorable fitness related to the binding energy, length, type, number, strength and the localization of the bonds and other intermolecular interactions would make a great contribution to drug design studies [1]. Molecular docking is essentially the study of intermolecular interaction that has become an important component of computer aided drug design process [2-4]. In these aspects, molecular docking is an important pre-study for the elimination of candidate molecules. Antineoplastic agents are generally the drugs used to recess or prevent tumor growth which is promoted in many cases by certain factors like vascular endothelial growth factor-2 (VEGFR-2) and cyclooxygenase-2 (COX-2). These two factors seem important in angiogenesis and

lymphangiogenesis in fetal, normal and neoplastic tissue. Prevention of VEGF family of proteins and cyclooxygenase-2 enzyme is a good strategy to inhibit the growth of tumor tissue eventually may give rise to recession [5-8]. In this study, three previously synthesized [9-11] potentially active ligands were tested for their binding properties to two synergistically active target molecules (VEGFR-2 and COX-2) by molecular docking study. It is aimed to compare three different molecules according to their binding affinities, binding energies and the nature of bonds formed between the ligand and the target molecules. Showing the 3D structures will localize the fitted ligands on proteins and the possible hydrogen bonds formed will be defined. The data obtained were compared to an active compound lenalidomide®, found in the market, as an anti-angiogenic factor.

2. Material and Methods

Molecular docking studies were performed on SwissDock web server using EADock DSS

algorithm [12]. High resolution crystal structures of VEGFR-2 (PDB ID: 2XIR) and COX-2 (PDB ID:1CX2) were obtained from protein data bank. The GaussView 5.0.9 program was used to visualize the optimized geometries of the ligands [13]. All graphical data obtained from the molecular docking studies were visualized using UCSF Chimera software [14].

3. Results and Discussions

Previously synthesized three ligands were studied for molecular docking properties. The three ligands share a common structural similarity of having a backbone composed of a biphenyl, a keto and an oxime group as shown in Figure 1. This study based on the determination of the effects of functional amine groups attached to identical structures for comparison of their docking behaviors. The design of the ligands primarily based on the conformational stability of the overall molecule and reactivity of the functional groups. In order to start molecular docking, candidate molecules were optimized by molecular mechanics for reaching the minimal energy levels. The 3D structures of the target proteins were checked and removed for unwanted groups like water molecules and co-crystallized structures which may interfere with docking. Than Gastegier charges were assigned and polar hydrogens were added as in a routine preparation process. Table 1 shows the overall data obtained from molecular docking studies. All three ligands bonded to the targets spontaneously. Binding energies of Ligands 1, 2 and 3 with VEGFR-2 were Ligand 1 > Ligand 2 > Ligand 3 > lenalidomide® from higher to lower, respectively (with omitted minus sign). All ligands showed a higher binding energy (ΔG) compared to commercial agent. Ligand 1 and lenalidomide® formed a hydrogen bond while Ligand 2 and 3 formed 2 hydrogen bonds with the target which suits with the binding energies. Another important parameter for molecular docking is the full fitness score for ligand-VEGFR-2 couples studied. Obtained fitness scores were directly proportional with the ΔG values of the couples. In addition to the binding energies, total energy of the formed ligand- protein couples indicates the stability of the formed molecule. Lenalidomide®-VEGFR-2 couple formed the most stable molecule with the lowest molecular energy. Secondly, the Ligand 1 and both proteins had four times the lowest molecular energy compared to other ligands. Therefore, the stability of the ligand- protein couples from the most stable to the least were like lenalidomide® > Ligand 1 > Ligand 2 > Ligand 3. As can be seen from the space-filled views in Figure 2; Ligand 1 fits the
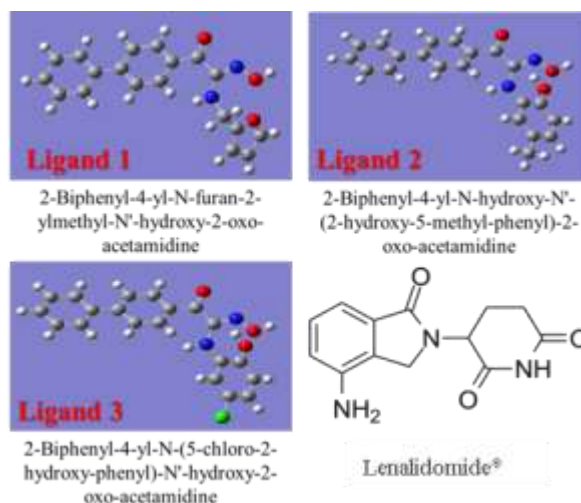

Figure 1. *Optimized structures of Ligands 1, 2, 3 and lenalidomide®.*

VEGFR-2 protein with a higher proximity and orientation, which is in accordance with the full-fitness score, ΔG value and total energy of the Ligand 1-protein couple. In the larger views of ribbon graphics of three ligands (second row from the left) formed H bonds (in orange color) also can be seen which is one for Ligand 1 and two for Ligand 2 and 3. In Figure 3 Ligand 1, 2, 3- COX-2 complexes can be seen. One H bond was formed between the Ligand 1, 2 and COX-2 while two H bonds were formed between Ligand 3 and COX-2. The H bonds contribute a lot to the stability of proteins and other macromolecules, but there seems no correlation between the fitness scores, ΔG values, energy of the couples and the number of H bonds for this study. Proximity may be the determining factor which is directly depended on the 3D shape of the ligand and the protein site it was plugged in. Ligand 2 and 3 are structurally similar only differing in Cl on phenyl group of Ligand 2 was replaced by a methyl group in Ligand 3 while the Ligand 1 bears a furan group attached to the amine group. Three ligands are similar in structure bearing a biphenyl, a carbonyl, an oxime and the amine group. The similarities are strongly correlated to the energy data obtained. Ligand 2 and 3 have closer total energy (39.51 and 38.81 kcal/mol, respectively) compared to Ligand 1 (10.59 kcal/mol) which carries a furan group attached to amine while others carry a phenyl group. The phenyl and furan replacement after the amine group causes a big difference in the energy of the Ligands 2 and 3 which was about four times higher than the energy of Ligand 1. It is also the same for VEGFR-2 and ligand couples. The H bonds were formed between the same amino acids and the functional groups (Arg 44-N-H and Glu 465-C=O) of COX-2 with the same functional groups (C=O and Oxime-H) of the three ligands which accurately

Table 1. *Molecular docking numerical data of Ligands 1, 2, 3 with VEGFR-2 and COX-2*

Target protein	Ligand	ΔG (kcal/mol)	Full fitness score (kcal/mol)	Energy (kcal/mol)	H-bond location (Target&Ligand)	H-bond length (Å)
VEGFR-2 (2XIR)	**Ligand 1**	-8.33	-1573.17	10.27	Asp 174-N-H & Furan-O	2.48
	Ligand 2	-8.20	-1544.39	44.92	Asp 174-C=O & -NH	1.97
					Arg 155-NH & C=O	2.26
	Ligand 3	-7.70	-1537.76	47.29	Asp 174-C=O & Phenyl-OH	2.07
					Arg 155-NH & C=O	1.98
	Lenalidomide®	-7.02	-1629.29	3.43	Serine 154-C=O & Isoindole-NH	2.13
COX-2 (1CX2)	**Ligand 1**	-9.10	-2387.39	10.59	Arg 44-N-H & C=O	2.03
	Ligand 2	-9.62	-2360.63	39.51	Glu 465-C=O & Oxime-H	1.90
	Ligand 3	-9.22	-2359.39	38.81	Arg 44-N-H & C=O	2.49
					Glu 465-C=O & Oxime-H	1.83
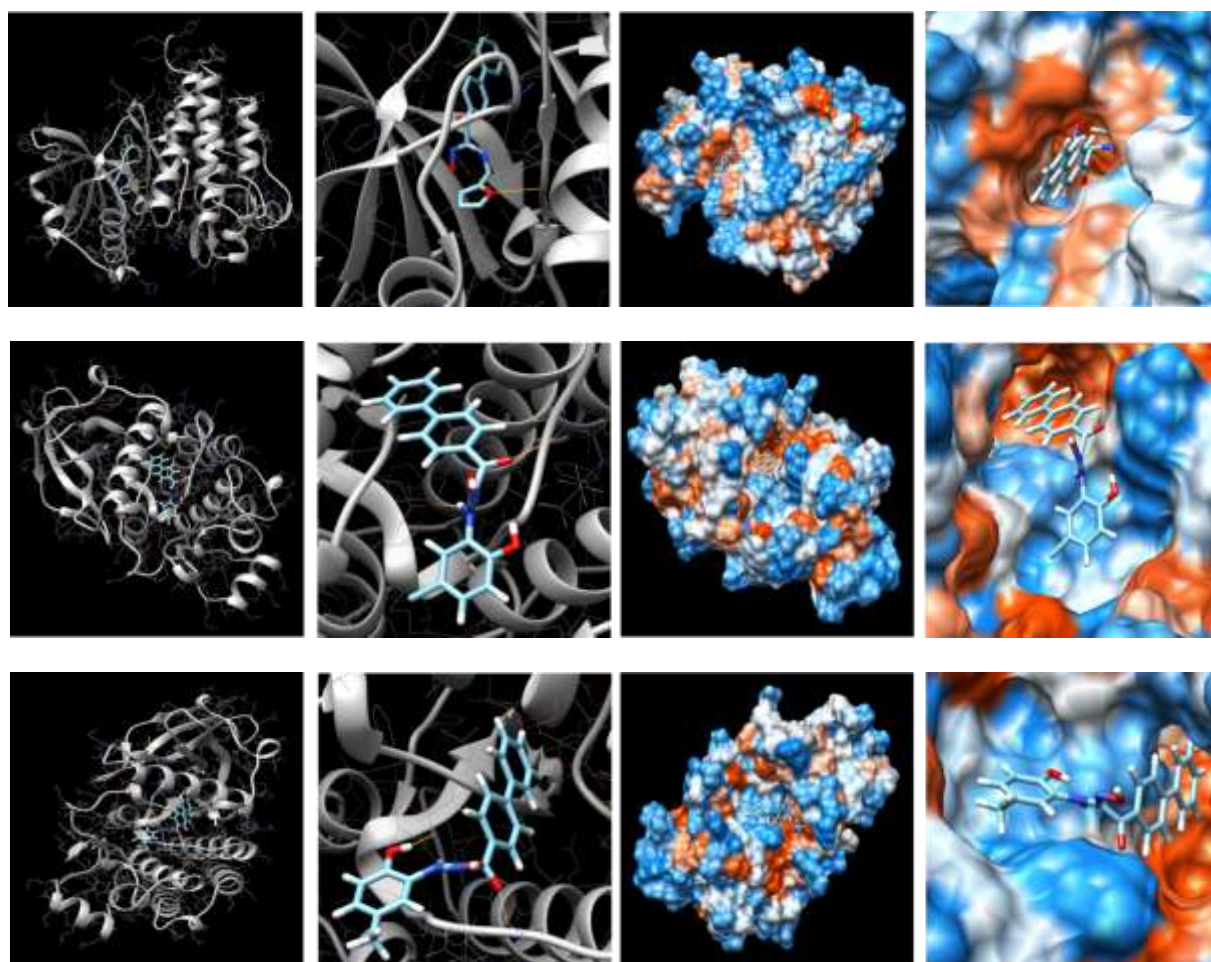
Figure 2. *Ligand 1, 2, 3-VEGFR-2 complexes (from top to bottom). Ribbon (left) and space filled (right) demonstration with closer views.*
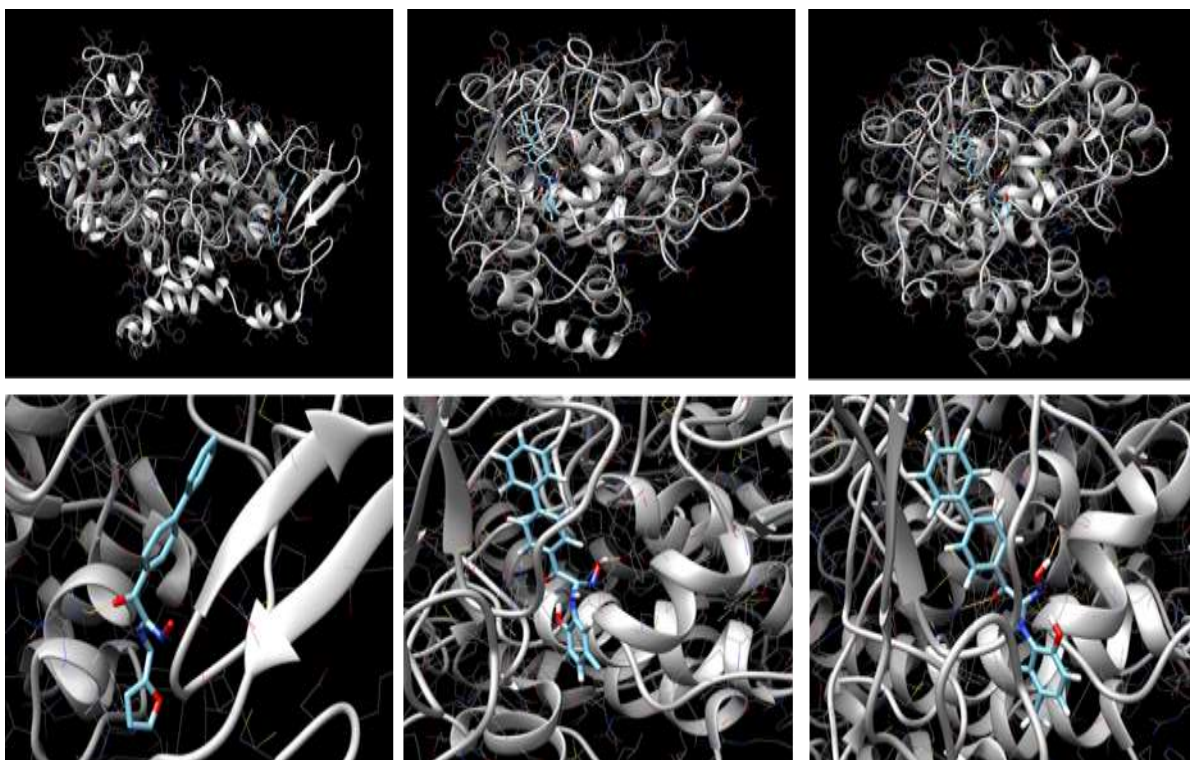
Figure 3. *Molecular docking visuals of complexes of Ligand 1, 2, 3 with (COX-2) enzyme (from left to right) with closer views just below.*
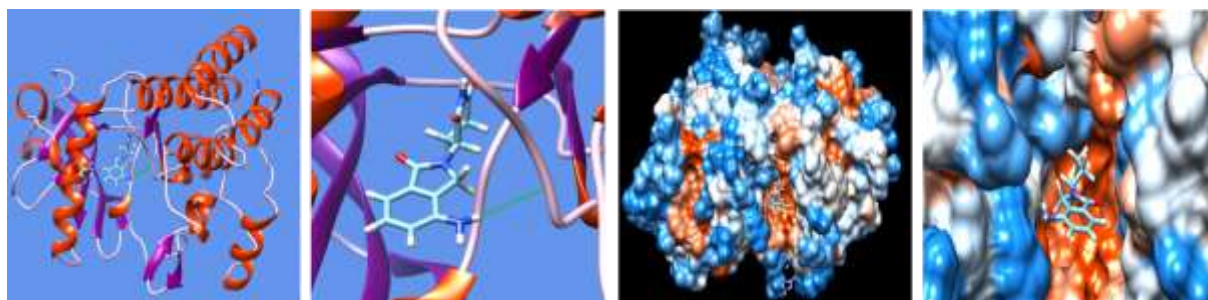
Figure 4. *Lenalidomide®-2XIR complex. Ribbon (left) and space filled (right) demonstration with closer looks.*

indicates that these three ligands were docked to the same site in COX-2. This is also valid for VEGFR-2 ligand complexes. Lenalidomide®-2XIR interactions can be seen in Figure 4. The ribbon shape demonstration shows the location of H bond while the space-filled figures shows the placement of the active ligand to the groove on the 2XIR protein. Potentiality of the three ligands were compared with the active drug lenalidomide® by molecular docking study which is a good indicator for a candidate molecule.

4. Conclusion

Comparison of the commercial product lenalidomide® with the three ligand by molecular docking data provide us information about the interaction status of our molecules with the target proteins. The ΔG values and fitness scores are close while the energy of lenalidomide® is much lower (3.43 kcal/mol) than the proposed ligands (10.27, 44.92 and 47.29 kcal/mol, respectively). It is about three times lower than the Ligand 1 and about 13 times lower than Ligand 2 and 3. This shows us that the commercial product is much more stable than the Ligand 1, 2 and 3. Stability is an important factor for a binding molecule which supposed to inhibit the target protein. However, the other indicators like ΔG and fitness scores are also important for the potentiality of the ligand synthesized. In this study, the Ligand 1 has the closest data to lenalidomide® which may be evaluated as a potential agent. For various reasons, new agents have been synthesized, characterized and tested for their binding behaviors. As a further research, these three ligands may be evaluated and processed for phase studies.

Author Statements:

- **Ethical approval:** The conducted research is not related to either human or animal use.
- **Conflict of interest:** The authors declare that they have no known competing financial interests or personal relationships that could have appeared to influence the work reported in this paper
- **Acknowledgement:** The authors declare that they have nobody or no-company to acknowledge.
- **Author contributions:** The authors declare that they have equal right on this paper.
- **Funding information:** The authors declare that there is no funding to be acknowledged.
- **Data availability statement:** The data that support the findings of this study are available on request from the corresponding author. The data are not publicly available due to privacy or ethical restrictions.

References

[1] Kenakin, T. (2018). A Pharmacology Primer: Techniques for More Effective and Strategic Drug Discovery, 4ᵗʰ ed. *San Diego, CA, Academic Press*,

[2] Strømgaard K, Krogsgaard-Larsen P, Madsen U, (2017). Eds. *Textbook of Drug Design and Discovery. CRC Press*;

[3] Gorgulu, G., Cicek, M. B., Dede, B. (2018). Novel Aminoketooxime Ligand and Its Cu(II) and Mn(II) Complexes: Synthesis, Characterization and Molecular Docking Studies. *Acta Physica Polonica A*, 133(2); 250–255.
DOI: 10.12693/APhysPolA.133.250

[4] Sliwoski, G., Kothiwale, S., Meiler, J., Lowe, E. W. (2014). Computational methods in drug discovery. *Pharmacological Reviews*, 66(1); 334-395. DOI:10.1124/pr.112.007336

[5] Tammela, T., Enholm, B., Alitalo, K., Paavonen, K. (2005). The biology of vascular endothelial growth factors, *Cardiovascular Research*, 65(3);550–563.
DOI:10.1016/j.cardiores.2004.12.002

[6] Wilkinson-Berka, J. L. (2004). Vasoactive factors and diabetic retinopathy: vascular endothelial growth factor, cycoloxygenase-2 and nitric oxide. *Current Pharmaceutical Design*, 10(27); 3331-3348.
DOI:10.2174/1381612043383142

[7] Tuccillo, C., Romano, M., Troiani, T., Martinelli, E., Morgillo, F., De Vita, F., Bianco, R., Gabriella, F., Bianco, R.A., Tortora, G., Ciardiello, F. (2005). Antitumor activity of ZD6474, a vascular endothelial growth factor-2 and epidermal growth factor receptor small molecule tyrosine kinase inhibitor, in combination with SC-236, a cyclooxygenase-2 inhibitor. *Clinical Cancer Research*, 11(3); 1268-1276.
DOI: 10.1158/1078-0432.1268.11.3

[8] Ferrara, N., Gerber, H.P., LeCouter, J. (2003). The biology of VEGF and its receptors, *Nature Medicine*, 9(6); 669-676. DOI:10.1038/nm0603-669

[9] Karipcin, F., Arabali, F., Karatas, I. (2006). Synthesis and characterization of 4-(alkylaminoisonitrosoacetyl) biphenyls and their complexes. *Russian Journal of Coordination Chemistry*, 32(2); 109-115.
DOI:10.1134/S1070328406020059

[10] Karipcin, F., Dede, B., Cengiz, M. (2010). Synthesis of (2-hydroxo-5-chlorophenylaminoisonitroso acetyl) phenyl ligands and their complexes: Spectral, thermal and solvent-extraction studies. *Russian Journal of Inorganic Chemistry*, 55(4); 530-540.
DOI:10.1134/S0036023610040078

[11] Dede, B., Karipcin, F., Arabalı, F., Cengiz, M. (2010). Synthesis, structure, and solvent-extraction properties of tridentate oxime ligands and their cobalt (II), nickel (II), copper (II), zinc (II) complexes. *Chemical Papers*, 64(1); 25-33.
DOI: 10.2478/s11696-009-0095-6

[12] Grosdidier, A., Vincent Z., Olivier M. (2011). Swissdock, A Protein-Small Molecule Docking Web Service Based on EADock DSS. *Nucleic Acids Res*, 39(2); 270-277. DOI: 10.1093/nar/gkr366

[13] GaussView, Revision 5.0.9, R. Dennington, T. A. Keith, J. M. Millam, Semichem Inc., *Shawnee Mission, KS, 2009.*

[14] Pettersen, E. F., Goddard, T. D., Huang, C. C., Couch, G. S., Greenblatt, D. M., Meng, E. C., Ferrin, T. E. (2004). UCSF Chimera-a visualization system for exploratory research and analysis. *Journal of Computational Chemistry*, 25(13); 1605-1612. DOI: 10.1002/jcc.20084

Research Article
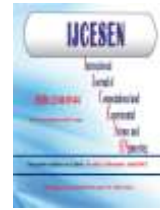
Hydrothermal Synthesis of Mordenite Type Zeolite

Sabiha Anas BOUSSAA[1*], Djamel NIBOU[2], Karima BENFADEL[3], Lamia TALBI[4], Assia BOUKEZZATA[5], Yahia OUADAH[6], Djaouida ALLAM[7], Samira KACI[8]

[1]Research Center On Semiconductor Technology for Energetic, CMSI-CRTSE, Algiers, Algeria
University of Sciences and Technology Houari Boumediene USTHB, Laboratory of Materials Technologies, Algeria
* **Corresponding Author**: **Email:** anassabiha@crtse.dz - **ORCID:** 0000-0003-2384-0056

[2]University of Sciences and Technology Houari Boumediene USTHB, Laboratory of Materials Technologies, Algeria
Email: dnibou@yahoo.fr - **ORCID:** 0000-0001-8924-6047

[3]Research Center On Semiconductor Technology for Energetic, CMSI-CRTSE, Algiers, Algeria
Email: benfadelkarima@gmail.com - **ORCID:** 0000-0001-8929-5244

[4]Research Center On Semiconductor Technology for Energetic, CMSI-CRTSE, Algiers, Algeria
Email: lamias19@yahoo.fr - **ORCID:** 0000-0002-0398-4557

[5]Research Center On Semiconductor Technology for Energetic, CMSI-CRTSE, Algiers, Algeria
Email: boukezzataassia@crtse.dz - **ORCID:** 0000-0002-6346-166X

[6]Research Center On Semiconductor Technology for Energetic, CMSI-CRTSE, Algiers, Algeria
Email: y.ouadah@gmail.com - **ORCID:** 0000-0002-2869-0790

[7]Sciences Faculty, University Mouloud Mammeri of Tizi Ouzou, LCAGC-UMMTO, Tizi Ouzou, Algeria
Email: allamdjaouida788@gmail.com - **ORCID:** 0000-0002-3430-7735

[8]Research Center On Semiconductor Technology for Energetic, CMSI-CRTSE, Algiers, Algeria
Email: k_samira05@yahoo.fr - **ORCID:** 0000-0001-6697-7015

Abstract:

Zeolite is a crystalline alumino-silicate microporous material, which has been widely used as ion-exchangers, adsorbent and catalyst. Recently, several researches highlights the progress of zeolite-based catalysts in the CO_2 conversion to valuable products. In the present work, hydrothermal synthesis of mordenite zeolite crystals, with composition of the chemical products Al_2O_3, 12.5 SiO_2, 2.4 NaOH, 110 H_2O at 160°C for 96 hours (4 days) at Ph 11 is described. Results of characterization of the mordenite zeolite by XRD, FTIR, EDAX, SEM, TGA, are presented and discussed. In the present work, hydrothermal synthesis and characterization of mordenite zeolite crystals is described.

1. Introduction

Zeolites are used as absorbents and desiccants in gas purification processes, and separation processes such as para xylene from its isomers [1,2]. They are also used as potential catalysts in petroleum production, petrochemicals and refining. Catalytic cracking on Y and ZSM-5 zeolites is by far the largest application followed by catalytic hydrocracking on mordenite zeolites [3-5]. Tons of zeolites are currently on the market as part of detergent formulations. Zeolite A is used exclusively as a phosphate substitute. Other natural zeolites are used in a number of applications such as wastewater

treatment, nuclear effluents and CO_2 conversion [6-8]. The main user countries of zeolites worldwide are the USA, Japan and Western European countries Nowadays, zeolites have an economic impact in some areas, notably in the field of ion exchange reactions, which make zeolites economically attractive as small quantities of zeolites are sufficient to treat large volumes of water. Zeolites have great potential for ecosystem protection, ranging from wastewater and gas treatment to the replacement of undesirable and environmentally damaging polyphosphates [9-14]. The industrial exploitation of zeolites often requires their preparation. They are obtained by hydrothermal crystallisation of

aluminisilicates and active alkali metals at moderate temperatures and pressures.

In the present work, hydrothermal synthesis and characterization of mordenite zeolite crystals is described.

2. Material and Methods

Mordenite zeolite was prepared by hydrothermal crystallisation at 160°C for 96 hours (4 days) at Ph 11, from starting gels of molar composition Al_2O_3, 12.5 SiO_2,2.4 NaOH, 110 H_2O. After the crystallization process the obtained powder was washed with distillate water   and dried at 120°C.

Chemical components of products are SiO_2 :41.6%. Al_2O_3 :77%. The obtained powder was analyzed by powder X ray diffractometer (Philips PW 1800, using Cu Ke radiation), infrared spectroscopy (Philips PU 9800), scanning electron microscope (Philips XL 30) and differential thermal analyzer (M2 BDL SETARAM).

3. Results and Discussions

3.1 XRD analysis

The XRD patterns of as-elaborated samples are given in figure 1. They are in good agreement with jcpds card 0110155. We observe in table 1 the appearance of all peaks related to the presence of mordenite zeolite, confirming the high crystallinity. According to these results, we attest the absence of other phases than mordenite. When we compare between the results found by the XRD and those presented in the jcpds 0110155 card, also shown in Table 1. We certify that there is a very good similarity between the measured parameters and those present in this card.
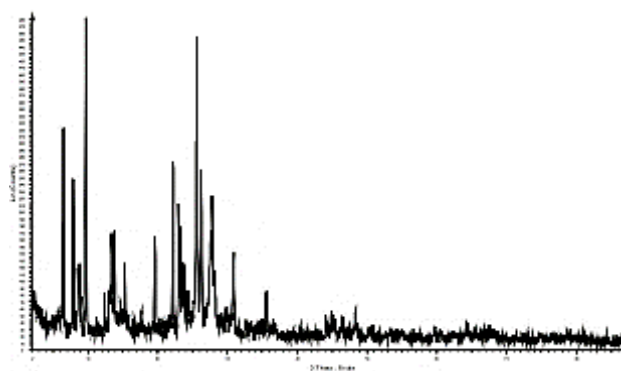

Figure.1 *XRD spectrum of mordenite zeolite*

The table 1 represents the parameters of XRD peaks of mordenite zeolite and its reference parameters.

Table.1 *Parameters of XRD peaks of mordenite zeolite and reference parameters.*

| According to jcpd card0110155			Mordenite powder	
hkl	d(A°)	I(%)	d(A°)	I(%)
110	13.581	100	13.569	88
020	10.265	13.1	10.197	34
200	9.055	56.4	9.089	100
220	6.791	0.3	6.764	1
111	6.584	40.4	6.556	49
130	6.402	29.1	6.367	9
021	6.071	13..3	6.035	5
310	5.791	9.5	5.808	9
040	5.133	0.6	5.098	2
221	5.042	2.3	5.027	2
131	4.877	4.4	4.850	1
311	4.59	3.2	4.589	5
330	4.527	22.7	4.523	16
240	4.465	0.6	4.446	1
041	4.241	1.4	4.214	1
420	4.142	5.7	4.150	1
150	4.004	46.1	3.979	21
331	3.880	1.0	3.871	1
241	3.840	16.9	3.823	9
002	3.764	6.9	3.744	4
421	3.629	4.5	3.630	1
112	3.627	0.3	3.609	1
510	3.567	2.3	3.579	1
151	3.535	0.3	3.514	2
022	3.534	4.3	3.514	2

3.2 FTIR analysis

The investigation by infrared spectroscopy technique in the mid-infrared region of the zeolite spectrum   is useful in this regard since it contains the fundamental vibrations of the framework Al, Si-4 or (T 4) tetrahedral. A different vibration bands are observed in the FTIR absorption spectrum of mordenite zeolite shown in figure 2. The first class of vibrations found at 1223 -1230, 680 -700 and 438-454 cm-' are assigned to the internal tetrahedral. The second group of frequencies observed at 547-546, 446,792-789 and 1084-1102 cm-' are assigned to the linkages between tetrahedral and the topology of the units of structure of samples. The main bands of absorption obtained from Figure 2, are shown in Table 2.

3.3 SEM characterization

The morphology of the crystalline phases was demonstrated by observation with a scanning electron microscope.

Table .2 *The main bands of IR absorption and associated bond vibration of mordenite zeolite*

	Link type	Frequency cm^{1} D.W.Breck	Mordenite
Internal vibrations (tétraèdres TO$_4$)	Asymmetric elongation Si-O-Al. Si-O-Si.	1250-950	1230
	Symmetric elongation Al-O. stretching	720-650	700
	Bending T-O link.	500-420	450
External vibrations	Double cycle 2C$_4$ et 2C$_6$ Si. Al-O.	650-500	550
	Pores openning	420-300	400
	Symmetric elongation Si-O-Al, Si-O-Si.	820-750	800
	Asymmetric elongation Si-O-Al.	1150-1050	1010

Figure.2 *FTIR absorption spectrum of mordenite zeolite*
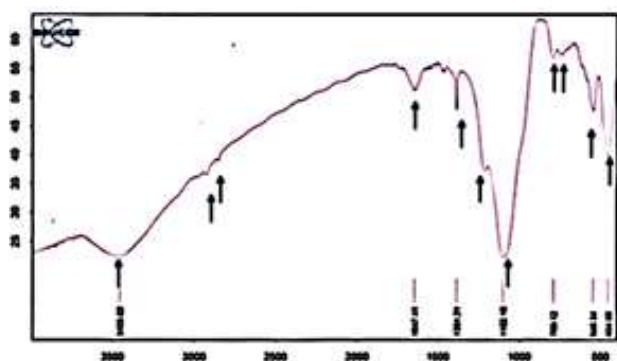
Figure .3 *Scanning electron micrographs of mordenite zeolite*

Figures 3 illustrates the micrographs of these samples. We note that the morphology of the crystals is generally hexagonal prismatic, regular and that the dimensions of mordenite samples are of 10-15 µm respectively. According to the EDS characterization, the chemical composition of the as prepared powder is presented in figure 4. and table 3.

3.4 DTA analysis

According to the DTA analysis shown in figure 5, we observe a succession of endotherms ranging from

Table.3 *Chemical composition of mordenite zeolite*

Element	Weight %	Atomic%
O	50.29	59.79
Na	4.18	3.46
Al	4.58	3.23
Si	34.57	23.42

Figure.4 *EDS analysis of mordenite zeolite*

50 to 250 °C. The differential thermal analysis of the sample allowed us to determine that the departure of the physisorbed water takes place from 100 to about 250 where the dehydration is complete. We noticed the vitreous state of the mordenite sample after characterization which explains the vitreous transformation of this material at a temperature exceeding transformation of this material at a temperature exceeding 1200°C.
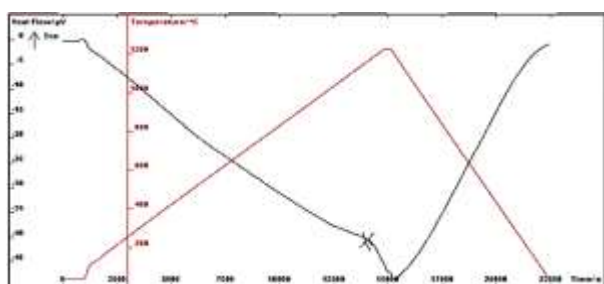

Figure.5 DTA curve of mordenite zeolite

4. Conclusions

In the present work, the pure Mordenite zeolite types are obtained for contact times of 96 hours, at temperatures of 170 C and under autogenous pressure. The skeletal structure of the Mordenite material is very thermally stable. The initial structural change starts to take place from 1100°C onwards and above 1250°C the Mordenite structure vitrifies. The differential thermal diagram proves the stability of this structure.

The infrared spectroscopy technique allowed the characterisation of the absorption bands attributed to the different Si-O-Si, Si-O-Al, Si-O and Al-O bonds linked to the tetrahedra forming the structures of the Mordenite phases. Sites belonging to hydroxyl groups -OH were also revealed by this technique.

With their dual capacity for ion exchange and adsorption, these materials can be used in the very long term in the decontamination of any very dilute waste water.

Author Statements:

References

[1] Eduardo Pérez-Botella, Susana Valencia, and Fernando Rey (2022). Zeolites in Adsorption Processes: State of the Art Future Prospects. *Chemical Reviews* 122(24);17647-17695 doi.:10.1021/acs.chemrev.2c00140

[2] Milad Rasouli, Nakisa Yaghobi, Fatemeh Allahgholipour, Hossein Atashi. (2014). Para-xylene adsorption separation process using nano-zeolite Ba-X, *Chemical Engineering Research and Design* 92(6):1192–1199 doi.:10.1016/j.cherd.2013.10.008

[3] Liu, M. N., Xie, Z. X., Luo, Q. X., Zhang, J., Chen, H., Xu, L. & Hao, Q. Q. (2022). Synthesis of Nanosized Mordenite with Enhanced Catalytic Performance in the Alkylation of Benzene with Benzyl Alcohol. *Industrial & Engineering Chemistry Research,*61(2);1078-*1088.* doi:10.1021/acs.iecr.1c03419

[4] Li, S., van de Poll, R. C., Kosinov, N., & Hensen, E. J. (2022). Facile synthesis of nanosized mordenite and beta zeolites with improved catalytic performance: non-surfactant diquaternary ammonium compounds as structure-directing agents. *Inorganic Chemistry Frontiers.* 2022,**9**, 3200-3216 doi:10.1039/D2QI00696K

[5] Du, T., Cui, M., Chao, Y., Xiao, Y., Ren, Z., An, Y., & Meng, C. (2022). Preparation and photocatalytic properties of highly dispersed samarium vanadate nanoparticles supported on H-mordenite composites by template-free method. *Journal of Photochemistry and Photobiology A: Chemistry*, 433*; 114207.* doi:10.1016/j.jphotochem.2022.114207

[6] Collins, F., Rozhkovskaya, A., Outram, J. G., & Millar, G. J. (2020). A critical review of waste resources, synthesis, and applications for Zeolite LTA. *Microporous and mesoporous Materials*, 291; 109667. https:doi.org/10.1016/j.micromeso.2019.109667

[7] Ghasemi, Z., Sourinejad, I., Kazemian, H., & Rohani, S. (2018). Application of zeolites in aquaculture industry: a review. *Reviews in Aquaculture*, 10(1); 75-95. doi.org/10.1111/raq.12148

[8] Madhu, J., Ramakrishnan, V. M., Santhanam, A., Natarajan, M., Palanisamy, B., Velauthapillai, D and Pugazhendhi, A. (2022). Comparison of three

different structures of zeolites prepared by template-free hydrothermal method and its CO2 adsorption properties. *Environmental Research, 214; 113949.* doi: 10.1016/j.envres.2022.113949

[9] Weckhuysen, B. M., & Yu, J. (2015). Recent advances in zeolite chemistry and catalysis. *Chemical Society Reviews,* 44(20); 7022-7024. doi:10.1039/C5CS90100F

[10] Yoldi, M., Fuentes-Ordoñez, E. G., Korili, S. A., & Gil, A. (2019). Zeolite synthesis from industrial wastes. *Microporous and Mesoporous materials,* 287; 183-191.
doi:10.1016/j.micromeso.2019.06.009

[11] Lin, C. C., Dambrowitz, K. A., & Kuznicki, S. M. (2012). Evolving applications of zeolite molecular sieves. *The Canadian Journal of Chemical Engineering,* 90(2);207-216.
doi: 10.1002/cjce.20667

[12] Moshoeshoe, M., Nadiye-Tabbiruka, M. S., & Obuseng, V. (2017). A review of the chemistry, structure, properties and applications of zeolites. *Am. J.Mater.Sci*,7(5);196-221.
doi:10.5923/j.materials.20170705.12

[13] Houhoune, F., Khemaissia, S., Nibou, D., Chegrouche, S., & Menacer, S. (2018). Kinetic study and sorption mechanism of uranium (VI) onto NaY zeolite. *In AIP Conference Proceedings* (Vol. 1994, No. 1, p. 070008). AIP Publishing LLC.
doi.org/10.1063/1.5048180

[14] Baouali, N. Y., Nibou, D., & Amokrane, S. (2022). NaY Zeolite and TiO2 Impregnated NaY Zeolite for the Adsorption and Photocatalytic Degradation of Methylene Blue under Sunlight. *Iran. J. Chem.Chem. Eng. Volume 41, Issue 6 - Serial Number 116 June 2022,1907-1920*
doi ; 10.30492/IJCCE.2021.128624.4168

Research Article
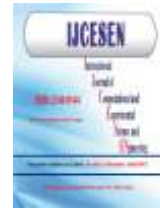
PTGNG: An Evolutionary Approach for Parameter Optimization in the Growing Neural Gas Algorithm

Mohanad ALALKAWI[1], Shadi AL SHEHABI[2]*, Meltem Y. IMAMOGLU[3]

[1]Directorate General of Education in Diyala Govgovernorate, 32001, Diyala-Iraq
Email: mohanadalalkawi@gmail.com - **ORCID:** 0000-0002-1181-3053

[2]University of Turkish Aeronautical Association, Faculty of Engineering, Departmant of Computer Engineering, 06790, Ankara-Turkey
* **Corresponding Author** : **Email:** salshehabi@thk.edu.tr - **ORCID:** 0000-0003-0545-9104

[3]University of Turkish Aeronautical Association, Faculty of Engineering, Departmant of Computer Engineering, 06790, Ankara- Turkey
Email: meltemyi@gmail.com - **ORCID:** 0000-0002-8574-4097

Abstract:

Growing Neural Gas (GNG) algorithm is an unsupervised learning algorithm which belongs to the competitive learning family. Since then, GNG has been a subject to vaious developments and implementations found in the literatures for two main reasons: first, the number of neurons (i.e., nodes) is adaptive. Meaning, it is periodically changed through adding new neurons and removing old neurons accordingly in order to find the best network which captures the topological structure of the given data, and to reduce the overall error in that representation. Second, GNG algorithm has no restrictions when compared to other competitive learning algorithms, as it is both free in the space and the number of the neurons. In this paper, we propose and implement an evolutionary based approach, namely PTGNG, to tune GNG algorithm parameters for dealing with data in multiple dimensional space, namely, 2D, 3D, and 4D. The idea basically relies on finding the optimum set of parameter values for any given problem to be solved using GNG algorithm. The evolutionary algorithm by its nature searches a vast space of applicable solutions and evaluates each solution individually. When we implemented our approach of parameters tuning, we can note that GNG captured datasets topological structure with a smaller number of neurons and with a better accuracy. It also showed that the same results appeared when working on datasets with three and four dimensions.

1. Introduction

The Growing Neural Gas (GNG) is an unsupervised learning neural network algorithm which was proposed by Bernd Fritzke [1]. It is one of the competitive learning algorithms such that their common aim is to represent any data distribution in multidimensional space using lower number of neurons (nodes) [2]. GNG is a popularization from the Growing Cell Structure (GCS) [3], and it is based on the Neural Gas (NG) algorithm [4].

There are two alternatives of GNG algorithm. The first one, Robust Growing Neural Gas algorithm (RGNG) which was proposed in 2004 to make the GNG algorithm more robust than the original algorithm by adding parameters to enhance the GNG algorithm and the optimal numbers of nodes

(neurons) is determined dynamically during the execution time [5]. The second one, Merge Growing Neural Gas (MGNG) algorithm was proposed in 2009 and it is a combination between Merge Neural Gas (MNG) algorithm and GNG algorithm [6]. The above mentioned algorithms are based and derived from self-organizing map algorithm (SOM) which is an unsupervised algorithm that is able to represent high dimensional data in a fixed network dimensionality namely, two-dimensional grid [7]. The NG algorithm was proposed to find the best data representation that based on the feature vectors. The NG algorithm is able to represent data in any dimension such that the reference vectors (neurons) are adapted without any fixed topology and there are two variants of the NG algorithm. First one, Enhance Neural Gas Algorithm (ENG) was proposed in 2005

to make the NG algorithm more stable than the previous algorithm by sorting the position and inputs of NG algorithm parameters [8]. The second one, Merge Neural Gas Algorithm (MNG) is comparable to NG algorithm, but it is work by three steps (initialization, sampling and matching and the last one is adoption), In the MNG algorithm they merge second and third steps of the ENG algorithm in one step [9].

The main advantage of GNG as compared to the other competitive learning algorithms is that the number of neurons increases periodically according to the distribution of the input data. The mechanism of changing the number of neurons during the learning process overcomes the problem of finding an appropriate number of neurons generated for reducing the error in the data representations.

Unfortunately, GNG algorithm, is like the other competitive algorithms, such that it has a lot of parameters that should be set correctly at the beginning of the learning process. Setting these parameters for a given data distribution is usually done experimentally [10]. Inappropriate tuning of these parameters may lead to represent poorly the data and also may stuck in deleting and adding neurons during the learning process [11]. The result provided by GNG gives more appropriate representation of 2 dimensional data than SOM and NG due to the original tuning of GNG parameters for representing two dimensional data [2]

The tuning of GNG parameters is usually done experimentally for each given data distribution. Therefore, tuning GNG parameters is time consuming. However, several parameter tuning algorithms such as, Evolutionary Algorithm (EA) [12], Relevance Estimation and Value Calibration of Parameter (REVAC) [13], F-Race [14] and Design of Experiments (DoE) [15] can be used for optimizing GNG parameters. The idea of REVAC is to find an optimal vector of parameters by estimation the distribution of promising values on the domain of each parameter and creation vectors based on values from this distribution. In F-Race algorithm, combinations of predefined parameter are examined, and the ones that perform poorly are discarded as soon as any relevance emerges. Design of Experiments (DoE) tries to reduce the number of required experiments for an analysis, while reserving high quality results. Experiments are considered to have input variables and output variables. It aims to optimize the input variables by comparing and evaluating the quality of the output variables. Genetic algorithms are evolutionary algorithms (EA) that optimize functions by modeling biological processes, they are known to be very effective methods to solve combinatorial optimization problems [16]. In [17] it shows that GA is more

consistent than REVAC and F-Race, it shows also that GA is much faster than DoE and gives better solution quality. Therefore, we propose and implement an evolutionary based approach, namely PTGNG, to tune the GNG parameters for dealing with data described in multiple dimensional space.

2. Literature Review

2.1 Growing Neural Gas (GNG)

This model was proposed in 1995 by Fritzke [1] as an unsupervised learning model. GNG also belongs to the competitive learning family and it is a popularization of the GCS algorithm and based on the NG algorithm. What make this algorithm special from the other models is that its number of neurons changes periodically according to the need of these node for representing the data distribution. Unfortunately, this model works well when two dimensional data is present but it doesn't work properly if multidimensional data is present. This is done because of the inappropriate tuning of the parameters for data described in more than two dimensions [11].

GNG algorithm behaviour is controlled by six main parameters, the maximum connection age (AGEMAX), Cycle interval between nodes insertions (λ), Error reduction factor upon insertion (α), Wining node adaption factor (ε_b), Wining node neighbour adaption factor (ε_n) and the Error reduction factor for each cycle (β) [2]. These parameters must be carefully tuned if an accurate result is required either by applying prior knowledge about the nature of the presented problem to be solved or by setting them empirically. However, tuning these parameters based on the nature of one particular problem doesn't necessarily ensure the optimum results. Also, the empirical tuning of these parameters values for each case can be both extensive and time consuming [10].

2.2 Related Studies

In [18], Ventocilla, Elio, et al. suggested two methods for improving GNG in order to visualize the cluster patterns in large-scale and high-dimensional datasets. The first is to provide more precise and relevant 2D visual representations of cluster patterns in high-dimensional datasets, by avoiding connections that generate high-dimensional graphs that result in overplotting and clutter. The second one reduces the execution times of the learning phase by modeling and merging seperate parts of a big dataset.

In [19], Mendes, Carlos Augusto Teixeira, et al. suggested a new algorithm called the Fast Growing

Neural Gas (FGNG) algorithm such that some modifications were done on some steps in the GNG algorithm. They proposed the adoption of a set of techniques and suitable data structures to reduce the time complexity order, without changing the original GNG semantics. R-tree technique, which is a tree data structures, is used for spatial access methods. The experiment was done on 2, 4, 6 and 8. The result of applying the FGNG and GNG on 8 dimension was not good; so, they tested the proposed method for 2 dimensional data and that what the results of this paper approve it. The aims of this paper is to enhance the time execution of GNG algorithm for 2 dimensional data.

In [20], Fišer, Daniel, et al. suggested two techniques for optimizing GNG; the first one is done to enhance the nearest neighbour search and the second one is done to handle node errors for accelerating the GNG algorithm. However, these two optimization techniques focus only on the efficient execution of the GNG algorithm. They focus on the internal structure of the GNG algorithm instead of modifying the original GNG algorithm. The suggested techniques keep all characteristics of GNG algorithm and make it appropriate to be used on a huge problem.

In [21], García-Rodríguez, José, et al. suggested a fast autonomous growing neural gas (FAGNG) algorithm by modifying the original GNG algorithm. The aim of FAGNG algorithm is to accelerate the GNG algorithm for supporting application of time constraint.

In [22], Guillermo S, et al. suggested to use the evolutionary algorithms (EA) to optimize the parameters of the GNG algorithm when the GNG algorithm deals with 2D image recognition problem.

3. Methodology

3.1. Evolutionary Algorithms

Evolutionary or Genetic Algorithms are a class of optimization algorithms which are based on the principles of Darwinian evolution. Such algorithms are capable of improving/optimizing the solution of a certain problems for which a fitness value can be defined. When several populations are generated which comprised of several individuals (i.e. several possible solutions), the fitness value for each individual (i.e. solution) indicates the suitability of that solution to the subset problem, hence, influences its survival to the next generations. For our implementation of Genetic Algorithm, we used GALIB [23], a C++ based Genetic Algorithm library. GALIB was developed by MIT and it contains a wide range of different types of genomes,

configurable genetic operators such as crossover, mutation, selection algorithms, and several terminations conditions.
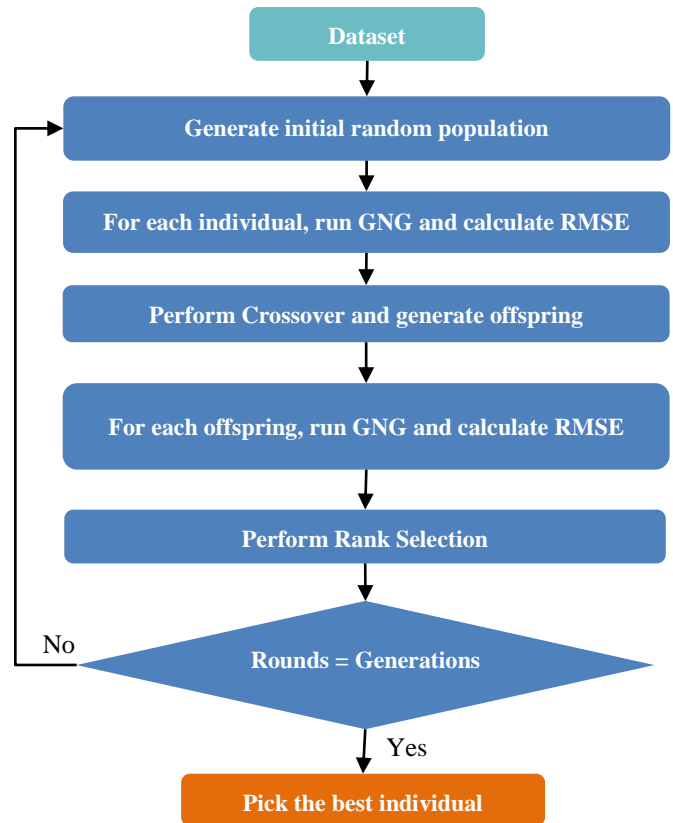

Figure 1. The flowchart of proposed method PTGNG

The premise of using the Genetic Algorithm in this study is to tune the parameters of GNG algorithm for making it enable to work properly on multiple dimensions (i.e. 2D, 3D, and 4D). However, GNG algorithm by default uses six main parameters which are:

1. LAMBDA: represents the steps between nodes creation
2. EPSILON_B: defines the adaptation factor for the winning node
3. EPSILON_N: defines the adaptation factor for neighbours of the winning node
4. AGEMAX: sets the maximum age for edges
5. ALPHA: error decrements factor after node insertion
6. BETA: defines the aging factor for nodes

These parameters must be carefully tuned from its default values if an accurate result is required either by applying prior knowledge about the nature of the presented problem to be solved, or by setting them empirically. However, tuning these parameters based on the nature of one particular problem doesn't necessarily ensure the optimum results. Also, the empirical tuning of these parameters values

for each problem can be both extensive and time consuming.

The use of evolutionary optimization algorithm will ensure that these parameters are optimally tuned for any given problem, since it continuously searches and optimizes a vast space of applicable solutions until it reaches to one final good solution. Second, it requires no prior knowledge about the problem itself, therefore it is field or problem independent

3.2 Implementation of the Evolutionary Algorithm for Parameter Optimization

Our proposed PTGNG algorithm is summarized in Fig. 1 such that the evolution cycle starts through randomly generating the values (i.e. genes) for each individual, the random generation function takes two inputs, a minimum value and a maximum value for each individual parameter.

Table 1 describes the minimum and maximum value of each GNG parameter [1,24,25].

Table 1. The minimum and maximum values of GNG parameters

Parameter Name	Default value	Min	Max
LAMBDA	30	20	70
EPSILON_B	0.0500	0.0010	1
EPSILON_N	0.0006	0.0001	1
AGEMAX	88	1	1000
ALPHA	0.5000	0	1
BETA	0.0005	0	1.0

Then, for each individual which is an array of real numbers (i.e. chromosome composed of six genes, one gene per-parameter), GNG is tested and the fitness value for that particular chromosome is evaluated and returned.

In this paper Root Mean Square Error (RMSE) is used as a fitness function to evaluate each chromosome/solution. The equation of the RMSE showing below:

$$RMSE = \sqrt{\frac{sum\ of\ squared\ error}{number\ of\ points}} \qquad (1)$$

The returned values are encoded in each chromosome and used later by the Genetic Algorithm, the fitness value represents the base by which individuals are selected/survive onto the next generation. Then, the Genetic Algorithm performs crossover operation and evaluate the offspring using the same procedure described above, and then the best of these offspring are picked using the defined selector for the next round of evolution. Special consideration must be given on how and why the

stop condition of the evolutionary algorithm is defined. Two ways can be used as stop conditions:

- By defining a network error threshold (i.e. the minimum fitness value).
- By defining the number of generations the evolutionary algorithm performs.

In our implementation, the second way is used because of three reasons; the first reason is that its simplicity as compare to the first way where network error threshold is hard to be determined, the second reason is that the execution time is lower, the third reason is that, through our experiments on the tested datasets we found that our proposed method doesn't give better solutions after 50 generations.

Fig. 2 – 13 show the results of applying our proposed method to the different datasets described in 2D, 3D and 4D with a different number of generations and populations. Fig. 2 and 3 illustrate the progress of the genetic algorithm in optimizing parameters for the results obtained from applying the Sphere 2D problem. They demonstrate the decreasing RMSE from an initial value of 4.01 at generation 25, reaching stability at 3.99 beyond generations 35 and 45, respectively. Furthermore, Fig. 4 reveals that with a population size of 20, the algorithm rapidly converged to a consistent and optimal solution early on, leading to no significant improvements in subsequent generations. Similarly, Fig. 5-13 consistently demonstrate the genetic algorithm's effective optimization for the results obtained from applying the Tours 2D, Shapes 3D, and Rings 4D problems, with decreasing RMSE values followed by stable performance.
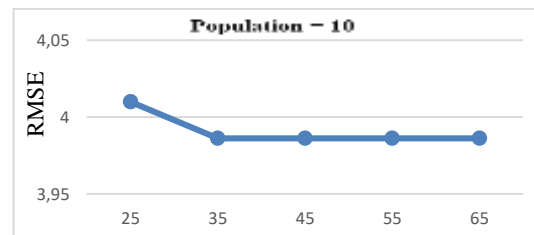
Figure 2. The results of applying Sphere 2D data with a different number of generations with population=10
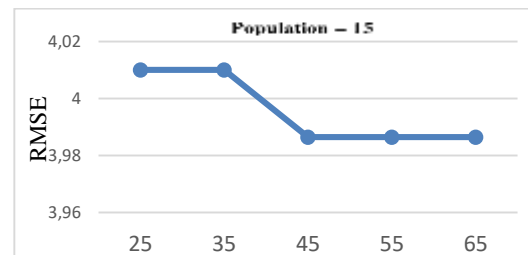
Figure 3. The results of applying Sphere 2D data with a different number of generations with population=15
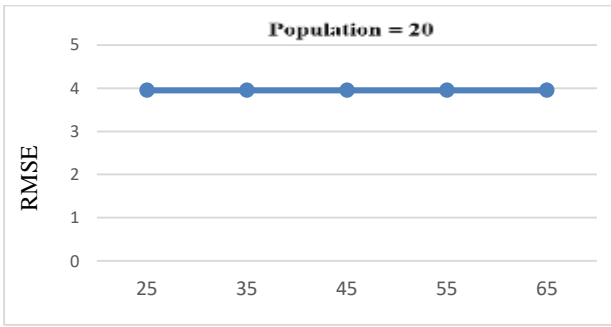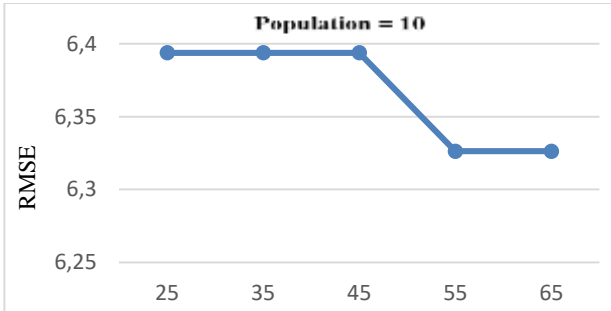
Figure 4. *The results of applying Sphere 2D data with a different number of generations with population= 20*

Figure 5. *The results of applying Tours 2D data with a different number of generations with population=10*
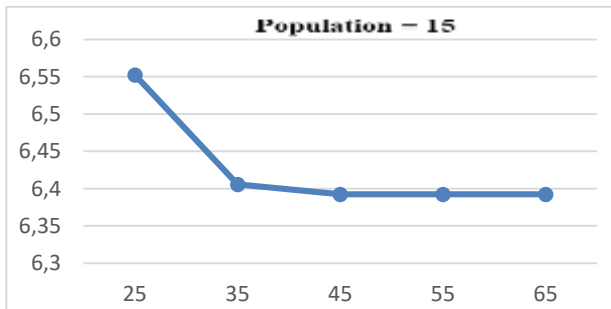

Figure 6. *The results of applying Tours 2D data with a different number of generations with population= 15*

Figure 7. *The results of applying Tours 2D data with a different number of generations with population= 20*

Figure 8. *The results of applying Shapes 3D data with a different number of generations with population= 10*
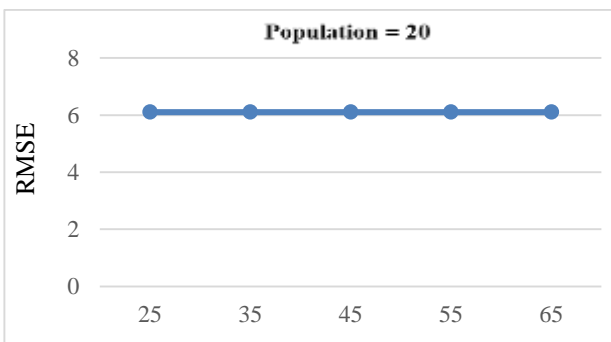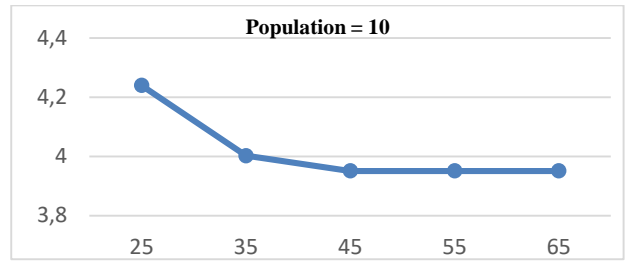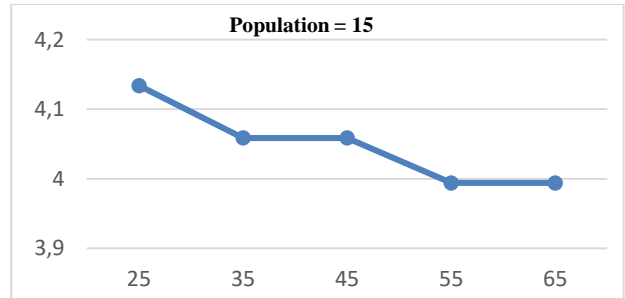

Figure 9. *The results of applying Shapes 3D data with a different number of generations with population= 15*
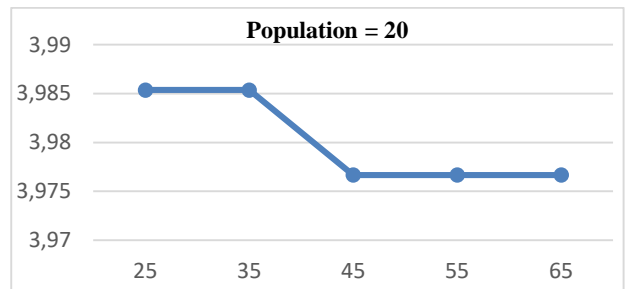

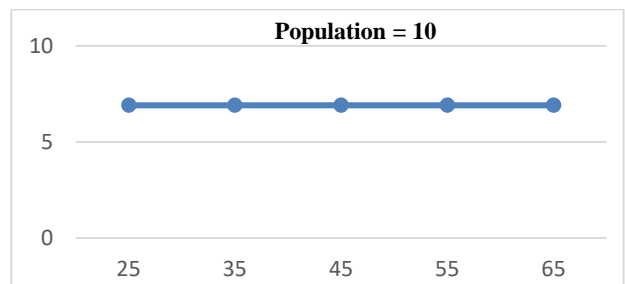***Figure 10.*** *The results of applying Shapes 3D data with a different number of generations with population= 20*

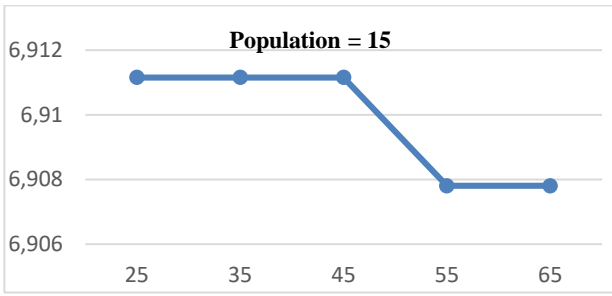***Figure 11.*** *The results of applying Four rings 4D data with a different number of generations with population= 10*

Population = 15

Figure 12. The results of applying Four rings 4D data with a different number of generations with population= 15
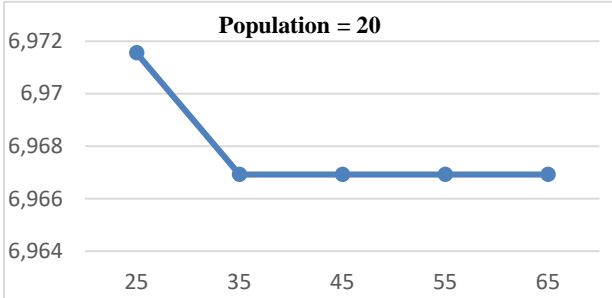

Population = 20

Figure 13. The results of applying Four rings 4D data with a different number of generations with population= 20

4. Experimental Study and Discussions

To test the proposed method, we used the following four datasets, four concentric rings, different shapes (rectangle, line, circle and triangle), circle, and a torus, each of which contains 350 points. Each dataset has been drawing by using Excel 2016 as shown in Fig. 14. The other 3D and 4D shapes are also generated randomly using Excel 2016.

From our preliminary test of GNG algorithm on the aforementioned datasets, we found several cases were GNG algorithm goes into an infinite run. In that – for example – when we set the desired number of neurons to be 80 on a dataset of 65 points, GNG algorithm runs infinitely after it reaches a certain number of connected neurons. Such situation is better explained as "when GNG adds new neurons, at the same exact time another neuron in the network is expired", in other words, that specific neuron age passed AGEMAX value. Following on the same dataset, Table 2 presents the desired number of neurons and the correct value of which AGEMAX must be set to. Table 2 shows that for each number of desired neurons, it needs at least AGEMAX value, otherwise the GNG algorithm will not give an appropriate results and it may not stop From the presented values, a linear relationship between the number of desired neurons and AGEMAX value is found and a linear regression line (Fig. 15) has the following equation:
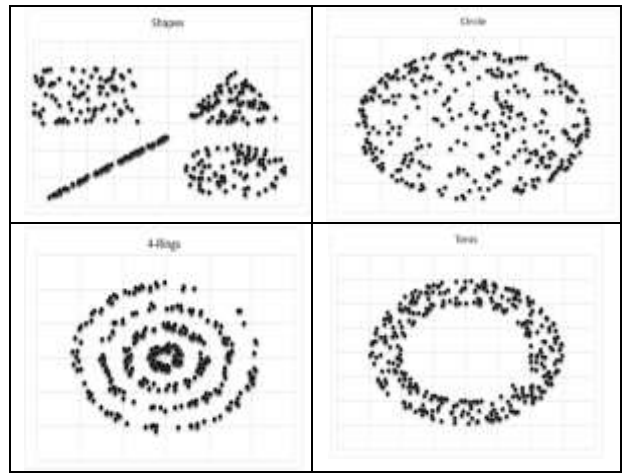
Figure 14. The four datasets: Shapes, Circle, 4-Rings and Torus

Table 2. The desired number of neurons and the correct value of which AGEMAX must be set to.

Number of Desired Neurons (x)	Correct *AGEMAX* Value (y)
30	>=60
40	>=80
50	>=120
60	>=140
70	>=160
80	>=180
90	>=220
100	>=240
110	>=270

$$AGEM = 2.6000\ Number\_of\_desired\_neurons - 18.667 \tag{2}$$
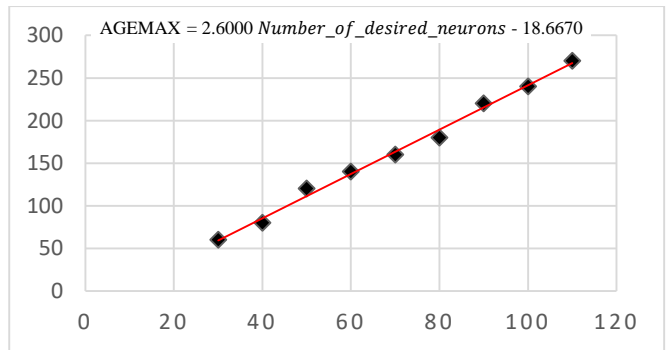
Figure 15. Liner relationship trend-line between number of desired neurons and AGEMAX values

With such relation exists between the two variables, we excluded the *AGEMAX* from the evolutionary cycle and the chromosome length changed from seven to six genes only. However, *AGEMAX* is still passed on to GNG algorithm since it is still a requirement, but as a variable derived from the number of desired neurons according to the linear equation. The previous algorithm work with seven

parameters (number of desired neurons, E_b, E_n, AGEMAX. In the proposed method PTGNG by depending on the linear relationship between the AGEMAX and number of desired neurons, we excluded AGEMAX from the set of parameters. Fig. 16 shows the new chromosome after excluding AGEMAX.

# neurons	E_b	E_n	AGEMAX	λ	α	B

(a)

# neurons	E_b	E_n	λ	α	B

(b)
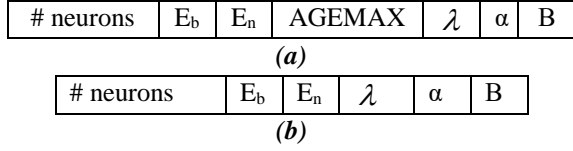
Figure 16. *(a) previous chromosome, (b) new chromosome after applying linear relationship*

For identifying the clustering method with better results, Purity is also used to evaluate the quality of resulting clusters for each of the datasets [26]. It measures how much the cluster has the data of a class (or a cluster in an optimal model). A perfect clustering solution will be the one that leads to clusters that contain data from only a single class (or cluster in an optimal model). The larger the values of Purity, the better the clustering solution is. Purity is defined as:

$$Purity = \frac{1}{n}\sum_i max_j(n_{ij})$$

(3)

Where n is the number of elements in the dataset, n_{ij} represents the number of elements of class j (or a cluster j in an optimal model) in cluster i.

In our experiment, the clusters of an optimal model (or class) can be found by generating several clustering models with different number of clusters using K-means algorithm then the extended contrast index (EC) measure is used to evaluate and select the optimal model [27].

Tables 3, 4, 5, 6, 7 and 8 show the accuracy results, using RMSE and Purity, obtained by applying GNG algorithm to each dataset with number of desired neurons being set to 350, and the proposed method PTGNG along with an optimal number of desired neurons, and the optimized parameters for 2D, 3D and 4D data.

Table 3. *2D datasets: **(a)** RMSE, **(b)** Purity, **(c)** default and optimized parameter values for each dataset.*

Dataset	GNG	PTGNG
Shapes	5.7640	4.0537
Circle	6.2694	3.9415
Four Concerentic Rings	9.0498	7.1466
Tours	6.8910	6.4171

(a)

Dataset	GNG	PTGNG
Shapes	0.9029	0.9686
Circle	0.6057	0.6571
Four Concerentic Rings	0.5971	0.5857
Tours	0.6314	0.6743

(b)

Dataset	Default parameters	PTGNG Optimized Parameters
Shapes	# neurons:350 Eb: 0.05 En: 0.0006 Age: 895 Lambda: 30 Alpha: 0.5 Beta: 0.0005	# neurons:55 Eb: 0.3457 En: 0.5138 Age: 207 Lambda: 21 Alpha: 0.5353 Beta: 0.2355
Circle	# neurons:350 Eb: 0.05 En: 0.0006 Age: 895 Lambda: 30 Alpha: 0.5 Beta: 0.0005	# neurons:185 Eb: 0.8106 En: 0.2485 Age: 463 Lambda: 28 Alpha: 0.0010 Beta: 0.0640
Four concentric Rings	# neurons:350 Eb: 0.05 En: 0.0006 Age: 895 Lambda: 30 Alpha: 0.5 Beta: 0.0005	# neurons: 227 Eb: 0.7099 En: 0.6092 Age: 573 Lambda: 31 Alpha: 0.0010 Beta: 0.4956
Torus	# neurons:350 Eb: 0.05 En: 0.0006 Age: 895 Lambda: 30 Alpha: 0.5 Beta: 0.0005	# neurons: 236 Eb: 0.6987 En: 0.9368 Age: 595 Lambda: 44 Alpha: 0.8468 Beta: 0.2939

(c)

Table 4. *3D datasets: **(a)** RMSE, **(b)** Purity, **(c)** default and optimized parameter values for each dataset.*

Dataset	GNG	PTGNG
Shapes	4.0695	4.0440
Circle	7.0349	6.5702
Four Concerentic Rings	8.6143	7.1652
Tours	7.7065	6.1692

(a)

Dataset	GNG	PTGNG
Shapes3D	0.8657	0.9886
Circle	0.8114	0.8286
Four Concerentic Rings	0.5914	0.6314
Tours	0.5143	0.7200

(b)

Dataset	Default parameters	PTGNG Optimized Parameters
Shapes	# neurons:350 Eb: 0.05 En: 0.0006 Age: 895 Lambda: 30 Alpha: 0.5 Beta: 0.0005	# neurons: 181 Eb: 0.7842 En: 0.6258 Age: 450 Lambda: 58 Alpha:0.1158 Beta: 0.4250

Circle	# neurons:350 Eb: 0.05 En: 0.0006 Age: 895 Lambda: 30 Alpha: 0.5 Beta: 0.0005	# neurons: 77 Eb: 0.4316 En: 0.7367 Age: 182 Lambda: 35 Alpha:0.2123 Beta: 0.6312
Four concentric Rings	# neurons:350 Eb: 0.05 En: 0.0006 Age: 895 Lambda: 30 Alpha: 0.5 Beta: 0.0005	# neurons: 266 Eb: 1 En: 0.0901 Age: 674 Lambda: 40 Alpha: 0.6034 Beta: 0.3895
Torus	# neurons:350 Eb: 0.05 En: 0.0006 Age: 895 Lambda: 30 Alpha: 0.5 Beta: 0.0005	# neurons: 37 Eb: 0.0774 En: 0.5617 Age: 79 Lambda: 43 Alpha: 0.6440 Beta: 0.1357

(c)

Table 5. *4D datasets: (**a**) RMSE, (**b**) Purity, (**c**) default and optimized parameters for each dataset.*

Dataset	GNG	PTGNG
Shapes	5.8721	4.0477
Circle	7.1254	6.7734
Four Concerentic Rings	8.7718	6.6763
Tours	6.5536	5.7802

(a)

Dataset	GNG	PTGNG
Shapes4D	0.9114	0.8771
Circle	0.6114	0.7143
Four Concerentic Rings	0.6771	0.7829
Tours	0.5571	0.8800

(b)

Dataset	Default parameters	PTGNG Optimized Parameters
Shapes	# neurons:350 Eb: 0.05 En: 0.0006 Age: 895 Lambda: 30 Alpha: 0.5 Beta: 0.0005	# neurons: 347 Eb: 0.9439 En: 0.2040 Age: 884 Lambda: 27 Alpha:0.1342 Beta: 0.4871
Hyper sphere	# neurons:350 Eb: 0.05 En: 0.0006 Age: 895 Lambda: 30 Alpha: 0.5 Beta: 0.0005	# neurons: 118 Eb: 1.0000 En: 0.0969 Age: 289 Lambda: 42 Alpha:0.8717 Beta: 0.5854
Four concentric Rings	# neurons:350 Eb: 0.05 En: 0.0006 Age: 895 Lambda: 30 Alpha: 0.5 Beta: 0.0005	# neurons: 52 Eb: 0.9712 En: 0.6639 Age: 119 Lambda: 58 Alpha: 0.4892 Beta: 0.3840

Torus	# neurons:350 Eb: 0.05 En: 0.0006 Age: 895 Lambda: 30 Alpha: 0.5 Beta: 0.0005	# neurons: 16 Eb: 0.3073 En: 0.6819 Age: 25 Lambda: 38 Alpha: 0.2028 Beta: 0.2297

(c)

Table 6. *2D datasets: (**a**) RMSE with Flip mutation, (**b**) Purity, (**c**) default and optimized parameters for each dataset with Flip mutation.*

Dataset	GNG	PTGNG with Flip mutation
Shapes	5.7640	3.8443
Circle	6.2694	3.9762
Four Concerentic Rings	9.0498	7.1631
Tours	6.8910	6.4171

(a)

Dataset	GNG	PTGNG with Flip mutation
Shapes	0.9029	0.9057
Circle	0.6057	0.7486
Four Concerentic Rings	0.5971	0.6429
Tours	0.6314	0.6629

(b)

Dataset	Default parameters	PTGNG Optimized Parameters with Flip mutation
Shapes	# neurons:350 Eb: 0.05 En: 0.0006 Age: 895 Lambda: 30 Alpha: 0.5 Beta: 0.0005	# neurons: 122 Eb: 0.8080 En: 0.7589 Age: 298.3333 Lambda: 40 Alpha:0.9712 Beta: 0.0707
Hyper sphere	# neurons:350 Eb: 0.05 En: 0.0006 Age: 895 Lambda: 30 Alpha: 0.5 Beta: 0.0005	# neurons: 110 Eb: 0.4456 En: 0.3734 Age: 296.3333 Lambda: 53 Alpha:0.9609 Beta: 0.1804
Four concentric Rings	# neurons:350 Eb: 0.05 En: 0.0006 Age: 895 Lambda: 30 Alpha: 0.5 Beta: 0.0005	# neurons: 157 Eb: 0.7257 En: 0.6800 Age: 389.3333 Lambda: 20 Alpha:0.4945 Beta: 0.7722
Torus	# neurons:350 Eb: 0.05 En: 0.0006 Age: 895 Lambda: 30 Alpha: 0.5 Beta: 0.0005	# neurons: 295 Eb: 0.5796 En: 0.3734 Age: 748.3333 Lambda: 21 Alpha: 0.9609 Beta: 0.1804

(c)

Table 7. *3D datasets: (**a**) RMSE with Flip mutation, (**b**) Purity, (**c**) default and optimized parameters for each dataset with Flip mutation.*

Dataset	GNG	PTGNG with Flip mutation

Shapes	4.0695	3.8967
Circle	7.0349	6.0591
Four Concerentic Rings	8.6143	5.6651
Tours	7.7065	6.3903

(a)

Dataset	GNG	PTGNG with Flip mutation
Shapes	0.8657	0.9000
Circle	0.8114	0.8714
Four Concerentic Rings	0.5914	0.7314
Tours	0.5143	0.6086

(b)

Dataset	Default parameters	PTGNG Optimized Parameters with Flip mutation
Shapes	# neurons:350 Eb: 0.05 En: 0.0006 Age: 895 Lambda: 30 Alpha: 0.5 Beta: 0.0005	# neurons: 254 Eb: 0.7355 En: 0.9438 Age: 642.3333 Lambda: 60 Alpha:0.0561 Beta: 0.3773
Hyper sphere	# neurons:350 Eb: 0.05 En: 0.0006 Age: 895 Lambda: 30 Alpha: 0.5 Beta: 0.0005	# neurons: 26 Eb: 0.4284 En: 0.7529 Age: 51.3333 Lambda: 21 Alpha:0.0561 Beta: 0.0707
Four concentric Rings	# neurons:350 Eb: 0.05 En: 0.0006 Age: 895 Lambda: 30 Alpha: 0.5 Beta: 0.0005	# neurons: 26 Eb: 0.5796 En: 0.8279 Age: 51.3333 Lambda: 36 Alpha:0.0742 Beta: 0.0398
Torus	# neurons:350 Eb: 0.05 En: 0.0006 Age: 895 Lambda: 30 Alpha: 0.5 Beta: 0.0005	# neurons: 215 Eb: 0.0979 En: 0.7529 Age: 540.3333 Lambda: 40 Alpha: 0.9712 Beta: 0.7067

(c)

Table 8. *4D datasets: (a) RMSE with Flip mutation, (b) Purity, (c) default and optimized parameters for each dataset with Flip mutation.*

Dataset	GNG	PTGNG with Flip mutation
Shapes	5.8721	3.9361
Circle	7.1254	6.7735
Four Concerentic Rings	8.7718	6.6763
Tours	6.5536	5.7802

(a)

Dataset	GNG	PTGNG with Flip mutation
Shapes	0.9114	0.8943
Circle	0.6114	0.8343
Four Concerentic Rings	0.6771	0.7829
Tours	0.5571	0.8400

(b)

Dataset	Default parameters	PTGNG Optimized Parameters with Flip mutation
Shapes	# neurons:350 Eb: 0.05 En: 0.0006 Age: 895 Lambda: 30 Alpha: 0.5 Beta: 0.0005	# neurons: 260 Eb: 0.2923 En: 0.7529 Age: 657.3333 Lambda: 40 Alpha: 0.3719 Beta: 0.2988
Hyper sphere	# neurons:350 Eb: 0.05 En: 0.0006 Age: 895 Lambda: 30 Alpha: 0.5 Beta: 0.0005	# neurons: 118 Eb: 1.0000 En: 0.0969 Age: 289 Lambda: 42 Alpha: 0.8717 Beta: 0.5854
Four concentric Rings	# neurons:350 Eb: 0.05 En: 0.0006 Age: 895 Lambda: 30 Alpha: 0.5 Beta: 0.0005	# neurons: 52 Eb: 0.9713 En: 0.6639 Age: 119 Lambda: 58 Alpha:0.4892 Beta: 0.3840
Torus	# neurons:350 Eb: 0.05 En: 0.0006 Age: 895 Lambda: 30 Alpha: 0.5 Beta: 0.0005	# neurons: 16 Eb: 0.3073 En: 0.6819 Age: 26 Lambda: 38 Alpha: 0.2028 Beta: 0.2297

(c)

Each chromosome in PTGNG consists of six genes, and each gene's value is represented by a real value. Using real genome in Genetic Algorithms only permits the use of two mutation types, Flip Mutation and Swap Mutation. The first type randomly picks two genes and flip all 0's to 1's, and vice versa. This type of mutation is usually used in the binary application or encoding. The second type, however, swaps the values of the two randomly selected genes. To perform the swap mutation, two alleles are chosen randomly and exchange their locations. Testing Swap Mutation failed to produce any results due to the reason that swapping genes caused the assignments of gene to a value which beyond the predefined Min and Max value for that particular gene (i.e. parameter), hence, GNG failed to build the topological network. However, testing Flip Mutation showed noticeable improvements when compared to previous results. Tables 6, 7 and 8 summarize the obtained results after applying the Flip mutation on the different datasets 2D, 3D and 4D.

5. Results

From the results we obtained from testing the proposed approach, and from comparing the

proposed method to what we found in the literatures, we can conclude the following findings:

- From the approach proposed in [22], we found that the suggested method in this research article covers the optimization of GNG algorithm for multiple dimensions if compared to only two dimensional data. Second, our approach can work on any dataset described in multiple dimensions.

- The execution time for all experiments were between 10s and 2m. However, two of 3D datasets took more than 3m.

- During testing the proposed approach on the aforementioned datasets, we found quite often that there are no better results can be achieved after fifty generations.

- When using two-point crossover approach instead of one point, we only observed few cases of improvements. Also the same occurred when changing the crossover ratio value. Also, using Flip Mutation combined with Single Point crossover showed a noticeable improvement in solution accuracy, but with a huge increase of execution time. We observed a minimum of ~10m and a maximum of ~35m compared to ~15s to 1m.

- From the proposed approach, namely FGNG, presented in 2014 [19], the researchers were interested in optimizing GNG execution time compared to other four published approaches. Our proposed approach in this paper demonstrates relatively fast execution time but still slower when compared to the FGNG. However, reducing the number of generations and populations in the propose method can guarantee a good execution time, but it will be on the cost of producing less optimized results which is beyond the scope of this paper.

- We found a linear relationship between the number of desired neurons and *AGEMAX* parameters. We used such relationship to derive the value of *AGEMAX* from the number of desired neurons, hence, excluding *AGEMAX* from evolution cycle can reduce the occurrence of GNG local optima problem. In our implementation, it was reduced to 10 and sometimes to 16 for every complete evolution cycle.

6. Conclusions

The GNG algorithm is an unsupervised learning algorithm which belongs to the competitive learning algorithms. It was proposed in 1995 by Fritzke as unsupervised learning model and it is a popularization of the GCS algorithm and based on the NG algorithm. What makes such algorithm special from other learning models is that nodes (neurons) are periodically change (adding and removing) according to the need of presented data and to reduce the overall representation error. GNG algorithm has no restrictions if compared to SOM model.

In this paper we proposed and implemented an evolutionary based approach, namely PTGNG, to improve the performance of GNG algorithm by tuning its parameters when it works in multiple dimensional space. Root Mean Square Error (RMSE) is used as a fitness function to evaluate each chromosome/solution. The returned values are encoded in each chromosome and used later by the Genetic Algorithm, the fitness value represents the base by which individuals are selected/survive onto the next generation. At that time, the Genetic Algorithm performs crossover operation and evaluate the offspring using the same procedure described above, and then the best of these offspring are picked using the defined selector for the next round of evolution. Special consideration must be given on how and why the stop condition of the evolutionary algorithm is defined. The idea basically relies on finding the optimum set of parameter values for any given problem to be solved using GNG algorithm. The evolutionary algorithm by its nature searches a vast space of applicable solutions and evaluate each solution individually. The results showed that, after applying our proposed algorithm by tuning the set of GNG parameter values, GNG can represent and capture the structure of data described in multiple dimensional space with a small number of neurons and with a better accuracy.

Author Statements:

References

[1] Fritzke, B. (1994). A growing neural gas network learns topologies. *Advances in neural information processing systems*, 7.

[2] Fritzke, B. (1997). Some competitive learning methods. *Artificial Intelligence Institute, Dresden University of Technology*, 100.

[3] Fritzke, B. (1994). Growing cell structures—a self-organizing network for unsupervised and supervised learning. *Neural networks*, 7(9), 1441-1460. DOI:10.1016/0893-6080(94)90091-4

[4] Martinetz, T. and Schulten, K. (1991), "A" neural-gas" network learns topologies," *Artif. Neural Networks*, pp. 397–402.

[5] Qin, A. K., & Suganthan, P. N. (2004). Robust growing neural gas algorithm with application in cluster analysis. *Neural networks*, 17(8-9), 1135-1148. DOI:10.1016/s0893-6080(04)00166-2

[6] Andreakis, A., Hoyningen-Huene, N. V., & Beetz, M. (2009). Incremental unsupervised time series analysis using merge growing neural gas. In *Advances in Self-Organizing Maps: 7th International Workshop, WSOM 2009, St. Augustine, FL, USA, June 8-10, 2009. Proceedings 7* (pp. 10-18). Springer Berlin Heidelberg. DOI:10.1007/978-3-642-02397-2_2

[7] Kohonen, T. (1997, June). Exploration of very large databases by self-organizing maps. In *Proceedings of international conference on neural networks (icnn'97)* (Vol. 1, pp. PL1-PL6). IEEE. DOI:10.1109/icnn.1997.611622

[8] Qin, A. K., & Suganthan, P. N. (2005). Enhanced neural gas network for prototype-based clustering. *Pattern recognition*, 38(8), 1275-1288. DOI:10.1016/j.patcog.2004.12.007

[9] Strickert, M., & Hammer, B. (2005). Merge SOM for temporal data. *Neurocomputing*, 64, 39-71. DOI:10.1016/j.neucom.2004.11.014

[10] Lomp, O. (2008). Finding Optimal Parameters for Neural Gas Networks Using Evolutionary Algorithms.

[11] Al Shehabi, S., & Lamirel, J. C. (2005, July). Multi-Topographic Neural Network Communication and Generalization for Multi-Viewpoint Analysis. In *Proceedings. 2005 IEEE International Joint Conference on Neural Networks, 2005.* (Vol. 3, pp. 1564-1569). DOI:10.1109/ijcnn.2005.1556111

[12] Holland, J. H. (1992). *Adaptation in natural and artificial systems: an introductory analysis with applications to biology, control, and artificial intelligence*. MIT press. DOI:10.7551/mitpress/1090.003.0007

[13] Nannen, V., & Eiben, A. E. (2007, September). Efficient relevance estimation and value calibration of evolutionary algorithm parameters. In *2007 IEEE congress on evolutionary computation* (pp. 103-110). IEEE. DOI:10.1109/cec.2007.4424460

[14] Maron, O., & Moore, A. W. (1997). The racing algorithm: Model selection for lazy learners. *Artificial Intelligence Review*, 11, 193-225.

DOI:10.1007/978-94-017-2053-3_8

[15] Dobslaw, F. (2010). A parameter tuning framework for metaheuristics based on design of experiments and artificial neural networks. In *International conference on computer mathematics and natural computing*. WASET.

[16] Goldberg, D. E. (1988). Holland, JH. Genetic Algorithms in Search. *Optimization, and Machine Learning. Mach. Learn*, 3, 95-99. DOI:10.1023/a:1022602019183

[17] TAN, R. K., & Şebnem, B. O. R. A. (2017). Parameter tuning algorithms in modeling and simulation. *International Journal of Engineering Science and Application*, 1(2), 58-66. DOI:10.1109/cicn.2017.8319375

[18] Ventocilla, E., Martins, R. M., Paulovich, F., & Riveiro, M. (2021). Scaling the growing neural gas for visual cluster analysis. *Big Data Research*, 26, 100254. DOI:10.1016/j.bdr.2021.100254

[19] Mendes, C. A. T., Gattass, M., & Lopes, H. (2014). FGNG: A fast multi-dimensional growing neural gas implementation. *Neurocomputing*, 128, 328-340. DOI:10.1016/j.neucom.2013.08.033

[20] Fišer, D., Faigl, J., & Kulich, M. (2013). Growing neural gas efficiently. *Neurocomputing*, 104, 72-82. DOI:10.1016/j.neucom.2012.10.004

[21] García-Rodríguez, J., Angelopoulou, A., García-Chamizo, J. M., Psarrou, A., Escolano, S. O., & Giménez, V. M. (2012). Autonomous growing neural gas for applications with time constraint: optimal parameter estimation. *Neural Networks*, 32, 196-208. DOI:10.1016/j.neunet.2012.02.032

[22] Donatti, G. S., Lomp, O., & Würtz, R. P. (2010, July). Evolutionary optimization of growing neural gas parameters for object categorization and recognition. In *The 2010 International Joint Conference on Neural Networks (IJCNN)* (pp. 1-8). IEEE. DOI:10.1109/ijcnn.2010.5596682

[23] Wall, M. (1996). GALib: A C++ library of genetic algorithm components. *Mechanical Engineering Department, Massachusetts Institute of Technology*, 87, 54.

[24] Fritzke, B. (1994). Fast learning with incremental RBF networks. *Neural Process. Lett.*, 1(1), 2-5. DOI:10.1007/bf02312392

[25] Fritzke, B. (1995). Growing grid—a self-organizing network with constant neighborhood range and adaptation strength. *Neural processing letters*, 2, 9-13. DOI:10.1007/bf02332159

[26] Zaki, M. J., & Meira, W. (2014). *Data mining and analysis: fundamental concepts and algorithms*. Cambridge University Press. DOI:10.1017/cbo9780511810114

[27] Lamirel, J. C., & Al Shehabi, S. (2015). Feature maximization based clustering quality evaluation: a promising approach. In *Trends and Applications in Knowledge Discovery and Data Mining: PAKDD 2015 Workshops: BigPMA, VLSP, QIMIE, DAEBH, Ho Chi Minh City, Vietnam, May 19-21, 2015. Revised Selected Papers* (pp. 210-222). Springer International Publishing. DOI:10.1007/978-3-319-25660-3_18

Automatic Storage and Retrieval System (AS/RS) Design for Manufacturing System

Yusuf Ziya KOÇ*

IT Vice President, Ceva Logistic, Istanbul -Turkiye
* **Corresponding Author Email:** yusuf.koc@cevalogistics.com - **ORCID:** 0009-0007-3139-4064

Abstract:

In this article, the Automatic Storage and Retrieval System (AS/RS) desing used in automatic production systems and the AS/RS simulation technique were studied in this design. Part 1, which was created by simulating with computer code, was composed of two types of cells according to the dimensions of the space. Thanks to the prepared simulation, it offers the performance of AGVs, robots and collection-deposit stations. The simulation created has tested how long the warehouse can withstand periods of recession and depression. The simulation was run in two modes as single command mode and dual command mode. According to the obtained data, it has been obtained that the binary mode gives better performance compared to the single instruction. At the same time, this study; He proved that when the input speed is greater than the output speed, the binary instruction allows more items to be translated in a given time frame compared to a single instruction.

1. Introduction

In AS/RS; materials under a certain degree of automation; A combination of precision, accuracy and speed, storing or receiving, equipment control is created. AS/RS has a series of storage aisles which are served one or more (S/R) usually using one S/R machine per aisle (Figure 1). These stations have one or more inputs/outputs. In the terminology of AS/RS systems, I/O stations are often referred to as receive and drop (P/D) stations. Pick/Drop is operated manually or connected to some type of automated processing system, such as a conveyor system (or AGVS) [1]. If different categories of the automatic storage/retrieval system are examined;

• **Unit load in the AS/RS system:** A automated system is designed to handle loads stored on pallets and this system is computer controlled and S/R machines are automatic [2].

• **Mini-load in AS/RS system:** This storage system is used to transport small loads in boxes or drawers.

• **Man-on-board in AS/RS system:** This is an alternative method for the problem of storing and retrieving individual items in the created system [Table 1].

• **Automatic product (parts) picking system:** It is designed for picking up products. The flow of products is ensured. In this way, it is suitable for first-in/first-out inventory and control (Table 2).

• **Deep lane AS/RS:** Deep lane AS/RS is used where large quantities are to be stored. However, it is a high-density unit load storage system used in cases where product types and numbers are low. Each shelf section is designed with an inlet on one side and an outlet on the other. The loads are taken by the S/R type machine, which is specially designed to be taken from one side of the rack system.

Table 1. System Performance

Description	Result
Single Command	76.465 min. (53 Working Days)
Dual Command	95.389 min. (66 Working Days)

Table 2. Small and large items retrieved and stored [3]

	SC		DC	
	Stored	**Retrieved**	**Stored**	**Retrieved**
Small	344	264	411	332
Large	348	270	423	343
Total	692	534	834	675

Table 3. Delay and Rise Times [3]

Description	SC	DC	SC/DC
td The delay time	76.000	95.000	0,80
tr The rise time	48.000	47.000	1,02
tr/td	0,63	0,50	

Table 4. Equipment Utilization

Description	Result
AGV	36%
Robot	42%
Output P/D	35%

2. Material and Methods

A warehouse area was designed with a sufficient number of AGVs and robots (Table 3). Dual signal automatic and recovery system is used. They all have technical features such as speeds, loading and unloading times. While designing, as many P/O stations were kept as necessary. A method has been proposed to model large-scale AS/RS-AGV systems that would accurately and flexibly describe AS/RS where many products are stored and retrieved.

There are two important steps to run simulation; while first stage; is to create a code by placing the number of AS/RS levels and the number of AGVs (Table 4). For the second stage, in the designed model; Each part number placed on each shelf. The arrival and departure times from the warehouse were recorded. We can quickly simulate/animate the findings using the module-based modelling method developed in this study.

There are specific modules that work to simulate situations (robots, unload signals, AGVs, load signals). Each module detects the next event time. A scheduling procedure is created and ranks the times of these events. Users are determined to be dealers located in very different geographical points throughout the country, including abroad.

2.1 System Performance

The simulation was run in two modes. These are single and double command loops. As the results of the performance analysis in both cycles. Flow time refers to the time interval between the point when a task is ready to be processed and the point at which it is completed. Flow time is measured as follows:
Single workflow; It is concluded with storage by designing that a storage cycle starts with the L/U station, the AGV receives the product, goes to the P/O station, and finally the robot receives the

product. Similarly, if it is an undo loop; The robot is defined as starting at the P/O station, traveling empty to the retrieve location, picking up the product, going to the P/O station, dropping the product, AGV picking up the product, going to the L/U station, and finally leaving the L/U station. The dual workflow starts with the L/U station of a storage loop, the AGV picks up the product, goes to the P/D station, and finally, the robot is assumed to pick up the product and go to the storage location and store it.

In the undo loop, however, the robot goes to the receive location empty, picks up the object from there, goes back to the P/D station and drops the object, then the AGV picks up the object, goes to the L/U station, and finally releases the L/U.

These two workflow times are measured and presented in Table 1. A working day includes 3 shifts and is designed in such a way that each shift consists of 8 hours.

3. Results and Discussions

The items stored in the binary command is 20% and the items retrieved in the binary command is 26%.
Therefore, with these conveniences and operating conditions, the binary command works better.
The simulation works in two modes; single command mode provides an extra stream of inputs in 53 business days, while dual command mode provides 66 business days. The results confirm that the dual mode gives better performance compared to the single instruction.

4. Conclusions

It was seen from this work that when the input speed is greater than the output speed, the binary instruction allows more items to be translated in a given time frame compared to the single instruction.
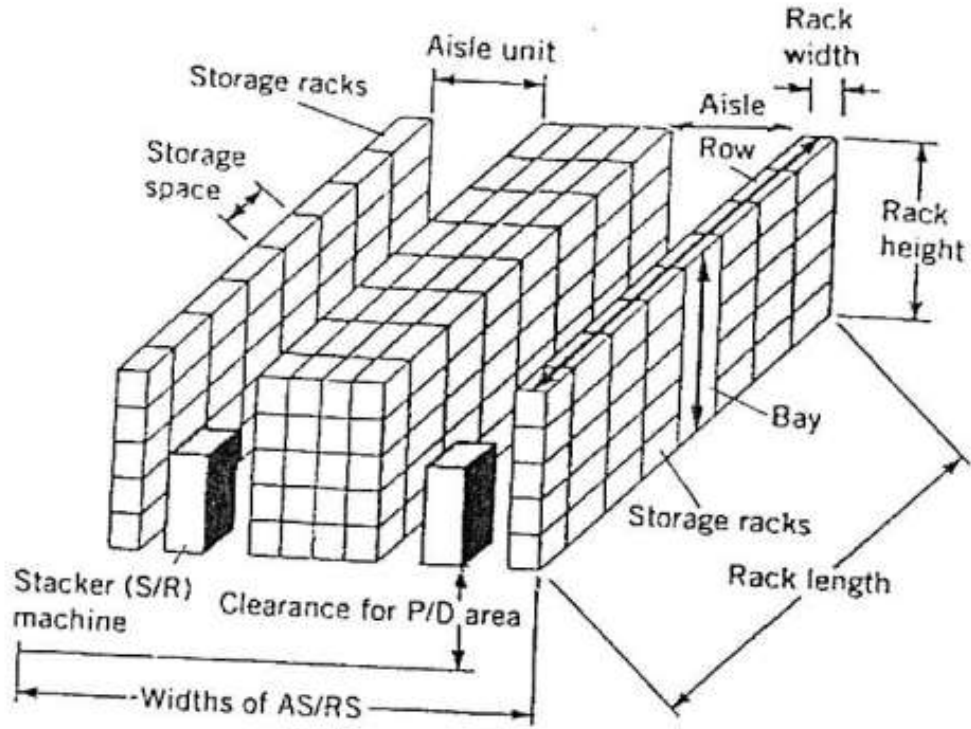
Figure 1. *Generic Structure of an AS/RS [3]*

- **Data availability statement:** The data that support the findings of this study are available on request from the corresponding author. The data are not publicly available due to privacy or ethical restrictions.

References

[1] Tompkins, White, Bozer, Frazelle, tanchoco, Trevino. Facility Planning. *John Wiley & Sons; 1st Edition*

[2] Sign; (1991). System Approach to Computer-Integrated Design and Manufacturing. *John Wiley & Sons; 1st Edition*

[3] Koç; (1998). Spare Part Warehousing. *Marmara University, Master Thesis*

Research Article
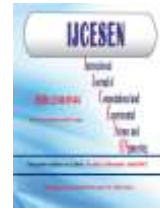
Fore Poppet Design and Optimization to Apply on Norway type Trawler Fishing Ships

Serap Ozhan DOGAN[1]*, Burak Galip ANIK[2]

[1]Department of Mechanical Engineering, Beykent University, Istanbul/ Turkey
* **Corresponding Author Email:** serapdogan@beykent.edu.tr - **ORCID:** 0000-0001-5210-1549

[2]R&D Manager, Tersan Shipyard, Yalova/Turkey
Email: burakgalipanik@gmail.com - **ORCID:** 0000-0002-8315-9441

Abstract:

In the classical sea landing methods of ships, aquaplaning and slipway support systems are used. In Norwegian Type Trawler Fishing vessels, the outer shell surface geometry is very delicate. Therefore; the incoming forces are extreme and the use of wooden poppets by these forces in normal sea landings is insufficient. This work; It includes two different steel fore poppet designs and analyses for the Norwegian type trawler fishing vessel, which cannot be launched with conventional slipway support systems after landing calculations. Within the scope of this study, two different steel fore poppets were designed. After the analyses and examinations, it was decided that the Norwegian type trawler fishing vessel, which is the subject of the article, with which steel fore poppet design will be launched without any problems. Studies carried out in this context; Two different steel fore poppet designs were made using the Rhinoceros analysis program, which is a 3D design program. Rhinoceros Scan & Solve analysis was performed and simulation was run by applying forces to the designed steel fore poppets. A force of 3e+06N, including gravity, was applied to both designed structures. As a result of this; In the first steel fore poppet structure, a maximum displacement of 1.18611mm occurred. In structures designed under a force of 3e+06N; In the first structure, the maximum Von Mises Stress value was found to be 505.761MPa. In the second structure, the maximum Von Mises Stress value was found to be 163.142MPa.

1. Introduction

The shipbuilding industry, which constitutes an important part of maritime activities, is a production, repair and assembly industry, and is an important industry branch where manpower and labour are most needed. In economy; the shipbuilding industry, which replaces foreign exchange, develops sub-industry, attracts technology transfer, provides employment, supports the national naval fleet, and contributes significantly to the defense needs of the country, is a locomotive sector. This branch of industry is a manufacturing industry that includes a combination of many industrial products. The 'Ship', a product of the shipbuilding industry, emerges as a result of the combination of steel industry, machinery industry, electrical-electronic industry, paint industry, plastic industry branch products.
Ships are usually built on land or in dry dock due to the difficulties of building at sea. Building in dry dock is preferable, as the construction of large ships on a slipway can present difficulties. Thus, the dangers and difficulties caused by sea launching are eliminated. However, dry construction costs are high and these pools can be operated more profitably for docking services. Construction on slipway is the most preferred method, and ships built in this way are launched by either stern or side launching methods. Side loading is more risky and is applied in river or gulf shipyards with limited sea area. Stern launching is the most commonly used method [1]. The Norwegian type Trawler fishing vessel, which is the subject of this study, was built on a slipway and then launched from the stern.
Different kinds of loads may be experienced by the ship due to handling. During launching, the ship undergoes stress changes from concentrated loading at the supports on land to concentrated loading on fore poppet during stern lift or tipping at the way ends [2].

Designing a ship is not just doing the calculations to realise the eventual vessel, there are other activities necessary to get the ship to sea. Literally, one set of activities is those tasks to get it in the water and this can be risky if not done adequately [3].

Predictions of the movement are vital to ship's safe control. A set of six curves is prepared to predict the behaviour of the ship during launch (Figure 1). They are curves plotted against the distance of travel down the slipway for end launching process [4].

• Weight, Buoyancy
• Moment of Weight about fore poppet and Moment of Buoyancy about fore poppet
• Moment of Weight about after end of groundways and Moment of Buoyancy about aft end of groundways.

The Important features of these curves are as follows;

• At the point at which the moment of buoyancy about the fore poppet equals the moment of weight about the fore poppet, the stern lifts.
• The difference between the weight and buoyancy curves at the position of stern lift is the maximum force on the fore poppet.
• The curve of the moment of buoyancy about the aft end of the ways must lie wholly above the curve of the moment of weight; the least distance between the two curves of the moment about the aft end of ways; gives the least moment against tipping about the end of ways.
• Crossing of the weight and buoyancy curves before the after end of ways, indicates that the fore poppet will not drop off the end of the ways.

Slipway is the concrete surface and used for the new ship building or thats launching. The sled must have an inclined angle. The slope of the Slipway must be able to produce a force large enough to overcome the friction between the slides and the slide surface. The slipway slopes that should be selected according to the size of the newly built ships are given in Table-1.

Longitudinal oil slipway launching is one of the oldest forms of launching systems. Using this system, the ship descends into the water by being translated in the direction of the longitudinal symmetry axis under a slipway and its own weight. Oil is used to assist the gliding process. Longitudinal launching can be carried out in two ways, from the fore and the stern. Longitudinal launching can be carried out in two ways, fore and stern. In the launching process, the fore of the ship enters the water first. In the stern launch, the stern enters the water first. Launching from the stern is performed in a shorter time than launching from the fore. Because the ship is mostly trimmed to the stern during launching. The main advantage of both methods is the use of simple equipment and for ships of different tonnage and type [5].

To exemplify some of the reasons that require a ship to be lowered from the stern;

• The stern of the ships is more rounded than the fore/stern profiles that have aerodynamic features. Therefore, it creates greater resistance when entering the water and therefore provides a better braking force.
• The stern of the ship provides a faster buoyancy than the fore in lifting the ship from the cradle or bed. Thus, there may be a more gradual separation from the slipways towards the sea.

As a result; The wider stern arch of the ship helps to keep the ship diagonally stable during immersion [6]. Another important reason is the installation of very sensitive devices such as the steering gear and shaft lines that need to be centered towards the stern. Any major deformation can prevent these devices from working, thus increasing the ship's construction process and cost [7].

The stern launch devices consist of a part connected to the ship and moving with it, and a fixed part on which this part moves. The moving part consists of one or more sliding parts attached to the ship [8]. The length of the slipway is approximately 80% of the length of the ship, and the ends of these slipways at the fore and stern are called for poppet and stern poppet. The stationary part consists of a sled attached to the ground, inclined towards the water. The part that moves with the ship is called a sliding sled, the part that is connected to the ground is called a fixed sled, and the part of the sled in the water is called a wet sled. The movable sliding slides can easily move on the fixed slides, as their contact surfaces are lubricated with oil. Fixed slides extend from land to sea with a small slope (α) [1].

The schematic representation of the stern launch process is shown in Figure 2. The movement of the ship during landing and the forces acting on the ship during this can be examined step by step. Each stage begins with a change in motion or the beginning of a new force (or the disappearance of a force acting on the ship).

The stage from the calm state of the ship to the entrance to the sea can be defined as the first stage. It continues from the moment the movement starts with the effect of gravity until the front end of the slide slides touch the water. At this stage, its own weight and the reaction force of the stationary slide act on the system.

The stage from the ship's entrance to the sea until it starts to turn can be defined as the second stage. At this stage, when the ship enters the sea, a buoyancy force will occur and the moment created by this buoyancy force will try to lift the ship from the slipway. When the moment of the buoyant force

relative to the fore rib is equal to or greater than the moment of the gravity force with respect to the same point, the ship will start to rotate around the fore rib. In the meantime, great pressures may occur on the fore poppet and these pressures may damage both the slipways and the ship. At this stage, the system is affected by its own weight, the reaction of the fixed slide and the water pressure force. The phase between the ship starting to turn and floating can be defined as the third. This stage is the time between when the ship starts to turn around the fore poppet and when it leaves the sled and begins to swim freely. At this stage, the system is affected by its own weight, the response of the stationary slide and the water pressure. The stage in which the ship starts to swim freely can be called the final stage. It is the time elapsed between when the ship starts to float and when it comes to a complete stop. At this stage, its own weight and water pressure affect the system. During the launching of the ship on the inclined slipway; After a while the ship enters the water, the ship starts to turn on its fore side and in the meantime, great forces come to the fore of the ship. In order to eliminate the effect of these large forces, steel-reinforced wooden constructions are added to the hull sides of the fore of the ship to increase the turning surface. This construction is called "Fore Poppet"[6].

At the moment the stern of the ship starts to rise in the sea, the load on the fore thruster gets the maximum value. This value is called poppet pressure. The poppet pressure is approximately 1/3 of the landing weight. Its schematic is shared in Figure 3. While the ship is being launched on the inclined slipway, it is under the influence of its own weight and the buoyancy force and other relatively small forces as it starts to enter the water. As the ship continues to slide on the slipway, due to the effect of these forces, the moment value that initiates the rotation of the ship is called the "tipping moment".

The most important value that determines the value of the turning moment is the length of the in-sea section of the inclined slipway. This length is related to the ship's length and the location of the ship's center of gravity. In Figure 4, the rotational moment of the ship at sea is shown.

2. Material and Methods

The Norwegian type trawler fishing vessel, which is the subject of the study, continued to be equipped on the slipway, since it stayed on the slipway longer than normal. This is the launching condition; the landing weight defined as the light weight and the weight of the ship were caused by the excessive weight of the ship.

Table 1. Slipway slope, which should be selected according to the size of the ship.

Ship Type	Tan α
Small ships	1/12 ↔ 1/16
Medium-sized ships	1/14 ↔ 1/20
Big ships	1/18 ↔ 1/24

Figure 1. Basic Ship Theory [1]

Figure 2. The schematic representation of the stern launch process

Figure 3. Fore poppet

Figure 4. Rotational moment (Torque)

This caused the ship's center of gravity to be too close to the stern. Thus, it required the ship to extend the length of the sliding slipway both at the fore and stern. In the sea landing calculations; head load should not exceed the maximum 550 tons, which is the slipway carrying capacity of in-sea barges. For this reason, the slider slipway length is adjusted at the head. The Norwegian trawler type fishing vessel cannot be landed using conventional slipway support systems. Because the incoming forces are extreme, as it is not possible for the wooden poppet systems in normal ship landings to meet these forces, making a steel fore poppet is necessary for a safe lowering of the ship. Within the scope of this study, two different steel fore poppets were designed. The first fore poppet design is shared in Figure 5 and the second fore poppet design in Figure 6. Analyzes were applied to both designed papers using the Rhinoceros scan & solve analysis program. As a result of the data obtained, it was decided with which steel fore poppet the ship would be launched safely. Static analysis was applied under the determined loads to determine the safety of the design. The data were changed many times to compare the applied force requirements, and the position and force analysis were performed repeatedly until the specified criteria were met. By using Rhinoceros workbench, static structural analysis of steel fore poppets designed with Rhinoceros, the displacements of the structure, the stresses caused by gravity and external loads have been determined. For the analysis of the design of the steel fore poppets, the material was chosen considering the research and quality standards. The mechanical and physical properties of the selected material are given in Table 2. The designed fixation points, force and force direction were selected in Figure 7 and 8. Rhinoceros scan&solve was chosen for this study as it is an analysis program that fully automates basic structural simulation on multiple surfaces, extrusions and meshes.

3. Results and Discussions

The displacement of the designed object was determined by measuring the distance between the first and last position, and the original position was accepted as a reference. The steel fore poppet is fixed to their design at the specified points. A force of 3e+06N, including gravity, was applied to both designed structures. As a result of this; In the first steel fore poppet structure, a maximum displacement of 1.18611 mm occurred. The data obtained as a result of the analysis are shared in Figure 9. In the second designed steel fore poppet structure, a displacement of 1.22784mm occurred. The data of

this analysis are shared in Figure 10. The response of the structure designed with stress-strain analysis under certain loads was examined. In Figure 11 and Figure 12, the stresses obtained in the structures designed under a force of 3e+06N are shared. In the first structure, the maximum Von Mises Stress value was found to be 505.761MPa, the maximum Von Mises Stress value occurring in the second steel fore poppet design was found to be 163.142MPa.

Table 2. Properties of the selected material (ST44&S275JR)

Property	Value
Description	Steel, Cast Carbon
Density	7.8e-09 Mg/mm^3
Elastic Modulus	200000 MPa
Poisson Ratio	0.32
Default Failure Criterion	Von Mises
Tensile Yield Strength	241.68 MPa
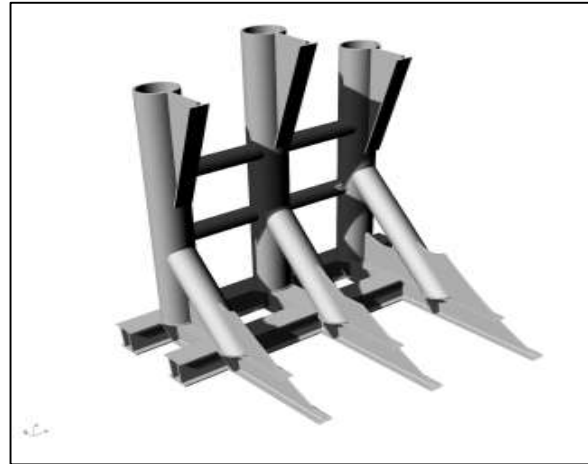
Figure 5. First steel fore poppet design (weight 947.92 kg)
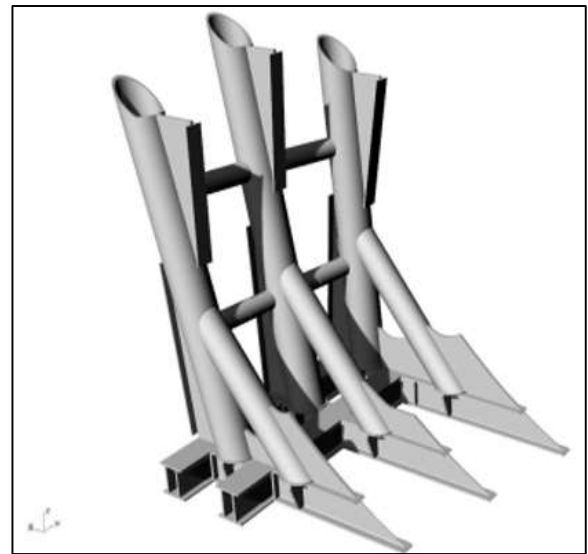
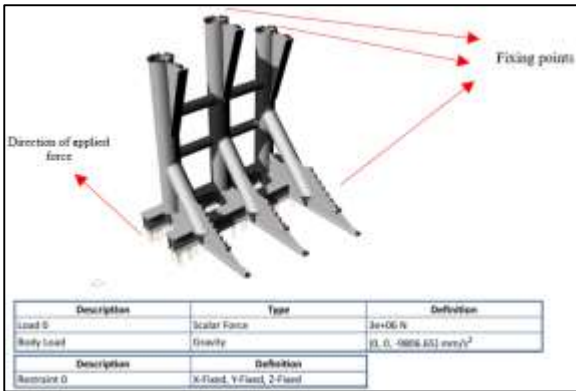*Figure 6. Second steel fore poppet design (weight 1030.45 kg)*

Figure 7. *The force applied to the first steel fore poppet design and the places to be fixed*
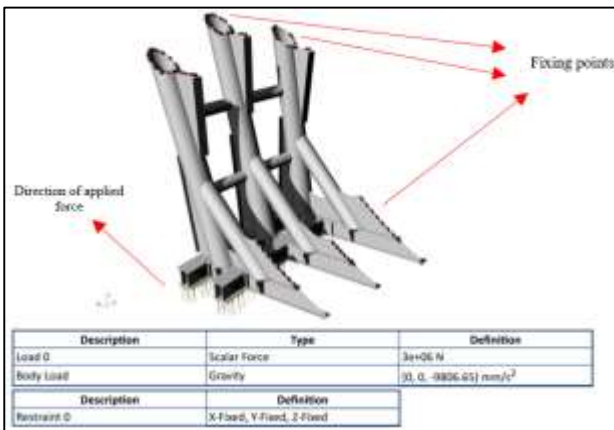

Figure 8. *The force to be applied to the second steel fore poppet design and the places where it will be fixed*
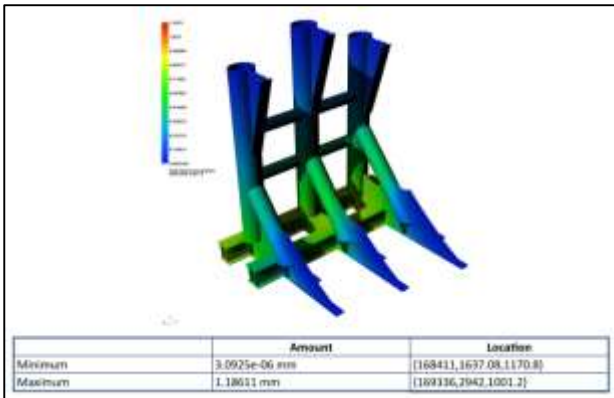

Figure 9. *Displacement in our first steel fore poppet design*

4. Conclusions

It is seen from Table 2 that the tensile yield stress of the material used in steel fore poppet designs is 241.68MPa. In order for steel fore poppet designs to be considered safe, a value of 241.68 MPa is accepted as the upper limit in the analysis study. Thus; In order for the steel fore poppet design to be considered safe, as a result of the analysis, the maximum Von Mises Stress value occurring in the structures should be under 241.68MPa.
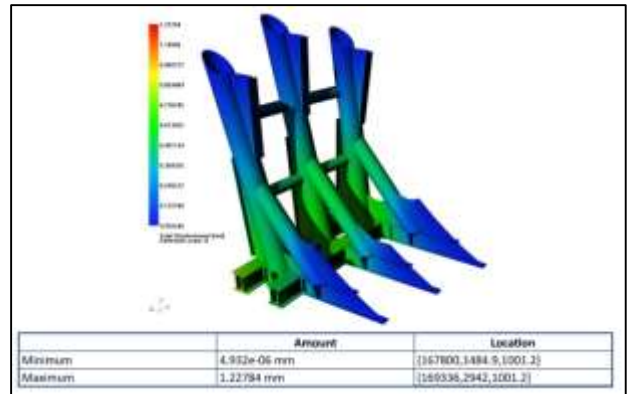
Figure 10. *Displacement in our second steel fore poppet design*
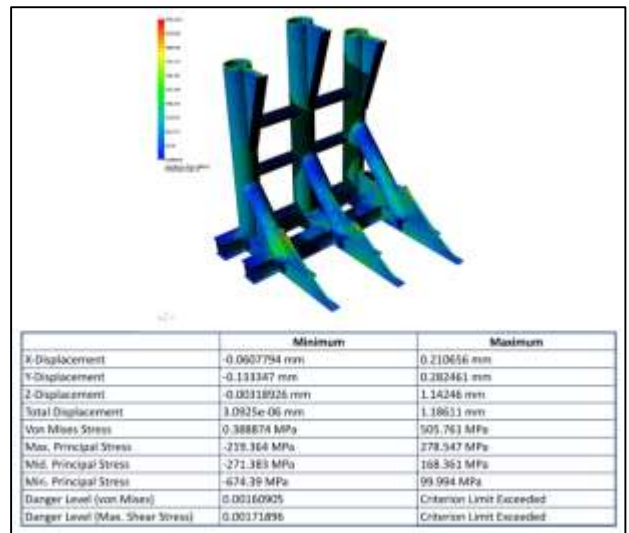
Figure 11. *Stresses occurring in the first steel fore poppet design*
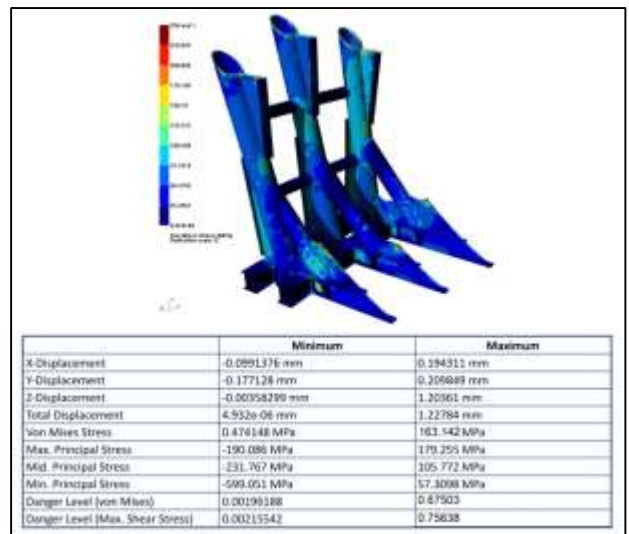
Figure 12. *Stresses occurring in the second steel fore poppet design*

As a result of the analysis of the first steel fore poppet, the maximum Von Mises Stress value of 505.761MPa is obtained. As a result of the analysis of the second steel head blade, the maximum Von Mises Stress value is obtained as 163.142MPa.

As a result of the evaluation of the obtained data, our second design problem has been solved. The steel fore poppet system seen in Figure 5 is positioned on the ship's hull, including frames 113 and 119. It is decided that the Norwegian type trawler fishing vessel, which is the subject of this study, can be safely launched into the sea.

Author Statements:

- **Ethical approval:** The conducted research is not related to either human or animal use.
- **Conflict of interest:** The authors declare that they have no known competing financial interests or personal relationships that could have appeared to influence the work reported in this paper
- **Acknowledgement:** The authors declare that they have nobody or no-company to acknowledge.
- **Author contributions:** The authors declare that they have equal right on this paper.
- **Funding information:** The authors declare that there is no funding to be acknowledged.
- **Data availability statement:** The data that support the findings of this study are available on request from the corresponding author. The data are not publicly available due to privacy or ethical restrictions.

References

[1] A. Biran (Çeviren: Y. Hüseyin). (2006) Gemi Hidrostatiği ve Stabilitesi; *Birsen Yayınevi*.

[2] S. C. Misra; Design Principles of Ships and Marine Structures; *International Standard E-Book* (Number-13: 978-1-4822-5447-1); 2016.

[3] D. Andrews. (2020). Design Errors in Ship Design; *Journal of Marine Science and Engineering*. 9(1);34 DOI:10.3390/jmse9010034

[4] KJ Rawson , E. C. Tupper; (2001). Basic Ship Theory, Combined Volume 5th Edition; *Elsevier Science*.

[5] K. Sarıöz (1999). Gemi Teorisi Ders Notları; *İTÜ Gemi İnşa Ve Denizcilik Fakültesi Deniz Teknolojisi Mühendisliği Bölümü*.

[6] M. Etingü. (1946). Gemilerin Geometrisi ve Statiği; *İstanbul Teknik Üniversitesi*.

[7] WQ. Shen (1996). Analysis of Ship End Launching Without Fore Poppet. *Journal of Ship Production* 12(3);172–177

[8] Ç.Fahri (2021). Gemi Hidrostatiği Ve Stabilitesi Ders Notları; *Yıldız Teknik Üniversitesi*.
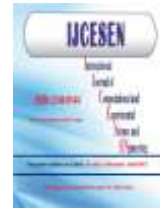
Process Improvement Study in a Tire Factory

Seher ARSLANKAYA[1,*], Asude DEMİR[2]

[1]Sakarya University, Engineering Faculty, Industrial Engineering Department, 54000, Sakarya-Turkey
* **Corresponding Author** : **Email:** aseher@sakarya.edu.tr - **ORCID:** 0000-0001-6023-2901

[2] Sakarya University, Engineering Faculty, Industrial Engineering Department, 54000, Sakarya-Turkey
Email: asude.demir1@ogr.sakarya.edu.tr - **ORCID:** 0000-0001-6488-0367

Abstract:

Today, motorsports are one of the sports branches with the world's largest audience and fan base. The production techniques of the tires used in these organizations are an indispensable factor in order to be the pioneer of the sector. In this study, SWOT Analysis and Failure Modes and Effects Analysis were performed for two different production lines, and the superiority of the lines against each other was evaluated. The process to be improved on the excellent line was determined as a result of brainstorming by an expert team. After the changed parameters, the effects on the final product and the process were evaluated. The study was concluded by determining that all the changes made do not constitute an obstacle to the continuity of the process and the quality of the final product. Time analysis was made by video recording the process whose cycle time changed. As a result of the calculations made after the time analysis, the annual tire gain was calculated as 7299. The production volume determined at the beginning of the period for 2022 is 71273 units, and while these tires were produced in 386,630.1 minutes with the old cycle time, they can be produced in 351.583.4 minutes with the new cycle times. Total time savings for 2022 production volume is 34,776.7 minutes, i.e., 24.15 days. With the new cycle times, the line's capacity has been increased by 10.24%. The company can produce 6,398 pieces of the tire with the highest cycle time and 8,105 pieces with the lowest cycle time in 34,776.7 minutes won.

1. Introduction

Process; It is a series of processes that produce outputs that will meet customer demands and expectations by processing resources such as humans, machines, materials, money, information, and time. Process management aims to monitor and improve processes continuously and regularly. The cycle includes the design and maintenance of processes, continuous evaluation, analysis, and improvements to meet customer needs better. Process improvement covers analysing a company's business processes, increasing efficiency, reducing errors, reducing costs, and increasing customer satisfaction.

The company, the sole tire supplier of prestigious races in motorsports, where interest is increasing daily, sends tires to racing organizations from many production facilities and warehouses. However, not all of the company's production facilities in different locations are within the motorsport organization.

There is only one factory that produces motorsport tires entirely. This factory's capacity needs to be increased for producing certain groups of tires. In order to change the production capacity, it seemed normal at first to transport the A group tires, which were produced with the help of five-axis robotic arms on the lines called "BX", to the machines called "AX", which used more primitive methods in the production stages. However, due to the prestige of the A group and the deterioration in the tire quality due to the changing method, it was decided to carry out process improvement studies in the "BX" lines to increase production.

A systematic study of activities and flows will be provided for each process to be improved with process improvement work. Details will be revealed by understanding the processes to provide high quality at lower prices. Continuous reviews will seek ways to eliminate unnecessary operations, limit expensive materials and services, improve the environment, or make work safer. In addition,

customer satisfaction will be ensured by preventing delays [1].

In order to increase the production capacity of the "BX" line, the pressure values of the extruder pump and extruder screw were increased at the same rate. Changing values reduced the cycle time. Video recordings are taken for the new conversion and Avidemux 2.0. The new cycle times were calculated by analyzing the program. The time caused by the difference between the changing and old cycle times corresponds to a total of 7299 tires based on production. There are many studies on process improvement methods in the literature. This literature review includes studies that were accepted between 2014-2021. Kirkham, Garza-Reyes, Kumar, and Antony (2014) surveyed what improvement methods companies prefer to increase their competitiveness and which ones they achieve more success in. According to the results of the survey, it was determined that the most successful method was six sigma [2]. Patel, Chauhan, and Trivedi (2015) scanned the literature and revealed the gains obtained as a result of value stream mapping applications in the machining industry in 6 study examples [3]. Türkan and Görener (2017) carried out process improvement with Kaizen, Poka-Yoke, 8D application, and FMEA application in the manufacturing department of a steel production company. With these studies, gains such as cost savings, time savings, and faster and error-free work have been achieved[4]. Gupta, Singh, and Suri (2018) examined the service quality parameters of an Indian-origin logistics provider company, which took part in supporting the supply chain processes in a business they determined, using the SWOT analysis method in order to increase customer satisfaction with the strategies determined as appropriate for supply chain management [5]. Avunduk (2019) performed a process improvement on the pet blow molding machine using the Lean Six Sigma method. This work and financial gain contributed to the company's long-term environmental sustainability goal and the vision of a more livable world with less energy consumption [6]. Sevgili and Antmen (2019) aimed at lean production by using value stream mapping in a metal processing factory and minimized intermediate stocks due to process improvement, shortened the production flow time, and increased the daily production amount [7]. Apilioğulları (2020) conducted quality improvement studies with Lean Six Sigma and Industry 4.0 Integration for a process with high waste in the aluminum industry [8]. Sarı, Sergi, and Ozuduruk (2020) made a process analysis in the customer service department of a tire manufacturing company. A comprehensive SWOT analysis was used, and matrices were formed due to internal and external factors evaluation. Accordingly, a strategic plan has been determined to use the software resources of the enterprise more efficiently [9]. Berber and Deste (2021) improved various processes in an ice cream factory by using a scoreboard diagram, Poka-Yoke, and Kaizen together with brainstorming [10]. In the literature, the importance of process management and process improvement studies have applications in different sectors using different methods. At the same time, the effects of these concepts on business performance were also evaluated [11-17]. It is also clearly seen in the literature that the ANN or FL approaches have been used in different motivations, and satisfactory results have been obtained [18-33].

2. Material and Methods

2.1. SWOT Analysis

SWOT analysis can be defined as a strategic planning technique used to help a person or business identify strengths, weaknesses, opportunities, and threats related to business competition or project planning [9].
SWOT Analysis consists of 4 steps:
- Strengths: Strengths are used to maximize opportunities and minimize threats.
- Weaknesses: Weaknesses are minimized by taking advantage of opportunities and avoiding threats.
- Opportunities: Strengths are maximized, and weaknesses are minimized by using them.
- Threats: Strengths are used to minimize, and weaknesses are minimized by avoiding.

It is an analysis technique used to determine the positive and negative aspects of the internal structure of the system, as well as to determine the opportunities and threats in its external environment. Based on this statement, it is understood that SWOT Analysis is a current situation analysis. SWOT Analysis is also an analysis technique that helps to detect and predict the system's future state. According to this second meaning, SWOT Analysis is a future situation analysis [34].

2.2. Failure Modes and Effects Analysis

Failure modes and effects analysis (FMEA) is a widely used technique in many fields to increase process reliability and establish systems to prevent potential failures. FMEA; "What could have caused the error?", "What could be the root causes of the error?", "What could be the effects as a result of the error?" It is a method that seeks answers to such questions and analyzes and documents the answers it receives. It has proven to be a valuable and

powerful tool in evaluating potential failures and preventing their occurrence [35].

FMEA implementation stages can be expressed as follows:
• Initial studies,
• Identification of hazard sources and hazards,
• Identification of possible fault effects, causes, and existing controls,
• Determination of probability, severity, detection, and ROS values,
• Sorting the errors according to RPN, determining the precautions to be taken,
• Recalculation of RPN values after the implementation of the foreseen measures.

At the method's core is determining risk priority numbers (RPN). The probability, severity, and detectability of the error calculate these numbers:

Risk Priority Number (RPN) = Probability of Occurrence x Severity x Detectability   (1)

In this equation, "Probability of Occurrence" is the frequency level of the error; "Severe" means the severity of the error; "Detection of Errors" or "Detection" refers to the level of detecting the error before it reaches the user [4]. In this study, scoring was done based on expert opinions. If the RPN value is less than 40, there is no need to take precautions, if it is between 40 and 100, it means that precautions can be taken, and if it is greater than 100, it means that precautions should be taken.

2.3. Brainstorming

It is a group activity when it is desired to collect ideas, solutions, and root causes on any subject. The number of participants in the group should be at least 5-6 people and not more than 19-20 people. In addition to the experts on the subject, there should be those not directly involved. In this way, it will be possible to look at the current problem from different angles without conditioning what is known [36].

2.4. Root Cause Analysis

Root causes analysis covers the studies to determine the main reason for the origin of the errors and the measures to be taken to prevent the errors from recurring [37]. Analysis, "What would not be what if it was not?" It is carried out in 5 steps by looking for an answer. The materials and also used methods should be detailed in this section.

3. Application

A tire company produces tires for motorsport organizations in its production facility. There are two types of production lines depending on the prestige and conditions of the organizations where the tires will be used. The lines are locally named "BX" and "AX". The "BX" line includes a more technological, innovative, and high-quality production process than the "AX" line. However, since the number of BX lines is less than that of AX lines, the production capacity is insufficient for tire groups produced only in BX lines. This leads to the production of tires with insufficient capacity in different locations; therefore, it causes an extra cost of production, logistics, and quality.

This scope of work; A SWOT analysis was conducted for the BX and AX lines, and an answer was sought to the question, "Can a production line change be made for a particular tire group?" Defect Modes and Effects Analysis (FMEA) was applied for tires produced in different lines. After determining a process by brainstorming method for the BX line, which has insufficient capacity, and arranging the cycle time, root cause analysis was performed for tires produced with two different cycles. As a result, the production capacity gained in a working year in the accelerating cycle is expressed numerically.
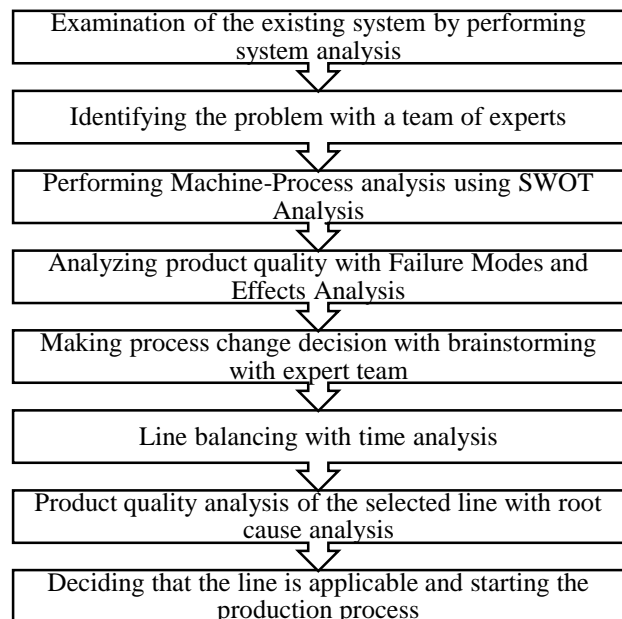
Examination of the existing system by performing system analysis

Identifying the problem with a team of experts

Performing Machine-Process analysis using SWOT Analysis

Analyzing product quality with Failure Modes and Effects Analysis

Making process change decision with brainstorming with expert team

Line balancing with time analysis

Product quality analysis of the selected line with root cause analysis

Deciding that the line is applicable and starting the production process

Figure 1. Application Steps

3.1. Examination of the Existing System

The final product is first visually checked. Then, X-Ray images are taken, and it is checked whether there is foreign matter in the tire paste. Finally, the tire is attached to a rim and moved. In this process, the mass values of the tire are checked. All completed and approved tires are labeled and stored. The business supplies tires to more than one race

organization. Similar or different tire groups can be produced in two different production lines. However, only BX production lines are preferred for certain groups of tires. Since quality errors are less in BX lines, this line is preferred for producing tires of high organizations. In addition, since the production in these lines is almost entirely automated, personnel errors may occur at a minimum level.

3.2. Identifying the Problem

The production capacity of BX lines remains below the demanded number. Since the open AX lines in demand cannot be closed by production, it is necessary to increase the capacity through process improvement studies in BX lines.

3.3. Machine – Process Analysis

For the BX and AX lines, the SWOT Analysis based on the tire group produced in both lines, quality results, and general conditions is as in Tables 1 and 2. As a result of the SWOT analysis, it was determined that the BX line is more advantageous than the AX line.

3.4. Product Quality Analysis – Failure Modes and Effects Analysis

Fault Types and Effects Analysis (FMEA) for tires with similar characteristics and belonging to the same group produced in different lines are given in Table 3 and Table 4. The severity, probability, and detectability values for FMEA were determined based on the opinions of the company's quality management system specialist.

Table 1. BX Line SWOT Analysis

Strengths	Weaknesses	Threats	Opportunities
• There is no joint on the tread of the produced tire • Use of high-end technology • Standardization of the manufactured product • Does not need a separate machine, operator and process for the production of the tread of the tire • High level of traceability	• Few lines • Insufficient capacity • Insufficient number of technician personnel to work on the lines • High installation and maintenance cost • High energy consumption • High equipment cost	• Reducing the product range due to the low capacity of the line • Possibility of change with AX lines due to the large area coverage in the layout	• Using a completely different production methodology than competitors • Industry support for automation and high technology • Modification capability

Table 2. AX Line SWOT Analysis

Strengths	Weaknesses	Threats	Opportunities
• Too many lines • Does not take up much space in the layout • Number of authorized personnel for use	• Having a joint on the tread of the produced tire • Use of low-level technology • Occupational safety risks • Low traceability level	• Risk of being discontinued due to low level technology use • Risk of being out of use for space purposes for BX in layout	• Insufficient BX production capacities • Possibility of replacement with BX lines as it takes up less space in the layout

Table 3. BX Line Failure Types and Effects Analysis

Fault Type No	Fault Types	Possible Effects of Fault	Severity	Fault Causes	Probability	Control	Detection	RPN
1	The appearance of the bandina on the outside, which provides durability to the tire	Non-durable tire production Discarding the carcass	7	Faulty semi-finished product production Rig issues Electronic malfunctions	3	Equipment control planned Paintenance Semi-finished quality control	2	42

2	2nd phase transfer error	Formed tire production Discarding the carcass or tire	9	Incorrect positioning of the 1st phase in the clichés Electronic malfunctions Incorrect machine setting	4	Machine recipe control 100% control of 1st phase placement	6	216
3	Carcass weight is out of limits	Heavier or lighter tire production Discarding the carcass or tire Machine posture	10	Incorrect machine setting Incorrect use of semi-finished products Incorrect cycle time	4	Control of semi-finished product cards Checking the machine weight setting	3	120
4	Parallel generation application	Positioning the belts in the same direction and direction	10	Operator error	2	Belt direction control Belt material - process conformity check	7	140

Table 4. AX Line Failure Types and Effects Analysis

Fault Type No	Fault Types	Possible Effects of Fault	Severity	Fault Causes	Probability	Control	Detection	RPN
1	Material folding in the sidewall of the tire	Deformity of the baked tire Discarding the carcass	6	Machine error Operator error	4	100% control of the cheek pressing process	3	72
2	Parallel generation application	Belts to be in the same direction and direction	10	Operator error	6	Belt direction control Machine process control	7	420
3	Splice join error	Lack of material and deformity in the tread of the tire Discarding the carcass	5	Incorrect use of equipment	5	Machinery equipment control Back material length control	3	75
4	Folding the backing material	Deformity of the baked tire Discarding the carcass	6	Operator error machine error Operator error Incorrect use of equipment	5	Machinery equipment control Machine process control 100% control of the ridge stamping process	3	90

FMEA were shared with experts and their opinions were taken. In the evaluations, since the BX line is more autonomous than the AX lines, it is less likely to encounter high-severity errors. BX lines are more powerful and flexible in the actions to be taken due to the high technology and modification power they use. Therefore, it is in a more advantageous position compared to AX lines. In order not to lose this advantage and to benefit more from the strengths of the line, it was decided to increase the production capacity of the BX lines.

3.5. Process Change Decision

BX lines consist of different zones called 1, 2, and 3 zones. It produces uncooked tires by completing different processes. The operator carries out the processes in Zone 1 of the line. After the processes in the first region are completed, the robot arm brings the semi-finished product to the second region. There needs to be operator access to Zone 2 of the line. The process here is completed autonomously with the help of a five-axis robotic arm. 2. The back of the semi-finished product is wrapped in the region. After the back wrapping, the process of the package in the second region is completed, and the tire package is sent to the tired phase placed by the operator in the determined area in the third region with the help of the robotic arm. Now the process continues in the 3rd zone of the line under operator control. After the operator controls the package transfer, the unbaked tire, which is in two separate phases, is subjected to the squeezing process. This process finalizes the tire. The operator measures the weight of the finished tire and sends it to the curing process to be cured if it is within the specified quality limits. Within the scope of the process improvement work to be carried out to increase the capacity of the expert opinions and the meetings held, the process in the first region is taken to the second region, and in the trial process in the second region, the winding of the tread of the tire has a faster cycle time. It was decided to increase the pressure.

3.6. BX Line Balancing

The tread region of the tire is currently wrapped in the B region of the BX line. The pressure of the extruder pump and the speed of the extruder screw have been increased to reduce the cycle time.
Figure 2 examined the screw speed trend when the screw speed and pump speed were 15 rpm and 18 rpm. The reason for increasing the screw and pump pressure values at the same rate is; If the pump works slowly while the screw is working fast, the accumulation of material in the extruder and the congestion in the pump prevent the process from working continuously. Within the scope of the values seen in Figure 2., the effect of the pressure value change made in the working recipe of the extruder on the process was evaluated, and it was approved by the electronic and mechanical maintenance team that the change did not prevent the process from working correctly. The increase in the pressure value increased the screw speed, and as it can be seen in Figure 2., when the pressure value was 15 rpm, the process that took 270 seconds was completed in 210 seconds when the value was increased to 18 pm.
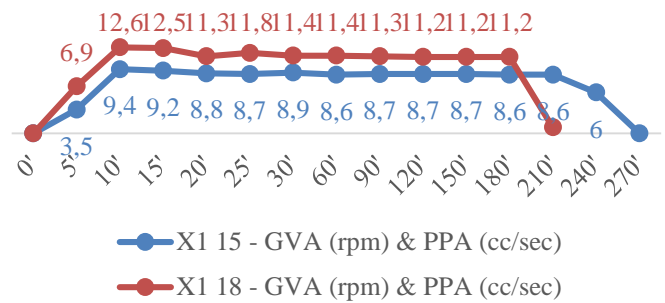

Figure 2. *Screw Speed Trend (rpm)*

Figure 3 examined the pump speed trend when the pump speed and screw speed were 15 rpm and 18 rpm. Within the scope of the values seen in Figure 3., the effect of the pressure value change made in the working recipe of the extruder on the process has been evaluated, and it has been approved by the electronic and mechanical maintenance team that the change does not prevent the process from working correctly. The increase in the pressure value increased the pump speed, and as can be seen in Figure 3. when the pressure value was 15 rpm, the process that took 270 seconds was completed in 210 seconds when the value was increased to 18 rpm.
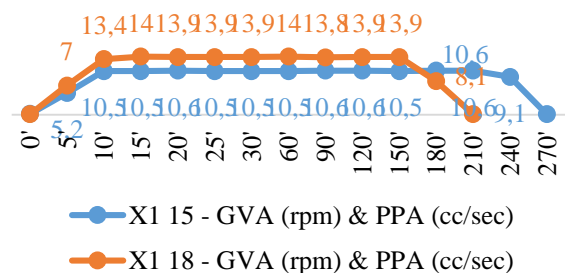
Figure 3. *Pump Speed Trend (bar)*

After the changes made, 9 samples were taken from the process working with the new values. The curing properties of all samples were tested in the rheometer. As a result of the vulcanization test,

chemical compatibility values and limit evaluations for 9 samples taken from the process are shown in Figure 4. These values give information about the flow behavior of the mixture in the process. Limits have been determined by the company's R&D Laboratory experts. As seen in Figure 4., all values are within the determined limits.
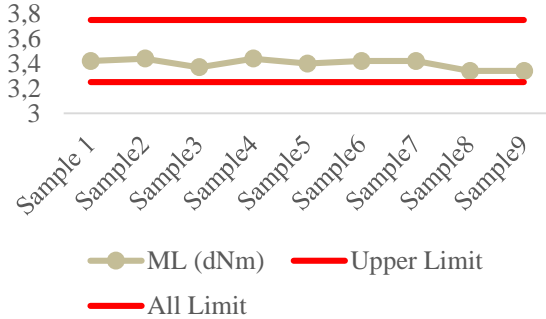

***Figure 4.** Chemical Compatibility Values and Limits*

The cooking time and limit evaluations for nine samples are shown in Figure 5. This value gives an idea about the number of tires produced per unit of time.
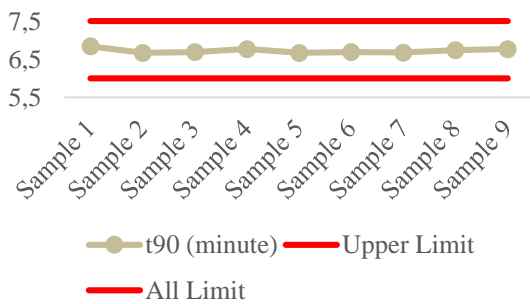
***Figure 5.** Cooking Time and Limit Values*

According to this evaluation, it is seen that the changes made in the extruder do not have a negative effect on the viscosity of the rubber material. In order to calculate the effect of the changes made on the cycle time, time analysis was made by separating each process down to its simplest element. The cycle times of the current situation are given in Table 5. After the time analysis study, the new state cycle times are shown in Table 6. Since zones 1, 2 and 3 can operate simultaneously, the zone with the maximum value from these three zones represents the cycle time. 2nd region has the maximum cycle time, and the actual cycle time has been reached with a tolerance of 6%. For example; It gives the value of cycle time = 4.8*(1+0.06) = 5.1 for the tire coded X1.

3.7. BX Product Quality Analysis

Problems in terms of quality were determined in the tires produced after the accelerated cycle. An unacceptable error is the formation of air pockets in the tread compound after the tire is cooked. The detected product defect was examined within the scope of the five-reason analysis, and action was taken. The five-reason analysis is as in Figure 6.The root cause identified is the manufacture of rubber strips with a wider mold opening. The wide opening of the mold reduces the cycle time. However, the problem encountered due to the increased width needs to be at an acceptable level. For this reason, the mold mouth width used in producing rubber strips has been reduced from 32.5 mm to 28.5 mm. In the examinations made after the action taken, it was observed that the problem disappeared.

4. Statistical Analysis

The hypothesis test was established using the cycle times given in Table 5 and Table 6, and the result was obtained with the T-Test. Whether there is an improvement in the current situation will be analyzed by T-Test. In this case, the hypotheses created are as follows:

H0: The optimization could not be performed.
H1: The improvement has been carried out.

The T-test result is given in Table 7. 26 observations were examined with a 95% confidence interval, and a t-value of 12.83 was reached. The acceptance value at both ends is 2.06. Since the value of 12.83 is outside the acceptance region, the H_0 hypothesis is rejected. H_1 hypothesis was accepted. According to these results, it has been proven by T-Test that an improvement is observed in the current situation

***Table 7.** T-Test Analysis of Cycle Times*

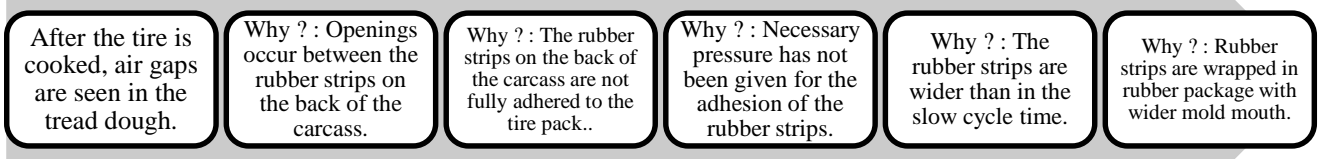|	Old Cycle Time	New Cycle Time
Average	5,30	4,88
Variance	0,19	0,11
Observation	26	26
Pearson Correlation	0,94	
Projected Average Difference	0,00	
Df	25,00	
t Stat	12,83	
P(T<=t) single-ended	0,00	
t Critical single-ended	1,71	
P(T<=t) double-ended	0,00	
t critical two-ended	2,06	

5. Conclusion

This study is an evaluation study using methods such as SWOT Analysis and Failure Modes and

Table 5. Baseline Cycle Times **Tire Size Code**	**2022 Production Volume (pieces/year)**	**Cycle Time (Specified)**	**Tread Cycle Time (min)**	**1. Cycle Time (min)**	**2. Cycle Time (min)**	**3. Cycle Time (min)**	**Cycle Time (Real Time Study)**
X1	1617	5,42	2,7	1,6	5,3	3,1	5,6
X2	144	5,42	2,8	2,6	5,2	3,1	5,5
X3	168	5,42	2,7	4,7	4,1	3,0	5,0
X4	312	5,42	2,6	1,7	5,3	3,1	5,6
X5	552	5,42	2,5	2,4	5,0	3,0	5,3
X6	432	5,42	2,5	2,4	5,0	3,0	5,3
X10	3875	5,42	2,7	4,0	4,3	3,1	4,5
X11	14258	5,42	2,8	2,6	5,0	3,1	5,3
X12	13463	5,42	2,5	1,7	5,3	3,1	5,6
X13	4894	5,42	2,7	2,6	5,1	3,2	5,4
X14	4894	5,42	2,8	1,7	5,5	3,1	5,8
X15	10918	5,42	2,8	2,5	5,3	3,0	5,7
X18	3923	5,42	2,8	1,7	5,5	3,1	5,8
X19	2324	5,42	2,5	2,4	5,0	3,0	5,3
X20	1051	5,42	2,7	4,0	4,3	3,1	4,5
X21	1356	5,42	2,7	2,5	5,3	3,0	5,6
X22	1128	5,42	2,7	4,0	4,3	3,1	4,5
X23	802	5,42	2,8	1,7	5,5	3,1	5,8
X24	550	5,42	2,8	2,6	5,1	3,2	5,4
X25	191	5,42	2,7	4,0	4,3	3,1	4,5
X26	144	5,84	2,0	1,6	5,5	3,1	5,8

Table 6. *New State Cycle Times*

Tire Size Code	**Time [RPM:18] (min)**	**1. Cycle Time (min)**	**2. Cycle Time (min)**	**3. Cycle Time (min)**	**Cycle Time (Real Time Study)**
X1	2,2	1,6	4,8	3,1	5,1
X2	2,3	2,6	4,7	3,1	5,0
X3	2,2	4,7	3,6	3,0	5,0
X4	2,1	1,7	4,8	3,1	5,1
X5	2,1	2,4	4,5	3,0	4,8
X6	2,1	2,4	4,6	3,0	4,8
X10	2,2	4,0	3,8	3,1	4,3
X11	2,3	2,6	4,5	3,1	4,7
X12	2,1	1,7	4,8	3,1	5,1
X13	2,2	2,6	4,6	3,2	4,9
X14	2,3	1,7	5,0	3,1	5,3
X15	2,3	2,5	4,8	3,0	5,1
X18	2,3	1,7	5,0	3,1	5,3
X19	2,1	2,4	4,6	3,0	4,9
X20	2,2	4,0	3,8	3,1	4,3
X21	2,2	2,5	4,8	3,0	5,1
X22	2,2	4,0	3,8	3,1	4,3
X23	2,3	1,7	5,0	3,1	5,3
X24	2,3	2,6	4,6	3,2	4,9
X25	2,2	4,0	3,8	3,1	4,3
X26	1,7	1,6	5,1	3,1	5,4

| After the tire is cooked, air gaps are seen in the tread dough. | Why ? : Openings occur between the rubber strips on the back of the carcass. | Why ? : The rubber strips on the back of the carcass are not fully adhered to the tire pack.. | Why ? : Necessary pressure has not been given for the adhesion of the rubber strips. | Why ? : The rubber strips are wider than in the slow cycle time. | Why ? : Rubber strips are wrapped in rubber package with wider mold mouth. |

Figure 6. Root Cause Analysis of the Final Product

Table 8. Tire Production Quantities

Tire Size Code	2022 Production Volume (pieces/year)	Old Cycle Time (Identified)	New Cycle Time	Production Volume Savings (tire/year)	Tire Size Code	2023 Production Volume (pieces/year)	Old Cycle Time	New Cycle Time	Production Volume Savings (tire/year)
X1	1617	5,42	5,1	100	X14	4894	5,42	5,3	140
X2	144	5,42	5,0	12	X15	10918	5,42	5,1	636
X3	168	5,42	5,0	15	X16	3977	5,42	4,9	461
X4	312	5,42	5,1	21	X17	144	5,42	4,3	38
X5	552	5,42	4,8	73	X18	3923	5,42	5,3	112
X6	432	5,42	4,8	52	X19	2324	5,42	4,9	269
X7	72	5,42	5,0	6	X20	1051	5,42	4,3	277
X8	12	5,42	5,1	1	X21	1356	5,42	5,1	86
X9	72	5,42	5,0	6	X22	1128	5,42	4,3	297
X10	3875	5,42	4,3	1020	X23	802	5,42	5,3	25
X11	14258	5,42	4,7	2080	X24	550	5,42	4,9	58
X12	13463	5,42	5,1	886	X25	191	5,42	4,3	50
X13	4894	5,42	4,9	567	X26	144	5,84	5,4	11

Effects Analysis (FMEA) for two different production lines. SWOT Analysis was used to identify each production line's strengths, weaknesses, opportunities, and threats. As a result of this analysis, the advantages between both production lines were evaluated. By Failure Modes and Effects Analysis, the probabilities of detecting the errors encountered in the lines were evaluated, and the line where risky errors could be detected more easily was selected.

With the brainstorming method, a team of experts determined a perfect and even process that needs improvement. The study was completed by evaluating the effects of the changed parameters on the final product and process. It has been determined that the changes made do not constitute an obstacle regarding continuity and final product quality.

It is concluded that the BX line is superior to the AX line. Then, video-time analysis and line balancing work were carried out on the BX line, and an improvement of 10% was achieved. Annual tire revenue is 7299. Since the product quality will directly affect the demand for the product, Root Cause Analysis was applied on the BX line, and a solution was found to the quality problem of the selected line by reducing the width of the mold mouth used in the production of rubber strips from 32.5 mm to 28.5 mm.

Decreased cycle times were calculated for 26 different tire productions. Table 8. shows how many more tires can be produced with the new cycle in the time spent for the number of tires to be produced with the old cycle time.

A total of 7299 volumes were saved for 26 different tire types. For example, In the time taken to produce 1617 pieces of the X1 tire, 1717 pieces can be produced with the new cycle time. The production volume determined at the beginning of the period for 2022 is 71273 units. While 71273 tires were produced in 386,630.1 minutes with the old cycle time, the same pieces can be produced in 351.583.4 minutes with the new cycle times. Total time savings for 2022 production volume is 34,776.7 minutes, ie., 24.15 days. Total time saving is 9%. The % time improvements based on tire types are shown in Table 9.

Table 9. % Time Recovery by Measure

Tire Size Code	% Improvement by Time	Tire Size Code	% Improvement by Time
X1	5,85	X14	2,78
X2	7,89	X15	5,50
X3	8,16	X16	10,38
X4	6,35	X17	20,84
X5	11,68	X18	2,78
X6	10,75	X19	10,39
X7	8,16	X20	20,84
X8	6,68	X21	5,93
X9	8,23	X22	20,84
X10	20,84	X23	3,00
X11	12,73	X24	9,47
X12	6,17	X25	20,84
X13	10,38	X26	6,93

With the new cycle times, the line's capacity has been increased by 10.24%. The firm can produce 6,398 units of the X26 tire with the highest cycle time of 34,776.7 minutes won and 8105 units of the X22 tire with the lowest cycle time. The averavalue of how many pieces of all tires can be produced with new cycle times in the time gained is 7155. The company shared symbolic information about the cost and sales prices of the tire group for which the process improvement study was carried out. The average production cost of the tire group, whose process has been improved, is 700 TL and the average selling price is 600 EUR. While the production cost of 7155 tires that can be produced in the time saved is 5008500 TL for the company, the selling price is 4293000 EUR. In the calculation made by taking the EUR exchange rate of 17.41 dated 29.05.2022, the company has made a profit of approximately 69.732.630 TL from the improvement work.

This study can be considered a comprehensive evaluation to improve the production process and increase efficiency. Methods such as SWOT Analysis and FMEA have helped to objectively evaluate the results by using them in stages such as identifying strengths and weaknesses, analyzing possible failure modes and their effects, and planning improvement steps.

Author Statements:

References

[1] Krajewski, L. J., Rıtzman L. P. and Malhotra M. K. (2014). *Üretim yönetimi süreçler ve tedarik zincirleri (9. Ed)*, (S. Birgün, Trans.), Nobel publications, Ankara. https://books.google.com.tr/books/about/%C3%9Cretim_y%C3%B6netimi.html?id=G5JqngEACAAJ&redir_esc=y

[2] Kirkham, L., Garza-Reyes, J. A., Kumar, V. and Antony J. (2014). Prioritisation of operations ımprovement projects in the europan manufacturing ındustry. *International Journal of Production Research*, 52(18); 5323-5345. Doi: 10.1080/00207543.2014.903345

[3] Patel N., Chauhan N. and Trivedi P. (2015). Benefits of value stream mapping as a lean tool ımplementation manufacturing ındustries: a review. *International Journal for Innovative Research in Science & Technology*, 1(8); 53-57. http://www.ijirst.org/articles/IJIRSTV1I8017.pdf

[4] Türkan, T. and Görener, A. (2017). Süreç iyileştirme: vasıflı çelik üretim sektöründe bir uygulama, *Optimum Ekonomi ve Yönetim Bilimleri Dergisi*, 4(2); 23-40. Doi: https://doi.org/10.17541/optimum.282050

[5]Gupta, A., Singh, R.K. and Suri P.K. (2018). Sustainable service quality management by logistics

service providers: an ındian perspective, *Global Business Review*, 19(3); 130-150. Doi: https://doi.org/10.1177/0972150918758098

[6] Avunduk, H. (2019). Yalın altı sigma: bir pet şişirme makinesinde süreç iyileştirme uygulaması, *Elektronik Sosyal Bilimler Dergisi*, 18(70); 633-653. Doi: https://doi.org/10.17755/esosder.428802

[7] Sevgili, A. and Antmen, Z. F. (2019). Yalın üretim tekniklerinden değer akış haritalandırmanın bir metal işleme fabrikasında süreç iyileştirme amacıyla uygulanması, *Avrupa Bilim ve Teknoloji Dergisi*, 16, 219-228. Doi: https://doi.org/10.31590/ejosat.555940

[8] Apilioğulları, L. (2020). Yalın altı sigma ve endüstri 4.0 entegrasyonu ile kalite iyileştirme vaka çalışması, *Anemon Muş Alparslan Üniversitesi Sosyal Bilimler Dergisi*, 8(5); 1497-150. https://dergipark.org.tr/tr/pub/anemon/issue/57135/640553

[9] Sarı, İ., Sergi, D. and Özuduruk, S. F. (2020). Müşteri hizmetleri bölümünde süreç analizi ve stratejik planlama lastik sektöründe bir uygulama, *Eskişehir Teknik Üniversitesi Bilim Ve Teknoloji Dergisi*, 8(2); 191-211. Doi: https://doi.org/10.20290/estubtdb.604569

[10] Berber, G. and Deste, M. (2018). Süreç iyileştirme uygulamaları üzerine bir literatür araştırması, *Uluslararası Ekonomi, İşletme ve Politika Dergisi*, 2(2); 213-230. Doi: https://doi.org/10.29216/ueip.462265

[11] Özan, M. (2021). Süreç yönetimi ve süreç iyileştirmenin işletme performansına etkilerinin analizi. *İşletme Araştırmaları Dergisi*, *13*(2), 1144-1161. Doi:https://doi.org/10.20491/isarder.2021.1189

[12] Çelik, H. (2020). Süreç iyileştirmede kaizen ve kaikaku uygulaması. *Avrasya Sosyal ve Ekonomi Araştırmaları Dergisi*, 7(4), 245-259. https://dergipark.org.tr/en/pub/asead/issue/54055/708375#article_cite

[13] Oskaloğlu, E. (2019). *Üretim işletmelerinde süreç iyileştirme tekniklerinin kullanılabilirliği üzerine bir araştırma* (Master's thesis, İnönü Üniversitesi Sosyal Bilimleri Enstitüsü). http://abakus.inonu.edu.tr/xmlui/handle/11616/15071

[14] Sütçü, A., Karşıyaka, O. & Burhan, M. E. (2019). Bir mobilya üretim tesisinde iş analizi ve benzetim uygulaması ile süreç verimliliğinin artırılması. *Avrupa Bilim ve Teknoloji Dergisi*, (17). 45-57. DOI: 10.31590/ejosat.609563

[15] Uluskan, M. (2019). Süreç yeterlilik analizinin genişletilmiş kaizen yöntemine entegrasyonu: otomotiv sektöründe bir uygulama. *Eskişehir Osmangazi Üniversitesi Mühendislik ve Mimarlık Fakültesi Dergisi*, 27(3), 165-183. DOI: 10.31796/ogummf.581278

[16] Yildiz, B., & Sayin, B. (2019). Süreç Yönetiminin Ürün İnovasyon Performansı Üzerindeki Etkisinde Rekabet Yoğunluğunun Düzenleyici Rolü. *Business and Economics Research Journal*, *10*(2), 575-586. https://www.ceeol.com/search/article-detail?id=762619

[17] Selimoğlu, S. K., Yeşilçelebi, G., & Altunel, M. (2021). İç denetim süreçlerini iyileştirme ve risk yönetimi araçları: Yalın altı sigma ve FMEA. *Muhasebe ve Finansman Dergisi*, 201-218. Doi: https://doi.org/10.25095/mufad.950760

[18] Akkurt, I Basyigit C., Kilincarslan S., Beycioglu, A. 2010. Prediction of photon attenuation coefficients of heavy concrete by fuzzy logic. *Journal of the Franklın Instıtute-Engıneerıng and Applıed Mathematıcs.* 347(9);1589-1597. DOI: 10.1016/j.jfranklin.2010.06.002

[19] Arslankaya, S. and Çelik, M. T. (2021). Prediction of Heart Attack Using Fuzzy Logic Method and Determination of Factors Affecting Heart Attacks. *International Journal of Computational and Experimental Science and Engineering,* 7(1); 1-8. https://doi.org/10.22399/ijcesen.837731

[20] Basyigit, C, Akkurt I, Kilincarslan S. and Beycioglu A. (2010). Prediction of compressive strength of heavyweight concrete by ANN and FL models. *Neural Computıng & Applıcatıons* 19(4);507-513 DOI: 10.1007/s00521-009-0292-9

[21] Caymaz, T., Çalışkan, S. and Botsalı, A.R. (2022). Evaluation of Ergonomic Conditions using Fuzzy Logic in a Metal Processing Plant. *International Journal of Computational and Experimental Science and Engineering,* 8(1); 9-24 https://doi.org/10.22399/ijcesen.932994

[22] Çilli, A., Beken, M. and Kurt, N. 2022. Determination of Theoretical Fracture Criteria of Layered Elastic Composite Material by ANFIS Method from Artificial Intelligence. *International Journal of Computational and Experimental Science and Engineering,* 8(2); 32-39. https://doi.org/10.22399/ijcesen.1077328

[23] Akkurt, İ. Boodaghi Malidarreh P. and Boodaghi Malidarre R.,., (2021): Simulation and Prediction the Attenuation Behavior of the KNN-LMN Based Lead Free Ceramics by FLUKA Code and Artificial Neural Network (ANN) - Based Algorithm, *Environmental Technology*, DOI: 10.1080/09593330.2021.2008017

[24] Boodaghi Malidarre R., Akkurt İ, Boodaghi Malidarreh P. and Arslankaya S. (2022). Investigation and ANN-based prediction of the radiation shielding, structural and mechanical properties of the Hydroxyapatite (HAP) bio-composite as artificial bone. *Radiation Physics and Chemistry*. 197;110208. https://doi.org/10.1016/j.radphyschem.2022.110208

[25] Ural, A. and Kilimci, Z. H. (2021). The Prediction of Chiral Metamaterial Resonance using Convolutional Neural Networks and Conventional Machine Learning Algorithms. *International Journal of Computational and Experimental Science and Engineering,* 7 (3); 156-163 . https://doi.org/10.22399/ijcesen.973726

[26] Ecer, B. , Aktas, A. , Kabak, M. and Dağdeviren, M. (2020). Determining the Best Maternity Hospital by Using a Fuzzy Decision Making Model. *International Journal of Computational and Experimental Science and Engineering,* 6(1); 7-12. https://doi.org/10.22399/ijcesen.646157

[27] Kırelli, Y., Arslankaya, S., Alcan, P. (2022). MRI Image Analysis with Deep Learning Methods in Brain Tumor Diagnosis. In: Sen, Z., Oztemel, E., Erden, C. (eds) Recent Advances in Intelligent Manufacturing and Service Systems. *Lecture Notes in Mechanical Engineering.* Springer, Singapore. Print ISBN 978-

981-16-7163-0Online ISBN 978-981-16-7164-7
https://doi.org/10.1007/978-981-16-7164-7_4

[28] Çelik M.T. and Arslankaya S. (2023). Analysis of Quality Control Criteria in An Business With The Fuzzy Dematel Method: Glass Business Example. *Journal of Engineering Research.* 11(2);100039, https://doi.org/10.1016/j.jer.2023.100039

[29] Boodaghi Malidarre R., Arslankaya S., Nar M., Kırelli Y., Erdamar I.Y.D., Karpuz N., Ozhan Dogan S. and Boodaghi Malidarre P. (2022). Deep learning prediction of gamma-ray-attenuation behavior of KNN–LMN ceramics. *Emerging Materials Research* 11(2);276-282
https://doi.org/10.1680/jemmr.22.00012

[30] Imamoglu, M.Y., Akkurt, I., Arslankaya, S. et al. (2022). Prediction of radiation shielding properties for concrete by artificial neural networks. *Eur. Phys. J. Plus* 137;865 https://doi.org/10.1140/epjp/s13360-022-02815-3

[31] Teke Ç., Akkurt İ., Arslankaya S., Ekmekci, İ and Gunoglu K. (2023). Prediction of gamma ray spectrum for 22Na source by feed forward back propagation ANN model. *Radiation Physics and Chemistry*, 202;110558,
https://doi.org/10.1016/j.radphyschem.2022.110558

[32] A. Bakeer, I. S. Mohamed, P. Boodaghi Malidarreh, I. Hattabi and L. Liu, (2022). An Artificial Neural Network-Based Model Predictive Control for Three-Phase Flying Capacitor Multilevel Inverter. *in IEEE* 10;70305-70316, 2022, doi: 10.1109/ACCESS.2022.3187996.

[33] Kırelli Y. and Arslankaya S. (2020). Sentiment Analysis of Shared Tweets on Global Warming on Twitter with Data Mining Methods: A Case Study on Turkish Language. *Computational Intelligence and Neuroscience* 2020;1904172
https://doi.org/10.1155/2020/1904172

[34] Erol, Y. (2019). Stratejik yönetimde swot analizi ve bir işletmede uygulanması, Master's thesis, İstanbul Kultur University.
https://acikerisim.iku.edu.tr/entities/publication/30df3ecb-6b5f-4544-9046-ed9e30d74a75

[35] Turan, M. and Ocaktan, D. (2019). Transformatör üreten bir firmada risk analizinde bulanık htea kullanımı ve uygulama yazılımı geliştirme, *Balıkesir Üniversitesi Fen Bilimleri Enstitüsü Dergisi*, 21(1); 474-487. Doi:
https://doi.org/10.25092/baunfbed.549171

[36] Berber, G. and Deste, M. (2021). Bir gıda işletmesinde süreç iyileştirme uygulaması: dondurma fabrikası örneği, *Anadolu Üniversitesi İktisadi ve İdari Bilimler Fakültesi Dergisi*, 22(3); 53-72. Doi: https://doi.org/10.53443/anadoluibfd.959147

[37] Kaya, D.Ş. (2017). Root cause analysıs: examples of scenarıo, *Gümüşhane University Journal Of Health Sciences*, 6(4); 247-251. https://search.trdizin.gov.tr/tr/yayin/detay/285749/root-cause-analysis-examples-of-scenario
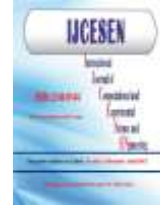
Applying the Fuzzy PERT Method in Project Management: A Real-Life Case Study

Emre KENAR[1], Mümtaz İPEK[2], Muharrem DÜGENCİ[3], Ömer Abdulaziz KORKMAZ[4]*

[1]Karabük University, Faculty of Engineering, Industrial Engineering Department, 78050, Karabük-Turkey
Email: emrekenar06@gmail.com - **ORCID:** 0000-0002-0989-3242

[2]Sakarya University, 54050, Sakarya-Turkey
Email: ipek@sakarya.edu.tr - **ORCID:** 0000-0001-9619-2403

[3]Karabük University, Faculty of Engineering, Industrial Engineering Department, 78050, Karabük-Turkey
Email: mdugenci@karabuk.edu.tr - **ORCID:** 0000-0001-7091-9096

[4]Karabük University, Faculty of Engineering, Industrial Engineering Department, 78050, Karabük-Turkey
* **Corresponding Author**: **Email:** o_aziz96@outlook.com - **ORCID:** 0000-0002-4603-0876

Abstract:

Time is the most precious resource for any business simply because no one can bring time back. Therefore, there is a huge need to be able to control time accurately. Also, the competitiveness between companies increased the value of time. Many investments were allocated to build methodologies that help to use time effectively. Because it became a fact that the speed of work accomplishment is the main factor for being a considerable competitor. Planning for future projects usually relays on non-fixed but mostly expected data. It is more reliable to use fuzzy methods for this situation. In this study, Fuzzy PERT (FPERT) was used as a project management technique to plan the construction of a marble factory from the establishment phase to the plan of the machines that will be used later on. FPERT showed more realistic results than any classical method would. Out of 16 routes, the final result of the completion time was (90.9,122.1,151.9) days which was determined after triangular fuzzy numbers for the activity times in the entire project. This article aims to prove the efficiency of fuzzy methodologies especially FPERT to be conducted in future planned projects through this real-life case study.

1. Introduction

Recently, the competition between companies forced all the owners and managers to develop their firms. Technology is a double-edged sword in this case because it is one of the most significant reasons for to increase in the competition rate between companies, and it is the solution using it to be improved. The main aim for all firms is to use all their resources (human & material) effectively. They seek to be more productive, complete their projects and achieve their targets without any waste and with the least costs. The most important resource that companies should focus on is time. By managing time appropriately, following up with the other sources can happen very smoothly. Therefore, there becomes a huge need for new models in order to manage complicated projects and operations' time to simplify tracking and

following up. Both CPM (Critical Path Method) and PERT (Program Evaluation and Review Technique) were developed based on the network to help project managers to schedule projects [1]. They were the most popular models that companies tend to use due to their efficiency in managing projects and simplifying the timeline of each process.

CPM and PERT were developed in the same period between 1956 and 1958 but by two different research groups. CPM was developed while building a chemical factory by the R&D department in E. I. Dupont De Nemours company. On the other hand, the PERT model was developed while conducting Polaris nuclear submarine project for the US Navy by Booz Allen Hamilton. As a result, by applying PERT, the US Navy could finish the project two years

before the scheduled time. By applying techniques such as CPM and PERT, it became easier to observe the important activities and operations that affect the project to focus on them and provide the critical resources to be able to schedule the project precisely. At the same time, the activities that could have less importance or efficiency on the project schedule can be postponed or neglected to finish the project on time. Nevertheless, the classical methods that gave very good results in a simple and isolated environment, may not give the same outcomes in complex business. As a matter of fact, the rapid improvement of science and technology makes the process of decision-making more difficult owing to the uncertainty and the difficulties of analyzing features. Therefore, modern business society became more complex, and the classical models need to be improved. The classical PERT model in the modern complex environment couldn't be accurate so the duration variance in projects in real-life became overestimated and as a result of these criticisms, many interesting and extensive studies had been conducted in the last 60 years to improve models which can be used instead of the classical ones [2].

In 1965, a new concept was developed by Lotfi A. Zadeh [3]. He developed the Fuzzy Set Theory which was concerned with uncertain and fuzzy data with the same importance as well-defined data. However, this concept started to be used only in the second half of the seventies, and this was regarding his articles in that period which were very effective and specific about the ability to apply fuzzy logic to systems that are characterized by uncertainty. In the second half of the eighties, fuzzy logic started to be used on some Japanese products which gave it a huge momentum and reached its current climax. Today, the applications of fuzzy logic can be observed in all fields. Additionally, the source is separated according to the application of the fuzzy logic, and each application is represented in a list according to the specification of its source. Instead of transferring the same list here, at this phase, it will be sufficient to list several fuzzy logic applications in the Electrical Engineering field [3]. The importance of the Fuzzy Set Theory is the ability to examine the real world and express it mathematically, so it goes beyond the boundaries of classical mathematics and involves uncertainty in the decision-making processes [4]. Many fields started to use this theory such as linear & nonlinear programming, operations research,

goal programming, transportation models, and even in-game theory [5].

The first sign of Fuzzy PERT was in 1979 by Prade, and then, Chanas and Kamburowski discussed the Fuzzy PERT method and defined the times of activities by triangular fuzzy numbers [6]. They argued that the Beta distribution can be used only based on previous experiments and include 30 activities or more in the network [7]. Generally, there is no big difference between the classical way and the fuzzy one but when there are uncertain values, it became difficult to define a deadline to end a project; so, in this case, the methods of fuzzy logic trigonal should be conducted [8].

In this study, a Fuzzy PERT method which is a combination between the PERT model and the concept of Fuzziness was examined to be able to make decisions with uncertain values. In order to make it more understandable, this study will be conducted on a real-life project to build and establish a marble factory. The study includes the foundation of the construction process, the construction of the factory building, and the assembling of the machines that will be used in production. All these activities will be included, and the results will be examined.

2. Material and Methods

Lastly, it was observed clearly that the PERT & CPM techniques used in many studies were built on the Fuzzy concept. Day by day, the usage of these Fuzzy models is increasing due to the fantastic and effective innovation to solve the issue of uncertainty. The usage of Fuzzy Methods in almost all since and technology fields led to new perspectives in decision-making especially in industrial systems [9].. The literature studies show that the FPERT provides more realistic results than the classical model. With fuzzy models, the uncertainty of sources that will be planned in projects for the first time can be minimized or even eliminated by using fuzzy numbers.

Fuzzy Pert and Fuzzy CPM were both developed to use fuzzy numbers to determine the times of activities in the second half of the 1970s. The classical formula of Fuzzy CPM is to find the determinant activity times and replace them with fuzzy numbers. There are different definitions for the Critical Path which provide different estimations regarding the degree of criticality by using the same path in the system [10]Click or tap here to enter text.

In 1980, the Fuzzy shortest path and Fuzzy PERT/CPM were analyzed by Dubois and Prade [6]. To compare and add Fuzzy values they used extended addition/subtraction and fuzzy maximum/minimum. After that in 1981, Chanas and Kamburowski suggested an approach based on extended aggregation and strong level sets in solving fuzzy PERT [11]..

McCahon and Lee (1988) compared the comparison and composite method of Lee and Li (1987) to find and determine the project completion time, and they stated that the comparison between these methods is more understandable [12].

Based on probability theory, Buckley 1989 developed a Fuzzy PERT model. However, the early starts and slack times were still difficult to be calculated. On the other hand, Klein 1991 proposed an approach using a dynamic programming formulation to solve the Fuzzy shortcut problem.

In this study, a benchmarking method was used by Gencer and Türkbey in 2001, which is known as FPERT [13]. Gencer and Türkbey were assuming that the fuzzy time for each job is known in their projects. In the comparison method to find out the completion time of a project, the earliest fuzzy start-end in forwarding transition is defined as, and for backward transition, the latest fuzzy start-end is defined, and they should be calculated as shown below.

$$E\tilde{S}_i = \max [E\tilde{S}_j (+) \tilde{A}_j] \quad (1)$$
$$v_j \in P_i$$
$$E\tilde{F}_i = E\tilde{S}_i (+) \tilde{A}_i \quad (2)$$
$$L\tilde{F}_i = \min [L\tilde{F}_j (-) \tilde{A}_j] \quad (3)$$
$$v_j \in S_i$$
$$L\tilde{S}_i = L\tilde{F}_i (-) \tilde{A}_i \quad (4)$$

A_j, J is the fuzzy duration for a job, (+) fuzzy addition, (-) fuzzy subtraction, v_j, j. job, p_i, j is the premise set of work, S_i, j is the post-work set. While using triangular fuzzy numbers and in the cases when more than one job should be finished before another job can start, the premise fuzzy factors will be used to find the earliest start time of a new job $S(\tilde{A}_i)$, $m(\tilde{A}_i)$,

$$m(\tilde{A}_i) > m(\tilde{A}_j) \quad \text{or} \quad m(\tilde{A}_i) = m(\tilde{A}_j)$$

and

$$s(\tilde{A}_i) < s(\tilde{A}_j) \quad (5)$$

When the conditions are fulfilled, $\tilde{A}_i > \tilde{A}_j$ will be accepted and, $\tilde{A}_{i_i}$ values will be considered as the earliest starting times. Here,

$$m(\tilde{A}) = 1/3(a+b+c) \quad \text{and} \quad s(\tilde{A})=1/18(a^2+b^2+c^2-ab-ac-bc) \quad (6)$$

The above formulation will be accepted.

3. Results and Discussions

The activity periods which are considered triangular fuzzy numbers from companies A, B, and C are identified in Table 2. While calculating the average times, the taken time from each company has been estimated at a ratio of 0.33 and by summing all the time, different average values were founded.

The average value: $a_{(A,B,C)}, m_{(A,B,C)}, b_{(A,B,C)}$

$a_{(A,B,C)}$ = is taken as the average of good periods from A, B and C companies and it is calculated with the formula $a_{(A,B,C)} = a_A + a_B + a_C$,
while $a_{(A)} = A_1/3, = a_B/3, = C_1/3$

It is expressed as:

A_1 = the best activity period of company A, B_1 = the best activity period of company B, and C_1 = the best activity period of company C.

$m_{(A,B,C)}$ = is accepted as the average of the most probable periods taken from companies A, B, and C. the calculation method is the same method of calculating the best activity period.

$b_{(A,B,C)}$ = is accepted as the average of the best activity period taken from companies A, B, and C. the calculation method is the same method of calculating the best and the most probable periods of activity.

Table 1 is showing all the activities times, the premise activities, activities periods from 3 different companies, the average of the periods of these companies, the earliest starting time ES, the earliest ending time EF, the latest starting time LS, and the latest ending time LF [14]. According to the calculated times, the project completion time T is the job of O6, EF in the table. Below, this situation is expressed mathematically.

$$(x-93.6) / (126.1-93.6), \quad 93.6 \ x \ 126.1$$

$$\mu_t (x)= (156.6-x) / (156.6-126.1), \quad 26.1 \ x \ 151.6$$

$$0, \quad 156.6 < x$$

It is calculated as Cpi = sup [Tpi ^ T], while Tpi in the formula is the fuzzy path length of i, ^ is the intersection of two sets, sup is the largest value of a set, and Tpi = (+)$_{j=pi}$ [13].

Table 1. The Activity Table

Code	Activity	Premise Activity	Activity Period	Average Value	ES	EF	LS	LF
	Excavation and Foundation Works							
A	Floor Arrangement	-	(1,2,5) (2,3,5) (3,4,6)	(2,3,5.3)	0	(2,3,5.3)	0	(2,3,5.3)
B	Drilling Column Pits	A	(2,2,5) (3,4,5) (2,4,5)	(2.3,3.3,5)	(2,3,5.3)	(4.3,6.3,10.3)	(2,3,5.3)	(4.3,6.3,10.3)
C	Laying Ground Sewer Pipes	B	(1,2,3) (2,2,4) (1,2,4)	(1.3,2,3.7)	(4.3,6.3,10.3)	(5.6,8.3,14)	(4.3,6.3,10.3)	(5.6,8.3,14)
D	Cracking Foundation Moulds in Column Pits	C	(3,4,6) (4,5,6) (3,5,7)	(3.3,4.7,6.3)	(5.6,8.3,14)	(8.9,13,20.3)	(5.6,8.3,14)	(8.9,13,20.3)
E	Laying Iron into Moulds	D	(5,6,7) (5,7,8) (6,7,9)	(5.3,6.7,8)	(8.9,13,20.3)	(14.2,19.7, 28.3)	(8.9,13,20.3)	(14.2,19.7,28.3)
F	Building Inspection	E	(0.4,0.5,0.6) (0.3,0.5,0.7) (0.5,0.7,0.9)	(0.4,0.6,0.7)	(14.2,19.7,28.3)	(14.6,20.3,29)	(14.2,19.7,28.3)	(14.6,20.3,29)
G	Pouring Concrete into Moulds and Hardening	F	(3,4,5) (2,4,6) (3,5,6)	(2.6,4.3,5.6)	(14.6,20.3,29)	(17.2,24.6,34.6)	(14.6,20.3,29)	(17.2,24.6,34.6)
H	Removal of Moulds	G	(1,2,2) (2,3,4) (1,2,3)	(1.3,2.3,3)	(17.2,24.6,34.6)	(18.5,26.9,37.6)	(17.2,24.6,34.6)	(18.5,26.9,37.6)
	Prefabricated Factory Building Construction Works							
G1	Placing Concrete Columns in Slots	H	(7,9,11) (8,9,10) (9,10,12)	(8,9.3,11)	(18.5,26.9,37.6)	(26.5,36.2,48.6)	(18.5,26.9,37.6)	(26.5,36.2,48.6)
G2	Connecting Columns with Beams	G1	(6,7,8) (5,6,9) (5,6,8)	(5.3,6.3,8.3)	(26.5,36.2,48.6)	(31.8,42.5,56.9)	(26.5,36.2,48.6)	(31.8,42.5,56.9)
G3	Pouring Concrete on the Factory Floor	G2	(3,4,5) (3,5,7) (4,6,7)	(3.3,5,6.3)	(31.8,42.5,59.6)	(35.1,47.5,63.2)	(31.8,42.5,56.9)	(35.1,47.5,63.2)
G4	Laying Concrete Floors on Administrative Building Floors	G3	(2,4,5) (3,4,5) (3,4,6)	(2.6,4,5.3)	(35.1,47.5,63.2)	(37.7,51.5,68.5)	(31.5,47.5,63.2)	(37.7,51.5,68.5)
G4'	Pouring Concrete at Assembly Points	G4	(1,2,2) (2,3,4) (2,3,3)	(1.6,2.6,3)	(37.7,51.5,68.5)	(39.3,54.1,71.5)	(37.7,51.1,68.5)	(39.3,54.1,71.5)
G5	Installation of Roof Panels	G4	(4,5,6) (4,6,7) (5,6,8)	(4.3,5.6,7)	(39.3,54.1,71.5)	(43.6,59.7,78.5)	(84.1,112.2,139.4)	(88.4,117.8,146.4)
G6	Laying Rainwater Pipes	G5	(3,4,5) (2,3,3) (3,5,6)	(2.6,4,4.6)	(43.6,59.7,78.5)	(46.2,63.7,83.1)	(88.4,117.8,146.4)	(91,121.8,151)
G7	Laying of Sewer Pipes	C	(3,4,5) (2,3,3) (3,5,6)	(2.6,4,4.6)	(5.6,8.3,14)	(8.2,12.3,18.6)	(49,65.7,85.6)	(51.6,69.7,90.2)
G8	Rainwater Line Laying	G6	(3,4,5) (2,4,6) (3,5,6)	(2.6,4.3,5.6)	(46.2,63.7,83.1)	(48.8,68,88.7)	(91,121.8,151)	(93.6,126.1,156.6)
G9	Welding Iron Profiles on Columns	G2	(16,19,21) (15,16,17) (18,20,21)	(16.3,18.3,19.6)	(31.8,42.5,56.9)	(48.1,60.8,76.5)	(43.4,66.5,89.1)	(59.7,84.8,108.7)
G10	Assembling of Wall Panels to Profiles	G9	(6,7,8) (5,6,9) (5,6,8)	(5.3,6.3,8.3)	(48.1,60.8,76.5)	(53.4,67.1,84.8)	(59.7,84.8,108.7)	(65,91.1,117)
G11	Installation of Factory Doors and Fire Doors	G10	(4,5,6) (3,4,4) (4,6,7)	(3.6,5,5.6)	(53.4,67.1,84.8)	(57,72.1,90.4)	(65,91.1,117)	(68.6,96.1,122.6)
G12	Laying of Electrical Installation in the Factory	G11	(21,24,26) (22,23,24) (20,25,28)	(21,24,26)	(57,72.1,90.4)	(78,96.1,116.4)	(68.6,96.1,122.6)	(89.6, 120.1,148.6)

G13	Laying of In-Factory Air Installation	G11	(2,2,5) (3,4,5) (2,4,5)	(2.3,3.3,5)	(57,72.1,90.4)	(59.3,75.4,95.4)	(91.3,122.8,151.6)	(93.6,126.1,156.6)
G14	Laying of In-Factory Plumbing	G11	(3,4,6) (4,5,6) (3,5,7)	(3.3,4.6,6.3)	(57,72.1,90.4)	(60.3,76.7,96.7)	(86.3,115.5,142.3)	(89.6,120.1,148.6)
G15	Production Units Partition with Sheet Metals	G11	(10,12,14) (9,11,12) (11,12,13)	(10,11.6,13)	(57,72.1,90.4)	(67,83.7,103.4)	(74.2,100.4,124.2)	(84.2,112,137.2)
	In-Factory Crane Installation							
H1	Laying Crane Rails with Mobile Crane	G15	(3,4,5) (2,3,3) (3,5,6)	(2.7,3.3,4.6)	(67,83.7,103.4)	(69.7,87,108)	(88.2,118.6,147)	(90.9,121.9,151.6)
H2	Sitting a Bridge on Two Rails	H1	(0.5,1,1.5) (0.4,0.6,1.2) (0.8,1,1.2)	(0.6,0.9,1.3)	(69.7,87,108)	(70.3,87.9,109.3)	(90.9,121.9,151.6)	(91.5,122.8,152.9)
H3	Assembling of Engines on the Bridge	H2	(0.4,0.5,0.6) (0.3,0.5,0.6) (0.5,0.7,0.8)	(0.4,0.6,0.7)	(70.3,87.9,109.3)	(70.7,88.5,110)	(91.5,122.8,152.9)	(91.9,123.4,153.6)
H3'	Laying of Electrical Cable Trays	G12, G14	(1,1.5,2) (0.9,1.3,1.6) (0.5,1,1.5)	(0.8,1.3,1.7)	(78,96.1,116.4)	(78.8,97.4,117.7)	(91.1,122.1,152.3)	(91.9,123.4,153.6)
H4	Pulling and Connection of Crane Electrical Installations	H3, H3'	(1,2,2) (2,3,4) (2,3,3)	(1.7,2.7,3)	(78.8,97.4,117.7)	(80.5,100.1,120.7)	(91.9,123.4,153.6)	(93.6,126.1,156.6)
	Establishment of the Knuckle Machine							
I1	Cracking Machine Wall Mouldings	G15	(3,4,5) (2,3,3) (3,5,6)	(2.6,4,4.6)	(67,83.7,103.4)	(69.6,87.7,108)	(84.2,112,137.2)	(86.8,116,141.8)
I2	Knitting of Machine Wall Irons	I1	(1,2,2) (2,3,4) (2,3,3)	(1.6,2.3,3)	(69.6,87.7,108)	(71.2,90,111)	(86.8,116,141.8)	(88.4,118.3,144.8)
I3	Pouring Machine Wall Concrete	I2	(0.3,0.4,0.5) (0.2,0.3,0.3) (0.3,0.5,0.6)	(0.3,0.4,0.5)	(71.2,90,111)	(71.5,90.4,111.5)	(88.4,118.3,144.8)	(88.7,118.7,145.3)
I4	Removal of Moulds	I3	(0.2,0.3,0.4) (0.1,0.2,0.2) (0.3,0.5,0.6)	(0.2,0.3,0.4)	(71.5,90.4,111.5)	(71.7,90.7,111.9)	(88.7,118.7,145.3)	(88.9,119,145.7)
I5	Placing the Machine Engine on the Concrete Floor	I4	(0.5,1,1.5) (0.4,0.6,1.2) (0.8,1,1.2)	(0.4,0.9,1.3)	(71.7,90.7,111.9)	(72.1,91.6,113.2)	(88.9,119,145.7)	(89.3,119.9,147)
I6	Body Assembly of Cutter Wires	I5	(1,2,5) (2,3,5) (3,4,6)	(2,3,5.3)	(72.1,91.6,113.2)	(74.1,94.6,118.5)	(89.3,119.9,147)	(91.3,122.9,152.3)
I7	Installation of Transfer Arm Between Motor and Cutter	I6	(0.5,1,1.5) (0.4,0.6,1.2) (0.8,1,1.2)	(0.6,0.5,1.3)	(74.1,94.6,118.5)	(74.7,95.1,119.8)	(91.3,122.9,152.3)	(91.9,123.4,153.6)
I7'	Laying of Electrical Cable Trays	G12, G14	(2,2,5) (3,4,5) (2,4,5)	(2.3,3.3,5)	(78,96.1,116.4)	(80.3,99.4,121.4)	(89.6,120.1,148.6)	(91.9,123.4,153.6)
I8	Assembly and Electrical Connection of Machine Electrical Panel	I7, I7'	(1,2,2) (2,3,4) (2,3,3)	(1.7,2.7,3)	(80.3,99.4,121.4)	(82,102.1,124.4)	(91.9,123.4,153.6)	(93.6,126.1,156.6)
	Establishment of Plate Wiping Line							
K1	Moulding into the Ground	G15	(1,1.5,2) (0.5,1,1.5) (1,1.5,2)	(0.8,1.3,3)	(67,83.7,103.4)	(67.8,85,106.4)	(85.5,112.9,138.2)	(86.3,114.2,141.2)
K2	Throwing Concrete on the Ground in a Balanced Way	K1	(0.4,1.1,2) (0.3,1.3,1.6) (0.3,1,1.2)	(0.3,1.1,1.6)	(67.8,85,106.4)	(68.1,86.1,108)	(86.3,114.2,141.2)	(86.6,115.3,142.8)
K3	Positioning the Machine	K2	(0.3,0.4,0.5) (0.2,0.3,0.3) (0.3,0.5,0.6)	(0.3,0.4,0.5)	(68.1,86.1,108)	(68.4,86.5,108.5)	(86.6,115.3,142.8)	(86.9,115.7,143.3)
K4	Installation of Input and Output Conveyors	K3	(2,4,5) (3,4,5) (3,4,6)	(2.7,4,5.3)	(68.4,86.5,108.5)	(71.1,90.5,113.8)	(86.9,115.1,143.3)	(89.6,119.7,148.6)

K5	Installing the Plate Loading Robot	K4	(2,3,5) (3,4,5) (2,4,5)	(2.3,3.7,5)	(71.1,90.5,113.8)	(73.4,94.2,118.8)	(89.6,119.7,148.6)	(91.9,123.4,153.6)
K5'	Laying of Electrical Cable Trays	G12, G14	(2,3,4) (1.5,2,4) (2,4,6)	(1.8,3,4.7)	(78,96.1,116.4)	(79.8,99.1,121.1)	(90.1,120.4,148.9)	(91.9,123.4,153.6)
K6	Machinery Electrical Installation and Connection	K5, K5'	(1,2,2) (2,3,4) (2,3,3)	(1.7,2.7,3)	(79.8,99.1,121.1)	(81.5,101.8,124.1)	(91.9,123.4,153.6)	(93.6,126.1,156.6)
	Bridge Cutting Machine Installation							
L1	Positioning the Machine	G15	(1,1.5,2) (0.9,1.3,1.6) (0.5,1,1.5)	(0.8,1.3,1.7)	(67,83.7,103.4)	(67.8,85,105.1)	(89.6,120.3,149.3)	(90.4,121.6,151)
L2	Levelling the Machine with Feet	L1	(1.2,1.6,2) (1,1.3,1.7) (0.5,1,1.5)	(0.9,1.3,1.7)	(67.8,85,105.1)	(68.7,86.3,106.8)	(90.4,121.6,151)	(91.3,122.9,152.7)
L2'	Laying of Electrical Cable Trays	G12, G14	(1,2,2) (2,3,4) (2,3,3)	(1.7,2.7,3)	(78,96.1,116.4)	(79.7,98.8,119.4)	(89.6,120.2,149.7)	(91.3,122.9,152.7)
L3	Machinery Electrical Installation and Connection	L2, L2'	(1.6,2,2.5) (1.4,2.2,2.8) (1.5,2,2.4)	(1.5,2.1,2.6)	(79.7,98.8,119.4)	(81.2,100.9,122)	(91.3,122.9,152.7)	(92.8,125,155.3)
L4	Making Cut Calibrations	L3	(0.8,1,1.4) (1,1.3,1.5) (0.6,0.9,1.1)	(0.8,1.1,1.3)	(81.2,100.9,122)	(82,102,123.3)	(92.8,125,155.3)	(93.6,126.1,156.6)
	Administrative Section Ground Floor Construction Works							
M1	Building a Wall with Brick	G4'	(8,11,12) (6,8,10) (5,9,11)	(6.3,9.3,11)	(39.3,54.1,71.5)	(45.6,63.4,82.5)	(39.3,54.1,71.5)	(45.6,63.4,82.5)
M1'	Opening Pipe Channels to Walls	M1	(4,5,6) (3,5,6) (5,7,8)	(3.3,5.7,6.7)	(45.6,63.4,82.5)	(48.9,69.1,89.2)	(48.3,64,83.5)	(51.6,69.7,90.2)
M2	Installation of Windows	M1	(3,4,5) (2,3,3) (3,5,6)	(2.7,4,4.7)	(45.6,63.4,82.5)	(48.3,67.4,87.2)	(50.2,68.4,88.5)	(52.9,72.4,93.2)
M3	Electrical Installation	M1	(6,8,11) (7,9,10) (9,10,11)	(7.3,9,10.7)	(45.6,63.4,82.5)	(52.9,72.4,93.2)	(45.6,63.4,82.5)	(52.9,72.4,93.2)
M4	Plumbing and Heating System Installation	M1	(2,2,5) (3,4,5) (2,4,5)	(2.3,3.3,5)	(45.6,63.4,82.5)	(47.9,66.7,87.5)	(50.6,69.1,88.2)	(52.9,72.4,93.2)
M5	Laying of Wastewater Pipes	M1', G7	(1,2,2) (2,3,4) (2,3,3)	(1.3,2.7,3)	(48.9,69.1,89.2)	(50.2,71.8,92.2)	(51.6,69.7,90.2)	(52.9,72.4,93.2)
M6	Screed Removal	M2, M3, M4, M5	(4,5,6) (3,4,4) (4,6,7)	(3.7,5,5.7)	(52.9,72.4,93.2)	(56.6,77.4,98.9)	(52.9,72.4,93.2)	(56.6,77.4,98.9)
M6'	Watering the Screed for Hardening	M6	(0.6,0.8,1) (0.5,0.8,1) (0.5,0.6,0.7)	(0.5,0.7,0.9)	(56.6,77.4,98.9)	(57.1,78.1,99.8)	(56.6,77.4,98.9)	(57.1,78.1,98.9)
M7	Plaster Works	M6'	(9,11,13) (8,10,11) (10,11,12)	(9,10.7,12)	(57.1,78.1,99.8)	(66.1,88.8,111.8)	(60.6,85,107.9)	(69.6,95.7,119.9)
M8	Ceramics, Tile Works	M7	(4,5,6) (4,6,7) (5,6,8)	(4.7,5.7,7)	(66.1,88.8,111.8)	(70.8,94.5,118.8)	(73.9,100.7,124.9)	(78.6,106.4,131.9)
M9	Paint Works	M8	(2,2,5) (3,4,5) (2,4,5)	(2.3,3.3,5)	(70.8,94.5,118.8)	(73.1,97.8,123.8)	(79,106.4,131.9)	(81.3,109.7,136.9)
M10	Natural Gas Installation and Honeycomb Installation	M9	(4,5,6) (4,6,7) (5,6,8)	(4.3,5.7,7)	(73.1,97.8,123.8)	(77.4,103.5,130.8)	(81.3,109.7,136.9)	(85.6,115.4,143.9)
M11	Installation of Parquet, Doors, Cabinets	M10	(4,5,6) (3,4,4) (4,6,7)	(3.7,5,5.7)	(77.4,103.5,130.8)	(81.1,108.5,136.5)	(86.2,116.1,145.2)	(89.9,121.1,150.9)
	Administrative Section 1st Floor							

	Construction Works							
N1	Building a Wall with Brick	G4'	(8,11,12) (6,8,10) (5,9,11)	(6.3,9.3,11)	(39.3,54.1,71.5)	(45.6,63.4,82.5)	(50.8,68.8,88.8)	(57.1,78.1,99.8)
N1'	Opening Pipe Channels to Walls	N1, M6'	(4,5,6) (3,5,6) (5,7,8)	(3.3,5.7,6.7)	(57.1,78.1,99.8)	(60.4,83.8,106.5)	(59.8,78.7,100.8)	(63.1,84.4,107.5)
N2	Installation of Windows	N1, M6'	(3,4,5) (2,3,3) (3,5,6)	(2.7,4,4.7)	(57.1,78.1,99.8)	(59.8,82.1,104.5)	(61.7,83.1,105.8)	(64.4,87.1,110.5)
N3	Electrical Installation	N1, M6'	(6,8,11) (7,9,10) (9,10,11)	(7.3,9,10.7)	(57.1,78.1,99.8)	(64.4,87.1,110.5)	(57.1,78.1,99.8)	(64.4,87.1,110.5)
N4	Plumbing and Heating System Installation	N1, M6'	(2,2,5) (3,4,5) (2,4,5)	(2.3,3.3,5)	(57.1,78.1,99.8)	(59.4,81.4,104.8)	(62.1,83.8,105.5)	(64.4,87.1,110.5)
N5	Laying of Wastewater Pipes	N1', G7	(1,2,2) (2,3,4) (2,3,3)	(1.3,2.7,3)	(60.4,83.8,106.5)	(61.7,86.5,109.5)	(63.1,84.4,107.5)	(64.4,87.1,110.5)
N6	Screed Removal	N2, N3, N4, N5	(4,5,6) (3,4,4) (4,6,7)	(3.7,5,5.7)	(64.4,87.1,110.5)	(68.1,92.1,116.2)	(64.4,87.1,110.5)	(68.1,92.1,116.2)
N6'	Watering the Screed for Hardening	N6	(0.6,0.8,1) (0.5,0.8,1) (0.5,0.6,0.7)	(0.5,0.7,0.9)	(68.1,92.1,116.2)	(68.6,92.8,117.1)	(69.1,95,119)	(69.6,95.7,119.9)
N7	Plaster Works	N6', M7	(9,11,13) (8,10,11) (10,11,12)	(9,10.7,12)	(68.6,92.8,117.1)	(77.6,103.5,129.1)	(69.6,95.7,119.9)	(78.6,106.4,131.9)
N8	Ceramics, Tile Works	N7, M8	(4,5,6) (4,6,7) (5,6,8)	(4.7,5.7,7)	(77.6,103.5,129.1)	(82.3,109.2,136.1)	(78.6,106.4,131.9)	(83.3,112.1,138.9)
N9	Paint Works	N8, M9	(2,2,5) (3,4,5) (2,4,5)	(2.3,3.3,5)	(82.3,109.2,136.1)	(84.6,112.5,141.1)	(83.3,112.1,138.9)	(85.6,115.4,143.9)
N10	Natural Gas Installation and Honeycomb Installation	N9, M10	(4,5,6) (4,6,7) (5,6,8)	(4.3,5.7,7)	(84.6,112.5,141.1)	(88.9,118.2,148.1)	(85.6,115.4,143.9)	(89.9,121.1,150.9)
N11	Installation of Parquet, Doors, Cabinets	N10, M11	(4,5,6) (3,4,4) (4,6,7)	(3.7,5,5.7)	(88.9,118.2,148.1)	(92.6,123.2,153.8)	(89.9,121.1,150.9)	(93.6,126.1,156.6)
	Exterior and Landscaping							
O1	Establishment of Scaffolding for Exterior Insulation	N6	(3,4,5) (2,3,3) (3,5,6)	(2.7,4,4.7)	(68.1,92.1,116.2)	(70.8,96.1,120.9)	(68.1,92.1,116.2)	(70.8,96.1,120.9)
O2	Laying of Insulation Materials	O1	(6,8,9) (6,7,8) (5,7,9)	(5.7,7.3,8.7)	(70.8,96.1,120.9)	(76.5,103.4,129.6)	(70.8,96.1,120.9)	(76.5,103.4,129.6)
O3	Exterior Plaster and Paint	O2	(2,3,3) (3,4,5) (3,4,4)	(2.7,3.7,4)	(76.5,103.4,129.6)	(79.2,107.1,133.6)	(76.5,103.4,129.6)	(79.2,107.1,133.6)
O4	Building the Garden Wall	O3	(7,9,11) (8,9,10) (9,10,12)	(8,9.3,11)	(79.2,107.1,133.6)	(87.2,116.4,144.6)	(79.2,107.1,133.6)	(87.2,116.4,144.6)
O5	Parquet Stone Laying	O4	(5,8,10) (5,7,8) (4,6,9)	(4.7,7,9)	(87.2,116.4,144.6)	(91.9,123.4,153.9)	(87.2,116.4,144.6)	(91.9,123.4,153.6)
O6	Green Field Works	O5	(1,2,2) (2,3,4) (2,3,3)	(1.7,2.7,3)	(91.9,123.4,153.6)	(93.6,126.1,156.6)	(91.9,123.4,153.6)	(93.6,126.1,156.6)

For the marble factory establishment, there are 16 alternative routes between the beginning and the end of the project. Since all activity durations are 3-sided fuzzy numbers, fuzzy path lengths are calculated as the sum of the fuzzy durations of all activities in the route. These routes are listed as follows.

1. Route: A-B-C-D-E-F-G-H-G1-G2-G3-G4-G4'-M1-M3-M6-M6'-N3-N6-O2-O3-O4-O5-O6: **(90.9,122.1,151.9)**

2. Route: A-B-C-G7-M5-M6-M6'M7-M8-M9-M10-M11-N11 : **(41.40,56.10,76.60)**

3. Route: A-B-C-D-E-F-G-H-G1-G2-G9-G10-G11-G12-L2'-L3 L4: **(82,102,123,30)**

4. Route: A-B-C-D-E-F-G-H-G1-G2-G3-G4-G4'-N1-N2-N6-N6'-N7-N8-N9-N10-N11 : **(76.5,103.5,130.5)**

5. Route: A-B-C-D-E-F-G-H-G1-G2-G9-G10-G11-G15-K1-K2-K3-K4-K5-K6: **(75.1,96.9,121.8)**

6. Route: A-B-C-D-E-F-G-H-G1-G2-G3-G4-G4'-M1-M1'-M5-M6-M6'-M7-M8-M9-M10-M11-N11: **(82.10,112.90,141.2)**

7. Route: A-B-C-D-E-F-G-H-G1-G2-G3-G4-G4'-M1-M4-M6-M6'-N1'-N5-N6-O1-O2-O3-O4-O5-O6: **(85.90,119.80,149.90)**

8. Route: A-B-C-D-E-F-G-H-G1-G2-G3-G4-G5-G6-G8: **(47.20, 65.40,85.7)**

9. Route: A-B-C-D-E-F-G-H-G1-G2-G9-G10-G11-G13: **(58, 73.1, 92.40)**

10. Route: A-B-C-D-E-F-G-H-G1-G2-G9-G10-G11-G14-H3'-H4: **(62.8, 80.7,101.4)**

11. Route: A-B-C-D-E-F-G-H-G1-G2-G9-G10-G11-G14-K5'-K5: **(64.4, 83.4, 106.4)**

12. Route: A-B-C-D-E-F-G-H-G1-G2-G9-G10-G11-G14-I7-I8: **(62.6,79.9,101)**

13. Route: A-B-C-D-E-F-G-H-G1-G2-G9-G10-G11-G15-L1-L2 L3-L4: **(72.7,92.2,113.7)**

14. Route: A-B-C-D-E-F-G-H-G1-G2-G9-G10-G11-G15-H1-H2-H3-H4: **(72.4,91.2,113)**

15. Route: A-B-C-D-E-F-G-H-G1-G2-G9-G10-G11-G15-I1-I2-I3-I4-I5-I6-I7-I8: **(76.4,97.8,122.8)**

16. Route: A-B-C-D-E-F-G-H-G1-G2-G3-G4-G4'-M1-M2-M6-M6'-N4-N6-01-02-03-04-05-06: **(84, 115.4, 144.9)**

After calculating the durations of all alternative paths in the network diagram, the degrees of the criticality of all paths can be calculated. The degrees of the criticality of all paths were calculated in Figure 1 and are shown in Table 2.
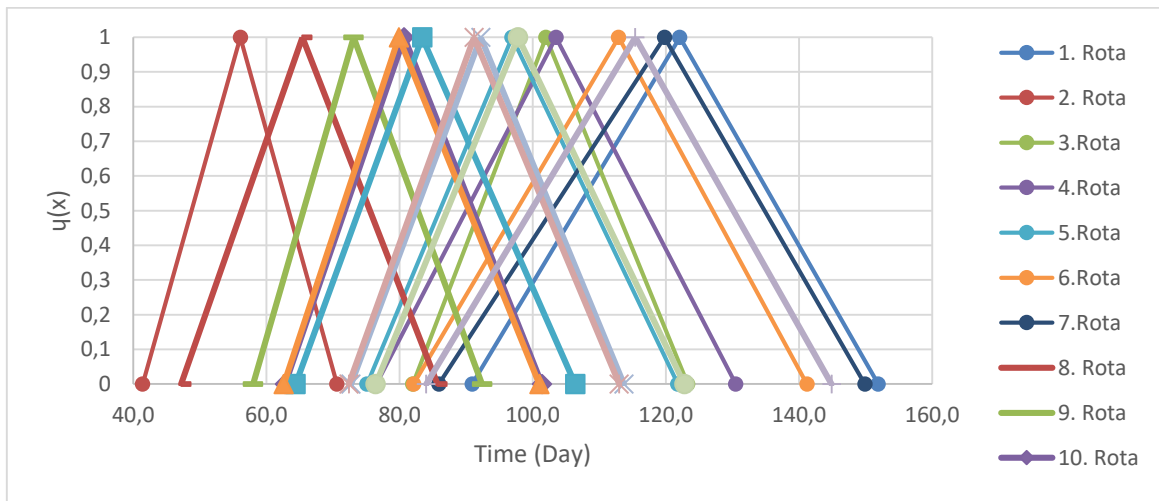
Figure 1. *Calculation of the Degrees of the Criticality of Alternative Routes* (Cp_i)

In this project management using the fuzzy PERT method, among the 16 alternative routes included in the whole network diagram, according to the results of the degrees of criticality in the chart, the 1st route as the critical path of the project, The route A-B-C-D-E-F-G-H-G1-G2-G3-G4-G4'-M1-M3-M6-M6'-N3-N6-O2-O3-O4-O5-06 was determined as (90.9,122.1,151.9) days as fuzzy completion times.

4. Conclusion

Project management is used extensively in production and the construction industry. Effective use of project management techniques is important because the construction process is difficult and involves many complex activities. The project management designed for the marble factory installation was implemented with the Fuzzy PERT method. As Chanas and Kamburowski discussed in the early eighties, this study converted the times of activities into triangular fuzzy numbers. Also, the huge number of activities and their complexity supported the possibility of applying the fuzzy concept effectively as mentioned in the literature review. Moreover, the study was very detailed and informative. It considered all the processes of

Table 2. Degrees of the Criticality of the Paths

Path	Cp_i
1. Route	1.00
2. Route	-0.44
3. Route	0.61
4. Route	0.68
5. Route	0.55
6. Route	0.84
7. Route	0.96
8. Route	-0.1
9. Route	0.03
10. Route	0.20
11. Route	0.28
12. Route	0.19
13. Route	0.43
14. Route	0.41
15. Route	0.56
16. Route	0.88

establishing and equipping a factory from the foundation works until the final accessory assembling bathing through building the production lines and setting up the machinery. Therefore, this application proves the efficiency of the used technique which is the FPERT method that had been developed by Gencer and Türkbey in 2001. According to the literature review, many studies relayed on fuzzy PERT in the last two decades to get more reliable results. This study should be an important addition to the other study because of the real data it worked on and the results it achieved. Furthermore, the study was very specialized in the marble industry, and this qualifies it to make great contributions either in the practical application or the research field in factories establishment generally or the marble industry particularly. It is expected to build on this article in different studies such as establishing factories in other sectors or in the same industry from different points of view, aspects, and details.

While a probability distribution is used in the estimation of the activity time in classical methods, there is no probability in the Fuzzy PERT technique and the working times are fuzzy, the project durations are calculated with uncertain limits. While making the calculations, unlike the classical PERT technique, the uncertainty dominates. This uncertainty can give the project team ideas about any deviations that may occur in the completion times of the projects. In other words, it provides flexibility to the project team while determining and planning the completion time of the project.

References

[1] Simion, M., Vasile, G., Dinu, C., & Scutariu, R. (2019). CPM and PERT techniques for small-scale R&D projects. *International Symposium "The Environmental and The Industry,"* (SIMI 2019). https://doi.org/10.21698/simi.2019.fp22

[2] Ballesteros-Pérez, P. (2017). M-PERT: Manual Project-Duration Estimation Technique for Teaching Scheduling Basics. *Journal of Construction Engineering and Management*, *143*(9). https://doi.org/10.1061/(asce)co.1943-7862.0001358

[3] Zadeh, L. A. (1973). Outline of a New Approach to the Analysis of Complex Systems and Decision Processes. *IEEE Transactions on Systems, Man and Cybernetics*, *SMC-3*(1). https://doi.org/10.1109/TSMC.1973.5408575

[4] Steyn, J., & Stoker, P. (2014). Does Measurement Theory Impact Project Performance? *Procedia - Social and Behavioral Sciences*, *119*. https://doi.org/10.1016/j.sbspro.2014.03.071

[5] Junior, R. R., & de Carvalho, M. M. (2013). Understanding the impact of project risk management on project performance: An empirical study. *Journal of Technology Management and Innovation*, *8*(SPL.ISS.2). https://doi.org/10.4067/s0718-27242013000300006

[6] Prade, H. (1979). Using fuzzy set theory in a scheduling problem: A case study. *Fuzzy Sets and Systems*, *2*(2). https://doi.org/10.1016/0165-0114(79)90022-8

[7] Chanas, S., & Kamburowski, J. (1981). The use of fuzzy variables in pert. *Fuzzy Sets and Systems*, *5*(1). https://doi.org/10.1016/0165-0114(81)90030-0

[8] Mazlum, M., & Güneri, A. F. (2015). CPM, PERT and Project Management with Fuzzy Logic Technique and Implementation on a Business. *Procedia - Social and Behavioral Sciences*, *210*. https://doi.org/10.1016/j.sbspro.2015.11.378

[9] Aziz, R. F. (2013). Optimizing strategy software for repetitive construction projects within multi-mode resources. *Alexandria Engineering Journal*, *52*(3). https://doi.org/10.1016/j.aej.2013.04.002

[10] Chanas, S., & Zieliński, P. (2001). Critical path analysis in the network with fuzzy activity times. *Fuzzy Sets and Systems*, *122*(2). https://doi.org/10.1016/S0165-0114(00)00076-2

[11] Chanas, S., Dubois, D., & Zieliński, P. (2002). On the sure criticality of tasks in activity networks with imprecise durations. *IEEE Transactions on Systems, Man, and Cybernetics, Part B: Cybernetics*, *32*(4). https://doi.org/10.1109/TSMCB.2002.1018760

[12] McCahon, C. S., & Stanley Lee, E. (1990). Comparing fuzzy numbers: The proportion of the optimum method. *International Journal of Approximate Reasoning*, *4*(3). https://doi.org/10.1016/0888-613X(90)90019-X

[13] Gencer, & Türkbey. (2001). Proje tamamlanma zamaninin bulunmasinda istatistiksel analiz yardimiyla bulanik-pert, klasik-pert ve gerçek-dağilim yöntemlerinin karşilaştirilmasi. *Dokuz Eylül Üniversitesi Mühendislik Fakültesi Fen ve Mühendislik Dergisi*, *3*(2); 29–39.

[14] Lootsma, F. A. (1989). Stochastic and fuzzy Pert. *European Journal of Operational Research*, *43*(2). https://doi.org/10.1016/0377-2217(89)90211-7
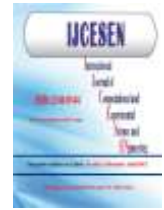
Dynamic Modelling of the Spring Attached Two-Link Planar Manipulator

Onur DENIZHAN*

Batman University, Department of Electronics and Automation, 72060, Batman-Türkiye
* **Corresponding Author**: **Email:** onur.denizhan@batman.edu.tr - **ORCID:** 0000-0001-8380-9507

Abstract:

Robot dynamics is necessary not just for simulation and control, but also for the analysis of robot motion planners and controllers. There are a number of dynamic modelling investigations of robots with the different approaches and these investigations mostly focus on the link flexibility, joint friction or actuator dynamics. In addition to that these studies present dynamic model without any attached linear or torsion springs. In this study, the dynamic modelling of a two-link rigid manipulator with attached torsion springs is presented using the Lagrangian approach. The Lagrangian approach is a variational method that relies on the kinetic and potential energy of the mechanism, making it well-suited for the analysis of the two-link planar manipulator considered in this study. Initially, the equations of motion for the two-link rigid mechanism is derived without any attached torsion springs. Subsequently, two torsion springs are attached to the joints of the mechanism, and the existing equations of motion are modified accordingly. The study also presents the kinetic, potential and total energies of the two link-manipulator, angular positions of the links and their velocities. By considering the dynamic modelling of the torsion spring attached two-link rigid manipulator, this study contributes to understanding and analysis of the two-link manipulators and the dynamic effects of the attached springs.

1. Introduction

The representative dynamic model is essential and required to design and control of the mechanisms; therefore, having accurate dynamic model is very significant. There are different mechanisms for the different tasks and robotic manipulator mechanism is one them. The robotic manipulators are widely used in the industrial manufacturing tasks due to their versatility and precision. Some of these tasks require high sensitivity, where even small deviations can have significant consequences. The robotic manipulators typically consist of joints and links, which can be either rigid or flexible. The flexible manipulators have some advantages over the rigid manipulators such as low energy consumption, small size, larger workspace or light weight. Hence, a number of studies and designs have been investigated for the flexible manipulators. On the other hand, there are not many studies on the dynamic modelling of the rigid manipulators because rigid manipulators are simpler to model due to their inherent stiffness and lack of deformations.

The following articles present some of the dynamic modelling investigations: Khairudin et. al [1] investigates the dynamic modelling and characterization of a two-link flexible robot manipulator. This study combines Euler and Lagrange approaches, considering structural damping, hub inertia and payload. Subudhi and Morris [2] present the dynamic modelling and control of a manipulator with multiple flexible links and flexible joints. This study uses a combined Euler-Lagrange formulation, which simplifies the control of the complex two-link flexible manipulator. In this study, the results demonstrate good tracking performance and stabilization of the links. Chen [3] investigates the dynamic model of a multi-link flexible robotic manipulator. This study proposes a linearized dynamic model for a planar flexible manipulator with an arbitrary number of flexible links. The study employs the Lagrangian approach with Euler-Bernoulli beams and presents numerical simulations. Subedi et. al [4] presents a closed-form dynamic model for planar multi-link flexible manipulators. This study utilizes the Lagrangian formulation and discuss the robot's

configuration with a payload. The study focuses on both static and dynamic modelling. Morris and Madani [5] investigate static and dynamic modelling for a two-link flexible robotic manipulator. This study separately examines the elastic and rigid motions of the two links and then combine them using the superposition principle. Nicosia et. al. [6] presents dynamic modelling and experimental validation of a two-link flexible robot. This article provides an exact dynamic model for the robotic arm and carries out simulations along with experimental validation. Mayeda et. al. [7] investigates the base parameters of dynamic models for parallel and perpendicular manipulators with only rotational joints. This study focuses on non-redundant parameters of the dynamic model for these manipulators. Thomas and Tesar [8] present dynamic modelling for serial manipulator arms. This article derives the dynamic model for a serial manipulator with a rigid link model. Mehrjooee [9] conducts a non-linear dynamic analysis of a flexible-link manipulator. The study investigates the possibility of chaos occurrence in a two-link flexible robot mechanism and provides experimental validation for verification. Gamarra-Rosado and Yuhara [10] explore dynamic modelling and simulation of a flexible robotic manipulator with flexible links and two revolute joints. This article employs the Newton-Euler formulation to derive the dynamic model. Vakil et. al [11] proposes a new method for dynamic modelling of a flexible-link rigid-joint manipulator. This article introduces a dynamic model in terms of independent generalized coordinates without Lagrange multipliers. The method is validated through simulation examples. De Luca and Sciliano [12] present an explicit dynamic model for a planar two-link lightweight flexible robot. This article introduces a complete and accurate dynamic model using Euler-Bernoulli beams with uniform density, a standard Lagrangian approach, and rotary joints. Lochan et al. [13] provides a survey on two-link flexible robots. The article discusses dynamical analysis, complexities, modelling methods, and various aspects of works related to two-link flexible manipulator. Hasting and Book [14] present a linear dynamic model for the flexile robotic manipulators. This article introduces a linear state-space dynamic model for a single-link flexible manipulator. Arteaga [15] investigates some properties for the dynamic model of the flexible robotic manipulators. This study presents a dynamic model of the flexible manipulators based on the Lagrange's equations and discusses several significant properties of the presented dynamic model. Springs are commonly used in various robot designs to provide compliance, damping, or force/torque sensing capabilities. When springs are

present, their dynamics should be properly incorporated into the overall dynamic model of the robot to accurately capture their effects on the system's behavior. In this study, the dynamic model of the torsion springs attached two-link rigid planar manipulator is presented. The dynamic model is developed using the Lagrangian formulation approach, which is a variational method based on the kinetic and potential energy of the system. Additionally, this study presents the positions and velocities of two-link planar manipulator rigid links and the kinetic, potential and total energies of the two-link manipulator without any attached springs. By presenting the dynamic model, this study contributes to the understanding and analysis of the two-link rigid planar manipulator with attached torsion springs. This information can be valuable for the designing controllers, analyzing system stability, and optimizing the manipulators performance in various applications.

2. Design of the Torsion Spring-Attached Two-Link Planar Manipulator
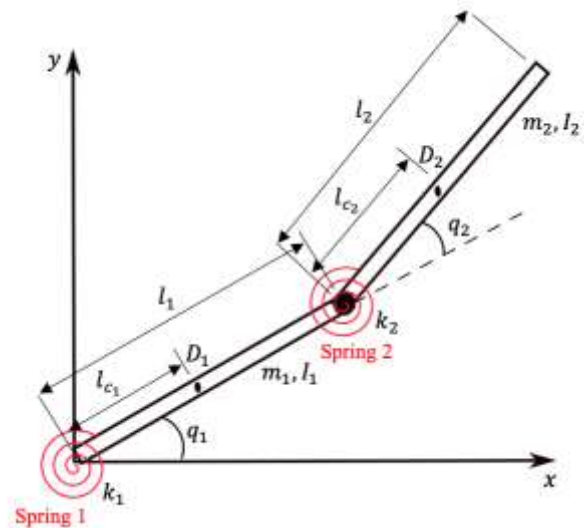
Figure 1. *The two-link planar manipulator with two torsion springs.*

Figure 1 illustrates the configuration of a two-link planar rigid manipulator with two torsion springs and its corresponding parameters. The manipulator consists of two revolute joints with torsion springs attached, and the links are rigid. The parameters l_1 and l_2 represent the lengths of Links 1 and 2, respectively. The parameter m_1 corresponds to the mass of Link 1, while m_2 denotes the mass of Link 2. The parameter I_1 refers to the centroid moment of inertia for Link 1 and I_2 denotes the centroid moment of inertia for Link 2. The parameters τ_1 and τ_2 represent the joint torques for Joints 1 and 2, respectively. The parameters l_{c_1} and l_{c_2} indicate the center of mass positions of Links 1 and 2 relatives to

Joints 1 and 2, respectively. The parameter q_1 represents the angle of Link 1 relative to the x- axis, and the parameter q_2 represents the angle of Link 2 relative to Link 1. The parameters D_1 and D_2 represent the center of mass points of the Links 1 and 2 respectively. The parameter k_1 denotes the stiffness of Spring 1, and k_2 refers to the stiffness of Spring 2. It is important to note that the two-link planar rigid manipulator does not have any motion limitations.

3. Equations of Motion for the Two-Link Planar Manipulator

There are four primary parameters involved in dynamic modelling: the joint angle, q; the joint velocity, $\dot{q}$; the joint torque, τ; and the joint acceleration, $\ddot{q}$. Dynamic modelling formulations can be approached in two ways: forward dynamics and inverse dynamics. Forward dynamics involves providing the values of q, $\dot{q}$ and τ and investigating the parameter $\ddot{q}$. This approach is particularly useful for simulation purposes, as it allows for the prediction of joint accelerations and the resulting motion of the system. On the other hand, inverse dynamics involves providing the values of q, $\dot{q}$ and $\ddot{q}$, and investigating parameter τ. Inverse dynamics is commonly employed for robot control, as it enables the determination of the required joint torques to achieve a desired motion.

In this study, the dynamic modelling of the mechanism is initially presented without attached torsion springs. This step allows for a detailed presentation of the dynamic modelling process and minimizes potential formulation errors. Once the dynamic model of the mechanism is established, the torsion springs are then introduced and incorporated into the equations of motion accordingly. By introducing the torsion spring equations, the equations of motion for the two-link planar manipulator can be easily modified. This sequential approach ensures a comprehensive understanding of the dynamics modelling steps and facilitates the proper integration of the torsion springs into the system.As previously mentioned, the dynamic modelling in this study utilizes the Lagrangian approach. The Lagrangian method is an energy-based approach to dynamic modelling, defined by the following formula:

$$L(q, \dot{q}) = T(q, \dot{q}) - V(q) \qquad (1)$$

where the parameter $L(q, \dot{q})$ denotes Lagrange, parameter $T(q, \dot{q})$ refers to the kinetic energy and the parameter $V(q)$ represents potential energy of the two-link manipulator. For a system with n-degree-of-freedom, the Euler-Lagrange formula is used to derive the equations of motion and is defined as follows:

$$\tau_i = \frac{d}{dt}\left(\frac{\partial L}{\partial \dot{q}_i}\right) - \frac{\partial L}{\partial q_i} \qquad (2)$$

where the parameter τ_i represents the ith joint torque, parameter L refers to the Lagrange function (Eq. (1)), parameter q_i refers to the angle of ith joint, parameter $\dot{q}_i$ denotes to the ith joint velocity, and parameter t represents time.

To further analyze the system, the kinetic energy formulas for Link 1 and Link 2 can be expressed separately. Starting with the kinetic energy formula for Link 1, it can be written as:

$$T_1 = \frac{1}{2}m_1 l_{c_1}(\dot{q}_1)^2 + \frac{1}{2}I_1(\dot{q}_1)^2 \qquad (3)$$

where the parameter T_1 refers to the kinetic energy of the Link 1, the parameter m_1 represents the Link 1 mass, the parameter l_{c_1} denotes the center of mass of Link 1 from Joint 1, the parameter I_1 refers to the moment of inertia of the Link 1 and parameter $\dot{q}_1$ refers to the Joint 1 angular velocity.

The kinetic energy formula for Link 2 can be expressed as:

$$\begin{aligned} T_2 = \frac{1}{2}m_2 l_1^2(\dot{q}_1)^2 &+ \frac{1}{2}m_2 l_{c_2}(\dot{q}_1 + \dot{q}_2)^2 \\ &+ m_2 l_1 l_{c_2}\dot{q}_1\cos q_2\,(\dot{q}_1 + \dot{q}_2) \\ &+ \frac{1}{2}I_2(\dot{q}_1 + \dot{q}_2)^2 \end{aligned} \qquad (4)$$

where parameter T_2 represents the kinetic energy of Link 2, parameter m_2 is the mass of Link 2, parameter l_{c_2} denotes the distance from Joint 2 to the center of mass of Link 2, parameter I_2 is the Link 2 moment of inertia and the parameter $\dot{q}_2$ represents the angular velocity of Joint 2, parameter l_1 denotes the length of Link 1.

The total kinetic energy of the two-link planar manipulator can be defined as:

$$T(q, \dot{q}) = T_1(q, \dot{q}) + T_2(q, \dot{q}) \qquad (5)$$

where parameter T represents total kinetic energy of the two-link planar manipulator. By substituting Eqns. (3) and (4) into Eq. (5), the following equation can be written:

$$\begin{aligned} T = \frac{1}{2}m_1 l_{c_1}(\dot{q}_1)^2 &+ \frac{1}{2}I_1(\dot{q}_1)^2 + \frac{1}{2}m_2 l_1^2(\dot{q}_1)^2 \\ &+ \frac{1}{2}m_2 l_{c_2}(\dot{q}_1 + \dot{q}_2)^2 \\ &+ m_2 l_1 l_{c_2}\dot{q}_1\cos q_2\,(\dot{q}_1 + \dot{q}_2) \\ &+ \frac{1}{2}I_2(\dot{q}_1 + \dot{q}_2)^2 \end{aligned} \qquad (6)$$

where the parameter T refers to the total kinetic energy of the two-link planar manipulator. As mentioned earlier, the potential energy of the mechanism is essential in the Lagrangian approach. The equation for the potential energy of Link 1 is defined as follows:

$$V_1 = m_1 g l_{c_1} \sin q_1 \qquad (7)$$

where the parameter V_1 is the Link1 potential energy, the parameter g refers to the gravitational acceleration and the parameter q_1 represents the angle of Link 1.
The equation for the potential energy of Link 2 can be defined as:

$$V_2 = m_2 g \big(l_1 \sin q_1 + l_{c_2} \sin(q_1 + q_2)\big) \qquad (8)$$

where parameter V_2 represents the Link 2 potential energy and parameter q_2 refers to the angle of Link 2 relative to Link 1. The total potential energy of the two-link planar manipulator is can be defined as:

$$V(q) = V_1(q) + V_2(q) \qquad (9)$$

where the parameter V refers to the total potential energy of the two-link manipulator. By substituting Eqns. (7) and (8) into Eq. (9), the following equation can be obtained:

$$V = m_1 g l_{c_1} \sin q_1 \\ + m_2 g \big(l_1 \sin q_1 \\ + l_{c_2} \sin(q_1 + q_2)\big) \qquad (10)$$

where the parameter V represents the total potential energy of the two-link manipulator. By substituting Eqns. (6) and (10) into the Lagrangian formula (Eq. (1)), the following equation can be written as:

$$L = \frac{1}{2} m_1 l_{c_1} (\dot{q}_1)^2 + \frac{1}{2} I_1 (\dot{q}_1)^2 + \frac{1}{2} m_2 l_1^2 (\dot{q}_1)^2 \\ + \frac{1}{2} m_2 l_{c_2} (\dot{q}_1 + \dot{q}_2)^2 \\ + m_2 l_1 l_{c_2} \dot{q}_1 \cos q_2 \, (\dot{q}_1 \\ + \dot{q}_2) + \frac{1}{2} I_2 (\dot{q}_1 + \dot{q}_2)^2 \\ - m_1 g l_{c_1} \sin q_1 \\ - m_2 g \big(l_1 \sin q_1 \\ + l_{c_2} \sin(q_1 + q_2)\big) \qquad (11)$$

where parameter L refers to the Lagrangian. The two-link rigid manipulator consists of two revolute joints, requiring the torque equations for these joints to be written separately. The Euler-Lagrange equations for Joint 1 and Joint 2 can be expressed as follows:

$$\tau_1 = \frac{d}{dt}\left(\frac{\partial L}{\partial \dot{q}_1}\right) - \frac{\partial L}{\partial q_1} \qquad (12)$$

$$\tau_2 = \frac{d}{dt}\left(\frac{\partial L}{\partial \dot{q}_2}\right) - \frac{\partial L}{\partial q_2} \qquad (13)$$

where parameter τ_1 refers to the Joint 1 torque and parameter τ_2 represents to the Joint 2 torque. By differentiating Eq. (11) and substituting Eqns. (12) and (13), the resulting equations of motion can be expressed as:

$$\big[m_1 l_{c_1}^2 + m_2\big(l_1^2 + l_{c_2}^2 + 2 m_2 l_1 l_{c_2} \cos q_2\big) \\ + I_{c_1} + I_{c_2}\big]\ddot{q}_1 \\ + \big(m_2 l_{c_2}\big(l_1 \cos q_2 + l_{c_2}\big) \\ + I_{c_2}\big)\ddot{q}_2 \\ - \big(2 m_2 l_1 l_{c_2} \sin q_2\big)\dot{q}_1 \dot{q}_2 \\ - \big(m_2 l_1 l_{c_2} \sin q_2\big)(\dot{q}_2)^2 \\ + m_1 g l_{c_1} \cos q_1 \\ + m_2 g\big(l_1 \cos q_1 \\ + l_{c_2} \cos(q_1 + q_2)\big) = 0 \qquad (14)$$

and

$$\big[m_2\big(l_{c_2}^2 + l_1 l_{c_2} \cos q_2\big) + I_{c_2}\big]\ddot{q}_1 \\ + \big[m_2 l_{c_2}^2 + I_{c_2}\big]\ddot{q}_2 \\ + m_2 l_1 l_{c_2} (\dot{q}_1)^2 \sin q_2 \\ + m_2 g l_{c_2} \cos(q_1 + q_2) = 0 \qquad (15)$$

The Eqns. (14) and (15) represent the equations of motion for the planar two-link rigid manipulator without any attached springs.

4. Equations of Motion for the Torsion Springs Attached Two-Link Planar Manipulator

As mentioned earlier, the Lagrange equation without any attached springs is defined as:

$$L(q, \dot{q}) = T(q, \dot{q}) - V(q) \qquad (16)$$

where the parameter $T(q, \dot{q})$ represents kinetic energy and $V(q)$ denotes potential energy of the mechanism. The torsion springs only possess potential energy. Therefore, the potential energies of the torsion springs need to be included in the potential energy component of the Lagrangian equation. As mentioned earlier, two torsion springs are attached to Joints 1 and 2. The potential energy of Spring 1 can be expressed as:

$$U_1 = \frac{1}{2} k_1 (q_1)^2 \qquad (17)$$

where parameter U_1 refers to the Spring 1 potential energy, parameter k_1 represents the Spring 1

stiffness and parameter q_1 denotes the angle of Link 1.

Spring 2 potential energy can be expressed as:

$$U_2 = \frac{1}{2}k_2(q_2)^2 \qquad (18)$$

where the parameters U_2, k_2 and q_2 represent the Spring 2 potential energy, Spring 2 stiffness and angle of Link 2 respectively. The torsion springs are assumed massless in this study. According to the attached springs potential energies, the modified Lagrangian equation (Eq. (16)) can be written as follows:

$$L(q, \dot{q}) = T(q, \dot{q}) - [V(q) + U_1(q) + U_2(q)] \qquad (19)$$

where parameters L, T and V represent Lagrange, kinetic energy and potential energy of the mechanism respectively and parameters U_1 and U_2 refer to in order to the Springs 1 and 2 potential energies. By substituting Eqns. (6), (10), (17) and (18) into the modified Lagrange equation (Eq. (19)), the resulting equation can be expressed as:

$$\begin{aligned}
L = &\frac{1}{2}m_1 l_{c_1}(\dot{q}_1)^2 + \frac{1}{2}I_1(\dot{q}_1)^2 + \frac{1}{2}m_2 l_1^2(\dot{q}_1)^2 \\
&+ \frac{1}{2}m_2 l_{c_2}(\dot{q}_1 + \dot{q}_2)^2 \\
&+ m_2 l_1 l_{c_2} \dot{q}_1 \cos q_2 \,(\dot{q}_1 \\
&+ \dot{q}_2) + \frac{1}{2}I_2(\dot{q}_1 + \dot{q}_2)^2 \\
&- m_1 g l_{c_1} \sin q_1 \\
&- m_2 g\big(l_1 \sin q_1 \\
&+ l_{c_2} \sin(q_1 + q_2)\big) \\
&- \frac{1}{2}k_1(q_1)^2 - \frac{1}{2}k_2(q_2)^2
\end{aligned} \qquad (20)$$

For the Euler-Lagrange formulation of the mechanism, derivation of the torsion spring potential energy equations (Eqns. (17) and (18)) can be expressed as:

$$\frac{\partial U_1}{\partial q_1} = k_1 q_1 \qquad (21)$$

$$\frac{\partial U_2}{\partial q_2} = k_2 q_2 \qquad (22)$$

$$\frac{d}{dt}\left(\frac{\partial U_1}{\partial \dot{q}_1}\right) = \frac{d}{dt}\left(\frac{\partial U_2}{\partial \dot{q}_2}\right) = 0 \qquad (23)$$

As observed in Eq. (23), the terms $\frac{d}{dt}\left(\frac{\partial U_1}{\partial \dot{q}_1}\right)$ and $\frac{d}{dt}\left(\frac{\partial U_2}{\partial \dot{q}_2}\right)$ will not affect the equations of motion as they are equal to zero. According to the Eqns. (21) and (22), the terms $\frac{\partial L_1}{\partial q_1}$ and $\frac{\partial L_2}{\partial q_2}$ will have terms $k_1 q_1$ and $k_2 q_2$ respectively. Since there is no change in the kinetic energy, the kinetic energy component

of the equations of motion remains unmodified. By substituting Eqns. (21), (22) and (23) into the Euler-Lagrange equations (Eqns. (12) and (13)), the following modified equations of motion can be obtained:

$$\begin{aligned}
\big[m_1 l_{c_1}^2 &+ m_2\big(l_1^2 + l_{c_2}^2 + 2m_2 l_1 l_{c_2}\cos q_2\big) \\
&+ I_{c_1} + I_{c_2}\big]\ddot{q}_1 \\
&+ \big(m_2 l_{c_2}(l_1 \cos q_2 + l_{c_2}) \\
&+ I_{c_2}\big)\ddot{q}_2 \\
&- \big(2m_2 l_1 l_{c_2}\sin q_2\big)\dot{q}_1 \dot{q}_2 \\
&- \big(m_2 l_1 l_{c_2}\sin q_2\big)(\dot{q}_2)^2 \\
&+ m_1 g l_{c_1}\cos q_1 \\
&+ m_2 g\big(l_1 \cos q_1 \\
&+ l_{c_2}\cos(q_1 + q_2)\big) - k_1 q_1 \\
&= 0
\end{aligned} \qquad (24)$$

and

$$\begin{aligned}
\big[m_2\big(l_{c_2}^2 &+ l_1 \, l_{c_2}\cos q_2\big) + I_{c_2}\big]\ddot{q}_1 \\
&+ \big[m_2 l_{c_2}^2 + I_{c_2}\big]\ddot{q}_2 \\
&+ m_2 l_1 l_{c_2}(\dot{q}_1)^2 \sin q_2 \\
&+ m_2 g l_{c_2}\cos(q_1 + q_2) \\
&- k_2 q_2 = 0
\end{aligned} \qquad (25)$$

The Eqns. (24) and (25) represent the modified equations of motion for the two-link planar robotic manipulator when two torsion springs are attached. As obtained in Eqns. (24) and (25), the inclusion of torsion springs introduces additional terms related to the stiffness and deformation of the springs, which affect the overall dynamics of the system.

The one of the important points about torsion spring is that they can be initially twisted, meaning they can have stored potential energy from the beginning. In such cases, the potential energy equations of the torsion springs will require an additional term for the initial twist angles, and the following equation can be written:

$$U_i = \frac{1}{2}k_i(q_i - q_{0_i})^2 \qquad (26)$$

where the parameters U_i, k_i, q_i and q_{0_i} represent spring potential energy, spring constant, spring angle and spring initial angle, respectively. In this study, q_{0_i} assumed to be 0; thus, Eqns. (24) and (25) can be written.

5. Results

In this study, thee motion of two-link rigid planar manipulator is simulated using MATLAB. The initial conditions for the simulation are set as $q_1(0) = \pi/3$, $q_2(0) = \pi/4$, $\dot{q}_1(0) = 0$, $\dot{q}_2(0) = 0$ and the simulation time is set to 10 seconds. Throughout the 10-second simulation, a total of 921

data points for the position, velocity, potential energy, kinetic energy and total energy of the two-link rigid planar manipulator are recorded using MATLAB.

The parameters used in the simulation are assumed as follows: $l_{c_1} = 0.5l_1$ and $l_{c_2} = 0.5l_2$, where all other parameters are set to 1.0 in their respective consistent MKS units. The gravitational acceleration is assumed to be 9.8 m/s², and the mechanism is considered to have free oscillation. The torsion springs are assumed to be massless, and joint frictions, external forces and vibrations are neglected in the simulation. Note that this study specifically simulates the two-link planar manipulator without any attached-torsion springs. For the direction convention, the clockwise direction is considered positive, while the counter-clockwise direction is considered negative.
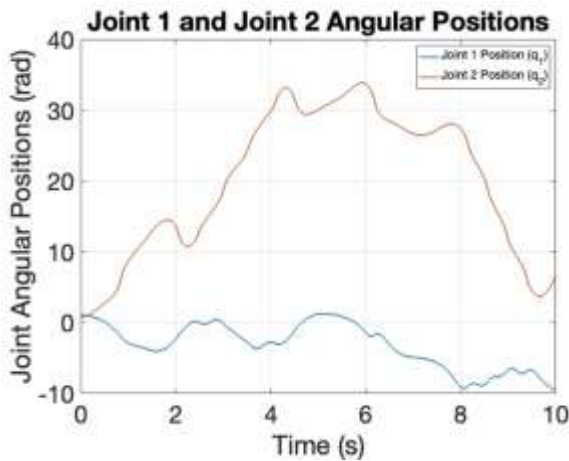
Figure 2. *The angular positions of the Link 1 and Link 2.*

Figure 2 illustrates the positions of Link 1 and Link 2, represented by the angles q_1 and q_2, respectively. Both of links undergo multiple rotations of 360 degrees during the 10-second simulation. The links sometimes change their rotation direction before completing a full 360 degrees. In the simulation, Link 1 rotates in the clockwise direction (assumed as the negative sign) from the beginning, while Link 2 rotates in the counter-clockwise direction (assumed as the positive sign). Consequently, the angle values of q_1 are negative, while the angle values of q_2 are positive. From Fig. 2, it can be observed that the initial values are $q_1 = 1,0472$ rad and $q_2 = 0,7854$ rad. After 10-second simulation, the final values are $q_1 = -9,8314$ rad and $q_2 = 6,6568$ rad. According to the Fig. 2, the Link 2 exhibits more pronounced oscillations compared to Link 1. It is important to note that the two-link manipulator mechanism is assumed to have free oscillation in this study. Figure 3 shows the velocities of Link1 and Link 2, represented by the angular velocities $\dot{q}_1$ and $\dot{q}_2$,
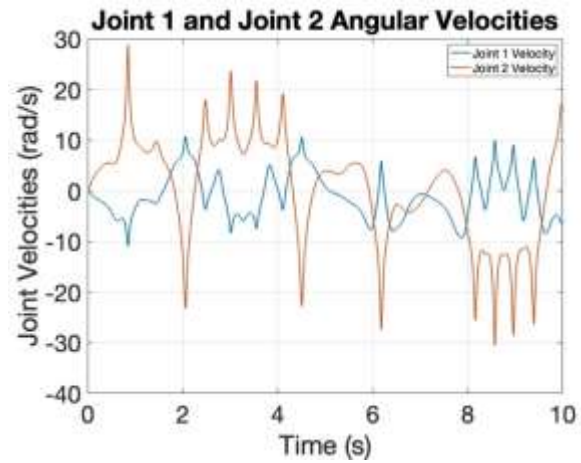
Figure 3. *The velocities of the Link 1 and Link 2.*

respectively. The velocities of both links exhibit positive and negative values due to the free oscillation of the mechanism. As a result, the links undergo rotations in both counter-clockwise and clockwise direction during the simulation, leading to changes velocity directions. From Fig. 3, it can be observed that the fluctuation of $\dot{q}_2$ is greater than the fluctuation of $\dot{q}_1$. Additionally, the rotation of link 2 is faster compared to that of Link 1. During the 10-second motion simulation, the values of $\dot{q}_2$ range between $-30,5479$ rad/s and $28,8705$ rad/s, while the values of $\dot{q}_1$ range between $-10,9336$ rad/s and $10,7907$ rad/s. as shown in Fig. 3.
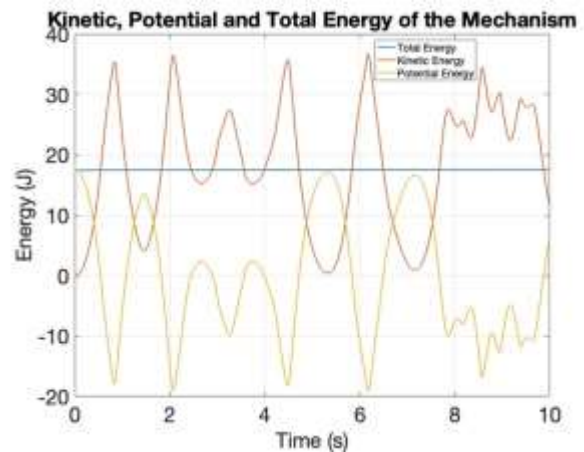
Figure 4. *The total, kinetic and potential energy of the two-link manipulator.*

Figure 4 illustrates the total, potential and kinetic energy of the two-link planar manipulator. As seen in Fig. 4, the total energy of the system remains constant throughout the motion simulation, with a value of 17,4636 J. This constancy validates the accuracy of the dynamic modelling in this study, as friction and attached springs were not considered. The potential and kinetic energy exhibit time-varying behavior during the simulation,

characterized by symmetric fluctuations. At the beginning of the motion simulation, the kinetic energy is zero since the mechanism is initially at rest. Conversely, the potential energy starts with a value of 17,4636 J, equal to the total energy of the system. As shown in Fig. 4, some potential energy values are negative, which occurs when certain positions of Link 1 and Link 2 fall below the reference x- axis. The kinetic energy values range from 0 to 36,7360 J, while the potential energy values range from $-19,1888$ J to 17,4636 J.

6. Discussion

In this article, the torsion springs attached two-link manipulator plots are not presented. The addition of torsion springs imposes limitations on the motions of the manipulator, resulting in different joint positions and velocities compared to the plots shown in this article. Furthermore, due to the potential energy stored in the torsion springs during motion, the total energy of the spring-attached two-link manipulator will not remain constant. The plots and comparison of the spring-attached two-link manipulator with case of no attached springs will be one of the future investigation directions. This will provide valuable insights into the impact of torsion springs on the dynamics of the manipulator and further enhance our understanding of the system's behavior. According to the results, it is observed that the rotation of Link 2 is faster compared to Link 1. This discrepancy can be attributed to the configuration of the mechanism, where Link 1 is fixed to the ground while Link 2 is connected to Link1. Due to the free oscillation of the system, Link 2 undergoes more rotations than Link 1 throughout the 10-second motion simulation in this study. The torsion springs in the system do not possess any kinetic energy. As a result, the modification in the equations of motion is limited to potential energy component. Only two additional terms, namely $k_1 q_1$ and $k_2 q_2$, are introduced due to the attachment of the torsion springs. Consequently, the overall equations of motion do not undergo significant changes. The influence of the torsion springs is primarily manifested though these two terms, ensuring that the modifications to the equations of motion remain relatively minor.

7. Conclusion

In this study, dynamic modelling of a two-link rigid planar manipulator with attached torsion springs is investigated. Initially, the dynamic model of the two-link manipulator is presented without the torsion springs. Subsequently, the equations of motion are modified to incorporate the torsion springs attached

to the joints of the manipulator. The addition of the torsion springs does not significantly alter the equations of motion. The results indicate that the total energy of the two-link manipulator remains constant, validating the accuracy of the dynamic model without the presence of attached springs. Furthermore, since the two-link manipulator exhibits free oscillation in this study, the position and velocity graphs illustrate the effects of this oscillatory behavior on the motion of the mechanism.

Author Statements:

- **Ethical approval:** The conducted research is not related to either human or animal use.
- **Conflict of interest:** The authors declare that they have no known competing financial interests or personal relationships that could have appeared to influence the work reported in this paper
- **Acknowledgement:** Author wishes to express his gratitude to the Ministry of National Education of the Republic of Türkiye which indirectly made this work possible.
- **Author contributions:** The authors declare that they have equal right on this paper.
- **Funding information:** The authors declare that there is no funding to be acknowledged.
- **Data availability statement:** The data that support the findings of this study are available on request from the corresponding author. The data are not publicly available due to privacy or ethical restrictions.

References

[1] Khairudin, M., Mohamed, Z., Husain, A. R., & Ahmad, M. A. (2010). Dynamic modeling and characterization of a two-link flexible robot manipulator. *Journal of Low Frequency Noise, Vibration and Active Control*, 29(3); 207-219. https://doi.org/10.1260/0263-0923.29.3.207

[2] Subudhi, B., & Morris, A. S. (2002). Dynamic modelling, simulation and control of a manipulator with flexible links and joints. *Robotics and Autonomous Systems,* 41(4); 257-270. https://doi.org/10.1016/S0921-8890(02)00295-6

[3] Chen, W. (2001). Dynamic modeling of multi-link flexible robotic manipulators. *Computers and Structures,* 79(2); 183-195. https://doi.org/10.1016/S0045-7949(00)00129-2.

[4] Subedi, D., Tyapin, I., & Hovland, G. (2021). Dynamic modeling of planar multi-link flexible manipulators. *Robotics,* 10(2); 70. https://doi.org/10.3390/robotics10020070.

[5] Morris, A.S., & Madani, A. (1996). Static and dynamic modelling of a two-flexible-link robot

manipulator. *Robotica,* 14; 289-300 doi:10.1017/S0263574700019603.

[6] Nicosia, S., Valigi, P., & Zaccarian, L. (1996). Dynamic modelling of a two link flexible robot and experimental validation, *Proceedings of IEEE International Conference on Robotics and Automation,* Minneapolis, MN, USA, 3, 1953-1958. doi: 10.1109/ROBOT.1996.506158.

[7] Mayeda, H., Yoshida, K., & Osuka, K., (June, 1990). Base parameters of manipulator dynamic models. *IEEE Transactions on Robotics and Automation*, 6(3); 312-321, doi: 10.1109/70.56663.

[8] Thomas, M., & Tesar, D. (1982) Dynamic modeling of serial manipulator arms. *J. Dyn. Sys. Meas. Control.* 104(3); 218-228. https://doi.org/10.1115/1.3139701

[9] Mehrjooee, O., Dehkordi, S. F., & Korayem, M. H. (2020). Dynamic modeling and extended bifurcation analysis of flexible-link manipulator, *Mechanics Based Design of Structures and Machines*, 48(1); 87-110, doi: 10.1080/15397734.2019.1665542

[10] Gamarra-Rosado, V. & Yuhara, E. (1999). Dynamic modeling and simulation of a flexible robotic manipulator. *Robotica,* 17(5); 523-528. doi: 10.1017/S0263574799001721

[11] Vakil, M., Fotouhi, R., & Nikiforuk, P. N. (December 28, 2011). A new method for dynamic modeling of flexible-link flexible-joint manipulators. *ASME* J. *Vib. Acoust.* 134(1); 014503. https://doi.org/10.1115/1.4004677.

[12] De Luca, A., & Siciliano, B. (1990). Explicit dynamic modeling of a planar two-link flexible manipulator, *29th IEEE Conference on Decision and Control*, Honolulu, HI, USA, 2, 528-530. doi: 10.1109/CDC.1990.203652.

[13] Lochan, K., Roy, B. K., & Subudhi, B. (2016). A review on two-link flexible manipulators, *Annual Reviews in Control*, 42; 346-367. https://doi.org/10.1016/j.arcontrol.2016.09.019.

[14] Hastings, G., & Book, W. (February, 1987). A linear dynamic model for flexible robotic manipulator, *IEEE Control Systems Magazine*, 7(1); 61-64, doi: 10.1109/MCS.1987.1105233.

[15] Arteaga, M. A. (March 1, 1998). On the properties of a dynamic model of flexible robot manipulators, *ASME J. Dyn. Sys. Meas., Control.,* 120(1); 8-14. https://doi.org/10.1115/1.2801326
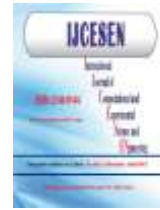
MARCMV: Mining Multi-View Association Rules from Clustered Multi-Views

Shadi AL SHEHABI[1]*, Meltem Y. IMAMOGLU[2]

[1]University of Turkish Aeronautical Association, Faculty of Engineering, Departmant of Computer Engineering, 06790, Ankara-Turkey
* **Corresponding Author** : **Email:** salshehabi@thk.edu.tr - **ORCID:** 0000-0003-0545-9104

[2]University of Turkish Aeronautical Association, Faculty of Engineering, Departmant of Computer Engineering, 06790, Ankara- Turkey
Email: meltemyi@gmail.com - **ORCID:** 0000-0002-8574-4097

Abstract:

Data mining involves examining vast quantities of data to uncover valuable insights that can be utilized for making informed decisions and driving business objectives. The study focuses on the task of finding relationships between features belonging to two different views using multi-view model, and proposes a novel approach called MARCMV. This approach extracts multi-view association rules from different views of the same data set using multi-clustering neural model. The study finds that MARCMV outperforms conventional symbolic methods in terms of association rule quality and running time.

1. Introduction

The importance of automated knowledge extraction techniques has increased with the amount of data that is now readily available. Extraction of implicit, undiscovered, and possibly practical knowledge from data is the goal of knowledge discovery. Data mining, is also known as Knowledge Discovering in Databases (KDD) [1], is a process that analyzes huge amounts of structured or unstructured information to create compact and practical summaries of information. Knowledge extraction from databases frequently uses symbolic techniques like Apriori [2], FP-growth [3], and Charm [4], although these techniques have limitations, including the creation of redundant association rules. As a result, choosing the regulations is a difficult issue. Unsupervised learning models (clustering models), which are adept in separating and gathering data from one another, have thus been suggested as alternatives to traditional approaches for extracting useful knowledge. However, when used with high-dimensional data description spaces, clustering models can also result in imprecise knowledge [5]. A multi-view approach that splits the description space of data into several subspaces, a subspace is known as a view, has been proposed to address this problem [6,7,8]. Knowledge extraction can be more precisely performed than with the global approach since each view can be clustered and represented by a clustering model [9]. Using the MultiSOM paradigm, the clustered views can communicate with one another while maintaining the connections between the subspaces [10]. In contrast to traditional symbolic methods, the unique strategy proposed in this study for mining association rules based on the communication of the clustered viewpoints produces fewer but more valuable association rules. Finding connections between various viewpoints, or subspaces, that represents the dataset in a space of several dimensions (multi-dimensional space), is the goal. A clustering model that allows things to be grouped together based on similarities is required to create a view. This approach is crucial when working with large databases because it allows us to accurately extract knowledge from clusters by using the presenter of the data rather than scanning the entire database. In order to solve the issue of producing straightforward association rules based on the communication of clustered views between

characteristics from various subspaces, this work provides a method for extracting numerical association rules between views. Overall, this research suggests a way for obtaining association rules from views using clustering models and shows that it produces more relevant association rules with fewer rules than traditional symbolic methods.

2. Related work

Association rule mining has been the subject of a variety of studies in the knowledge discovery in databases (KDD) sector. Symbolic techniques like Apriori, FP-growth, and Charm have been extensively applied to this. However, these methods have some limitations, including the generation of a huge number of redundant rules, making the rule selection process complex. Moreover, they cannot directly extract association rules between different views. Al Shehabi and Lamirel describe a method to extract straightforward association rules [9] using clustering models, where an association rule consists one feature in the preceding part and one feature in the following part. The space of high-dimensional data descriptions is first divided into a variety of subspaces, each of which is referred to as a view. A clustering model is then used to group each view. Unsupervised Neural Network Models are then utilized to preserve the relationship between the subspaces (views) by communicating between the clustered views. When compared to conventional symbolic methods, the suggested approach produces fewer but more beneficial simple association rules.

A technique to discover non-redundant association rules that explain the relationships between two perspectives of the same dataset was put out by Leeuwen and Galbrun [11] in 2015. They introduced translation tables that connect the two viewpoints and offer lossless translation between them. These translation tables are made up of bidirectional and unidirectional rules. They introduced three TRANSLATOR algorithms and a score that relies on the principle of Minimum Description Length. The evaluation of the method using real-world data demonstrates that it can recognize the two-view structure that is present in the data with a limited number of relations. The technique, however, is unable to distinguish between the significant and robust associations and the weak ones. It should be noted that there are very few works on this specific problem of extracting association rules between views using clustering models. Therefore, our proposed approach aims to fill this gap and provide a novel and effective solution

3. Theory Background

3.1. Multi-view notion

The principle of the multi-view building involves dividing the original space of dataset into various subspaces, which correspond to different subsets of features [12]. The union of these multi-views constitutes the original space of the dataset. The view subsets may overlap and can be associated with different feature subsets that correspond to specific dataset subfields. As long as they can be described using description vectors, the view model is adaptable enough to handle dataset descriptions from various media. The communication of the clustered views described below takes advantage of the inter-view model described above. It maintains an overall perspective of the interaction between the data while resolving the low-quality issue with a global clustering strategy.

3.2. Self-Organizing Map (SOM) clustering model

The SOM network architecture is founded on the hypothesis that representing data features is done by a self-organizing map (Fig. 1), this map is set up in a geometric grid [13].
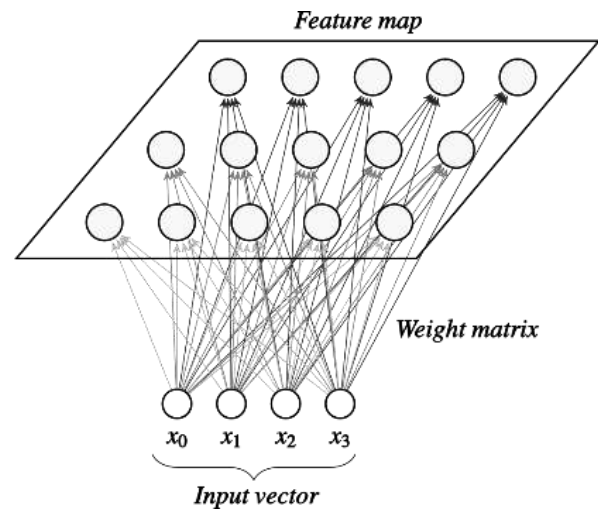
Figure 1. SOM Architecture

This grid represents a two-dimensional area occupied by neurons as a high-dimensional data space. The two main steps of the SOM algorithm are picking a winner on the map and changing the weights of the chosen winner's neighbours. The training data is assigned to the clusters (neurons) of the map once the Self-Organizing Map algorithm is finished. The creation a Self-Organizing Map is not done directly and requires a number of learning processes, each map will be evaluated and compared with some other created maps to identify a trustworthy or ideal one.

3.3. Communication of Clustered Multi-view

The views are clustered using MultiSOM neural clustering model, which is an extension of the original SOM algorithm [10]. MultiSOM improves the quality of the views needed for data analysis by clustering each view using a single SOM map. This approach helps to minimize noise that may be present when only one space of data is clustered. Moreover, the overall analysis of the views is maintained by establishing connections between the clustered SOM maps. The superiority of MultiSOM's multi-views analysis, as compared to SOM, is evident in its ability to achieve accurate mining results. The clustered SOM maps are linked in such a way that it enables the identification of significant relationships between different topics belonging to various subspaces [14]. This connection process is carried out in three steps (fig. 2). The initial placement of the original activity is onto the data-related source cluster. Then, a two-stage transmission takes place from the source cluster to the target cluster. The first stage of transmission is done by activating a cluster in the source map then it is transmitted to the cluster in the target map through the their shared data.
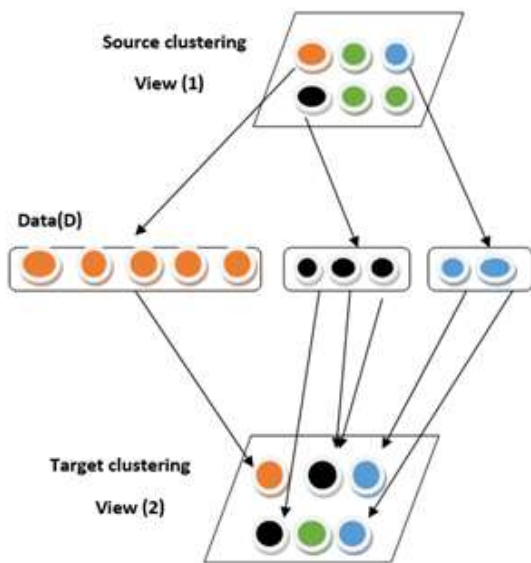
***Figure 2.** MultiSOM Architecture*

3.4. Association Rule Mining

Consider a dataset D, consider the features of D are represented by P. Suppose the function $f : P \rightarrow D$ that associates a set of features p with the set of data objects that, at least, contain all the features of p (i.e., $f(p) = D_p$; where D_p is a set of objects that contains p). Suppose the function $g : D \rightarrow P$ that associates a set of objects with the set of features that are shared to all the data objects of d (i.e., $g(d) = Pd$; where Pd

is a set of features that are shared to all the data objects of d).

Definition 1 (Support count (sup)): the term 'support count' of a set of features (p) refers to the number of data objects that contain the set of features.

Definition 2 (Support (s)): the term 'support' for a feature set (p) refers to the proportion of data items that contain that particular set of features.

Definition 3 (Frequent set of features): it is defined as a set of features whose support count is greater than or equal to a threshold called minsup.

Definition 4 (Closed set): A set of features (p) is a closed set if gof(p) = p [15].

Definition 5 (Association rule): it takes the form X→Y, where both X and Y are sets of features [16], and can be interpreted as an implication statement.

Definition 6 (Confidence (conf)): The confidence value of an association rule $X \rightarrow Y$ is determined by calculating the ratio of the support of the combined sets X and Y, to the support of set X. This can be expressed as conf(X→Y) = sup(X, Y) / sup(X) [16].

Definition 7 (Multi-view association rule): it is an association rule $X \rightarrow Y$ that the antecedent X is a set of features of a view and the consequent Y is a set of features of another view.

Definition 8 (Recall of a feature in a cluster): It measures to what extent a feature is associated with a single cluster [9].

Definition 9 (Precision of a feature in a cluster): It assesses the degree to which a feature is linked to the entirety of the data contained within a cluster [9].

4. Proposed Model

We propose an approach for mining multi-view association rules extracted between two clustered, known as MARCMV. In order to build a hybrid method for extracting useful knowledge, our strategy uses two criteria, recall (definition 8) and precision (definition 9), and combines a closed sets (definition 4) (using a symbolic method) with a cluster of a clustering method. Our method's algorithms each stand for a specific class of multi-view association rules, enabling deliberate rule selection. Importantly, these categories are not dependent on the confidence and support measures traditionally used to identify important rules. Under the first category (Fig. 3), when recall and precision for pertinent attributes are both 1, we extract the most important rules. Only attributes that are shared by all the data in the cluster and are present in the same cluster in both views, are included in these rules.

Algorithm 1: Category 1

Input: Two-view dataset D, first view clustering C, second view clustering C`

Output: set of association rules

```
1:      For each c ∈C
2:          Find P_c^v
3:          For each c` ∈C`
                if c ∩ c` ≠ φ
4:                  Find P_c`^v
                    % create A_cc`, the set of peculiar features from c such that their recall and
                    % precision are 1
5:                  A_cc` = {a |a ∈P_c^v , precision(a) = 1, recall(a) = 1}
                    % create B_cc`, the set of peculiar features from c` such that their recall and
                    % precision are 1
6:                  B_cc` = {b |b ∈P_c`^v , precision(b) = 1, recall(b) = 1}
                    % association rules extraction
7:                  if |A_cc`| ≠ 0 and |B_cc`| ≠ 0
8:                      ExtensionTest (A_cc`, B_cc`)
                    End if
9:              End if
10:         End for
11:     End for
```

Function ExtensionTest (A, B)

```
        if Extent(A) ⊂ Extent(B) then A → B
        else if Extent(B) ⊂ Extent(A) then B → A
        else if Extent(A) = Extent(B) then A ↔ B
            else if conf (A → B) > conf (B → A) then A → B
            else if conf (A → B) < conf (B → A) then B → A
                else A ↔ B
```

Figure 3. *First category of multi-view association rules*

Algorithm 2: Category 2

Input: Two-view dataset D, first view clustering C, second view clustering C`

Output: set of association rules

```
1:      For each c ∈C
2:          Find P_c^v
3:          For each c` ∈C`
                if c ∩ c` ≠ φ
4:                  Find P_c`^v
                    % create A_c^p the set of peculiar features from c such that their precision are 1
5:                  A_c^p = {a |a ∈P_c^v , precision(a) = 1, recall(a) ≠ 1}
                    % create B_c`^p the set of peculiar features from c` such that their precision are 1
6:                  B_c`^p = {b |b ∈P_c`^v , precision(b) = 1, recall(b) ≠ 1}
                    % association rules extraction
7:                  if |A_c^p| ≠ 0 and |B_c`^p| ≠ 0
8:                      ExtensionTest (A_c^p, B_c`^p)
                    End if
9:              End if
10:         End for
11:     End for
```

Figure 4. *Second category of multi-view association rules*

With a precision of 1, the second category (Fig. 4) concentrates on finding relationships between all of the data in the clusters in both views. Each view should have these properties in at least two clusters. In the third category (Fig. 5), our objective is to find correlations between exclusive features that are seen only in clusters in both viewpoints. The exclusive features do not appear in multiple clusters, and our method guarantees a recall of 1. The fourth category (Fig. 6) consists of the following three actions in order:

• Pick out a portion of the dataset that appears in a cluster of the first clustered view and a cluster in the second clustered view.
• Recognize two sets of features, one from each view, that are common to the previously found portion of the data.

Algorithm 3 Category 3

Input: Two-view dataset D, first view clustering C, second view clustering C`

Output: set of association rules

```
1:      For each c ∈C
2:          Find P_c^v
3:          For each c` ∈C`
                if c ∩ c` ≠ φ
4:                  Find P_c`^v
                    % create A_c^e the set of peculiar features from c such that their recall are 1
5:                  A_c^e = {a |a ∈P_c^v , precision(a) ≠ 1, recall(a) = 1}
                    % create B_c`^e the set of peculiar features from c` such that their recall are 1
6:                  B_c`^e = {b |b ∈P_c`^v , precision(b) ≠ 1, recall(b) = 1}
                    % association rules extraction
7:                  if |A_c^e| ≠ 0 and |B_c`^e| ≠ 0
8:                      ExtensionTest (A_c^e, B_c`^e)
                    End if
9:              End if
10:         End for
11:     End for
```

Figure 5. *Third category of multi-view association rules*

• Establish whether or not the two features subsets are closed sets of features. We extract correlations between the two subsets of attributes if they are closed.

To extract compact multi-view association rules, this category blends symbolic computation with numerical techniques.

Algorithm 4 Category 4

Input: Two-view dataset D, first view clustering C, second view clustering C`

Output: set of association rules

```
1:      For each c ∈C
2:          For each c` ∈C`
3:              if c ∩ c` ≠ φ
4:                  Find D_cc`, the set of data d that are shared between c and c`, D_cc` = c ∩ c`
5:                  D_cc` = { d |d ∈c, d ∈c` }
                    % create A_s the set of attributes from the first view which are shared with
                    % all data of D_cc`
6:                  A_s = {a |a ∈d, ∀d ∈D_cc`, a ∈V_1 }
                    % create B_s the set of attributes from the second view which are shared
                    % with all data of D_cc`
7:                  B_s = {b |b ∈d, ∀d ∈D_cc`, b ∈V_2 }
                    % association rules extraction
8:                  if |A_s| ≠ 0 and |B_s| ≠ 0
9:                      if h (A_s)=A_s and h (B_s)=B_s
10:                         ExtensionTest (A_s, B_s)        % Closed itemsets
11:                     Else
12:                         ExtensionTest (A_s, B_s)        % non-closed itemsets
13:                     End if
14:                 End if
15:         End for
16:     End for
```

Figure 6. *Fourth category of multi-view association rules*

5. Experimental Results and Discussions

5.1. Mining multi-view association rules with symbolic techniques

To assess our proposed approach, we will exhibit outcomes produced by two distinct algorithms for

multi-view association rule mining on two datasets, namely Car and Tic-Tac-Toe, acquired from UCI Machine Learning Repository [17]. To conduct these tests, we must specify minimum support and confidence values. We calculated the minimum support values for all our tests as 1 divided by the number of rows in each dataset. We used minimum confidence values of 0.0, 0.2, 0.4, 0.6, and 0.8. Our analysis employed the Charm and FP-Growth algorithms, which are all contained in the SMPF tool, which is a data mining library available as open-source software [18].
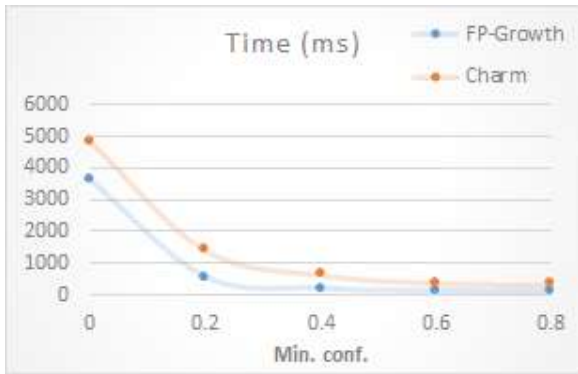
(a)
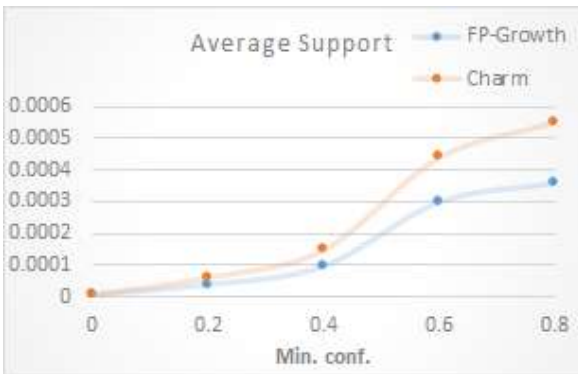
(b)
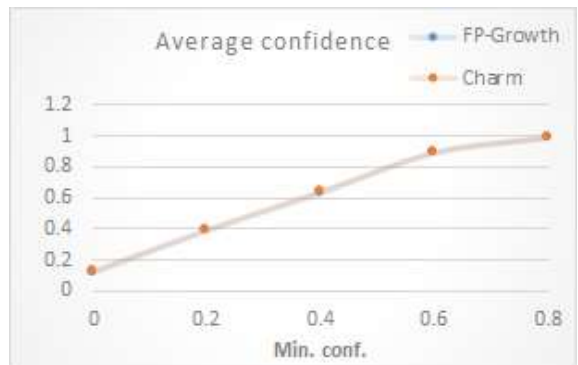
(c)

(d)

(e)

Figure 7. *Comparison of symbolic methods on the Car dataset*

(a)

(b)

145
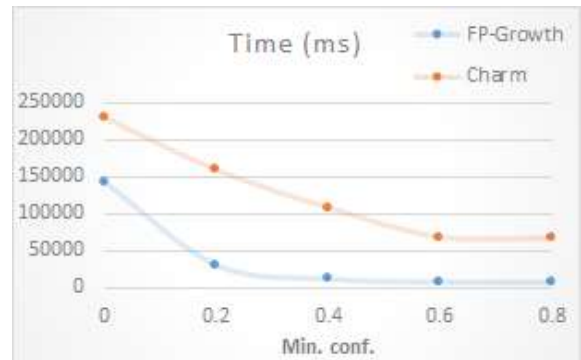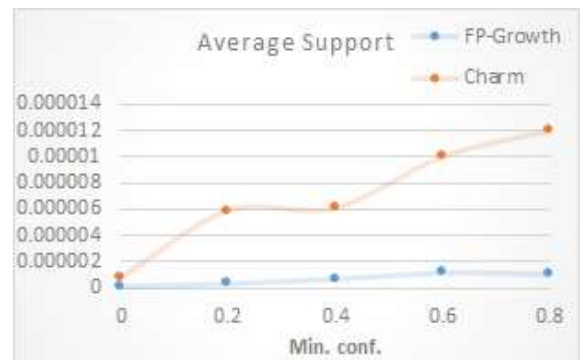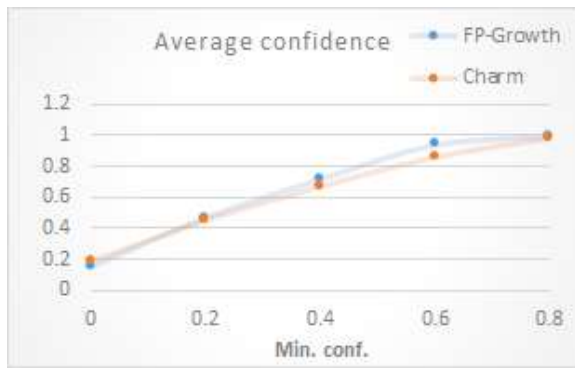
(c)
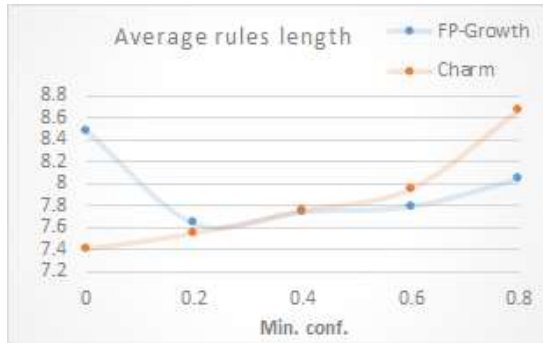
(d)
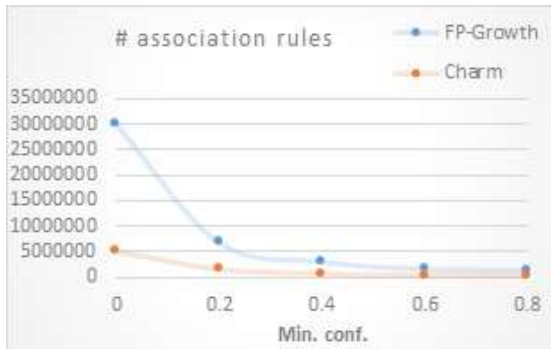
(e)

Figure 8. *Comparison of symbolic methods on the Tic-Tac-Toe dataset*

The FP-Growth method consistently outperforms the Charm approach, as seen in Figs. 7 and 8, with only a minor variation in average rule length for the two datasets. The average support values varied significantly in several experiments despite the average confidence differences between the two algorithms remaining equal due to the different numbers of association rules produced by each approach. Compared to FP-Growth method, which mines more redundant association rules and ineffective ones, the Charm method produces a comparatively fewer number of association rules, demonstrating its superior accuracy.

In our evaluation process, the second step, for extracting multi-view association rules, involves filtering the association rules obtained from the tests performed in the previous step. This is done by ensuring that the antecedent (left-hand side) of the rule contains features from the first view (source) and the consequent (right-hand side) contains features from the second view (target).

To do this, we created a straightforward application that evaluates all rules from each test via comparison and validation against a predefined condition. Depending on the dataset, the condition changes. For the car dataset, the requirement is that all attribute numbers on the first view's left side should fall between 1 and 15, while those on the second view's right side should do so between 16 and 25. We also take this condition's reverse order into account. The feature numbers of the first view's left side for the Tic-Tac-Toe dataset should be between 1 and 15, while those on the second view's right side should do so between 16 and 39. We also take this condition's reverse order into account.

Applying this filtering condition to each test from Figs. 7 and 8 leads in a significant decrease in the number of rules, as shown in Figs. 9 and Fig.10. As an illustration, the FP-Growth algorithm produced 732252 rules with a minimal confidence of zero, however after filtering, only 36322 rules were left.

5.2. Multi-View Association Rules Mining using MARCMV approach

To extract multi-view association rules using our proposed approach, it is necessary to cluster each of
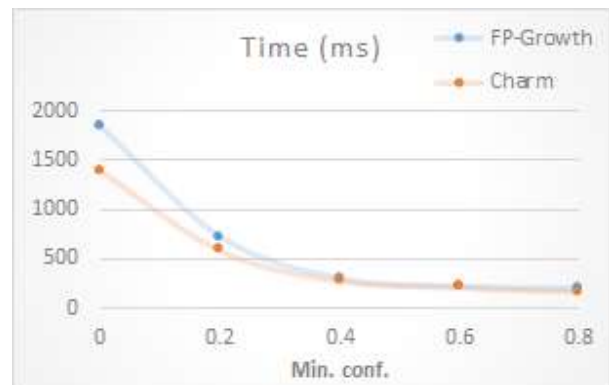
(a)
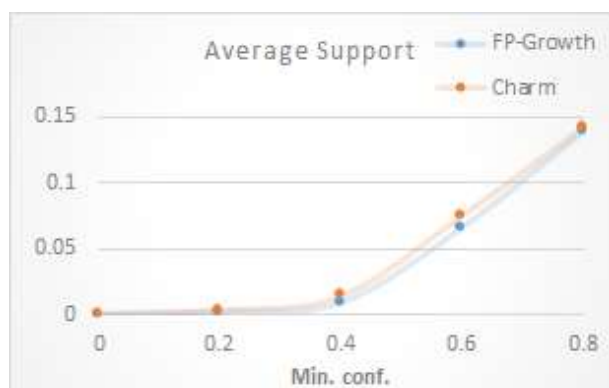
(b)
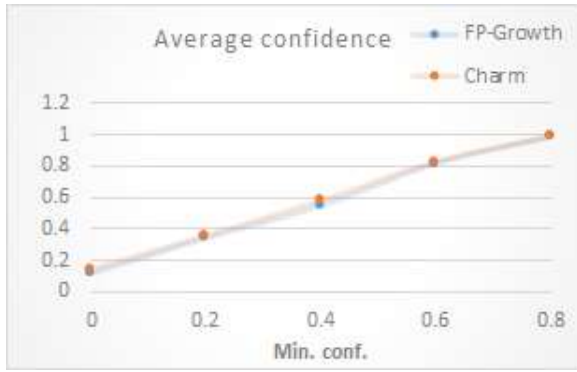
(c)
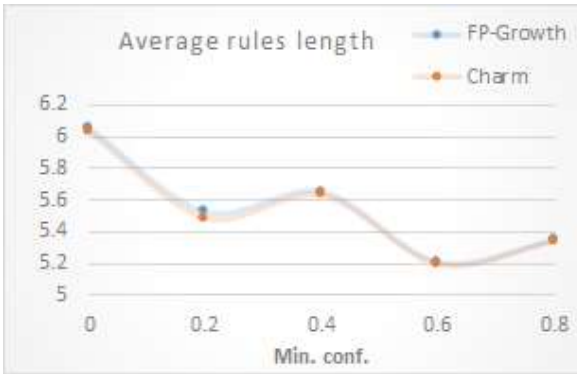
(d)
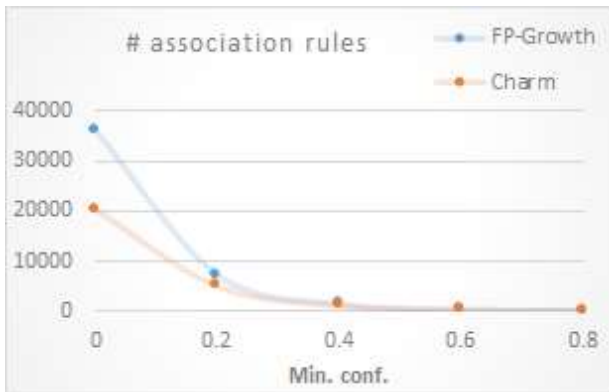
(e)

Figure 9. *Comparison of symbolic methods on the Car dataset after the filtering step*
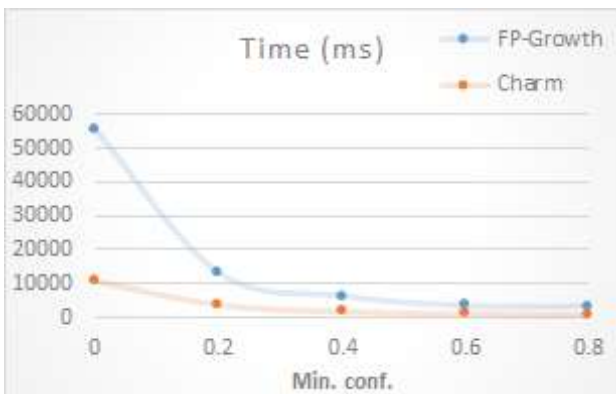
(a)
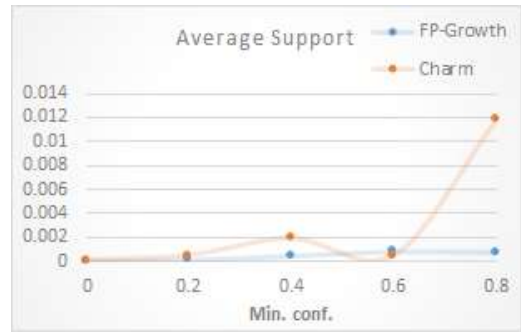
(b)
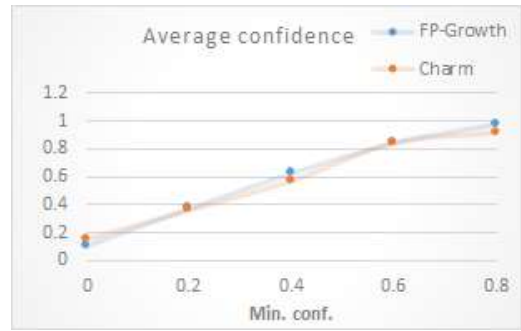
(c)
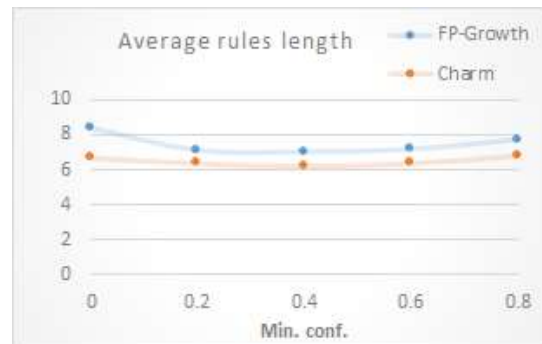
(d)
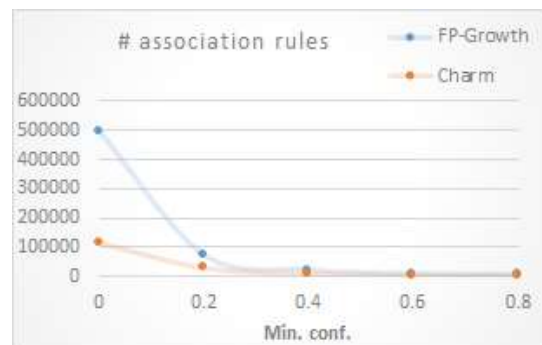
(e)

Figure 10. *Comparison of symbolic methods on the Tic-Tac-Toe dataset after the filtering step*

the datasets, Car and Tic-Tac-Toe, using MultiSOM with an optimal number of clusters. To determine this optimal number, we tested different numbers of clusters (2, 3, 4, 9, 16, and 25), with 20,000 iterations for each test. The clustering quality measures proposed in [19] were used to identify, for each dataset, the optimal number of clusters. Based on the

previously mentioned measures, three clusters are selected for each view of the Car dataset, also the same number of clusters as Car dataset are also selected for each view of the Tic-Tac-Toe dataset.

Multi-view association rules can then be extracted from the optimal clustering of each dataset using MARCMV.

A quick comparison of the outcomes in table 1 reveals that the quantity of association rules mined by the MARCMV approach is considerably less than what we discovered after using the Charm and FP-Growth algorithms on the experimental datasets. The averages estimated based on Figures 7 and 8 are shown for both algorithms in table 1. However, the times show the average duration of each algorithm as a whole, including the time for mining association rule and filtering them.

From experimental datasets, the number of multi-view association rules mined by MARCMV approach is considerably lower than the those extracted by symbolic algorithms. This shows that mining, from two views, association rules yields beneficial and easily understandable ones, while also excluding redundant and unhelpful rules. For example, only nine rules were produced when our method was applied to the Car dataset, as opposed to 5,446 and 9,164 rules generated by the Charm and FP-Growth algorithms, respectively. Similarly, for the Tic-Tac-Toe dataset, our approach generated only nineteen rules, as opposed to 31,804 and 121,069 rules generated by the Charm and FP-Growth algorithms, respectively.

In addition, we observed that the MARCMV approach was faster than the symbolic methods in terms of running time. For the Car dataset, the average time was 1.3 seconds, while for the Tic-Tac-Toe dataset, it was 1.2 seconds. In contrast, the average times for the symbolic methods were 2 seconds, 1.5 seconds, approximately 129 seconds, and 58 seconds, respectively.

Table 1. *Comparison results: (a) Car, (b) Tic-Tac-Toe.*

Algo.	Time	Support	Confidence	Rule Length	# Rules
Charm	2044.8	0.0472	0.577	5.53	5446
FP-Growth	1581.6	0.0432	0.562	5.55	9164
MARCMV	1362.9	0.1659	0.4593	2.25	9

(a)

Algo.	Time	Support	Confidence	Rule Length	# Rules
Charm	129552.6	0.003	0.572	6.49	31804
FP-Growth	57954.4	0.0004	0.587	7.46	121069
MARCMV	1258.8	0.1474	0.4588	2.15	19

(b)

When generating association rules using symbolic methods, a minimum confidence value must be set to determine the importance of the association rule. All association rule mined with a confidence level lower than minimum confidence will be removed. However, from the experiments, we discovered that setting a low minimum confidence value has three major drawbacks. The first one is the time-consuming, particularly for huge datasets. Then, it mines a large number of redundant and unhelpful association rules, which makes it difficult to use these association rules in any decision-making process based on two views. The third one is consuming a lot of resources, making it infeasible to apply symbolic methods, especially when working with large datasets or datasets with a high number of features. These drawbacks are mitigated by giving additional temporary storage resources.

Working on clustered views of a dataset ensures that data with high similarities are grouped together while weak relationships among variables are eliminated, and all variables within each group are given equal importance. As a result, the MARCMV approach does not rely on minimum confidence values in generating association rules. Thus, it becomes more achievable to implement, regardless of the size of the dataset.

6. Conclusion and future work

Due to the swift expansion of data, there is a need to develop techniques for extracting useful information from large datasets. Symbolic methods, which are commonly used for knowledge extraction, have drawbacks in generating a large number of rules, including weak and redundant ones. In this paper, a novel approach called MARCMV was proposed to mine multi-view association rules via clustered datasets. The strategy focuses on detecting relations between several views of the data using MultiSOM clustering. This helps to group items with strong relationships and exclude weak and not useful association rules. The MARCMV approach is more feasible to implement regardless of dataset size compared to symbolic methods.

We plan in the future work to add more important and correalted multi-view association rules by adding more catgories to our approach.

Author Statements:

- **Ethical approval:** The conducted research is not related to either human or animal use.
- **Conflict of interest:** The authors declare that they have no known competing financial interests or personal relationships that could have appeared to influence the work reported in this paper

References

[1] Han, J., Pei, J., & Tong, H. (2022). Data mining: concepts and techniques. Morgan kaufmann.

[2] Agrawal, R., & Srikant, R. (1994, September). Fast algorithms for mining association rules. In *Proc. 20th int. conf. very large data bases, VLDB* (Vol. 1215, pp. 487-499).

[3] Han, J., Pei, J., Yin, Y., & Mao, R. (2004). Mining frequent patterns without candidate generation: A frequent-pattern tree approach. *Data mining and knowledge discovery*, 8; 53-87.

[4] Zaki, M. J., & Hsiao, C. J. (2002, April). CHARM: An efficient algorithm for closed itemset mining. In Proceedings of the 2002 SIAM international conference on data mining (pp. 457-473). Society for Industrial and Applied Mathematics.

[5] Kanhere, S., Sahni, A., Stynes, P., & Pathak, P. (2021, January). Clustering Based Approach to Enhance Association Rule Mining. In *2021 28th Conference of Open Innovations Association (FRUCT)* (pp. 142-150). IEEE.

[6] Tang, C., Zheng, X., Liu, X., Zhang, W., Zhang, J., Xiong, J., & Wang, L. (2021). Cross-view locality preserved diversity and consensus learning for multi-view unsupervised feature selection. *IEEE Transactions on Knowledge and Data Engineering*, *34*(10); 4705-4716.

[7] Zhao, J., Xie, X., Xu, X., & Sun, S. (2017). Multi-view learning overview: Recent progress and new challenges. *Information Fusion*, *38;* 43-54.

[8] Li, Z., Tang, C., Zheng, X., Liu, X., Zhang, W., & Zhu, E. (2022). High-order correlation preserved incomplete multi-view subspace clustering. *IEEE Transactions on Image Processing*, *31;* 2067-2080.

[9] Lamirel, J. C., & Al Shehabi, S. (2005, September). Efficient Knowledge Extraction using Unsupervised Neural Network Models. In *5th Workshop On Self-Organizing Maps-WSOM 05*.

[10] Lamirel, J. C. (2002, May). MultiSOM: a multimap extension of the SOM model. Application to information discovery in an iconographic context. In *Proceedings of the 2002 International Joint Conference on Neural Networks. IJCNN'02 (Cat. No. 02CH37290)* (Vol. 2, pp. 1790-1795). IEEE.

[11] M. van Leeuwen and E. Galbrun, "Association discovery in two-view data," *IEEE Trans. Knowl. Data Eng.*, 27(12);3190–3202, 2015.

[12] Polanco, X., François, C., & Lamirel, J. C. (2001). Using artificial neural networks for mapping of scienceand technology: A multi-self-organizing-maps approach. *Scientometrics*, *51;* 267-292.

[13] Kohonen, T., Kaski, S., Lagus, K., Salojarvi, J., Honkela, J., Paatero, V., & Saarela, A. (2000). Self organization of a massive document collection. *IEEE transactions on neural networks*, *11*(3); 574-585.

[14] Lamirel, J. C., Shehabi, S., Francois, C., & Polanco, X. (2004). Using a compound approach based on elaborated neural network for Webometrics: an example issued from the EICSTES Project. *Scientometrics*, *61*(3); 427-441.

[15] Pasquier, N., Bastide, Y., Taouil, R., & Lakhal, L. (1999). Discovering frequent closed itemsets for association rules. In *Database Theory—ICDT'99: 7th International Conference Jerusalem, Israel, January 10–12, 1999 Proceedings 7* (pp. 398-416). Springer Berlin Heidelberg.

[16] Tan, P. N., & Kumar, V. (2000). Interestingness measures for association patterns: A perspective.

[17] Dua, D., & Graff, C. (2017). UCI machine learning repository.

[18] Fournier-Viger, P., Lin, J. C. W., Gomariz, A., Gueniche, T., Soltani, A., Deng, Z., & Lam, H. T. (2016). The SPMF open-source data mining library version 2. In *Machine Learning and Knowledge Discovery in Databases: European Conference, ECML PKDD 2016, Riva del Garda, Italy, September 19-23, 2016, Proceedings, Part III 16* (pp. 36-40). Springer International Publishing.

[19] Lamirel, J. C., Francois, C., Shehabi, S. A., & Hoffmann, M. (2004). New classification quality estimators for analysis of documentary information: application to patent analysis and web mapping. *Scientometrics*, *60*(3); 445-562.

Research Article
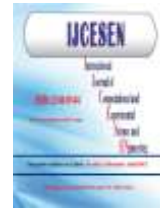
Isolator Detection in Power Transmission Lines using Lightweight Dept-wise Convolution with BottleneckCSP YOLOv5

İpek ATİK*

Gaziantep Islam Science and Technology University, Department of Electrical and Electronics Engineering, 27000, Gaziantep-Turkey
* **Corresponding Author Email:** ipek.atik@gibtu.edu.tr - **ORCID:** 0000-0002-9761-1347

Article Info:

Abstract:

The detection of insulators is of great importance in power transmission lines. This is because accurate detection ensures reliability and continuity of energy transmission, preventing line interruptions. The proposed method in this study utilizes the DWB-YOLOv5 (Dept-wise convolution with BottleneckCSP YOLOv5) model to effectively detect insulators, contributing to the safe and uninterrupted operation of power lines. In the suggested approach, the DWB-YOLOv5 model is employed to detect insulators. The bottleneckCSP module enhances the accuracy of targets at various scales, while the depth-wise c2onvolution module assists in reducing the model's complexity. Images undergo preprocessing steps such as automatic orientation and resizing. The preprocessed images are fed into the DWB-YOLOv5 model to extract deep features, perform object detection, and conduct classification. The insulator detection model obtained through this method exhibits a minimum of 8.53% better mean average precision (mAP) performance compared to existing methods. This study represents a significant step towards ensuring the safe and uninterrupted operation of power transmission lines. Accurate detection of insulators facilitates the smooth functioning of lines, ensuring reliability and continuity in energy transmission. The proposed method offers important advantages such as high accuracy, lightweight design, and efficiency.

1. Introduction

Electric power transmission lines are fundamental components of power systems, facilitating the effective transmission of electric energy over long distances. Given that these lines carry electric energy at high voltage levels, the safety and efficiency of their operation are of paramount importance. Insulators serve as critical elements in ensuring the healthy and safe operation of these transmission lines. They provide insulation between the transmission line structure on the line and the voltage, preventing the loads on the line from being grounded and transferring to other equipment by isolating them from the ground [1,2]. Due to the extensive distances covered by transmission lines, the condition and integrity of insulators should be continuously monitored. Faults in insulators can lead to negative impacts on the safety and ongoing functionality of the lines. Breakage, cracking, corrosion, or other damages in insulators can reduce the reliability of transmission lines and cause power

outages in case of failure. Thus, regular detection and maintenance of insulators are of great importance. Most studies on insulator detection have employed the following methods [3-5];

➢ Acoustic and Vibration-Based Approaches: These methods detect faults using acoustic or vibration properties of insulators. Microphones or vibration sensors are used in these approaches. They detect abnormalities by analyzing the sound or vibration patterns emitted by insulators under normal operating conditions.

➢ This approach is typically used for real-time monitoring and rapid fault detection [3–5].

➢ Remote Sensing and Sensor Networks: Sensor networks or remote sensing systems are used to monitor the condition of insulators. These systems consist of sensors measuring the electrical properties of insulators, as well as environmental parameters such as temperature, humidity, or vibration. These data are used to monitor the operating status of insulators, detect faults, and optimize maintenance planning [6,7].

➢ Image Processing-Based Approaches: Image processing algorithms are used to analyse the visual features of insulators. This approach captures and analyses images of insulators using imaging technologies such as thermal cameras or high-resolution cameras. It evaluates the colour, shape, and textures of insulators to detect issues like breakage, cracks, or surface damage [8].

➢ The common goal of these studies is to ensure the proper functioning of insulators and to increase the reliability of energy systems by early detection of faults. With the development of new technologies and ongoing research, further advancements in the field of insulator detection are expected.

➢ This study undertakes object detection based on image processing.

The significance and contributions of this study are as follows:

• This study aims to accelerate the detection and classification of insulators on transmission lines using YOLOv5's (You Only Look Once-YOLO) fast inference speed and high detection accuracy while intending to lighten the model and increase its accuracy. Thus, it aims to reduce the margin of error in insulator detection.

• Toward the task of insulator detection, improvements and innovations have been made to the YOLOv5 structure in this article. Firstly, the detection accuracy has been increased by using the bottleneckCSP module to obtain the semantic depth information of insulator images. Moreover, the Focus layer used in the YOLOv5 structure is specially designed to increase the detection accuracy of particularly smaller objects.

• In the proposed model, a depth-wise convolution structure is used, applying a separate kernel to each channel of the input data for computation, hence performing the operation in parallel. This method allows models to be lighter and operate efficiently in resource-constrained environments.

• This study has improved the mAP value of the proposed insulator detection approach by at least 8.53%. While reducing the computational cost of YOLOv5s, a lightweight and efficient structure is presented. Moreover, this method achieves better results compared to the latest technical methods.

2. Materials and Methods

The task of insulator detection possesses two fundamental characteristics: first, the location of the object is determined, and then the class of the insulator is detected. Models in the YOLOv5 series are quite successful in location detection, and YOLOv5s has a lighter structure. Compared with other deep learning techniques, YOLOv5s is a good option for this purpose, providing a balance between detection accuracy and speed [8,9].

In this research, the YOLOv5s network structure has been developed and applied. The network consists of four sections: head, backbone, neck, and prediction [10]. The head section represents the input and aims to resolve the imbalance in the distribution of the small target dataset using different frame settings for adaptive frame setting. The backbone network is implemented using focus, SPPF, and bottleneckCSP. The insulator detection model is designed using the focus structure and the depth-wise convolution layer to reduce the number of network layers and parameters, increase the forward and backward computation speed, and prevent information loss in sampling [11]. The architecture of the proposed model is provided in Figure 1. In this study, the task of insulator detection was conducted with a model obtained through the enhancement of the YOLOv5 network structure. The network consists of four sections: head, backbone, neck, and prediction. This structure maintains a balance between detection accuracy and speed, ensuring the accurate detection of various defects.

2.1 Dataset

The study used an open-access dataset containing 1547 insulator images [12]. Insulators can be classified into different types based on voltage type and usage purpose. The two main types of insulators commonly used in transmission lines are tension type and suspension type insulators. Tension type insulators are typically insulators that hang below or beside the transmission lines. These types of insulators isolate the loads on the line from the ground while carrying the voltage on the line. Suspension type insulators consist of a series of insulator rings and are used to support the transmission line [13]. These types of insulators carry the voltage on the line, protecting the line and the support structure. The images in the dataset labelled as tension and suspension types have been divided into 1083 for training, 233 for validation, and 232 for testing. Example images used in the study are given in Figure 2.

2.2 Performance Metric Measures

In this study, confusion matrix was used as an evaluation metric for supervised learning. Precision (P), Recall (R), and Mean Average Precision (mAP) values were the evaluation criteria obtained [14],

[15]. The equations for these metrics are given in Equation (1)-(3);

$$P = \frac{TP}{TP+FP} \times 100\% \quad (1)$$

$$R = \frac{TP}{TP+FN} \times 100\% \quad (2)$$

$$mAP = \frac{\sum_{k=1}^{N} P(k) \Delta R(k)}{C} \quad (3)$$

In the equations above, TP represents the number of true positives, FN represents the number of false negatives, FP represents the number of false positives, N represents the number of samples in the validation set, P(k) represents the magnitude of Precision when k targets are detected at the same time, and $\Delta R(k)$ represents the change in Recall when the number of detected samples changes from k-1 to k. C represents the number of classes in the model [11,16].

3. Results

The trained model was evaluated using mAP, precision, and recall evaluation metrics. A Tesla T4 with a 15110MiB memory NVIDIA GPU was used in this study. The proposed model was optimized using stochastic gradient descent. Table 1 shows the mAP, precision, and recall values. The dataset was randomly divided into 70% training, 15% validation, and 15% testing data. All analyses in the study used the same training, validation, and testing images, ensuring that the models were compared under equal conditions. Values for the 500 epochs used to track performance metrics were plotted and are given in Figure 3 and Figure 4 shows the isolators predicted by the model using randomly selected test images. As the loss curves show a downward trend while the performance metric values show an upward trend, this indicates the improvement during the training process. Another performance metric, the precision-recall curve, was plotted and is given in Figure 5. In the analysis carried out with four different models for insulator detection, the performance of each component has been analysed and the effect of each component is presented in Table 1. Also, the number of layers and parameters for each model is given in the table.

Effect of Dept-wise Convolution: Unlike traditional convolutions, dept-wise convolution performs separate operations along the depth (number of channels) of the input data. By applying separate filters along the depth of the input data, it reduces the computation cost and allows for model lightening.

Effect of BottleneckCSP: While reducing the depth and computational intensity of the model, it maintains the ability to learn more complex features. In this way, it is possible to obtain lighter and faster

operating models. Bottleneck structures enhance the generalization ability of the model and reduce the risk of overfitting. It allows obtaining more generally valid models with fewer parameters and more learnable features.

Effect of Model Merging: In the proposed model, a lighter model with high accuracy was obtained by replacing bottleneckCSP and normal convolutions with dept-wise convolution modules. Table 2 presents the layer count, parameter values, and average image processing time for the models. As indicated by the table, DWB-YOLOv5 has a lower layer count than YOLOv5s, leading to a reduced image processing time. This suggests that the model is both lighter and faster in performance. As can be seen from the figure, the curve shows a trend towards the top right corner, indicating that most values are close to one.

4. Conclusion

In this study, DWB-YOLOv5, an approach integrating dept-wise convolution and BottleneckCSP to the YOLOv5 model, is proposed for insulator detection. Bottleneck structures used in the model reduce the depth and computational intensity of the model, enhancing its ability to learn complex features. Additionally, the generalization ability of the model has been improved to reduce the risk of overfitting. DWB-YOLOv5 is a modified version of the YOLOv5 model, lightened and reduced computational cost with depth-wise convolution modules. Two modules and a focus module were added to improve the performance of the model. The proposed insulator detection network has provided at least 8.53% improvement in mAP (mean precision) performance compared to the YOLOv5s model. Future works may focus on improving the real-time performance of lighter network structures. Additionally, the use of this approach for the detection of other objects on transmission lines can be considered.

Author Statements:
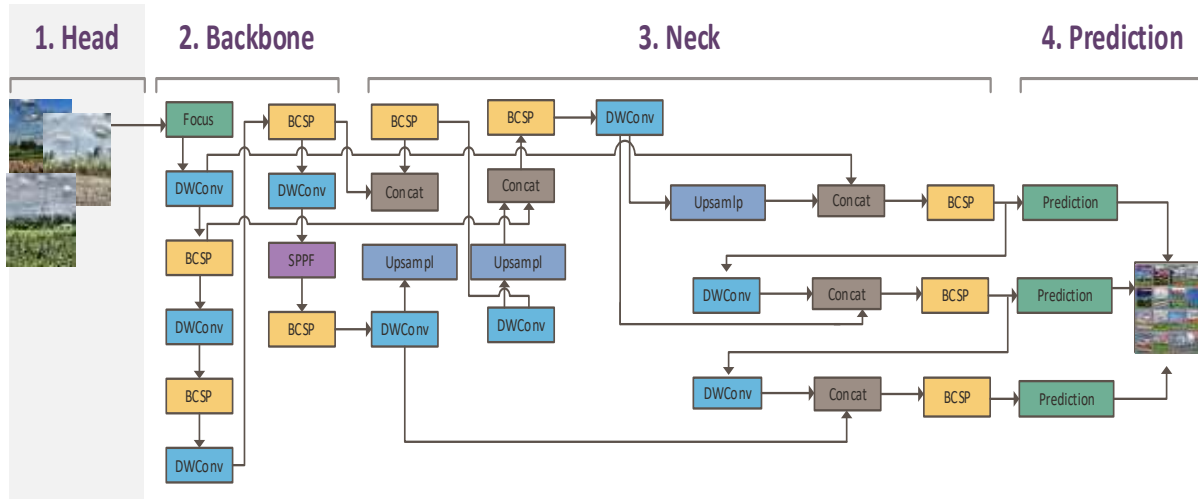
Figure 1. *Architecture of the proposed model*

Figure 2. *Sample images from the dataset*

Table 1. *Performance metrics values of the models.*

Methods	Description	mAP (%)	Precision (%)	Recall (%)
YOLOv5s	YOLOv5s	90.2±0.03	91.6±0.02	84.2±0.04
YOLOv5-2	YOLOv5s+DWConv	92.5±0.02	94.7±0.03	94.3±0.03
YOLOv5-1	YOLOv5s+BottleneckCSP	95.6±0.04	97.5±0.05	90.5±0.02
DWB-YOLOv5	YOLOv5s+BottleneckCSP+DWConv	97.9±0.03	97.1±0.04	95.7±0.04

Table 2. *The summary of the different models and the average elapsed time on the test set.*

Methods	Model Layers	Number of parameters (10⁴)	Average Time Consuming (s)
YOLOv5s	224	7.03	0.645
YOLOv5-2	226	7.02	0.842
YOLOv5-1	202	7.04	0.763
DWB-YOLOv5	208	7.01	0.563
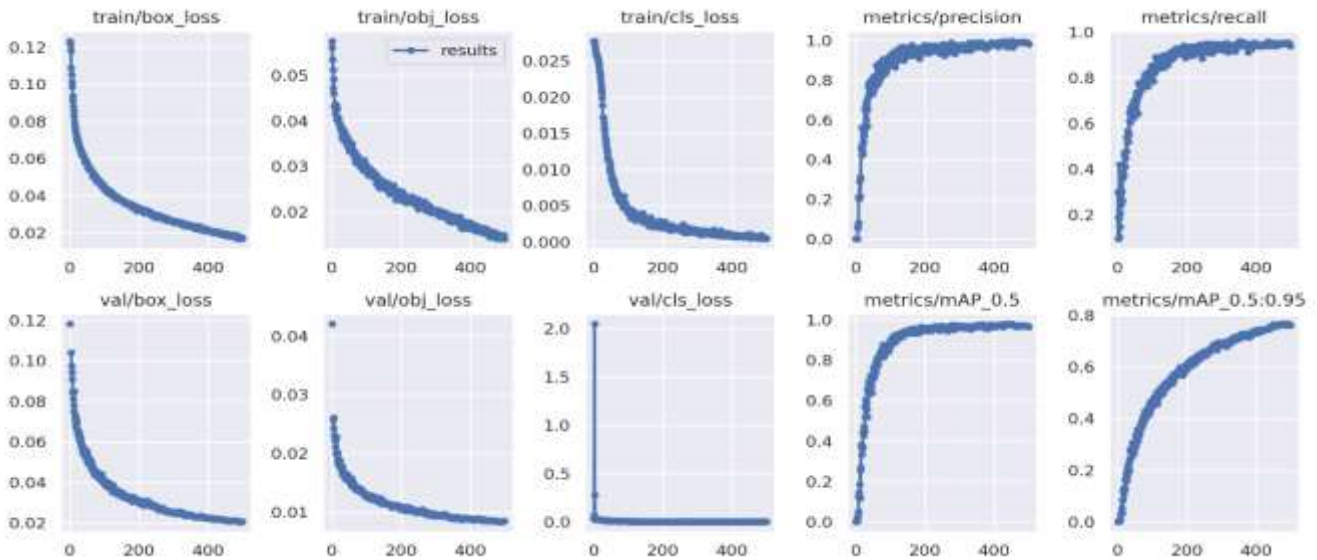
Figure 3. *Overall summary of training.*
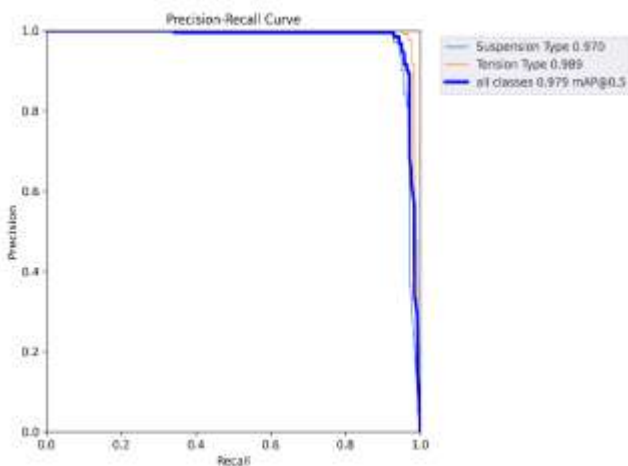
Figure 5. *Precision-recall curve*

- **Author contributions:** The authors declare that they have equal right on this paper.
- **Funding information:** The authors declare that there is no funding to be acknowledged.

- **Data availability statement:** The data that support the findings of this study are available on request from the corresponding author. The data are not publicly available due to privacy or ethical restrictions.

References

[1] E. B. M. Tayeb and O. A. A. A. Rhim, (2011). Transmission line faults detection, classification and location using artificial neural network. presented at the 2011 *International Conference & Utility Exhibition on Power and Energy Systems: Issues and Prospects for Asia (ICUE),* pp. 1–5. DOI:10.1109/ICUEPES.2011.6497761

[2] E. Karakose, "Performance evaluation of electrical transmission line detection and tracking algorithms based on image processing using UAV," presented at the *2017 International Artificial Intelligence and Data Processing Symposium (IDAP),* 2017, pp. 1–5. DOI:10.1109/IDAP.2017.8090302

Figure 4. *Isolators detected in test images*

[3] H. Liang, C. Zuo, and W. Wei, (2020). Detection and Evaluation Method of Transmission Line Defects Based on Deep Learning, *IEEE Access*, 8;38448–38458. DOI: 10.1109/ACCESS.2020.2974798

[4] H. Ha, S. Han, and J. Lee, (2012). Fault Detection on Transmission Lines Using a Microphone Array and an Infrared Thermal Imaging Camera," *IEEE Trans. Instrum. Meas.*, 61(1);267–275, DOI: 10.1109/TIM.2011.2159322

[5] C. Liu, Y. Wu, J. Liu, Z. Sun, and H. Xu, (2021). Insulator Faults Detection in Aerial Images from High-Voltage Transmission Lines Based on Deep Learning Model. *Appl. Sci.*, 11(10) DOI: https://doi.org/10.3390/app11104647

[6] H. Jiang, X. Qiu, J. Chen, X. Liu, X. Miao, and S. Zhuang. (2019). Insulator Fault Detection in Aerial Images Based on Ensemble Learning With Multi-Level Perception, *IEEE Access*, 7;61797–61810. DOI: 10.1109/ACCESS.2019.2915985

[7] C. Chen, G. Yuan, H. Zhou, and Y. Ma, (2023). Improved YOLOv5s model for key components detection of power transmission lines. *Math. Biosci. Eng.*, 20(5);7738–7760. DOI: 10.3934/mbe.2023334

[8] C. Liu, Y. Tao, J. Liang, K. Li, and Y. Chen, "Object Detection Based on YOLO Network," presented at the 2018 *IEEE 4th Information Technology and Mechatronics Engineering Conference (ITOEC)*, 2018, pp. 799–803. DOI:10.1109/ITOEC.2018.8740604

[9] N. Al-Qubaydhi, A. Alenezi, T. Alanazi, A. Senyor, N. Alanezi, B. Alotaibi, M. Alotaibi, A. Razaque, A. A. Abdelhamid, and A. Alotaibi, (2022). Detection of Unauthorized Unmanned Aerial Vehicles Using YOLOv5 and Transfer Learning. *Electronics*, 11(17); 2669, 2022. DOI: https://doi.org/10.3390/electronics11172669

[10] Z. Qiu, X. Zhu, C. Liao, D. Shi, and W. Qu, (2022). Detection of Transmission Line Insulator Defects Based on an Improved Lightweight YOLOv4 Model," *Appl. Sci.*, 12,;3 DOI: https://doi.org/10.3390/app12031207

[11] X. Wang, W. Li, W. Guo, and K. Cao, "SPB-YOLO: an efficient real-time detector for unmanned aerial vehicle images," presented at the 2021 *International Conference on Artificial Intelligence in Information and Communication (ICAIIC)*, 2021, pp. 099–104. DOI: https://doi.org/10.3390/drones7030190

[12] "Kaggle," *Kaggle data set*. [Online]. Available: https://www.kaggle.com/. [Accessed: 10-Dec-2021].

[13] E. Hewlett, (1907). new type of insulator for high-tension transmission lines," *Proc. Am. Inst. Electr. Eng.*, 26(6);975–979.

[14] I. Atik, (2023). Parallel Convolutional Neural Networks and Transfer Learning for Classifying Landforms in Satellite Images. *Inf. Technol. Control*, 52(1);228–244 DOI: https://doi.org/10.5755/j01.itc.52.1.31779

[15] I. Atik, (2022). Classification of Electronic Components Based on Convolutional Neural Network Architecture *Energies*, 15;7 DOI: https://doi.org/10.3390/en15072347

[16] I. Atik, (2022). Performance Comparison of Pre-Trained Convolutional Neural Networks in Flower Image Classification, *Eur. J. Sci. Technol.*, 35;315–321 DOI: https://doi.org/10.31590/ejosat.1082023
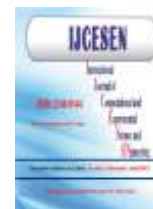
Preparation and Characterization of ZSM-5 Zeolite

Sabiha Anas BOUSSAA[1]*, Djamel NIBOU[2], Karima BENFADEL[3], Lamia TALBI[4], Assia BOUKEZZATA[5], Yahia OUADAH[6], Djaouida ALLAM[7], Samira KACI[8]

[1]Research Center On Semiconductor Technology for Energetic, CMSI-CRTSE, Algiers, Algeria
University of Sciences and Technology Houari Boumediene USTHB, Laboratory of Materials Technologies, Algeria
* **Corresponding Author**: **Email:** anassabiha@crtse.dz - **ORCID:** 0000-0003-2384-0056

[2]University of Sciences and Technology Houari Boumediene USTHB, Laboratory of Materials Technologies, Algeria
Email: dnibou@yahoo.fr - **ORCID:** 0000-0001-8924-6047

[3]Research Center On Semiconductor Technology for Energetic, CMSI-CRTSE, Algiers, Algeria
Email: benfadelkarima@gmail.com - **ORCID:** 0000-0001-8929-5244

[4]Research Center On Semiconductor Technology for Energetic, CMSI-CRTSE, Algiers, Algeria
Email: lamias19@yahoo.fr - **ORCID:** 0000-0002-0398-4557

[5]Research Center On Semiconductor Technology for Energetic, CMSI-CRTSE, Algiers, Algeria
Email: boukezzataassia@crtse.dz - **ORCID:** 0000-0002-6346-166X

[6]Research Center On Semiconductor Technology for Energetic, CMSI-CRTSE, Algiers, Algeria
Email: y.ouadah@gmail.com - **ORCID:** 0000-0002-2869-0790

[7]Sciences Faculty, University Mouloud Mammeri of Tizi Ouzou, LCAGC-UMMTO, Tizi Ouzou, Algeria
Email: allamdjaouida788@gmail.com - **ORCID:** 0000-0002-3430-7735

[8]Research Center On Semiconductor Technology for Energetic, CMSI-CRTSE, Algiers, Algeria
Email: k_samira05@yahoo.fr - **ORCID:** 0000-0001-6697-7015

Abstract:

Recently, zeolites attracted considerable research attention because they exhibit adsorption properties, ion exchange capabilities and a good catalytic property, a specific pore size distribution; a unique chemical and thermal properties and several applications. Actually zeolites play a crucial role as a catalyst to capture and convert Carbone dioxide into valuable products. In the present work, hydrothermal synthesis of ZSM-5 zeolite crystals, with composition of the chemical products 0.01 Al_2O_3,1SiO_2,2 NaOH, 0.15 TPABr, 18.34 H_2O at 170°C for 48 hours (2 days) at Ph 11 is described. Results of characterization of the ZSM-5 zeolite by XRD, FTIR, EDAX, SEM, TGA, are presented and discussed.

1. Introduction

Nowadays, microporous solid materials occupy a privileged place in the industrial field. Zeolites are microporous crystalline aluminosilicates that have a similar composition to the clay minerals but with their well-defined three-dimensional microporous structures. Zeolites were among the first solids to be widely used in materials science [1-3]. Their applications, which are too varied, particularly in the field of catalysis and the environment, are increasing in recent times [4-7]. Compared to other materials, zeolites have very interesting physical and chemical properties. They have a microporous character with

uniform pore size, a shape selectivity which allows certain hydrocarbon molecules with a crack diameter less than or equal to that of the crystal to diffuse into the pores of the crystal, ion exchange properties. They have the possibility of developing an internal acidity which allows zeolites to be interesting materials for catalysis [8] and a high thermal stability [9]. Since November ,1972, when the synthesis of a new type of zeolite, denoted by ZSM-5 (Zeolite Socony Mobil Number 5), was filed, several research papers as well as patents related to its synthesis have been issued [10-15]. This zeolite can be distinguished by its unique properties. It has

significant applications such as a catalysis, gas separation and purification industry.

In the present work, hydrothermal synthesis and characterization of ZSM-5 zeolite crystals is described.

2. Material and Methods

The production of ZSM-5 generally follows three steps that are divided into the formation of a primary gel, the subsequent hydrothermal conversion to a secondary gel with the final crystallization step.

ZSM-5 zeolite was prepared by hydrothermal crystallization at 170°C for 48 hours (2 days) at Ph 11, from starting gels of molar composition 0.01 Al_2O_3, $1SiO_2$, $2 NaOH$, $0.15 TPABr$, $18.34 H_2O$, as it is shown below:
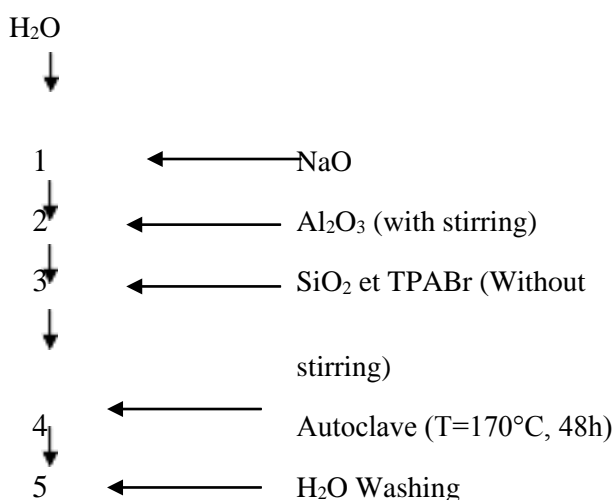
H_2O

1 ← NaO

2 ← Al_2O_3 (with stirring)

3 ← SiO_2 et TPABr (Without

stirring)

4 ← Autoclave (T=170°C, 48h)

5 ← H_2O Washing

After the crystallization process the obtained powder was washed with distillate water and dried at 120°C.

Chemical products used: SiO_2 :41.6%.

Al_2O_3 :77%.

The obtained powder was analyzed by powder X ray diffractometer (Philips PW 1800, using Cu Ke radiation), infrared spectroscopy (Philips PU 9800), scanning electron microscope (Philips XL 30) and differential thermal analyzer (M2 BDL SETARAM).

3. Results and Discussions

3.1 XRD analysis

The XRD patterns of as-elaborated samples are given in figure 1. They are in good agreement with

jcpds card048-0134. In Table I, the appearance of all peaks related to the presence of ZSM-5 was observed, confirming the high crystallinity.

According to these results, the absence of other phases than ZSM-5 were confirmed.

The comparison between the results found by the XRD analysis and those presented in the jcpds 048-0134 card, as shown in Table I, certify that there is a very good similarity between the measured parameters and those present in this card. The table .1 represents the parameters of XRD peaks of ZSM-5 zeolite and its reference parameters.
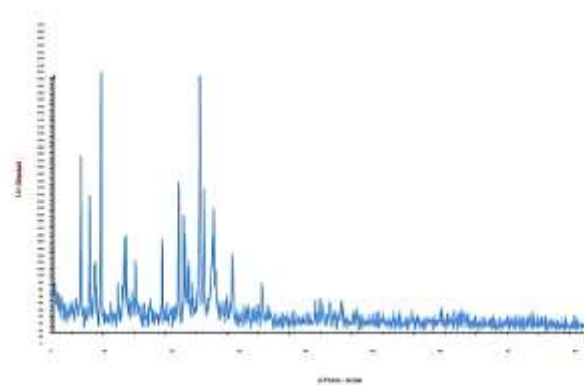
Figure.1 *XRD spectrum of ZSM-5 zeolite*

Table.1 *Parameters of XRD peaks of ZSM-5 zeolite and reference parameters.*

According to jcpds 048-0134			ZSM-5 powder	
hkl	d(A°)	I(%)	d(A°)	I(%)
101	11.163	96	11.158	100
200	9.997	62	10.067	31
002	6.682	13	6.707	4
102	6.348	18	6.065	1
301	5.981	20	6.003	9
131	5.701	13	5.713	7
202	5.574	16	5.578	8
122	5.372	7	5.368	2
400	4.996	13	5.034	3
103	4.353	18	4.364	4
421	4.250	22	4.261	5
203	4.095	14	4.087	1
501	3.858	100	3.857	43
133	3.655	29	3.649	14
432	3.437	14	3.444	5
104	3.312	16	3.308	4
080	2.488	6	2.491	1
1000	2.014	11	2.013	6
0100	1.991	11	1.994	4

3.2 FTIR analysis

The investigation by infrared spectroscopy technique in the mid-infrared region of the zeolite

spectrum is useful in this regard since it contains the fundamental vibrations of the framework Al, Si-4 or (T 4) tetrahedral. A different vibration bands are observed in the FTIR absorption spectrum of ZSM-5 zeolite shown in figure.2. The main bands of absorption obtained from Figure 2, are shown in Table 2.

Table 2. The main bands of IR absorption and associated bond vibration of ZSM-5 zeolite.

	Link type	Frequency cm¹ D.W.Breck	ZSM-5
Internal vibrations (tétraédres TO₄)	Asymmetric elongation Si-O-Al, Si-O-Si.	1250-950	1223
	Symmetric elongation Al-O, stretching	720-650	680
	Bending T-O link.	500-420	438
External vibrations	Double cycle 2C₄ et 2C₅ Si, Al-O.	650-500	547
	Pores openning	420-300	446
	Symmetric elongation Si-O-Al, Si-O-Si.	820-750	792
	Asymmetric elongation Si-O-Al.	1150-1050	1084

The first class of vibrations found at 1223 -1230, 680 -700 and 438-454 cm-' are assigned to the internal tetrahedral. The second group of frequencies observed at 547-546, 446,792-789 and 1084-1102 cm-' are assigned to the linkages between tetrahedral and the topology of the units of structure of samples.
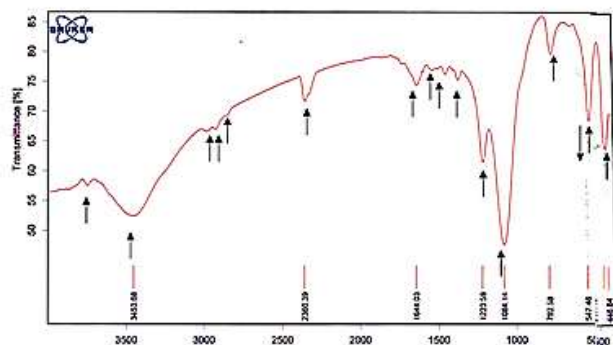
Figure.2 FTIR absorption spectrum of ZSM-5 zeolite

3.3 SEM characterization

The morphology of the crystalline phases was demonstrated by observation with a scanning electron microscope. The figure 3 illustrates the micrographs of these samples.

The morphology of the crystals is generally regular and that the dimensions of the ZSM-5 samples are of the order of 5-10 μm.
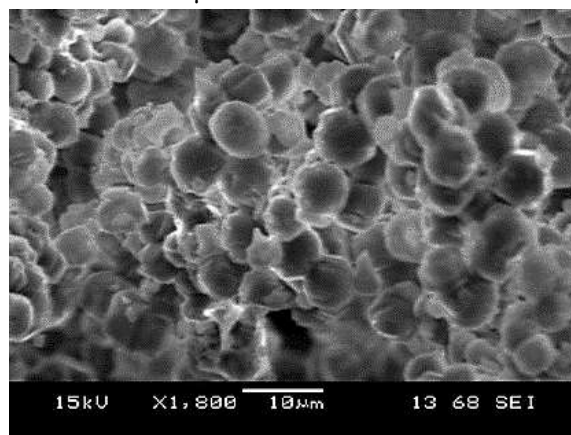
Figure .3 Scanning electron micrographs of ZSM-5 zeolite

According to the EDS characterization, the chemical composition of the as prepared powder is presented in figure. 4 and table.3
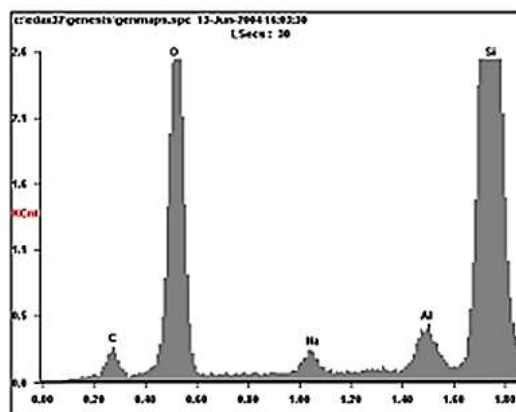
Figure.4 EDS analysis of ZSM-5 zeolite

Table.3 Chemical composition of ZSM-5 zeolite

Element	Weight %	Atomic%
O	49.57	53.88
Na	1.63	1.24
Al	1.77	1.14
Si	29.37	18.18
C	17.66	25.56

3.4 DTA analysis

Differential thermal analysis (DTA) of the sample revealed the organic structurant agent occluded in its basic structure. a succession of endotherms ranging were observed from 50 to 200 °C.

The differential thermal analysis of the sample allowed us to determine that the departure of the physisorbed water takes place from 100 to about 200 where the dehydration is complete.

The two most important transformations observed in the ATD curve of ZSM-5 zeolite presented in figure .5 can be interpreted as follows:

An endothermic peak at a temperature of 300 reflects the elimination of the organic structuring agent ((C3H7)4NBr) associated with the OH- ions and its subsequent removal by thermal decomposition.

A second exothermic peak at a temperature of 790 which probably translates into the beginning of the decomposition of the zeolite structure and finally a final peak at 1200 which necessarily translates into the total decomposition of the latter
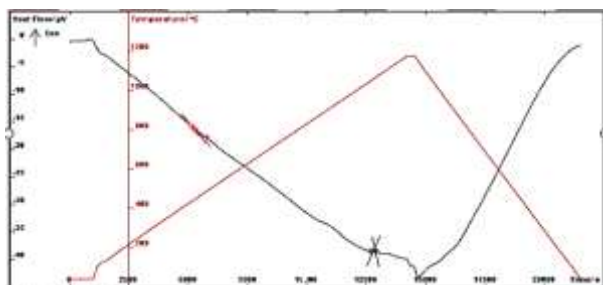
Figure.5 DTA curve of ZSM-5 zeolite

4. Conclusions

In the present work, pure ZSM-5 zeolite type is obtained for contact times of 48 hours, at temperatures of 160°C and under autogenous pressure.

The skeletal structure of the ZSM-5 material is thermally stable. The initial structural change starts to take place from 1026°C and above 1200°C the structure decomposes. The differential thermal diagram proves the stability of this structure.

The infrared spectroscopy technique allowed the characterization of the absorption bands attributed to the different Si-O-Si, Si-O-Al, Si-O and Al-O bonds linked to the tetrahedra forming the structures of ZSM-5 phases. Sites belonging to hydroxyl groups -OH were also revealed by this technique.

With their dual capacity for ion exchange and adsorption, these materials can be used in the very long term in the decontamination of any very dilute waste water

Author Statements:

- **Ethical approval:** The conducted research is not related to either human or animal use.

- **Conflict of interest:** The authors declare that they have no known competing financial interests or personal relationships that could have appeared to influence the work reported in this paper

- **Author contributions:** The authors declare that they have equal right on this paper.

- **Data availability statement:** The data that support the findings of this study are available on request from the corresponding author. The data are not publicly available due to privacy or ethical restrictions.

References

[1] Petrov, I., & Michalev, T. (2012). Synthesis of zeolite A: a review. Научни трудове на русенския университет, 51; 30-35.

[2] Ruiz, A., Brühwiler, D., Ban, T. et al (2005). Synthesis of Zeolite L. Tuning Size and Morphology. *Monatshefte für Chemi*e 136; 77–8.

[3] SMAIL, Heman A., REHAN, Mohammad, SHAREEF, Kafia M., et al. (2019). Synthesis of uniform mesoporous zeolite ZSM-5 catalyst for friedel-crafts acylation. *Chem Engineering,* 3(2):35.

[4] Ren, Z., Wang, L., Li, Y., Zha, J., Tian, G., Wang, F.,Liang, J. (2022). Synthesis of zeolites by in-situ conversion of geopolymers and their performance of heavy metal ion removal in wastewater: A review. *Journal of Cleaner Production,* 131441.

[5]Houhoune, F., Khemaissia, S., Nibou, D., Chegrouche, S., & Menacer, S. (2018, August). Kinetic study and sorption mechanism of uranium (VI) onto NaY zeolite. In *AIP Conference Proceedings* (Vol. 1994, No. 1, p. 070008). *AIP Publishing LLC.*

[6]Baouali, N. Y., Nibou, D., & Amokrane, S. (2022). NaY Zeolite and TiO2 Impregnated NaY Zeolite for the Adsorption and Photocatalytic Degradation of Methylene Blue under Sunlight. *Iran. J. Chem. Chem. Eng. Research Article* 41(6).

[7] Lee, J. S., Lee, Y. J., Tae, E. L., Park, Y. S., & Yoon, K. B. (2003). Synthesis of zeolite as ordered multicrystal arrays. Science, 301(5634);818-821.

[8] Wang, X., Ma, Y., Wu, Q., Wen, Y., & Xiao, F. S. (2022). Zeolite nanosheets for catalysis. *Chemical Society Reviews.*

[9] Kosinov, N., & Hensen, E. J. (2020). Reactivity, Selectivity, and Stability of Zeolite- Based Catalysts for Methane Dehydroaromatization. Advanced Materials, 32(44); 2002565.

[10] Jonscher, C., Seifert, M., Kretzschmar, N., Marschall, M. S., Le Anh, M., Doert, T.,& Weigand, J. J. (2022). Origin of Morphology Change and Effect of Crystallization Time and Si/Al Ratio during Synthesis of Zeolite ZSM- 5. *ChemCatChem*, 14(3); e202101248.

[11] REN, Nan, SUBOTIĆ, Boris, BRONIĆ, Josip, et al. (2012) Unusual pathway of crystallization of zeolite ZSM-5 in a heterogeneous system: phenomenology and starting considerations. *Chemistry of Materials*, 24(10);1726-1737.

[12]SADOWSKA, K., WACH, Anna, OLEJNICZAK, Zbigniew, et al. (2013). Hierarchic zeolites: Zeolite ZSM-5 desilicated with NaOH and NaOH/tetrabutylamine hydroxide. *Microporous and Mesoporous Materials*, 167;82-88.

[13]CONTE, Marco, LOPEZ-SANCHEZ, Jose A., HE, Qian, et al. (2012). Modified zeolite ZSM-5 for the methanol to aromatics reaction. *Catalysis Science & Technology* 2(1);105-112.

[14]KAMALUDDIN, Huda Sharbini, GONG, Xuan, MA, Pandong, et al. (2022). Influence of zeolite ZSM-5 synthesis protocols and physicochemical properties in the methanol-to-olefin process. *Materials Today Chemistry*, 26;101061.

[15] JEDLI, Hedi, ALMONEEF, M. M., MBAREK, Mohamed, et al. (2022). Adsorption of CO2 onto zeolite ZSM-5: Kinetic, equilibrium and thermodynamic studies. *Fuel,* 321;124097.

Research Article
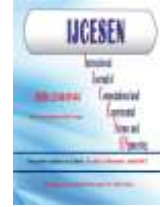
Dose Calibrator Measurements in the Case of Voltage Fluctuations

Osman GÜNAY[1,*], İrem Nur ALTINTAŞ[2] , Mustafa DEMİR[3], Nami YEĞİN[4]

[1] Yıldız Technical University, Faculty of Electrical & Electronics, Biomedical Engineering Dep., Istanbul, Turkiye
*** Corresponding author Email:** ogunay@yildiz.edu.tr - **ORCID:** 0000-0003-0760-554X

[2] Yıldız Technical University, Faculty of Electic & Electronics, Biomedical Engineering Dep., Istanbul 34220, Turkiye
Email: nur.altintas@std.yildiz.edu.tr - **ORCID:** 0009-0002-4535-7815

[3] Department of Nuclear Medicine, Cerrahpasa Faculty of Medicine, Istanbul University-Cerrahpasa, Istanbul, Turkey
Email: demirm@istanbul.edu.tr - **ORCID:** 0000-0002-9813-1628

[4] Department of Nuclear Medicine, Cerrahpasa Faculty of Medicine, Istanbul University-Cerrahpasa, Istanbul, Turkey
Email: namiyeyin@gmail.com - **ORCID:** 0000-0003-0262-4020

Abstract:

Radiation dose measurements of radiopharmaceuticals and measurements of dose calibrators at different voltages and fluctuations were evaluated. Low and high doses of technetium, iodine and fluorine pharmaceuticals were measured in different voltages. The results showed that only low doses could make small and insignificant differences.

1. Introduction

The field of nuclear medicine covers the process of imaging or treating structures by injecting radioactive materials into the body. Imaging (Diagnosis): Radiation is used to image organs or tissues with the help of a radioactive substance that is injected or inhaled into the body. Radiotherapy (Treatment): Radiotherapy is radiation therapy used to destroy or control cancerous cells [1].

Radiopharmaceuticals are frequently used in treatments or diagnosis processes. The radioactive part of the radiopharmaceutical given to the patient by mouth or intravenously emits radiation such as gamma rays or beta particles[2]. The Nuclear Regulatory Commission (NRC) has made it mandatory to measure the activity to be given to the patient using a dose calibrator before radiopharmaceuticals are administered.

The dose calibrators used for this purpose are used to measure the activity of the radiopharmaceutical to be given to the patient for diagnostic imaging or radionuclide therapy. One can refer to these dose calibrators as well-type ion chambers, which operate based on the principle of ion chambers [3]. A dose calibrator ion chamber includes high voltage source, an amplifier containing electronics, and a display unit.

The ion chambers used in the dose calibrator system are filled with high-pressure Argon gas[4]. When the radiopharmaceutical emits radiation in the ion chamber, it forms ion pairs that generate a potential difference between the two electrodes. As a result, the positively charged ions move toward the cathode and the negatively charged ions move toward the anode, which produces a signal that can be measured [5]. These signals are converted into current by devices connected to the ion chamber. The total current generated in the ion chamber is directly proportional to the amount of radioactive material.

Various problems can arise if the dose calibrator measures incorrectly. There is a risk of giving high doses to the patient because of erroneous measurements. For example, Tc-99m chemically binds to various bioactive substances and produces radiopharmaceuticals used in nuclear medicine imaging[1]. Patients exposed to excessive gamma-ray environmental radiation may suffer various damages. Overexposure to radiation can even bring about genetic effects. These genetic effects occur in mutations in reproductive cells and can be passed on to the next generation[6]. Also shooting with a low

dose will negatively affect the image quality [7]. Therefore, certain conditions are required for the stable operation of dose calibrators. Among these, calibrations such as the exact accuracy test, linearity test, and stability test should be measured.

Apart from calibration tests, the effects of power cuts and **voltage fluctuations** on electronic devices are known. Hospitals, on the other hand, contain devices that need a high voltage source such as MRI (Magnetic Resonance Imaging) and CT (Computer Tomography) devices, and electroshock devices[8]. To prevent these voltage fluctuations in hospitals, special devices designed to provide stable electrical current, and voltage are used. These devices are called regulators or UPS systems (uninterruptible power supply). Regulators provide a stable voltage by reducing voltage fluctuations, while UPS is keeping devices running by providing backup power in intermittent or low-voltage situations. Despite the presence of protective systems and circuits, voltage fluctuations may occur.

Due to these voltage fluctuations, errors may occur in radiation measurements in radiopharmaceutical applications when using dose calibrators. But today, there are high-technology voltage regulation circuits in devices, especially medical devices based on human health.

2. Material and Methods

Capintec - CRC ®-25PET Dose Calibrator [9], Technetium (Tc)-99m, Iodine (I)-131, Fluorine-18 (F-18) radioisotopes and VAR-SAN 0-250V voltage source as you can see in the Figure 1 were used as materials.

***Figure 1.** Voltage source*

The CRC-25PET dose calibrator device supply input is connected to the voltage source output. Then, the highly active Iodine-131 radioisotope was transferred to the calibrator well. Voltage values have been adjusted over the voltage source. Initially,

values from 10V to 250V were noted. Then the voltage values fluctuated rapidly between 10-250. This process was also applied to the low-activity Iodine-131 radioisotope, and the values were noted. The same procedure was repeated for Technetium (Tc)-99m and Fluorine-18 radioisotopes, with high and low activity for each.

3. Results and Discussions

The results are in *mCi* units. The voltage values were changed step by step at the power supply, from low to high and high to low.

Figure 2 shows the measurement of high-activity Iodine-131 from 20V to 250V. It has been observed that the difference between low voltage measurement and high voltage measurement is 0.03. With the same measurement method, the low activity Iodine-131 measurement results are shown in Figure 3, it was observed that the difference between 20V and 250V was only 0.003 (Figure 4). In Figure 5, the measurement of the highly active Fluor-18 radioisotope from 20V to 250V is shown. It was observed that the measured value between 50V and 150V increased by 0.06 mCi. In figure 6 the same measurement was made with low-activity
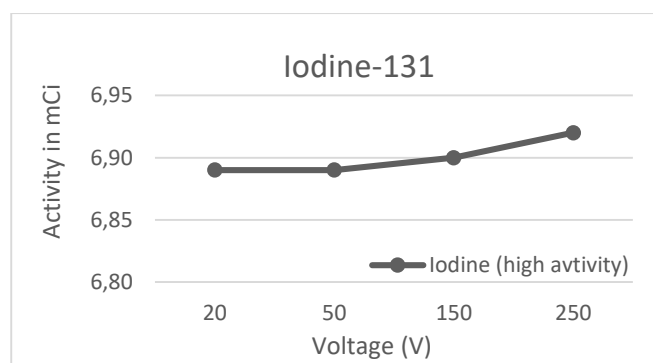
***Figure 2.** High-activity Iodine-131 radioisotope*
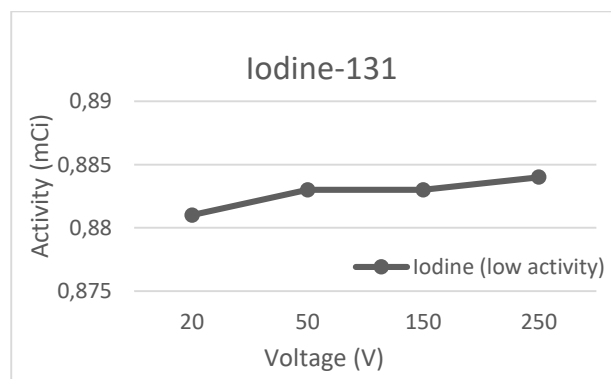
***Figure 3.** Low-activity Iodine-131 radioisotope*

Figure 4 *Low activity Iodine-131 at 20 ~ 30V*
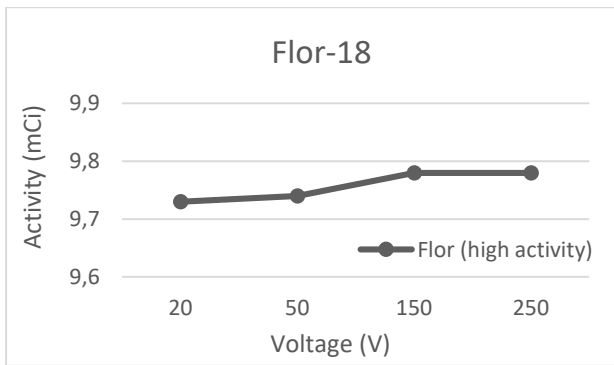
Figure 5. *High activity Flor-18 radioisotope*

Figure 6. *High activity Flor-18 at 20 ~ 30V*
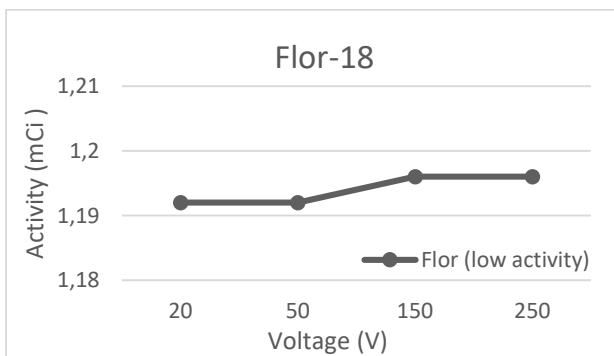
Figure 7. *Low activity Flor-18 radioisotope*

Fluor-18 in Figure-7 and it was observed that the difference in the 20-250V range was only 0.004 mCi. In Figure 8, the calibration device measurements of the high activity Technetium-99 isotope are given depending on the voltage (Figure 9). A deviation of 0.1 mCi was observed, especially between 50V-250V.

Figure 10 shows the measurements of the low-activity Technetium-99 isotope. A difference of 0.01 was noted in Technetium-99 low activity. The results from the measurements are shown in the graphs. We can say that a difference of 0.03 mCi to
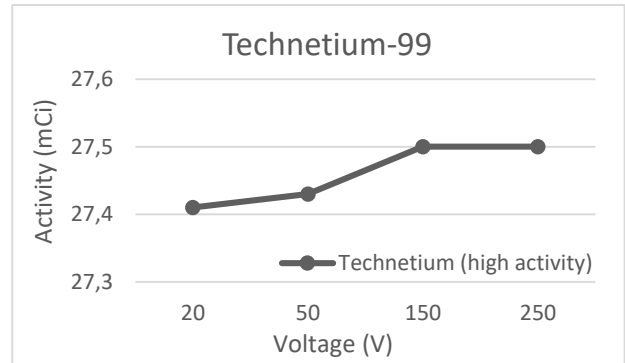
Figure 8. *High activity Technesium-99 radioisotope*

Figure 9. *High activity Technesium-99 at 150V*
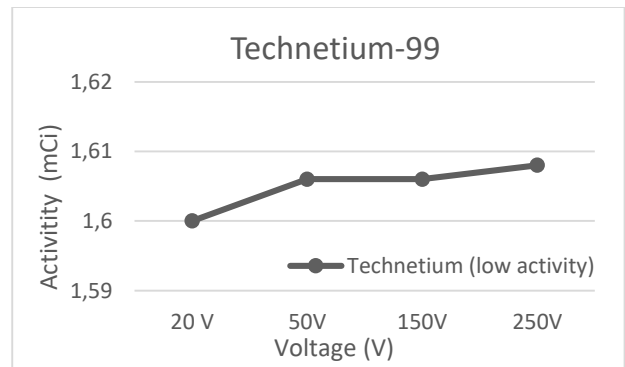
Figure 10. *Low activity Technesium-99 radioisotope*

Figure 11. *Low activity Technesium-99 at 20V*

0.1 mCi was observed from high voltage to low voltage (Figure 11). No change was observed when the voltage was fluctuated. We can say that a higher difference was observed in the technetium-99 high activity measurement. The least difference was observed at the low-activity dose of Iodine. In general, the difference in the higher activities of the isotopes was observed between 0.6 and 0.1. At low activities the difference is much less. There was no significant difference. The reasons will be explained in the next heading.

4. Conclusions

The results show us that nearly 0.1% differences in the radiation dose measurement of radiopharmaceuticals, which may occur from voltage fluctuations, will not have a great impact on human health. Low-activity radioisotopes may be slightly less than the required value at low voltage, and therefore imaging may be slightly impaired.
The reason for this is the strong safety circuits in the device. These safety circuits contain voltage & current protective circuit elements, and transformators. This means that even if the input voltage is 20V or 250V the device amplifies this voltage due to the regulation circuits in it.

Author Statements:

- **Ethical approval:** The conducted research is not related to either human or animal use.
- **Conflict of interest:** The authors declare that they have no known competing financial interests or personal relationships that could have appeared to influence the work reported in this paper
- **Acknowledgement:** The authors declare that they have nobody or no-company to acknowledge.

- **Author contributions:** The authors declare that they have equal right on this paper.
- **Funding information:** The authors declare that there is no funding to be acknowledged.
- **Data availability statement:** The data that support the findings of this study are available on request from the corresponding author. The data are not publicly available due to privacy or ethical restrictions.

References

[1] Günay, O., Sarıhan, M. , Abamor, E. & Yarar, O. (2019). Environmental Radiation Doses from Patients Undergoing Tc-99m DMSA Cortical Renal Scintigraphy. *International Journal of Computational and Experimental Science and Engineering*, 5(2);86-93.DOI: 10.22399/ijcesen.58926

[2] Zimmerman, B. E., & Cessna, J. T. (2000). Experimental determinations of commercial 'dose calibrator' settings for nuclides used in nuclear medicine. *Applied Radiation and Isotopes* : including data, instrumentation and methods for use in agriculture, industry and medicine, 52(3);615–619. https://doi.org/10.1016/s0969-8043(99)00219-5

[3] Jain AN, Rehman MA. (1981). Quality control of dose calibrators. *Nuklearmedizin* 20:247-50.

[4] Forwood, N., Willowson, K. P., Tapner, M., & Bailey, D. L. (2017). Assessment of the relative contribution of volume and concentration changes in Yttrium-90 labelled resin microspheres on ionization chamber measurements. Australasian physical & engineering sciences in medicine, 40(4);943–948. https://doi.org/10.1007/s13246-017-0601-z

[5] Assan, B. & Addison, Eric & Hasford, Francis & Sosu, Edem. (2012). callibration and effective use of a dose calibrator. *International journal of science and technology*. 2. 395-400.

[6] Javier, Eduardo & Arista Romeu, Eduardo Javier. (2020). Feasibility study for the development of a Dose Calibrator with a well ionization chamber.

[7] Günay, O.,Gündoğdu Ö.,Demir M., Abuqbeita M., Yaşar, Doğan & Aközcan, S.& Kapdan E., Yarar O., (2019). Determination of the Radiation Dose Level in Different Slice Computerized Tomography. *International Journal of Computational and Experimental Science and Engineering*. 5. 119-123. 10.22399/ijcesen.595645.

[8] Guven, D., Kayalica, M. O., & Kayakutlu, G. (2021). Critical Power Demand Scheduling for Hospitals Using Repurposed EV Batteries. *Technology and Economics of Smart Grids and Sustainable Energy,* 6(1), 21. https://doi.org/10.1007/s40866-021-00120-z

[9] Datasheet of device: https://pdf.medicalexpo.com/pdf/capintec/crc-25r-dose-calibrator/70709-191075.html
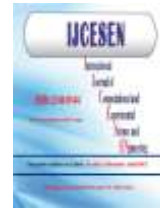
Performance Analyses of Combined Cycle Power Plants

Rabi KARAALİ*

Bayburt University, Fac. of Eng., Dep.of Mechanical Eng., Bayburt, Turkey.
*Corresponding Author : Email: rabikar@gmail.com ORCID: 0000-0002-2193-3411

Abstract:

In this article, different compressor pressure and different excess air rates for a gas turbine based combine cycle power plant with steam Rankine cycle as bottoming cycle were analyzed by using 1. and 2. laws of thermodynamics and exergy analyses methods to obtain the best performances of the cycle. Exergy efficiency of the cycle, net powers of the gas and steam turbines and the overall cycle, exergy loss of the components, the efficiencies of the components are obtained, compared and discussed. It was found that, increasing the compressor pressure increases exergy efficiency of cycle, gas turbine and total plant power, and the combustion chamber, the HRSG and the compressor efficiencies. However, increasing compression rates decreases steam turbine power, combustion chamber, steam turbine, and HRSG exergy losses and the gas turbine efficiency. Also, it is found that, increases in excess air ratios gives an optimum or a maximum exergy efficiency, at 2.5 excess air rate of the cycle.

1. Introduction

The environmental concerns regarding carbon emissions, rise in electricity demand with the rapid development of emerging economies and finite fossil fuel reserves have made the increased efficiency in energy conversions, the renewable energy sources and the recovery of previously unused energies very important [1, 2, 3]. To identify alternative sources of energy that can be used for power generation with minimal harmful effects to the environment is necessary. Today's environmental concerns are about the recovery and using of low-grade temperatures heat sources. Also, previously termed 'waste heat' in various industrial processes is now taken as a potential source for electricity generation. The CCPP technology includes two or more power cycles, to obtain high efficiency and to provide a decrease in pollutant emissions [4, 5, 6]. In power generation, gas turbine combined cycles have been used extensively. Also, combined cycles have the advantages low investment, operation and maintenance costs, suitability for plant operations and flexibility to fluctuations in demand. [7, 8].
Combined cycles include a topping cycle and a bottoming cycle. For the low temperatures, bottoming Organic Rankine Cycles (ORC) are

another alternative, those have shown good performance. The organic working fluids for Rankine cycles has been proposed for different applications: for renewable energy, for heat recovery and they are commercially available [9, 10].
The Organic Rankine Cycle is a widely investigated for the using of low temperatures energy sources like geothermal, industrial waste heat, biomass, and solar which is reduced the capital and operation costs [10]. They have the advantages of the simplicity of construction and operation, smaller equipment sizes, and high modularity [10]. In literature, studies on the increasing efficiency of CCPP are about the increase of the efficiencies of gas turbines, steam turbines, and both cycles (topping and bottoming) [11], and the increase of the organic fluids impact on efficiency [10].
By applying reheat and by reducing the irreversibilities in HRSG, the efficiency of the Rankine cycle can be increased. Also, different factors may change the ORC performance such as the configuration of the system, thermophysical properties of working fluids, the temperature of the external source, the components efficiency, etc. The efficiency of the CCPPs can be improved by modifying the performance of the components. While Organic Rankine Cycles (ORC) are used to gain heat energy from different sources to generate

power, the steam Rankine Cycles (SRC) are used to recover high temperature heat to generate power. Investigations for alternative, harmless, low emissions fuels to use in CCPPs can be found in literature [12, 13, 14].

In this study, gas turbine combined cycle with steam Rankine cycle was analyzed by using the 1., the 2. laws of thermodynamics and exergy analyses methods to obtain the best performances of the cycle by changing compression ratio and excess air rates.

2. Material and Methods

Gas turbine-based combine cycle power plant with steam Rankine cycle can be seen at Figure 1. Figure 1 shows that, the air is compressed to higher pressure, then it is combusted by fuel to obtain the combustion gas at 3. The gases at 3 are expanded to low pressure at 4. Gases at 4 enters the heat recovery steam generator to transfer heat to the steam. Steam at the outlet of HRSG at 8, is expanded in the steam-turbine at 9. Saturated water at the exit of the condenser at 10 is pumped to at 7.
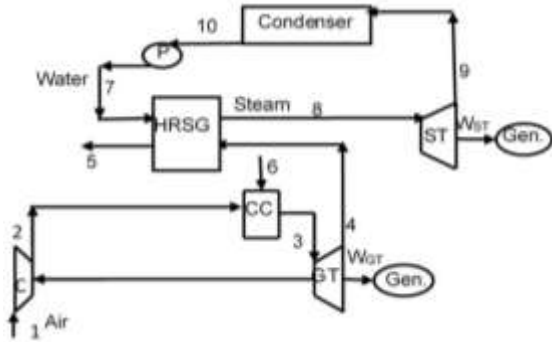
Figure 1. *Gas turbine based combine cycle power plant with steam Rankine cycle as bottoming cycle.*

These assumptions were made for the analyses; the components are taken as a steady-state steady-flow systems, pressure drop is negligibly small, in kinetic and potential energies changes are negligible [11].

The energy equation;

$$\dot{Q}_{CV} - \dot{W}_{CV} + \sum_{in} \dot{m}_{in}\left(h_{in} + \frac{V_{in}^2}{2} + gz_{in}\right) - \sum_{out} \dot{m}_{out}\left(h_{out} + \frac{V_{out}^2}{2} + gz_{out}\right) = 0 \quad (1)$$

The conservation mass law for steady state;

$$\sum \dot{m}_{in} = \sum \dot{m}_{out} \quad (2)$$

Efficiency of the system;

$$\eta = \frac{W + Q_{steam.}}{Q_{Fuel,inlet.}} \quad (3)$$

Electrical efficiency of the system;

$$\eta_{el} = \frac{W}{Q_{Fuel,inlet}} \quad (4)$$

For the calculations, the combustion was taken as ideally and completely [11]. The combustion is;

$$\overline{\lambda}CH_4 + (0.7748N_2 + 0.2059O_2 + 0.0003CO_2 + 0.019H_2O \rightarrow (1 + \overline{\lambda})(X_{N2}N_2 + X_{O2}O_2 + X_{CO2}CO_2 + X_{H2O}H_2O)$$
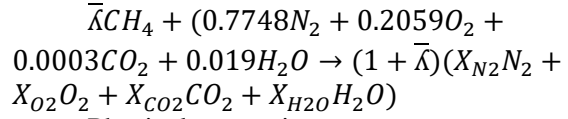
Physical exergy is;

$$e_{phyical} = (h - h_0)_{mixture} - T_0\cdot(s - s_0)_{mixture} = \sum_j x_j\left[\int_{T_0}^T c_{p0j}(T)dT - T_0\cdot\left(\int_{T_0}^T \frac{c_{p0j}(T)}{T}dT - \overline{R}\ln\frac{P_j}{P_0}\right)\right] \quad (5)$$

The chemical exergy is as [11];

$$\bar{e}_{chem,mixt} = \sum_i x_i\bar{e}_{chemical,i} + \overline{R}T_0\sum_i x_i\ln x_i \quad (6)$$

The total exergy are;

$$\overline{E} = \overline{E}_{phy} + \overline{E}_{chem} \quad (7)$$

Table 1: *Equations of energies, mass, entropies of the components of gas turbine based combine cycle power plant with steam Rankine cycle [11].*

Components	Mass Equation	Energy Equation	Entropy Equation
Compressor	$\dot{m}_1 = \dot{m}_2$	$\dot{m}_1.h_1 + \dot{W}_C = \dot{m}_2.h_2$	$\dot{m}_1.s_1 - \dot{m}_1.s_2 + \dot{S}_{gen,C} = 0$
Gas Turbine	$\dot{m}_3 = \dot{m}_4$	$\dot{m}_3 h_3 = \dot{W}_{GT} + \dot{W}_C + \dot{m}_4 h_4$	$\dot{m}_3 s_3 - \dot{m}_4 s_4 + \dot{S}_{gen,GT} = 0$
HRSG	$\dot{m}_4 = \dot{m}_5$ $\dot{m}_7 = \dot{m}_8$	$\dot{m}_4 h_4 + \dot{m}_7 h_7 = \dot{m}_5 h_5 + \dot{m}_8 h_8$	$\dot{m}_4 s_4 + \dot{m}_7 s_7 - \dot{m}_5 s_5 - \dot{m}_8 s_8 + \dot{S}_{gen,HRSG} = 0$
Steam Turbine	$\dot{m}_8 = \dot{m}_9$	$\dot{m}_8 h_8 = \dot{W}_{ST} + \dot{W}_P + \dot{m}$	$\dot{m}_8 s_8 - \dot{m}_9 s_9 + \dot{S}_{gen,ST} = 0$
Combustion Chamber	$\dot{m}_2 + \dot{m}_6 = \dot{m}_3$	$\dot{m}_2 h_2 + \dot{m}_6 h_6 = \dot{m}_3 h_3 + 0.02\dot{m}_6 LHV$	$\dot{m}_2 s_2 + \dot{m}_6 s_6 - \dot{m}_3 s_3 + \dot{S}_{gen,CC} = 0$
Pump	$\dot{m}_{10} = \dot{m}_7$	$\dot{m}_{10} h_{10} = \dot{m}_7 h_7 + \dot{W}_P$	$\dot{m}_{10} s_{10} - \dot{m}_7 s_7 + \dot{S}_{gen,P} = 0$
Condenser	$\dot{m}_{10} = \dot{m}_9$	$\dot{m}_9 h_9 = \dot{m}_{10} h_{10} + \dot{Q}_c$	$\dot{m}_9 s_9 - \dot{m}_{10} s_{10} + \dot{S}_{gen,P} = 0$
Overall Cycle	$\bar{h}_i = f(T_i)$ $\bar{s}_i = f(T_i, P_i)$ $\dot{m}_{air}h_{air} + \dot{m}_{fuel}LHV_{CH4} - \dot{Q}_{Loss,CC} - \dot{m}_{eg,out}h_{eg.,out} - \dot{W}_{GT} - \dot{W}_{ST} - \dot{Q}_{Loss,c} = 0$ $\dot{Q}_{Loss,CC} = 0.02\dot{m}_{fuel}LHV_{CH4}$		

For open systems exergy equation;

$$\sum_i \dot{m}_i.h_i - \sum_i T_0.S_i - \sum_j \dot{m}_j.h_j + \sum_j T_0.S_j + \sum \dot{Q}_k - \sum \dot{Q}_k.\frac{T_0}{T_k} - \dot{W} = \dot{E}_{loss} \quad (8)$$

In Table 1 equations of energy, mass, entropy of components of gas turbine based combine cycle power plant with steam Rankine cycle are given. In Table 2 the equations of exergies, exergy efficiencies, and performance criteria of components of gas turbine based combine cycle power plant with steam Rankine cycle are shown.

Table 2: *The equations of exergies, exergy efficiencies, and performance criteria of components of gas turbine based combine cycle power plant with steam Rankine cycle [11].*

Components	Exergy Equation	Exergy Efficiency
Compressor	$\dot{E}_{D,C} = \dot{E}_1 + \dot{W}_C - \dot{E}_2$	$\eta_{ex,C} = \dfrac{\dot{E}_{out,C} - \dot{E}_{in,C}}{\dot{W}_C}$
Turbine	$\dot{E}_{D,T} = \dot{E}_3 - \dot{E}_4 - \dot{W}_C - \dot{W}_{GT}$	$\eta_{ex,GT} = \dfrac{\dot{W}_{net,GT} + \dot{W}_C}{\dot{E}_{in,T} - \dot{E}_{out,T}}$
HRSG	$\dot{E}_{D,HRSG} = \dot{E}_4 - \dot{E}_5 + \dot{E}_7 - \dot{E}_8$	$\eta_{ex,HRSG} = \dfrac{\dot{E}_{steam,HRSG} - \dot{E}_{wate}}{\dot{E}_{in,exhaust,HRSG} - \dot{E}_{out,e}}$
Steam Turbine	$\dot{E}_{D,T} = \dot{E}_8 - \dot{E}_9 - \dot{W}_P - \dot{W}_{ST}$	$\eta_{ex,ST} = \dfrac{\dot{W}_{net,ST} + \dot{W}_P}{\dot{E}_{in,ST} - \dot{E}_{out,ST}}$
Combustion Chamber	$\dot{E}_{D,CC} = \dot{E}_2 + \dot{E}_6 - \dot{E}_3$	$\eta_{ex,CC} = \dfrac{\dot{E}_{out,CC}}{\dot{E}_{in,CC} + \dot{E}_{fuel}}$
Pump	$\dot{E}_{D,P} = \dot{E}_{10} + \dot{W}_P - \dot{E}_7$	$\eta_{ex,P} = \dfrac{\dot{E}_{out,P} - \dot{E}_{in,P}}{\dot{W}_P}$
Condenser	$\dot{E}_{D,c} = \dot{E}_9 - \dot{E}_{10}$	$\eta_{ex,c} = \dfrac{\dot{E}_{in,c}}{\dot{E}_{out,c}}$
Overall Cycle	Exergy efficiency	$\dot{E} = \dot{E}_{ph} + \dot{E}_{ch}$ $\dot{E}_{ph} = \dot{m}(h - h_0 - T_0(s - s_0))$ $\dot{E}_{ch} = \dfrac{\dot{m}}{M}\left\{\sum x_k \bar{e}_k^{ch} + \bar{R}T_0 \sum x_k \ln x_k\right\}$ $\eta_{ex} = \dfrac{\dot{W}_{net,GT} + \dot{W}_{net,ST}}{\dot{E}_{fuel}}$

3. Results and Discussions

The ambient conditions were taken as $P_0=101.3$ kPa and $T_0=25\ ^0C$, in this article. Compressor air flow is $m_{air}=91.3$ kg/sec, and fuel flow is $m_{fuel}=1.64$ kg/sec. The isentropic efficiency of the steam, gas turbines and compressor were taken as $\eta_{izST}=\eta_{izC}=\eta_{izGT}=0.86$. The compressor ratio is 10, temperature of steam $T_{steam}=485.57$ K. HRSG outlet temperature is taken as $T_{exh}=426$ K [11].
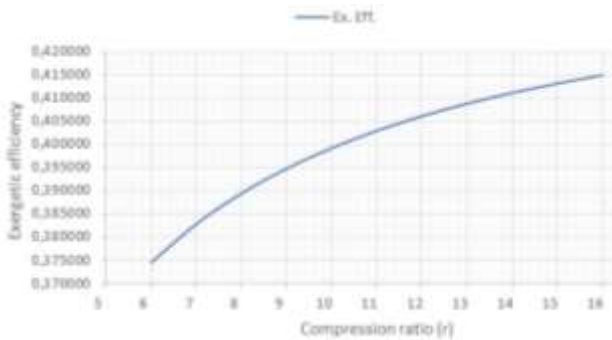
Figure 2. *Variation of the exergy efficiency with compression ratios of CCPPs.*
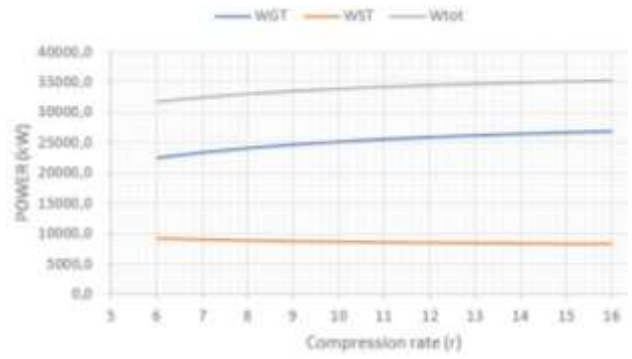
Figure 3. *Variation of the power with compression ratios of CCPPs.*

In figure 2, variation of the exergy efficiency with pressure ratios of CCPPs is given. That is shown that, increasing pressure ratios from 6 to 16 increases exergy efficiency, about % 11 of the gas turbine based combine cycle power plant with steam Rankine cycle.

In figure 3, variation of the power with pressure ratios of CCPPs is given. Increasing compression rates, increases gas turbine and the total plant power, but decreases the steam turbine power. Increasing compression rates from 6 to 16 increases gas turbine, total plant power about % 15 and % 11. But decreases the steam turbine power about % 8.
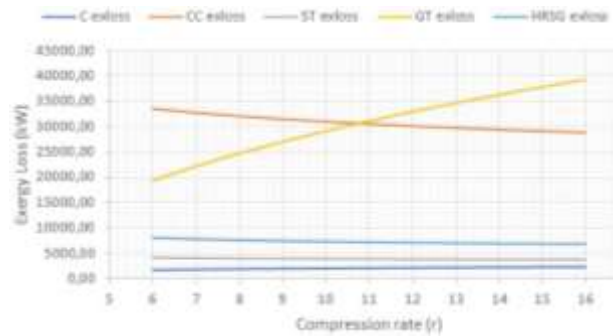
Figure 4. *Variation of the exergy losses of the components with compression rates for CCPPs.*

In figure 4, variation of the exergy losses of components with compression rates for CCPPs are given. Increasing compression rates increases gas turbine and compressor exergy loss about % 76 and % 29, respectively. However, increasing compression rates decrease combustion chamber, steam turbine, and HRSG exergy losses about, % 12, % 8, % 16, respectively. In figure 5, variation of efficiencies of components with pressure ratios of CCPPs are given. That is seen, increasing compression rates increases the combustion, the HRSG and the compressor
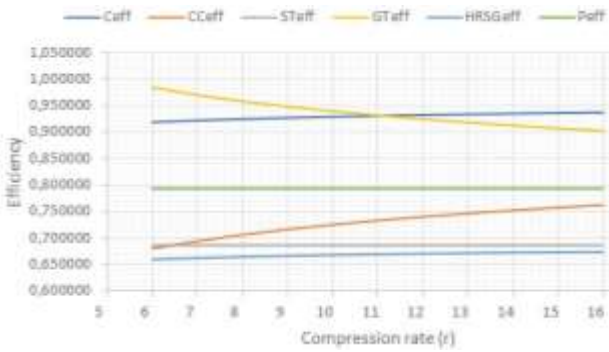
Figure 5. *Variation of efficiencies of the components with pressure rates for CCPPs.*

efficiencies about % 11, % 2 and % 2, respectively. However, increasing compression rates decreases the gas turbine efficiency, about % 7, while the steam turbine, and the pump efficiencies stay constant.
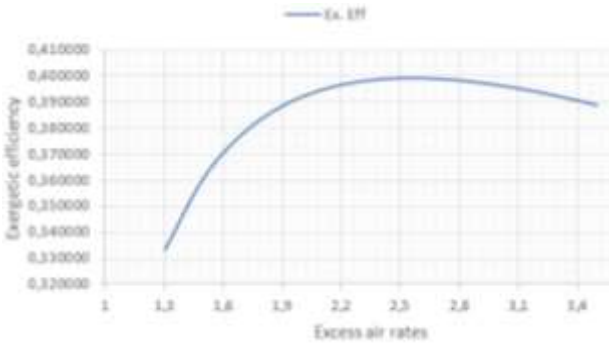

Figure 6. *Variation of the exergy efficiency with excess air ratios of CCPPs*

In figure 6, variation of the exergy efficiency with excess air ratios of CCPPs is given. It can be seen, increasing excess air rates gives an optimum or maximum exergy efficiency, at 2.5 excess air ratio of the turbine based combine cycle power plant with steam Rankine cycle.
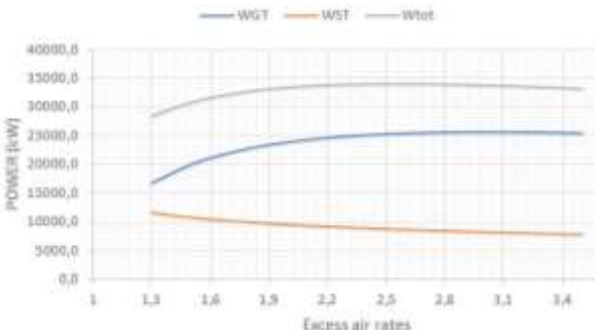
Figure 7. *Variation of the net power of the turbines with excess air ratios of CCPPs.*

In figure 7, variation of net power with excess air ratios of the CCPPs is shown. That is seen, increasing excess air rates gives a maximum power point for gas turbine and total plant power at 2.9 and

2.5 excess air rates, respectively. But decreases the steam turbine power about % 34.
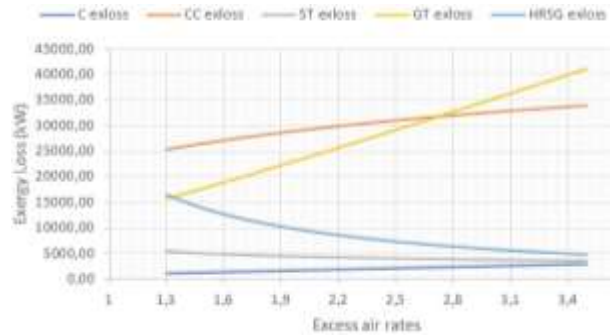
Figure 8. *Variation of exergy loss of components with excess air ratios of CCPPs.*

In figure 8, variation of exergy loss of components with excess air ratios of CCPPs is given. An increase in excess air ratios increases gas turbine, combustion chamber and compressor exergy loss about % 161, % 34 and % 170, respectively. Also, increasing excess air rates decrease steam turbine, and HRSG exergy losses about, % 34, % 71, respectively.
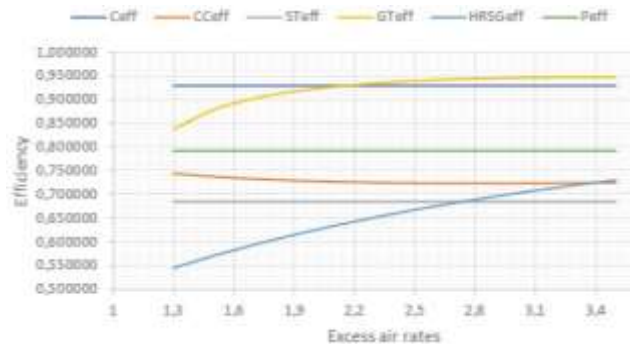
Figure 9. *Variation of efficiencies of devices with excess air ratios of CCPPs.*

In figure 9, variation of efficiencies of devices with excess air ratios of CCPPs can be seen. An increase in excess air ratios increases gas turbine, and HRSG efficiencies % 13 and % 34, respectively. However, increasing excess air ratio has an affect to decrease combustion chamber efficiency, about % 3, while compressor, the steam turbine, and the pump efficiencies stay constant.

4. Conclusions

In this article, different compressor pressures and excess air ratios for a gas turbine based combine cycle power plant with steam Rankine cycle as bottoming cycle are analyzed by using 1. and 2. laws of thermodynamics and exergy analyses methods to obtain the best performances of the cycle. Exergy efficiency of the cycle, net powers of gas turbine, steam turbine and the cycle, exergy loss of the components, the efficiencies of the components are

obtained, compared and discussed. That is found, an increase in compression rate increase exergy efficiency of this cycle, gas turbine and the total plant power, and the combustion chamber, the HRSG and the compressor efficiencies. However, increasing compression rates decreases the steam turbine power, combustion chamber, steam turbine, and the HRSG exergy losses and the gas turbine efficiency. Also, that is found, increasing excess air ratios from 1.3 to 3.5 gives an optimum or a maximum exergy efficiency, at 2.5 excess air ratio of the cycle. Increasing excess air ratios, increases gas turbine, combustion chamber and compressor exergy losses, but decreases steam turbine, and HRSG exergy losses.

Author Statements:

References

[1] Keven A., Karaali R., (2015). Investigation of an Alternative Fuel for Diesel Engines. *Acta Physica Polonica A*, 128(2B);282 – 286.

[2] Karaali, R., (2016). Thermodynamic Analysis of a Cascade Refrigeration System. *Acta Phys. Pol. A* 130(1);101-106. DOI: 10.12693/APhysPolA.130.101

[3] Karaali, R., (2016). Exergy Analysis of a Combined Power and Cooling Cycle. *Acta Phys. Pol. A* 130(1);209-213. DOI: 10.12693/APhysPolA.130.209

[4] Karaali, R. (2010). *Thermoeconomic optimization of cogeneration power plants* (Doctoral dissertation, PhD Thesis. Kocaeli Univ).

[5] Karaali R., Öztürk İ.T. (2017). Performance Analyses of Gas Turbine Cogeneration Plants. *ISI Bilimi ve Teknigi Dergisi-Journal of Thermal Science and Technology*. 37(1);25 – 33.

[6] Karaali R., Keven A., (2022). Evaluation of Four Different Cogeneration Cycles by Using Some Criteria. *Applied Rheology*, 32(1);122 – 137.

[7] Jiangfeng Wang, Yiping Dai, and Lin Gao, (2008). Parametric analysis and optimization for a combined power and refrigeration cycle. *Applied Energy*. 85;1071–1085

[8] Christoph Koch, Frank Cziesla and George Tsatsaronis, (2007). Optimization of combined cycle power plants using evolutionary algorithms. *Chemical Engineering and Processing* 46;1151–1159

[9] M. A. Javadi, S. Hoseinzadeh, M. Khalaji and R. Ghasemiasl, (2019). Optimization and analysis of exergy, economic, and environmental of a combined cycle power plant. *Sadhana* 44;121. https://doi.org/10.1007/s12046-019-1102-4

[10] Keyvan Bahlouli, (2018) Multi-objective optimization of a combined cycle using exergetic and exergoeconomic approaches. *Energy Conversion and Management*. 171;1761–1772. https://doi.org/10.1016/j.enconman.2018.06.100

[11] Bejan, A., Tsatsaronis, G,, Moran, M. (1996). Thermal Design and Optimization. Danvers, Massachusetts: Wiley Pub.

[12] Şanlı, H., Alptekin, E., Çanakç, M., (2022). Using low viscosity micro-emulsification fuels composed of waste frying oil-diesel fuel-higher bio-alcohols in a turbocharged-CRDI diesel engine, *Fuel,* 308;1-13.

[13] Alptekin, E., Şanlı, H., Çanakç, M., (2019). Combustion and performance evaluation of a common rail DI diesel engine fueled with ethyl and methyl esters, *Applied Thermal Engineering*, 149;180-191.

[14] Şanlı, H., (2018). An experimental investigation on the usage of waste frying oil-diesel fuel blends with low viscosity in a Common Rail DI-diesel engine. *Fuel,* 222;434-443.

Research Article

An Analysis on Radiation Protection Abilities of Different Coloured Obsidians

Zeynep AYGUN[1]*, Murat AYGUN[2]

[1]Bitlis Eren University, Vocational School of Technical Sciences, 13000, Bitlis, Turkey
* **Corresponding Author** : **Email:** zeynep.yarbasi@gmail.com ; **ORCID:** 0000-0002-2979-0283

[2]Bitlis Eren University, Faculty of Science and Arts, Department of Physics, 13000, Bitlis, Turkey
Email: maygun@beu.edu.tr ; **ORCID:** 0000-0002-4276-3511

Abstract:

Obsidians are naturally occurring structures which have great interest and are widely used in engineering, nuclear and medical applications. Obsidian, a glassy volcanic rock, is formed as a result of volcanic activity and lava eruptions. In the present study, it is aimed to determine the radiation protection parameters of obsidians with different colours in order to examine the radiation shielding capabilities of the samples. The parameters were determined in the range of 4keV-100 GeV photon energies by using Phy-X/PSD code. In order to make a meaningful analyse for the radiation shielding potentials of the obsidians, the calculated mass attenuation and linear attenuation coefficients were compared with ordinary concrete which can be widely used as shielding material in the nuclear application.

1. Introduction

The increase in radiation applications in our daily lives leads to the investigation of radiation protection and therefore alternative radiation protective materials. Many researches were carried out for determining radiation shielding properties of different materials before [1-8]. Obsidian is a natural glassy structure associated to volcanic rocks. Since the glassy volcanic rocks are formed as a result of volcanic activity and lava eruptions, regional differences add various features to the structures. Mexico, Ecuador, Japan, Turkey, Iran, Georgia and Armenia can be considered among the countries with high volcanic activity where the large obsidian deposits are formed. Obsidians can have different colours due to their compositions. Black to brown colours of obsidians are caused by iron and other transition elements of ingredients [9]. Due to the great interest in such structures, obsidians were studied widely before [7,10-13]. Aygun et al. reported the spectroscopic features and radiation shielding potentials of four obsidians from different regions in Turkey [7]. Aygun and Aygun studied radiation protection properties of Rize-İkizdere and Van-Erciş obsidians by Phy-X/PSD code [8]. Build up factors of natural black obsidian ores extracted from Artvin and Van regions [11]. Acıkgöz et al.

studied the physical, structural, and mechanical properties of natural volcanic obsidian glass doped with Er_2O_3 [12]. Radionuclide and absorption properties of 14 İkizdere obsidian samples were reported and it was concluded that obsidian is a potential material in radiation protection [13].

In this study, it is aimed to calculate radiation shielding parameters of the different coloured obsidians reported by Safaryan et al. [9]. For this purpose, we used a Phy-X/PSD code which can calculate quickly and accurately all specified shielding parameters such as mass attenuation coefficient (MAC), linear attenuation coefficient (LAC), effective atomic number (Z_{eff}), half-value layer (HVL), tenth-value layer (TVL), total electronic cross section (ECS), total atomic cross section (ACS), effective electron number (N_{eff}), effective conductivity (C_{eff}) and fast neutron removal cross section (FNRCS) in photon energies between 4keV and 100GeV [14].

2. Material and Methods

The MAC can be determined by the Beer–Lambert given as:

$$I = I_0 e^{-\mu t} \tag{1}$$

$$\mu_m = \frac{\mu}{\rho} = ln(I_0/I)/\rho t = ln(I_0/I)/t_m \qquad (2)$$

where I_0, I, ρ (g/cm^3), μ_m(cm^2/g), μ(cm^{-1}), t (cm) and t_m (g/cm^2) are incident and attenuated photon intensities, density of material, mass, linear attenuation coefficients, the thickness and sample mass thickness (the mass per unit area), respectively.

If the sample has various elements, the total MAC for any compound can be given by Eq. (3) [15];

$$\mu/\rho = \sum_i w_i(\mu/\rho)_i \qquad (3)$$

ACS (σ_a) for any sample can be obtained by the equation;

$$ACS = \sigma_a = \frac{N}{N_A}(\mu/\rho) \qquad (4)$$

ECS (σ_e) is given by the following equation [16]

$$ECS = \sigma_e = \frac{\sigma_a}{Z_{eff}} \qquad (5)$$

By using the Equations (4) and (5), we can find the Z_{eff} of the material as follows;

$$Z_{eff} = \frac{\sigma_a}{\sigma_e} \qquad (6)$$

We can calculate N_{eff} as follows [17],

$$N_{eff=\frac{\mu_m}{\sigma_e}} \qquad (7)$$

HVL and TVL are the thickness related parameters. MFP is the average distance at which a photon travels through the material between two interactions. The μ is used to calculate the parameters given by

$$HVL = \frac{In(2)}{\mu} \qquad (8)$$
$$MFP = \frac{1}{\mu} \qquad (9)$$
$$TVL = \frac{In10}{\mu} \qquad (10)$$

C_{eff} of the sample can be calculated by the equation [18]:

$$C_{eff} = (\frac{N_{eff}\rho e^2\tau}{m_e})10^3 \qquad (11)$$

FNRCS ($\sum R$) values of the sample can be obtained with the following equation [19,20]:

$$\sum R = \sum_i \rho_i(\sum R/\rho)_i \qquad (12)$$

where ρ_i is the partial density of the material and $(\sum R/\rho)_i$ is the mass removal cross-section of the i$_{th}$ constituent element.

3. Results and Discussions

The chemical compositions of different coloured obsidians are given in Table 1 [9]. Variations of the calculated MAC values of the obsidians versus photon energies (4keV-100GeV) are shown in Fig. 1(a). At low energies (1-100keV) where the photoelectric process (PE) is predominant, a decrease in MAC values with increasing energy is observed. In mid-energy region (100keV–5MeV) where the Compton scattering (CS) is dominant, MAC values slightly changed. Above 5 MeV, the Pair production (PP) process starts and an increase in MAC values is obtained with increasing energy [5,21].

Table 1. Chemical compositions of black, brown and gray obsidians.

Obsidian	SiO₂	Al₂O₃	Fe₂O₃	CaO	MgO	SO₃	NaO+K₂O
Gray	73.60	14.53	0.69	1.20	0.25	0.31	8.92
Black	74.46	14.20	1.12	1.25	0.28	0.14	8.23
Brown	76.96	13.33	0.96	1.19	0.22	0.16	6.97

LAC is an important parameter for defining the photon-matter interaction. The value of LAC depends on both MAC and density of sample. Variation of the calculated LAC values versus photon energies (4keV-100GeV) is shown in Fig. 1(b). Differences of LAC values are greater than those of MAC values depending on the density effect. It was obtained that the MAC values of the obsidians are very near to each other for the given energies. Obsidians are arranged according to their LAC values as brown>black >gray. Comparison of MAC and LAC values of obsidians with those of ordinary concrete (OC), reported by Bashter [22], to evaluate the shielding potential of the samples is given in Table 2. It can be observed that obsidians show higher protection features than OC.

The interaction possibility of per atom and per electron in a unit volume of any material is given by ACS and ECS, respectively. Dependence of ACS and ECS values on incident photon energies are given in Fig. 2(a-b). The obsidian with higher ACS and ECS values can be accepted as better shielding obsidian. According to the obtained results for ACS and ECS parameters of the samples, the shielding potential cannot be determined clearly. The HVL and TVL parameters give the information about the penetration ability of the radiations in materials.
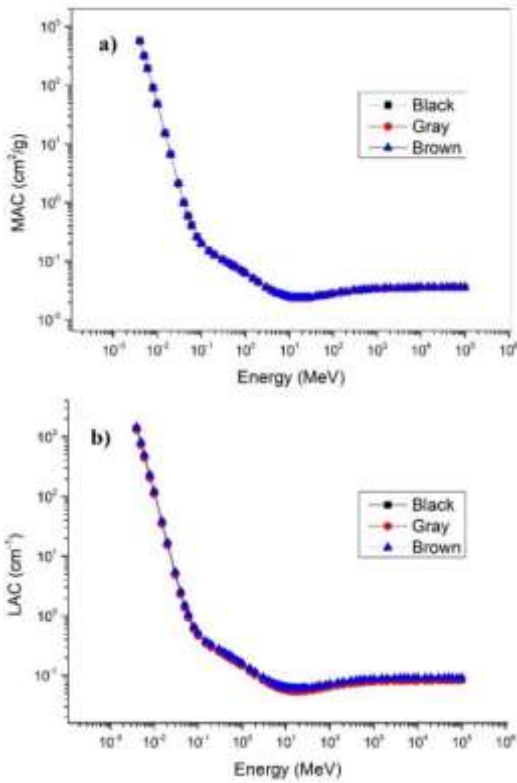
Figure 1. *The changes of MAC (a) and LAC (b) values as a function of incident photon energy.*
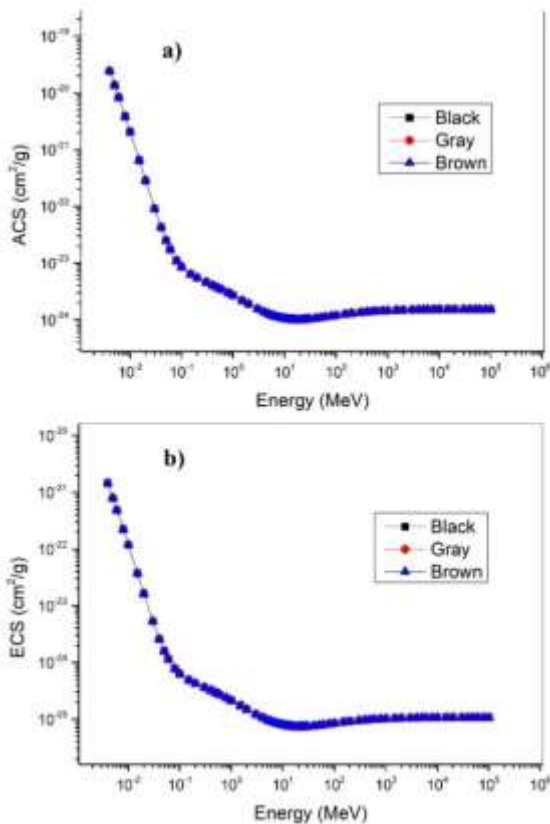

Figure 2. *The variations of ACS (a) and ECS (b) values as a function of incident photon energy.*

HVL, TVL and MFP parameters changing as a function of incident photon energies are given in Fig 3(a-c). In the mid-energy region with CS, most photons are more likely to be scattered. Therefore, their absorption probabilities are lower and hence thicker materials are required and longer MFP would be. As a result of this, an increase in HVL, MFP and TVL values can be observed in the mid-energy region. It is preferred to have low HVL, MFP and TVL values in the high energy regions for better shielding property.
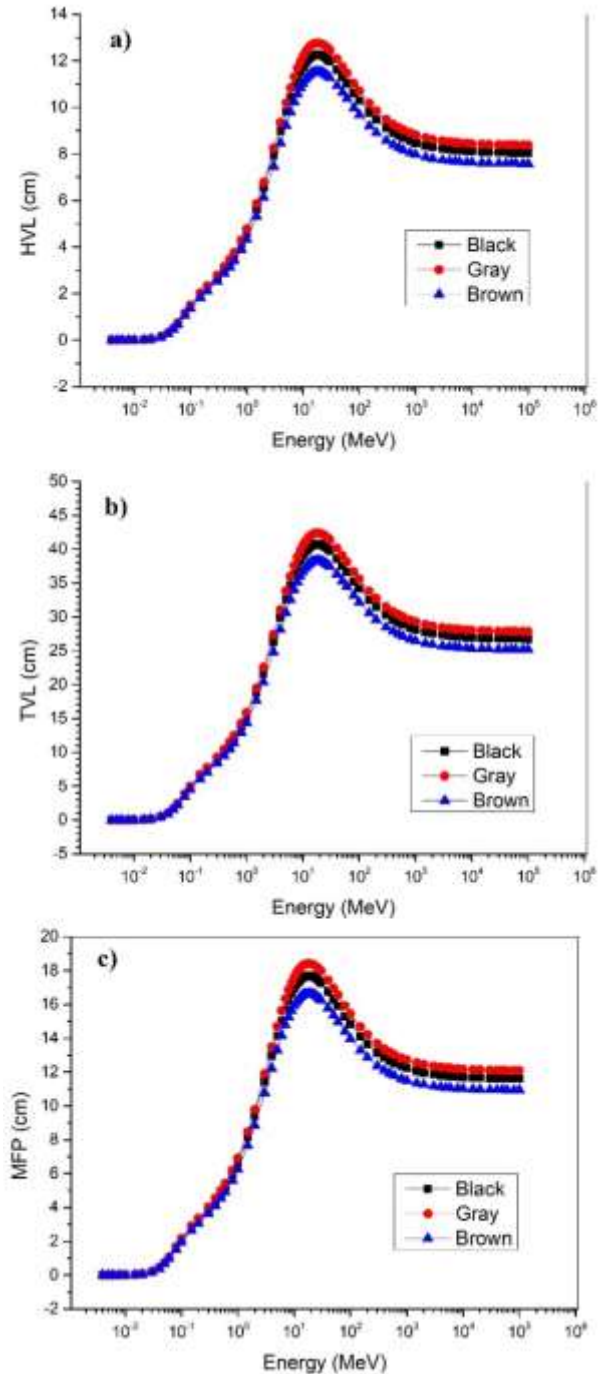
Figure 3. *Dependence of HVL (a) TVL (b) and MFP (c) values versus incident photon energy.*

Table 2. *MAC and LAC values of the obsidians and OC between the energies of 10keV and 1GeV.*

| Energy	Black MAC	Black LAC	Brown MAC	Brown LAC	Gray MAC	Gray LAC	OC MAC	OC LAC
MeV	cm²/g	1/cm	cm²/g	1/cm	cm²/g	1/cm	cm²/g	1/cm
1.00E-02	48.17	115.6	48.07	122.5	47.80	110.4	22.56	51.89
1.50E-02	15.18	36.44	15.14	38.63	15.05	34.78	7.079	16.28
2.00E-02	6.652	15.96	6.635	16.91	6.594	15.232	3.105	7.142
3.00E-02	2.119	5.087	2.114	5.391	2.101	4.854	1.048	2.410
4.00E-02	0.994	2.386	0.992	2.529	0.986	2.278	0.541	1.245
5.00E-02	0.589	1.413	0.587	1.498	0.584	1.350	0.358	0.824
6.00E-02	0.407	0.977	0.406	1.036	0.405	0.935	0.241	0.555
8.00E-02	0.258	0.619	0.258	0.657	0.257	0.594	0.204	0.469
1.00E-01	0.201	0.481	0.200	0.511	0.200	0.462	0.172	0.396
1.50E-01	0.149	0.357	0.149	0.379	0.149	0.343	0.142	0.328
2.00E-01	0.128	0.308	0.128	0.327	0.128	0.296	0.127	0.292
3.00E-01	0.107	0.258	0.107	0.274	0.107	0.248	0.108	0.249
4.00E-01	0.095	0.228	0.095	0.243	0.095	0.220	0.096	0.222
5.00E-01	0.086	0.208	0.087	0.221	0.086	0.200	0.088	0.202
6.00E-01	0.080	0.191	0.080	0.204	0.080	0.184	0.079	0.183
8.00E-01	0.070	0.168	0.070	0.178	0.070	0.161	0.071	0.164
1.00E+00	0.063	0.151	0.063	0.160	0.063	0.145	0.064	0.147
1.50E+00	0.051	0.123	0.051	0.130	0.051	0.118	0.052	0.120
2.00E+00	0.044	0.106	0.044	0.113	0.044	0.102	0.045	0.103
3.00E+00	0.036	0.087	0.036	0.093	0.036	0.084	0.036	0.084
4.00E+00	0.032	0.077	0.032	0.082	0.032	0.074	0.031	0.073
5.00E+00	0.029	0.071	0.029	0.075	0.029	0.068	0.028	0.066
6.00E+00	0.028	0.067	0.028	0.071	0.028	0.064	0.026	0.061
8.00E+00	0.026	0.062	0.026	0.065	0.026	0.059	0.024	0.056
1.00E+01	0.025	0.059	0.025	0.063	0.025	0.057	0.022	0.052
1.50E+01	0.024	0.057	0.024	0.060	0.024	0.055	0.021	0.048
2.00E+01	0.024	0.057	0.024	0.060	0.024	0.054	0.019	0.043
5.00E+01	0.026	0.061	0.026	0.065	0.026	0.059	0.021	0.048
1.00E+02	0.028	0.067	0.028	0.072	0.028	0.065	0.022	0.052
5.00E+02	0.033	0.079	0.033	0.084	0.033	0.076	0.026	0.061
1.00E+03	0.034	0.082	0.034	0.087	0.034	0.079	0.027	0.063
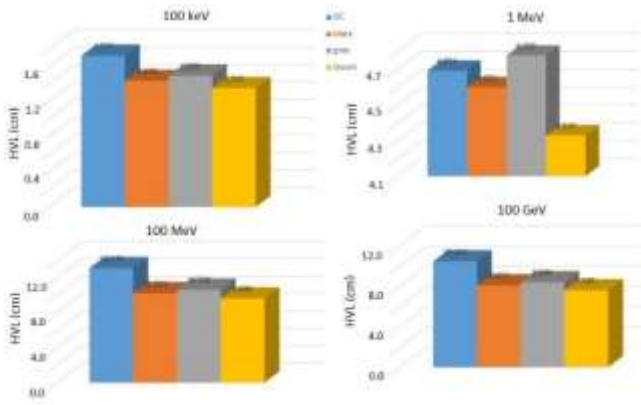
Figure 4. *HVL values of obsidians and OC for 100 keV,1 MeV, 100 MeV and 100 GeV.*

It was obtained that HVL, MFP and TVL values of the studied obsidians are brown<black<gray. Comparison of HVL values of obsidians and OC for 100 keV,1 MeV, 100 MeV and 100 GeV can be seen in Fig. 4. The energy dependence of Z_{eff}, N_{eff} and C_{eff} are given in Fig. 5(a-c). In the low energy region due to the photoelectric effect, maximum Z_{eff} values were obtained. By increasing energy, these values decreased sharply. The values gradually increased and be stable in high energies. It was seen that Z_{eff} values of the obsidians are very close. N_{eff} is one of the parameter that represents the effective conductivity of the compound depending on the excitatory photon energy [17]. As shown in Fig. 5, the change of the N_{eff} values on the incident photon energies is similar with the change of Z_{eff} values. The interactions between photons and material with PE, CS, and PP interaction processes can change the number of free electrons in the material. The order of C_{eff} values in the given energies is brown>black>gray.

Fast neutron attenuation ability of the samples is also determined by Phy-X/PSD. FNRCS values of black, gray and brown obsidians are obtained as 0.073, 0.070 and 0.078, respectively. It is obtained that brown obsidian has higher neutron attenuation among the obsidians. It can be seen that FNRCS values of the obsidians are higher than the other reported samples (Fig. 6).

4. Conclusions

In this study, radiation-matter interaction parameters of colored obsidians were obtained to determine the radiation shielding capabilities. For this purpose, the MAC, LAC, HVL, TVL, MFP, ACS, ECS, Z_{eff}, N_{eff}, C_{eff} and FNRCS parameters of the present samples were calculated by Phy-X / PSD code in the range of 4keV-100GeV. According to the obtained results,
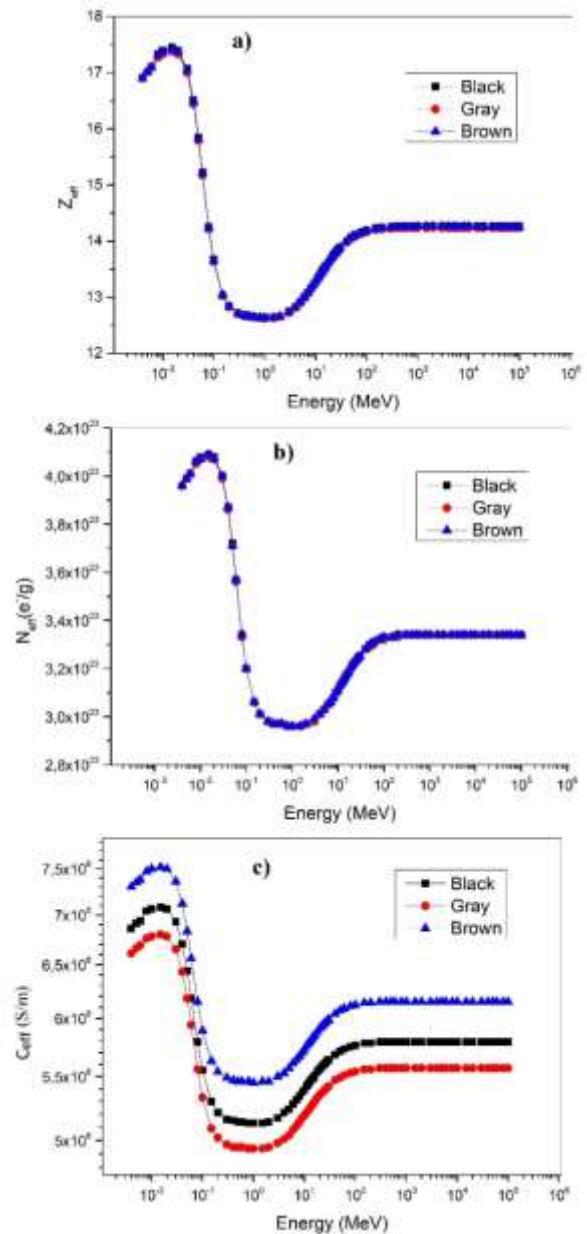
Figure 5. *The changes of Zeff (a) Neff (b) and Ceff (c) values as a function of incident photon energy.*
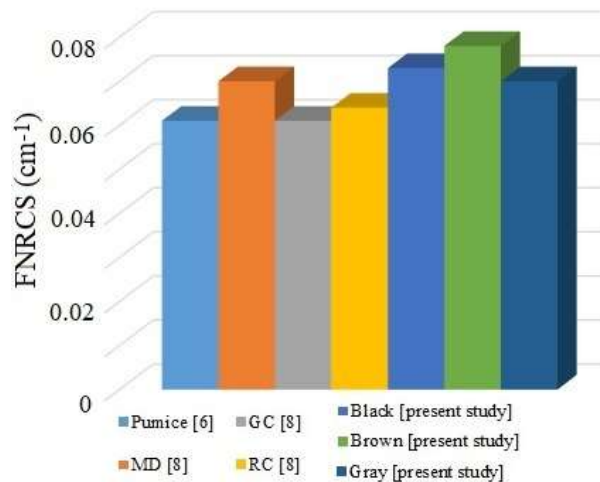
Figure 6. *FNRCS values of the obsidians and previously reported materials.*

although, some of the parameters of the studied obsidians have near values, it was concluded that brown obsidian has the highest shielding potential compared to others. FNRCS is also greater for brown obsidian than the others, therefore fast neutron attenuation potential is higher for brown sample.

Author Statements:

- **Ethical approval:** The conducted research is not related to either human or animal use.
- **Conflict of interest:** The authors declare that they have no known competing financial interests or personal relationships that could have appeared to influence the work reported in this paper
- **Acknowledgement:** The authors declare that they have nobody or no-company to acknowledge.
- **Author contributions:** The authors declare that they have equal right on this paper.
- **Funding information:** The authors declare that there is no funding to be acknowledged.
- **Data availability statement:** The data that support the findings of this study are available on request from the corresponding author. The data are not publicly available due to privacy or ethical restrictions.

References

[1] Akkurt, I., Akyıldırım, H., Mavi, B., Kılıncarslan, S., Basyigit, C., (2010). Radiation shielding of concrete containing zeolite. *Radiat Measur.* 45:827−830. DOI: 10.1016/j.radmeas.2010.04.012

[2] Akkurt, I., Tekin, H.O. (2020). Radiological parameters of bismuth oxide glasses using the Phy-X/PSD software. *Emerging Mater. Res.* 9:1020-1027. DOI: 10.1680/jemmr.20.00209

[3] Alım, B. (2020). A comprehensive study on radiation shielding characteristics of Tin Silver, Manganin R, Hastelloy B, Hastelloy X and Dilver P alloys. *Appl. Phys. A* 126:262. DOI:10.1007/s00339-020-3442-7

[4] Gur, A., Artıg, B., Çakır, T. (2017). Photon attenuation propertıes of concretes containing magnetite and lımonite ores. *Physicochem. Probl. Miner. Process.* 53(1):184−191. DOI: 10.5277/ppmp170115

[5] Kurudirek, M., Türkmen, I., Özdemir, Y. (2009). A study of photon interaction in some building materials: High-volume admixture of blast furnace slag into Portland cement. *Radiat. Phys. Chem.* 78:751–759. DOI: 10.1016/j.radphyschem.2009.03.070

[6] Aygun, Z., Aygun, M. (2022). A study on usability of Ahlat ignimbrites and pumice as radiation shielding materials, by using EpiXS code. *Inter. J. Environ. Sci. Tech.* 19: 5675–5688. DOI: 10.1007/s13762-021-03530-9

[7] Aygun, Z., Yarbasi, N., Aygun, M. (2021). Spectroscopic and radiation shielding features of Nemrut, Pasinler, Sarıkamıs and Ikizdere obsidians in Turkey: Experimental and theoretical study. *Ceramics Inter.* 47:34207−34217. DOI: 10.1016/j.ceramint.2021.08.330

[8] Aygun, Z., Aygun, M., Yarbasi, N. (2021). A study on radiation shielding potentials of green and red clayey soils in Turkey reinforced with marble dust and waste tire. *J. New Results Sci.* 10:46-59. DOI: 10.54187/jnrs.986038

[9] Safaryan, A., Sarkisyan, T., Paytyan, T., Baghdagyulyan, A. (2020). *The origin and bloating of the obsidian.* E3S Web of Conferences 175:12020. DOI: 10.1051/e3sconf/202017512020

[10] Aygun, Z., Aygun, M. (2022). Theoretical evaluation on radiation shielding features of Van-Ercis¸and Rize-˙lkizdere (Türkiye) obsidians by using Phy-X/PSD code. *Sigma J. Eng. Nat. Sci.* 40(4): 845–854. DOI: 10.14744/sigma.2022.00100

[11] Küçük, N., Gezer O. (20170). Doğal Siyah Obsidyen Cevherleri İçin Yığılma Faktörlerinin Belirlenmesi. *AKU J. Sci. Eng.* 17(3): 872–880. DOI: 10.5578/fmbd.66223

12] Acikgoz, A., Ceyhan, G.,Aktas, B., Yalcin, S., Demircan, G. (2021). Luminescent, structural and mechanical properties of erbium oxide doped natural obsidian glasses. *J. Non-Crystall. Solids* 572:121104. DOI:10.1016/j.jnoncrysol.2021.121104

[13] Duran, S.U., Küçükömeroğlu, B., Çiriş, A., Ersoy, H. (2022). Gamma-ray absorbing characteristic of obsidian rocks as a potential material for radiation protection. *Radiat. Phys. Chem.* 199:110309. DOI:10.1016/j.radphyschem.2022.110309

[14] Sakar, E., Özpolat, Ö.F., Alım, B., Sayyed, M.I., Kurudirek, M. (2020). Phy-X / PSD: Development of a user friendly online software for calculation of parameters relevant to radiation shielding and dosimetry. *Radiat Phys Chem*, 166:1-12. DOI: 10.1016/j.radphyschem.2019.108496

[15] Jackson, D.F., Hawkes, D.J. (1981). X-ray attenuation coefficients of elements and mixtures. *Phys. Reports* 70:169–233. DOI: 10.1016/0370-1573(81)90014-4

[16] Han, I., Demir, L. (2009). Determination of mass attenuation coefficients, effective atomic and electron numbers for Cr, Fe and Ni alloys at different energies. *Nucl Instr Methods Phys Res Sec B* 267:3–8. DOI: 10.1016/j.nimb.2008.10.004

[17] Han, I., Demir, L. (2009). Studies on effective atomic numbers, electron densities from mass attenuation coefficients in TixCo1-x and CoxCu1-x alloys. *Nucl Instr Methods B* 267:3505–3510. DOI: 10.1016/j.nimb.2009.08.022

[18] Manjunatha, H.C. (2017). A study of gamma attenuation parameters in poly methyl methacrylate and Kapton. *Radiat Phys Chem*, 137:254–259. DOI: 10.1016/j.radphyschem.2016.01.024

[19] Şakar, E. (2020). *Radiat. Phys. Chem.* 172:1-13. DOI: 10.1016/j.radphyschem.2020.108778

[20] Wood, J. (2013). *Computational methods in reactor shielding*, Elsevier.

[21] Alım, B. (2020). Determination of Radiation Protection Features of the Ag2O Doped Boro-Tellurite Glasses Using Phy-X / PSD Software. *J. Ins. Sci. Tech.* 10(1):202-213. DOI: 10.21597/jist.640027

[22] Bashter, I.I. (1997). Calculation of radiation attenuation coefficients for shielding concretes. *Annl. Nucl. Energy* 24(17):1389-1401. DOI: 10.1016/S0306-4549(97)00003-0

Research Article

EPR Analysis of Dinitrobenzoic Acid Anion Radicals

Hüsnü YOLBURUN[1], Fatih UCUN[2]*

[1]Suleyman Demirel University, Science and Arts Faculty, Physics Department, 32200, Isparta-Turkey
Email: husnuyolburun1@gmail.com **ORCID:** 0000-0001-7377-7468

[2]Suleyman Demirel University, Science and Arts Faculty, Physics Department, 32200, Isparta-Turkey
* **Corresponding Author Email:** fatihucun@sdu.edu.tr **ORCID:** 0000-0001-7464-7788

Abstract:

EPR hyperfine coupling constants of dinitrobenzoic acid anion radicals were calculated by using (DFT) with the use of B3LYP functional at LanL2DZ, LanL2MB, EPR-II, EPR-III, 6-31+G(d) and 6-31++ G(d,p) basis sets. It was found that LanL2DZ is the best basis set from the correlation graphs between the theoretical and experimental results. Thus, in this set, the hyperfine structures formed EPR spectra and the distributions of the spin density of all the anion radicals were determined. From the optimized structures of all the radicals it was decided whether the nitro groups are out of plane or not. The reason of the different distributions of the spin density on the nitro groups were also investigated by Natural Bond Orbital (NBO) and Mulliken charge analyses. In these analyses, the interactions of the nitro groups with the ring were examined. The NBO analysis the anion radical of 2,4-dinitrobenzoic acid showed that there is a strong O-H…O hydrogen bond interaction (182.8 kcal/mol) between the carboxyl and nitro groups. The simulated EPR spectra of some radicals obtained by EPR Simulator software program were harmoniously given with together their experimental spectra.

1. Introduction

Dinitrobenzoic acid is one of the most important organic synthesis intermediates and, is widely used in the preservative and chemical industry. Dinitrobenzoic acid has four different isomers according to the different placement of the carboxyl and nitro groups in the benzene ring. These are 2,4-, 2,5-, 3,4- and 3,5-dinitrobenzoic acid. All of them are used in different fields. For example, 2,4-dinitrobenzoic acid is an important pharmaceutical intermediate, often used in the synthesis of antibacterial. It is also used in clinical and medical research. Similarly, 3,5-dinitrobenzoic acid is used to synthesize intermediates for dyes and liquid crystals. The optical properties of dinitrobenzoic acid isomers, both experimentally and theoretically, have been studied by Zhang and et al. [1]. The investigation of the electronic structures of the radical anions of aromatic nitro derivatives has attracted attention [2, 3]. EPR spectra of dinitro-derivatives of benzoic acid reduced by electrolysis in dimethyl formamide solution were obtained [4].

They suggested that one of the two nitro groups in some dinitro-derivatives must be out of plane. They have attributed the out-of-plane nature of one of the nitro groups to the bigger coupling constant belonging to the nitrogen in that nitro group. In addition, the hyperfine splitting belonging to the proton in the carboxyl group attached to the benzene ring was not observed in the studies [5, 6]. In this study, Electron Paramagnetic Resonance (EPR) hyperfine coupling constants and spin density distributions of dinitrobenzoic acid anion radicals were theoretically calculated in different sets by Density Functional Theory (DFT) with the use of B3LYP functional. Since the optimized structures of the radicals were determined by this study, it was easily decided, theoretically, whether the nitro groups in the radicals are out of plane or not. Consistent with the literature, it was observed that the hyperfine coupling constant belonging to the nitrogen in the out-of-plane nitro group is also bigger than the other nitro group. In addition, the hyperfine coupling constant belonging to the hydrogen in the carboxyl group of all the radicals, which could not

be determined in the literature, is determined theoretically by this study, even though it is small.

2. Computational Methods

The calculations of the optimized structures and hyperfine coupling constants of the radicals were done by the Gaussian 09 software package [7], and the results were displayed with the GaussView 5.0 program [8]. Density Functional Theory (DFT) has been widely used both in the gas phase [9] and on catalytic surfaces [10] in modeling the chemical interactions of atoms and molecules by considering their internal structures. Therefore, in our calculations, we have also used DFT [11, 12] with the use of Becke hybrid three-parameter variable functionality [13], and electronic correlation of Lee, Yang, and Par (B3LYP) [14]. Our previous studies have showed that DFT(B3LYP)/ LanL2DZ basis set gives very good values in hyperfine coupling constant calculations in terms of agreement with experimental results [15, 16]. Therefore, we have used LanL2DZ as well as LanL2MB, EPR-II, EPR-III, 6-31+G(d) and 6-31++ G(d,p) basis sets to determine the reality of this. Simulated EPR spectra were obtained using the EPR Simulator software program [17].

3. Results and Discussion

The hyperfine coupling constants (hfccs) calculated at different basis sets by DFT(B3LYP) for all the radicals are given in Table 1. The table also includes experimental values for comparison [4]. Considering that the calculated values are obtained for a single gas molecule, a full agreement cannot be expected with the experimental results having multiple interactions, we can say that the experimental and theoretical values are in good agreement. For all the anion radicals the correlation values between the theoretical and experimental hffcs are given in the bottom line of the table. From these correlation values, we can say that the best basis set is LanL2DZ, which is in agreement with our previous studies [15, 16]. Figure 1 shows its correlation graph as an example. The optimized structures and unpaired electron spin density distributions of all the anion radicals calculated at DFT(B3LYP)/LanL2DZ basis set are given in Fig.2. As can be seen, the spin density distributions of 2,4- and 2,5-dinitrobenzoic acid anion radicals are concentrated on only one nitro group. It can be seen from table 1that the nitrogen hfcc value of this nitro group is bigger than that of the other nitro group. For an example, from Table 1, for 2,4-dinitrobenzoic acid, the nitrogen hfcc value of one nitro group is calculated as
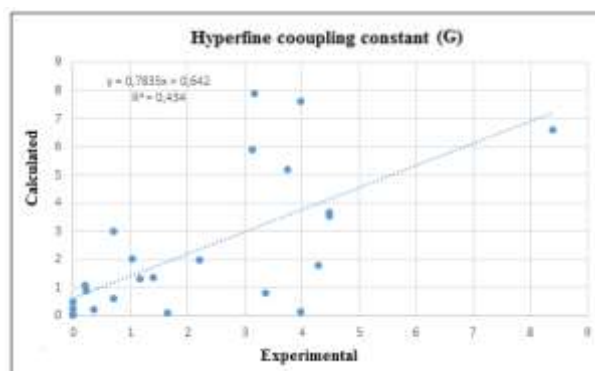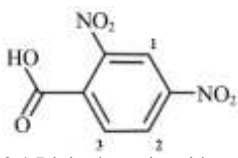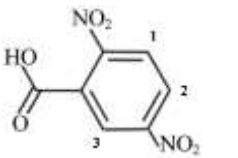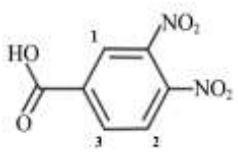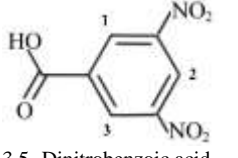

Figure 1. *Correlation graph between the calculated and experimental nitrogen hffcs of all the anion radicals.*
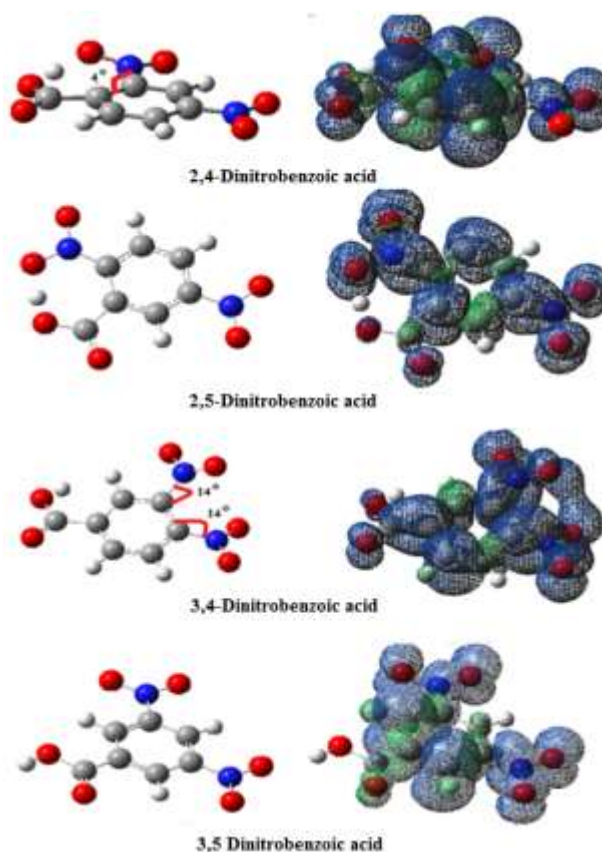
**Figure 2.** *The optimized structures and spin densities of all the anion radicals.*

6.68 G, while the other is calculated as 1.07 G. These values are experimentally found to be 8.38 and 0.20 G, respectively. However, the spin densities for 3,4- and 3,5-dinitrobenzoic acid anion radicals are almost equally distributed in the both nitro groups. Thus, the nitrogen hfcc values of the nitro groups of these radicals should be quite close to each other. For an example, for 3,5-dinitrobenzoic acid, these values are calculated as 3.66 and 3.54 G, respectively, and they are experimentally found to be equal and 4.47 G (see Table 1). As seen from the optimized structures of the anion radicals in Fig.2, one nitro group of 2,4-dinitrobenzoic acid is out of the ring plane with a dihedral angle of 4°.

Table 1. *Experimental [4] and calculated hyperfine coupling constants for all the anion radicals.*

| Anion Radical	Hfcc (G)	Exp.	DFT(B3LYP)					
			LanL2DZ	LanL2MB	EPR-II	EPR-III	6-31+G(d)	6-31 ++G(d,p)
2,4-Dinitrobenzoic acid	a_{N1}	8.38	6.62	1.73	2.95	3.17	3.83	4.12
	a_{N2}	0.20	1.07	0.22	0.48	0.51	0.78	0.71
	a_{H1}	3.36	-0.79	-2.03	-0.44	-0.41	-0.23	-0.45
	a_{H2}	3.13	-5.92	-5.31	-0.86	-5.72	-5.99	-5.96
	a_{H3}	1.04	2.04	1.75	1.86	1.81	1.88	1.88
	a_{H4}	0.00	-0.06	-0.68	0.23	0.07	0.15	0.05
2,5- Dinitrobenzoic acid	a_{N1}	3.74	5.21	2.09	2.17	2.42	3.20	3.36
	a_{N2}	0.36	0.22	1.65	-0.40	-0.25	0.15	0.11
	a_{H1}	2.20	-1.97	-0.95	-1.75	-1.74	-1.82	-1.88
	a_{H2}	1.65	-0.11	-1.31	-0.37	-0.38	-0.51	-0.39
	a_{H3}	0.22	0.88	0.30	0.82	0.74	0.78	0.77
	a_{H4}	0.00	-0.51	0.26	-0.02	-0.30	-0.30	-0.33
3,4-Dinitrobezoic acid	a_{N1}	4.28	1.78	0.06	0.52	0.59	1.04	1.04
	a_{N2}	1.40	1.37	-0.41	0.09	0.35	0.93	0.92
	a_{H1}	1.16	1.30	1.20	1.45	1.58	1.54	1.53
	a_{H2}	0.70	0.60	0.84	0.63	0.63	0.54	0.56
	a_{H3}	0.70	-3.00	-3.60	-2.61	-2.77	-2.97	-2.93
	a_{H4}	0.00	-0.27	-0.16	-0.30	-0.31	-0.30	-2.29
3,5- Dinitrobenzoic acid	a_{N1}	4.47	3.66	0.70	1.55	1.81	2.44	2.42
	a_{N2}	4.47	3.54	0.68	1.45	1.66	2.25	2.24
	a_{H1}	3.98	-7.63	-2.18	-7.60	-7.25	-7.76	-7.65
	a_{H2}	3.98	- 0.13	-11.95	0.00	-0.03	-0.02	-0.01
	a_{H3}	3.17	-7.89	-2.04	-7.94	-7.72	-8.04	-7.95
	a_{H4}	0.00	0.04	-0.30	0.03	0.01	0.03	0.02
R^2(all)			0.43	0.08	0.14	0.18	0.23	0.22
R^2(for only a_N's)			0.77	0.08	0.71	0.73	0.73	0.74

This result is also consistent with the literature [4]. Thus, since this nitro group will interact more effectively with the π system of the ring, it is expected that the hfcc value of its nitrogen will be bigger. Again from the optimized structures in Fig. 2, it can be seen that the nitro groups in 3,4-dinitrobenzoic acid anion radical are out of the ring plane with a dihedral angle of about 14º up and down, respectively. This is suitable for their nitrogen hfcc values o be quite close to each other. These values are calculated as 1.78 and 1.37 G, respectively (see Table 1). In Table 1, the hfcc value of the proton in the carboxyl group of all the anion radicals, which cannot be observed according to the literature, is calculated and given, albeit small. In Figs. 3 and 4, the experimental and simulation EPR spectra of 2,4- and 3,5-dinitrobenzoic acid anion radicals of which the experimental spectra were obtained from the literature [4], are given. The simulation spectra were found by using the theoretical hfcc values of the radicals in the EPR Simulator program [17]. The optimal linewidth values are given in the figures. As can be seen, the simulation spectra are compatible with the experimental spectra. The highest occupied molecular orbital HOMO (or SOMO for half-filled molecular orbitals, i.e. radicals) energy indicates electron donating ability, while the lowest unoccupied molecular orbital LUMO energy indicates electron accepting ability. The LUMO-HOMO energy gap ($\Delta E = E_{LUMO} - E_{HOMO}$)
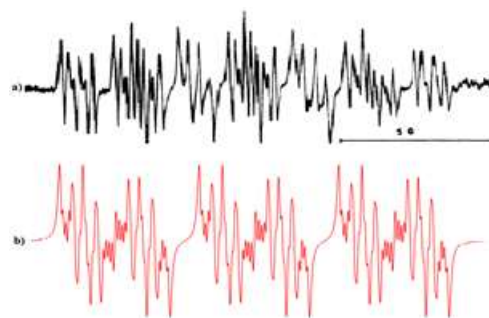
Figure 3. *a) Experimental [4] and b) simulation spectra of 2,5-dinitrobenzoic acid anion radical. The linewidth for the simulation spectrum is 0.11 G.*
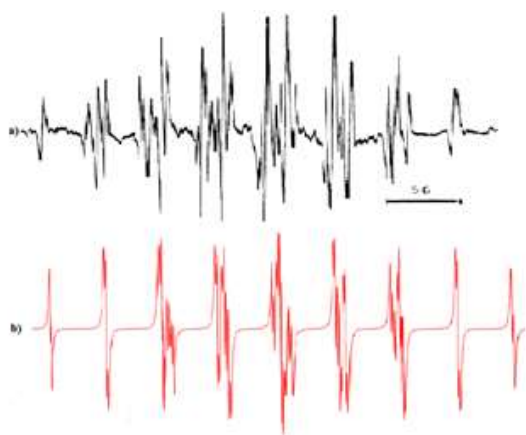
Figure 4. *a) Experimental [4] and b) simulation spectra of 3,5-dinitrobenzoic acid anion radical. The linewidth for the simulation spectrum is 0.10 G.*
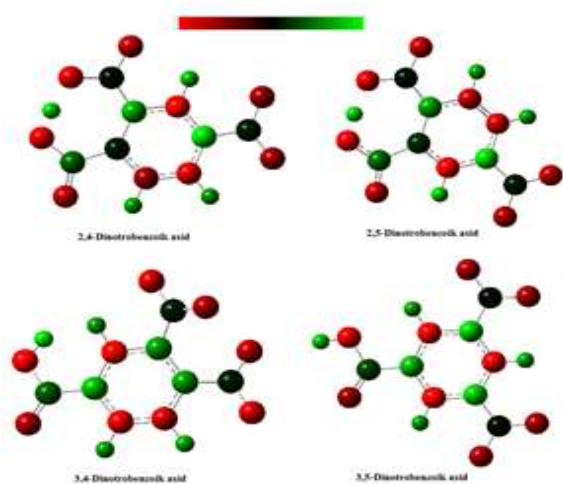
Figure 5. *The Mulliken atomic charges for all the anion radicals.*

Table 2. *Electronic, relative and LUMO-HOMO energy difference values of all the radicals calculated at the B3LYP/LanL2DZ basis set.*

Anion Radical	Electronic (Hartree/par.)	Relative (kkal/mol)	ΔE=E_{LUMO}- E_{HOMO} (Hartree/par.)
2,4- Dinitrobenzoic acid	-829.793137	5.17	0.04268
2,5- Dinitrobenzoic acid	-829.801385	0.0	0.07477
3,4- Dinitrobenzoic acid	-829.768096	20.89	0.07006
3,5- Dinitrobenzoic acid	-829.786248	9.50	0.03672

value is an important parameter as a function of a molecule's reactivity. A molecule with the low energy gap (also called soft molecule) has high chemical reactivity, while the one with the high energy gap (also called hard molecule) has low chemical reactivity [18]. The electronic, relative and E_{LUMO}-E_{HOMO} energy gap values calculated at the DFT(B3LYP)/ LanL2DZ basis set for all the anion radicals are given in Table 2. From the table, we can

say that 2,5-dinitrobenzoic acid anion radical has the most stable structure while 3,5-dinitrobenzoic acid anion radical has the highest chemical reactivity. The stabilization energy values E(2) between the atom and bond orbitals at DFT(B3LYP)/ LanL2DZ basis set were calculated using the second order perturbation theory of Fock Matrix on the basis of natural bond orbital (NBO) of all the anion radicals. A large E(2) value means that the interactions between electron donors and electron acceptors are stronger. NBO analysis of 2,4-dinitrobenzoic acid shows that there is a strong hydrogen bonding interaction between the carboxyl and the near-nitro group, namely the O-H…O interaction, between the LP(O) (donor) atom orbital and the O…H (acceptor) unbounded orbital. This interaction energy is found to be 182.8 kcal/mol. The optimized structure was also checked for an imaginary frequency on suspicion of a trans structure. The O··H distance is 1.40 Aº, and the hydrogen atom is very close to the nitro group oxygen. It is also seen from the optimized structure in Fig. 2 that this nitro group is out of plane as we said before. Thus, it can be understood that the nitrogen of this nitro group will have a bigger hfcc value since it can interact more easily with the π system of the ring. In NBO analysis of 2,5-dinitrobenzoic acid, the charge transfer occurs (133.2 kcal/mol) from the ring carbon atom to which the first nitro group is attached, to the N-O bonds while the charge transfer (319.6 kcal/mol) to the ring carbon atom to which the second nitro group is attached, from the N-O bonds, on the contrary. This is resulted in a bigger nitrogen hfcc value of the former group and the smaller one of the latter group. From Table 1 these values are calculated as 5.22 G versus 0.21 G for this radical. We can say that in 3,4-dinitrobenzoic acid anion radical, the repulsion between the oxygens in the closely related carboxyl and nitro groups causes the nitro groups to be out of the ring plane with an almost equal dihedral angle in opposite directions in the optimized structure (see Figure 2). Its NBO analysis shows that there is a very high interaction (798.01 kcal/mol) between the ring carbon atoms to which the nitroxy groups are attached, and the high charge transfer (330.0 kcal/mol) from the ring carbon atom to which the second nitro group is attached, to the N-O bonds of the same group. This explains the close nitrogen hfcc values for the both groups (see Table 1). Finally, the optimized structure of 3,5 dinitrobenzoic acid anion radical is planar as seen in Fig. 2, and its NBO analysis is based on the LP(N) (donor) atom orbital in the both nitro groups and the BD(O…O) (acceptor) orbitals in the same groups. It shows that there is a high and almost equal energy interaction of E(2)= 320.0 kcal/mol between those orbitals. This result explains their close nitrogen hfcc values in

Table 1. The above comments can also be supported by the Mulliken charges given in Fig. 5. As can be seen in the figure, for 2,4- and 2,5-dinitrobenzoic acid anion radicals the charges on the ring carbon atoms which enable the interaction of the nitro groups with the ring are different (different colors) and so, their nitrogen hfcc values are far from each other. But for 3,4- and 3,5- dinitrobenzoic acid anion radicals these charges are approximately same (similar colors) and so their nitrogen hfcc values are close to each other (see Table 1).

4. Conclusions

In this study, EPR hyperfine coupling constants and spin density distributions of dinitrobenzoic acid anion radicals were calculated at different basis sets with DFT(B3LYP). The LanL2DZ basis set was found to be the best basis set in hfcc calculations in terms of agreement with experimental results. For 2,4- and 2,5-dinitrobenzoic acid anion radicals, the spin density distribution is concentrated on a single nitro group, while for 3,4- and 3,5-dinitrobenzoic acid, it is observed that it concentrates almost equally on the both nitro groups. In 2,4-dinitrobenzoic acid anion radical, the nitro group with high spin density is observed to be out of plane in accordance with the literature. The distribution differences of the spin density on the nitro groups were investigated by NBO and Mulliken charge analyzes of the anion radicals. NBO analyzes showed that there is a strong hydrogen bonding interaction between the carboxyl and nitro groups in 2,4-dinitrobenzoic acid, and in 2,5-dinitrobenzoic acid the charge is transferred from the ring carbon atom to the first nitro group while the opposite is calculated for the second nitro group. Again, the NBO analysis of 3,4-dinitrobenzoic acid showed that there is a high charge transfer from the ring carbon atom to the N-O bonds of the second nitro group. Finally, in 3,5 dinitrobenzoic acid it showed a high and almost equal charge transfer from the nitrogen atom in the both nitro groups to the BD(O…O) orbitals in the same groups. In summary, NBO analyzes explain the nitrogen hfcc values of the nitro groups which are far or close to each other for all the anion radicals. In addition, the EPR simulation spectra obtained by using the theoretical hfcc values in the EPR Simulator software program for some radicals were harmonically given with their experimental spectra.

Author Statements:

- **Ethical approval:** The conducted research is not related to either human or animal use.

- **Conflict of interest:** The authors declare that they have no known competing financial interests or personal relationships that could have appeared to influence the work reported in this paper

- **Acknowledgement:** The authors declare that they have nobody or no-company to acknowledge.

- **Author contributions:** The authors declare that they have equal right on this paper.

- **Funding information:** The authors declare that there is no funding to be acknowledged.

- **Data availability statement:** The data that support the findings of this study are available on request from the corresponding author. The data are not publicly available due to privacy or ethical restrictions.

References

[l] J-Na Zhang, B. Zhang and J-J. Shen, (2017). The optical properties of dinitrobenzoic acid isomers in the tarahertz and infrared regions. *J. Infrared Milim. Waves* 36(5);536-542. DOI: 10.11972/j.issn.1001-9014.2017.05.005

[2] S. E. Barrows, C. J.Cramer, D. G.Truhlar, M. S. Elovitz and E. J. Weber. (1996) Factors controlling regioselectivity in the reduction of polynitroaromatics in aqueous solution. *Environ. Sci. Technol.* 30(10);3028–3038. DOI: 10.1021/es960004x

[3] M. N. Mikhailov, A. S. Mendkoich, M. B. Kuzminski, A. Kapranov and A. I. Rusakov. (2005) Electronic structure of 1.3-dinitrobenzene radical anion; a multi-configurational quantum chemical study. *Russian Chem. Bulletin, Internat. Ed.* 54;2735-2737. DOI:10.1007/s11172-006-0185-3

[4] P. L. Nordio, M. V. Pavan and C.Corvaja. (1964) E.s.r. Spectra of Reduced Mono- and Dinitro-Derivatives of Phenol and Benzoic Acid. *Trans. Faraday Soc.*, 60;1985-1990. DOI: 10.1039/TF9646001985

[5] L. H. Piette, P. Ludwig and R. N. Adams. (1962) Electron Paramagnetic Resonance of Aromatic and Aliphatic Nitro Anions in Aqueous Solution" *J. Chem. Soc.* 84;4212-4215. DOI: 10.1021/ja00881a005

[6] P. H. Reiger and G. K. Fraenkel. (1963). Analysis of the Electron Spin Resonance Spectra of Aromatic Nitrosubstituted Anion Radicals *J. Chem. Phys.*, 39; 609-629. DOI:10.1063/1.1734301

[7] M. J. Frisch, G. W. Trucks, H. B. Schlegel, et al., Gaussian 09, Revision D.01 (Gaussian, Inc., Wallingford, CT, 2009). https://gaussian.com/g09citation/

[8] R Dennington. T. Keith and J. Milliam, Gaussview Version 5 (Semichem Inc, Shawnee Mission, KS, 2009). https://gaussian.com/g09citation/

[9] Y. Wang, G. Fu, Y. Zhang, X. Xu and H. Wan. (2009) O-atom transfer reaction from N_2O to CO: A

theoretical investigation" *Chem. Phys. Lett.*, 475;202-207. DOI: 10.1016/j.cplett.2009.05.044.

[10] D. Tiana, C. Zenga, H. Wanga, Xianming Chenga, Y. Zhenga, C. Xiangd, K. Lia and X. Zhu. (2017). Effect of transition metal Fe adsorption on $CeO_2(110)$ surface in themethane activation and oxygen vacancy formation: a density functional theory study" *Appl. Surf. Sci.*, 416;547-564.
DOI: 10.1016/j.apsusc.2017.04.028

[11] P. Hohenberg and W. Kohn, (1964). Inhomogeneous electron gas *Phys. Rev.* 136;b864-b871.
 DOI: 10.1103/PhysRev.136.B864

[12] W. Kohn and L.J. Sham, (1965). Self-consistent equations including exchange and correlation effects *Phys. Rev.,* 140;a1133–a1138.
https://doi.org/10.1103/PhysRev.140.A1133

[13] A. D. Becke, (1988). Density-functional exchange-energy approximation with correct asymptotic behavior. *Phys. Rev. A.*, 38(6);3098-3100.
DOI: 10.1103/PhysRevA.38.3098

[14] C. Lee, W. Yang and R.G. Parr, (1988). Development of the Colle-Salvetti correlation-energy formula into a functional of the electron density. *Phys. Rev. B* 37;785-789.
DOI: 10.1103/PhysRevB.37.785

[15] Ş. Nardali, F. Ucun and M. Karakaya, (2017). Calculated hyperfine coupling constants for 5,5-dimethyl-1-pyrroline N-oxide radical products in water and benzene" *Russian J. Phys. Chem. A* 91;2137-2148. DOI:10.1134/S0036024417110164

[16] F. Ucun and S.G. Aydın, (2014). Calculated optimized structures and hyperfine coupling constants of some radical adducts of α-phenyl-N-tert-buthyl nitrone in water and benzene solutions *J. Organomet. Chem.* 759;27-32.
DOI:10.1016/j.jorganchem.2014.02.011.

[17] https://www.eprsimulator.org/isotropic.html

[18] W. Yang, R. G. Parr, (1985). Hardness, softness and the Fukui function in the electronic theory of metals and catalysis *Proc. Natl. Acad. Sci.* 82;6723–6726.
https://www.jstor.org/stable/26691

Copyright © IJCESEN

The Impact of Dynamic Shocks and Special Days on Time Series Data

Zehra Hafızoğlu GÖKDAĞ[1*], Ayşe Hümeyra BİLGE [2]

[1]Kadir Has University, Faculty of Eng. and Natural Sciences, Depart. of Industrial Engineering, 34083, İstanbul-Turkey.
* **Corresponding Author** : **Email:** zehrahafizoglu.gokdag@stu.khas.edu.tr - **ORCID:** 0000-0002-5804-31057

[2] Kadir Has University, Faculty of Eng. and Natural Sciences, Depart. of Industrial Engineering, 34083, İstanbul-Turkey.
Email: ayse.bilge@khas.edu.tr - **ORCID:** 0000-0002-6043-0833

Abstract:

This paper includes an examination of a 4-year time series data on retail delivery demand generated by a logistics company based on the dates of creation. The periodic fluctuations observed in the data's normal structure are caused by the accumulation of demands over the weekend and their fulfillment at the beginning of the week. The aim of the study is modeling the response to unexpected changes in demand, which we refer to as "shocks," similar to the weekend effect. Special days, including single-day public holidays, religious holidays, and campaign periods in November, which represent specific periods, were also analyzed to interpret the patterns during these periods. The patterns created by single-day public holidays and religious holidays are significantly influenced by whether these days fall on a weekend or a weekday. By excluding weeks with special days from the overall data, the presence of shock effects in the remaining ordinary weeks was examined. During this period, the shock caused by the Covid-19 pandemic and adverse weather conditions was observed. The impact of the Covid-19 shock lasted longer compared to other shocks. When the increase in demand due to shocks exceeds the capacity of existing vehicles, the problem can be resolved by arranging daily rental vehicles from companies that provide vehicle allocations. Extracting the demand model for special days and unexpected shocks will ensure operational preparedness and prevent process delays. When ordinary weeks were examined, a monotonically decreasing trend from Monday to Sunday was observed based on the weekly average demand. The maximum demand was 58.3% on Monday, 17.2% on Tuesday, 15.9% on Wednesday, 7.3% on Thursday, and 1.3% on Friday. The provided graphs also demonstrate a significant increase in demands in early 2020 due to the widespread adoption of e-commerce as a result of the Covid-19 pandemic.

1. Introduction

In this study, a 4-year time series data on retail delivery demand based on the creation dates were analyzed in a logistics company, covering the years 2019-2022. The data was normalized and analyzed. It covers a 207-week time range starting from the first Monday of 2019 and ending on the last Sunday of 2022. The study examines the patterns created by special days and discount campaigns, as well as the dynamic shocks resulting from unexpected events.

The daily demand counts in the data were analyzed on a weekly basis, and the averages and standard deviations were calculated for each day of the week. The results are shown in Figure 1. Figure 1 illustrates that the daily averages decrease monotonically from Monday to Sunday (Monday:

56910, Tuesday: 52790, Wednesday: 50977, Thursday: 48835, Friday: 47318, Saturday: 39445, Sunday: 27456). In the literature, some studies investigate the impact of shocks on time series data. For instance, in the article [1], the effect of oil price shock on time series data was examined. The study focused on analyzing the influence of oil price shocks on the observed time series data. Furthermore, [2] conducted a study to measure the dynamic shock effects in time series data using a non-parametric approach. Leduc and Liu (2016) examined the shock that affects aggregate demand through the labor market, where increased uncertainty leads to higher unemployment and lower inflation, [3]. In the article [4], the impact of demand shocks in the automotive sector was investigated using data from the San Diego region
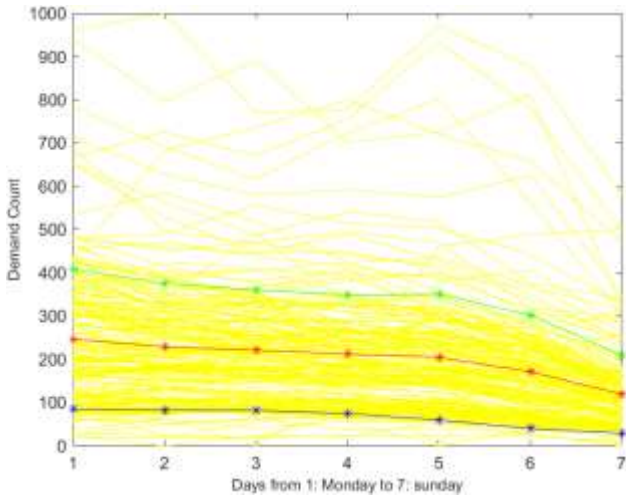
Figure 1. *Yellow: Daily demand counts for 207 weeks. Red: Daily average. Green: Average + standard deviation. Blue: Average - standard deviation.*

and it was found that the 2008-2009 economic crisis led to a decrease in demand.

2. Special Days

Official holidays and campaign days, weekends, or exceptional circumstances, can disrupt the general demand pattern. Official holidays and November discounts are special days that occur on specific dates each year. New Year's Day, April 23rd National Sovereignty and Children's Day, May 1st Labor and Solidarity Day, May 19th Commemoration of Atatürk, Youth and Sports Day, July 15th Democracy and National Unity Day, August 30th Victory Day, October 29th Republic Day, Eid al-Fitr, and Eid al-Adha are official holidays.

2.1 Single-Day Official Holidays

The weeks in which single-day special occasions fall for each year are provided in Table 1. The changes in the daily demand counts for a total of 6 days, including the single-day special occasions given in Table 1, along with 2 days before and 3 days after, were plotted to examine the pattern of these special days. In Figure 2, the impact of New Year's Day on a yearly basis is presented. Here, unlike the others, there is an increase at $x = 2$ for the year 2022. The reason for this is that the day coincides with Monday. Apart from that, patterns can be observed for $x = -1, 0,$ and 1 values. In Figure 3, the impact of April 23rd National Sovereignty and Children's Day on a yearly basis is presented. Here, unlike the others, there is an increase at $x = 2$ for the year 2022. The reason for this is that the day coincides with Monday. Apart from that, patterns can be observed for $x = -1, 0,$

and 1 values. In Figure 4, the impact of May 1st Labor and Solidarity Day on a yearly basis is presented. Compared to the year 2021, the pattern is shifted by one day in the year 2022, and reason for this is that the value $x = 1$ in 2022 corresponds to the start of Eid al-Fitr (Ramadan Bayram). In the year 2020, the declines continue after May 1st, and this is because these two days coincide with the weekend. In Figure 5, the impact of the May 19th Commemoration of Atatürk, Youth and Sports Day on a yearly basis is presented. In 2019, 2020, and 2021, there are patterns observed for $x = -1, 0,$ and 1 values. However, unlike the others, in the year

Table 1. *Table of weeks and days in which one-day special days are included. (Mon: Monday; Tues: Tuesday,; Wed: Wednesday; Thurs: Thursday; Fri:Friday; Sat: Saturday; Sun:Sunday)*
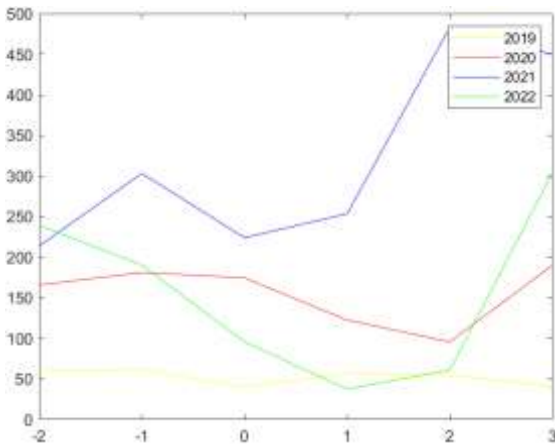
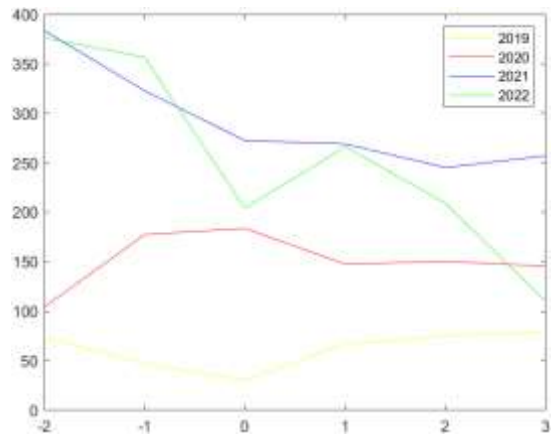| Single-day special days	2019	2020	2021	2022
New Year's Day	0. week Tues	52. week Wed	104. week Fri	156. week Sat
April 23rd National Sovereignty and Children's Day	16. week Tues	68. week Thurs	120. week Fri	172. week Sat
May 1st Labor and Solidarity Day	17. week Wed	69. week Fri	121. week Sat	173. week Sun
May 19th Commemoration of Atatürk, Youth and Sports Day	19. week Sun	72. week Tues	124. week Wed	176. week Thurs
July 15th Democracy and National Unity Day	28. week Mon	80. week Wed	132. week Thurs	184. week Fri
August 30th Victory Day	34. week Fri	86. week Sun	139. week Mon	191. week Tues
October 29th Republic Day	43. week Tues	95. week Thurs.	147. week Fri	199. week Sat
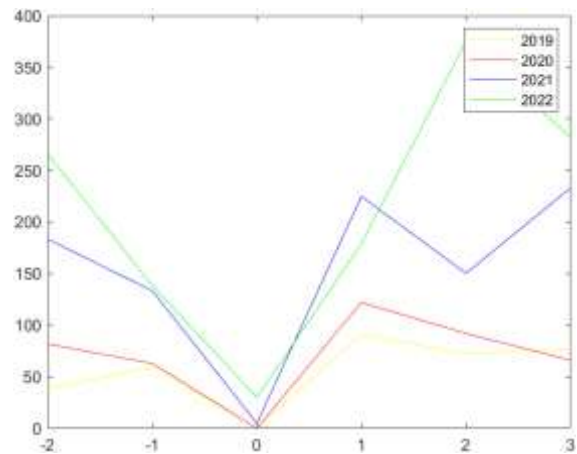
Figure 2. *6 days of data including the New Year on January 1 by year (0 on the x-axis denotes the special day, others 2 days before and 3 days after)*
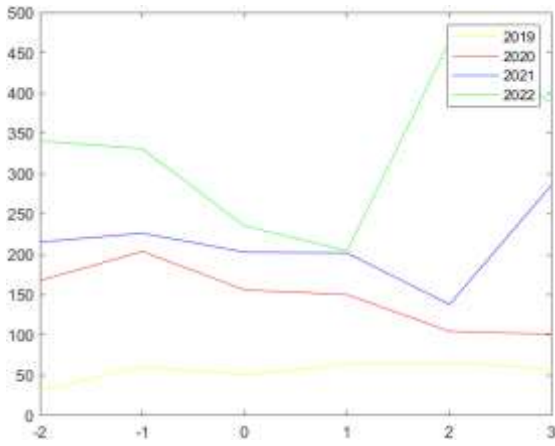
Figure 3. *6 days of data including the April 23rd National Sovereignty and Children's Day by year (0 on the x-axis denotes the special day, others 2 days before and 3 days after)*
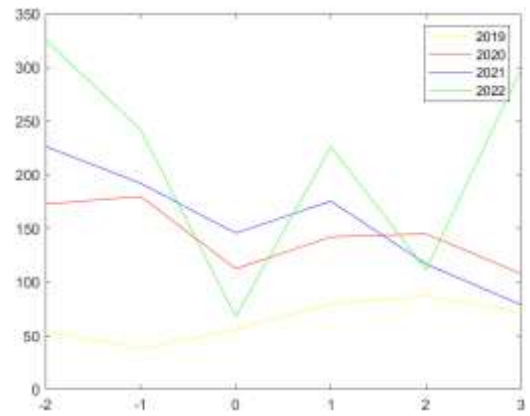
2022, there is a significant decline at $x = 2$ and $x = 3$ values, and the reason for this is that it coincides with the weekend. In the year 2020, the special day falls on Tuesday, and no decline is observed. This date corresponds to the week before Eid al-Fitr (Ramadan Bayram), and the absence of decline may be due to the high demand before the holiday. Figure 6 illustrates the impact of July 15th Democracy and National Unity Day on a yearly basis. In the years 2020, 2021, and 2022, there are patterns observed for $x = -1, 0$, and 1 values. In the year 2019, at $x = -1$, it is expected to be low as it coincides with Sunday. Figure 7 presents the impact of August 30th Victory Day on a yearly basis. In the years 2020 and 2022, there are patterns observed for $x = -1, 0$, and 1 values. In the year 2019, at $x = 1$ and $x = 2$, it is expected to be low as they coincide

Figure 4. *6 days of data including the May 1st Labor and Solidarity Day by year (0 on the x-axis denotes the special day, others 2 days before and 3 days after)*

Figure 6. *6 days of data including the July 15th Democracy and National Unity Day by year (0 on the x-axis denotes the special day, others 2 days before and 3 days after)*

Figure 5. *6 days of data including the May 19th Commemoration of Atatürk, Youth and Sports Day by year (0 on the x-axis denotes the special day, others 2 days before and 3 days after)*
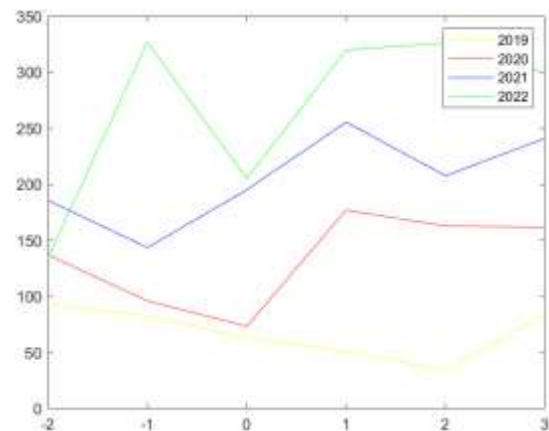
Figure 7. *6 days of data including the August 30th Victory Day by year (0 on the x-axis denotes the special day, others 2 days before and 3 days after)*
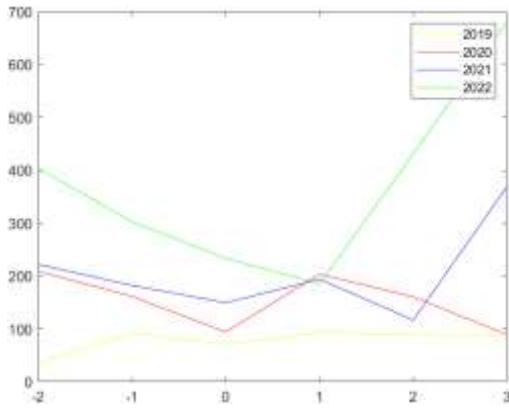
Figure 8. *6 days of data including the October 29th Republic Day by year (0 on the x-axis denotes the special day, others 2 days before and 3 days after)*

with the weekend, and in the year 2021, at $x = -1$, it is expected to be low as it falls on Sunday.

Figure 8 illustrates the impact of October 29th Republic Day on a yearly basis. In the years 2019, 2020, and 2021, patterns can be observed for $x = -1, 0$, and 1 values. In the year 2022, at $x = 1$, it is expected to have a decrease as it falls on Sunday. In this part, it has been observed that, except for exceptions, there is an impact on the following days of one-day special holidays, indicating a decrease on these special days followed by a one-day increase effect. Special days create a $'V'$ shaped pattern, with a decrease one day before and an increase one day after the special day.

2.2 Religious Holidays

The tables indicating the weeks containing Eid al-Fitr and Eid al-Adha for each year are presented in Table 2 and Table 3, respectively. To examine the patterns of religious holiday breaks, figures including 8 days prior and 10 days following these special days have been plotted and shown in Figure 9 and Figure 10, respectively. In Figure 9, the first day of Eid al-Fitr for four years is represented as $x = 0$, the second day as $x = 1$, and the third day as $x = 2$. $x = -1$ and $x = -7$ correspond to one day and seven days before the first day of the holiday, respectively. $x = 3,4,5,6,7,8$, and 9 represent the days following the holiday. In Figure 9, a pattern can be observed for $x = -1,0,1$ values. However, in contrast to other years, there is a continued decrease for $x = 1$ in the year 2022. In Figure 10, the first day of Eid al-Adha for four years is represented as $x = 0$, the second day as $x = 1$, the third day as $x = 2$, and the fourth day as $x = 3$. $x = -1$ and $x = -7$ correspond to one day and seven days before the first day of the holiday, respectively. $x = 4,5,6,7,8,9$, and 10 represent the days following the holiday. In Figure 10, a pattern

can be observed for $x = -1,0,1$ values in years other than 2022. However, in the year 2022, there is a continued decrease for $x = 1$ and $x = 2$ as well. In this section, it can be seen that there is a pattern for $x = -1,0,1$ values in religious holidays, except for the year 2022. In 2022, there has been less activity following the first days of the religious holidays compared to other years. Overall, the first day of religious holidays, one day before, and one day after create a $'V'$ shaped pattern.

2.3 November Discount Period

Regular discount campaigns take place in November every year. Table 4 presents five weeks containing November for four years, and the demand graph is illustrated in Figure 11.

Table 2. *Table of the weeks including Eid al-Fitr by year (Mon: Monday; Tues: Tuesday, Wed: Wednesday; Thurs: Thursday; Fri: Friday; Sat: Saturday; Sun :Sunday)*

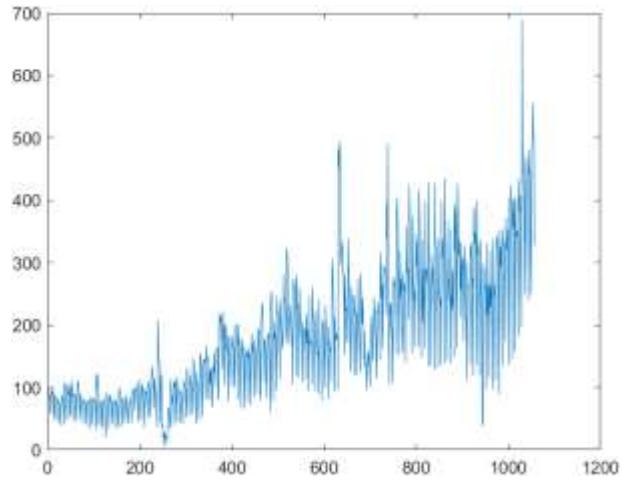| 2019	2020	2021	2022
22. week (Tues, Wed, Thurs)	72. week (Sun)	123. week (Thurs, Fri, Sat)	174. week (Mon, Tues ,Wed)
	73. week (Mon, Tues)		
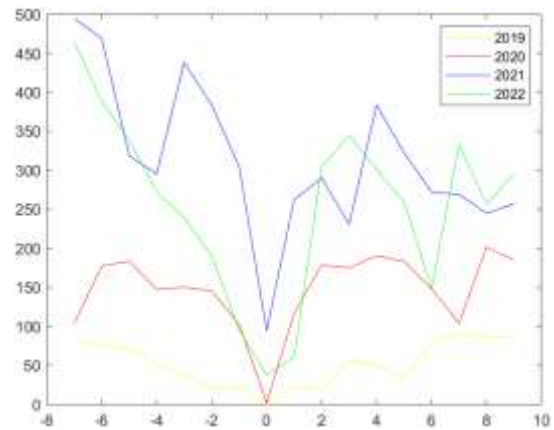
Figure 9. *17 days of data including the Eid al-Fitr by year (On the x-axis, 0 represents the beginning of Eid, minuses represent the days before Eid, 3,4,5,6,7,8 and 9 represent the days after Eid)*

Table 3. *Table of the weeks including Eid al-Adha by year (Mon: Monday; Tues: Tuesday, Wed: Wednesday; Thurs: Thursday; Fri: Friday; Sat: Saturday; Sun: Sunday)*

| 2019	2020	2021	2022
31. week (Sun)	82. week (Fri, Sat, Sun)	133. week (Tues, Wed, Thurs, Fri)	182. week (Tues, Wed, Thurs, Fri)
32. week (Mon, Tues, Wed)	83. week (Mon)		

186
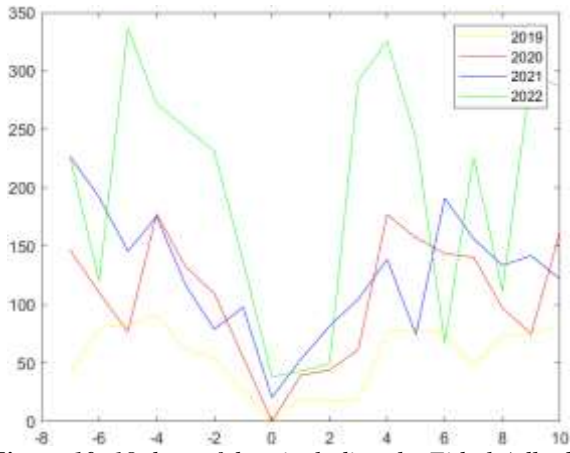
Figure 10. *18 days of data including the Eid al-Adha by year (On the x-axis, 0 represents the beginning of Eid, minuses represent the days before Eid, 4,5,6,7,8,9 and 10 represent the days after Eid)*

Table 4. *Table of weeks containing November by year*

2019	2020	2021	2022
43 week	96. week	148. week	200. week
44. week	97. week	149. week	201. week
45 week	98. week	150. week	202. week
46 week	99. hafta	151. week	203. week
47. week	100. hafta	152. week	204. week
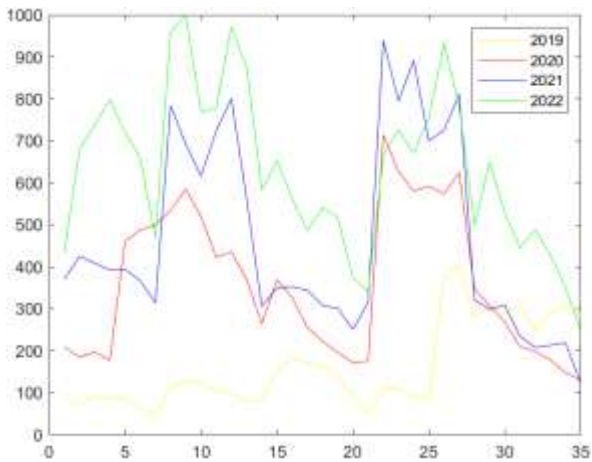
Figure 11. *5 weeks (35 days) demand graph including November by year*

Upon examining Figure 11, a pattern of fluctuations can be observed within a specific period. The demand tends to be low one day before the start of the campaign, while significant demand increases occur as the campaign begins.

3. Weekly Variation

The overall structure of the data forms a weekly fluctuation pattern. The time series data of regular weeks, excluding special days, is plotted in Figure 12.

Figure 12. *Normal weeks time series demand graph (151 weeks= 1057 days)*

The results obtained using Discrete Fourier Transform to observe the prominent frequencies in the data shown in Figure 12 are provided in Figure 13. The mathematical representation of the Discrete Fourier Transform is as follows [5]:

$$F(k) = \sum_{n=0}^{N-1} f(n).e^{(-i..2\pi.k.n/N)}$$

- $F(k)$: The value obtained for the index k of the frequency component as a result of the Discrete Fourier Transform.
- $f(n)$: The value at index n in the initial time series data.
- N: The length of the initial time series.
- i: The imaginary number $(\sqrt{-1})$.

In Figure 13, significant peaks can be observed at $x = 2, x = 152, x = 303,$ and $x = 454$ values. These notable increases at these points indicate the presence of weekly periodic patterns in the data and the strength of these periodicities.
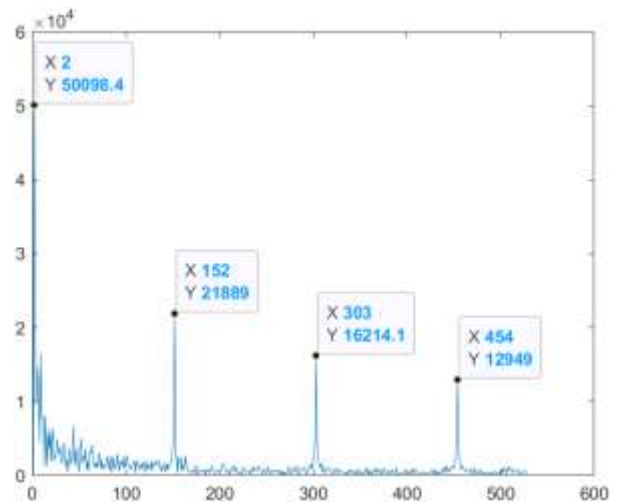
Figure 13. *The figure of peaks in demand during normal weeks.*

3.1 Weekly Average Pattern

In this section, the weekly average demands are examined on a yearly basis and presented in Figure 14.
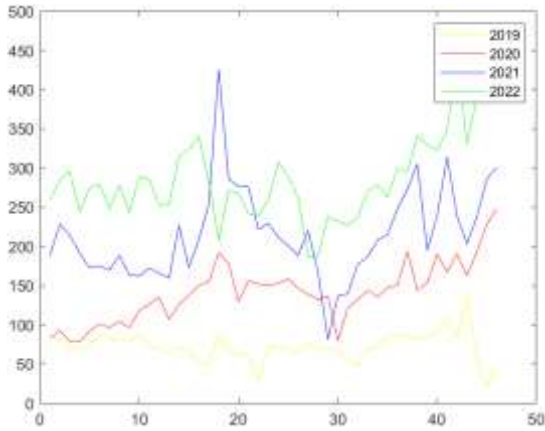

Figure 14. The figure of weekly average demand

In Figure 14, a general pattern can be observed. However, in the year 2021, there were significant increases and decreases in the 18th and 29th weeks. The 18th week corresponds to the period between May 3rd and May 9th, during which Summer Shopping and Mother's Day discounts were offered. The 29th week falls between July 19th and July 25th, which includes the dates of the Eid al-Adha. In the year 2019, there were significant drops in the 45th and 46th weeks, attributed to adverse weather conditions such as fog and snowfall. Additionally, Figure 12 shows an increase in demands starting from the first quarter of 2020, which can be attributed to the widespread adoption of E-commerce due to the impact of COVID-19, as mentioned in [6] and [7] articles.

4. Dynamic Shock Effect

Unpredictable factors that occur annually can lead to unexpected increases or decreases in the data. Situations that disrupt the expected patterns are defined as shock effects. In this part, the weeks that include the special days mentioned in Section 2 were excluded from the entire data, and the cases of unexpected shock effects were examined. In Figure 15, when observing the red line representing the averages, a monotonically decreasing pattern from Monday to Sunday can be observed. When examined on a weekly basis, out of the 151 weeks analysed, there were 26 weeks (%17.2) where there was a monotonically decreasing trend from Monday to Sunday. Figure 16 represents the figure for these weeks. Out of the 151 weeks analysed in Figure 15, it was observed that Monday had the
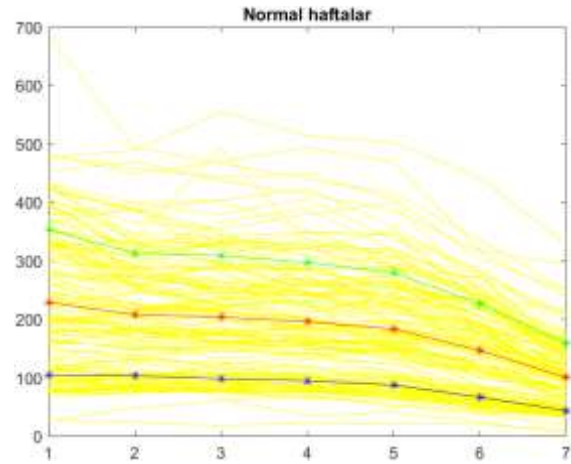

Figure 15. Yellow: Daily demand numbers of the 151-week data excluding the weeks in Section 2. Red: Daily average. Green: Average + standard deviation. Blue: Average - standard deviation.
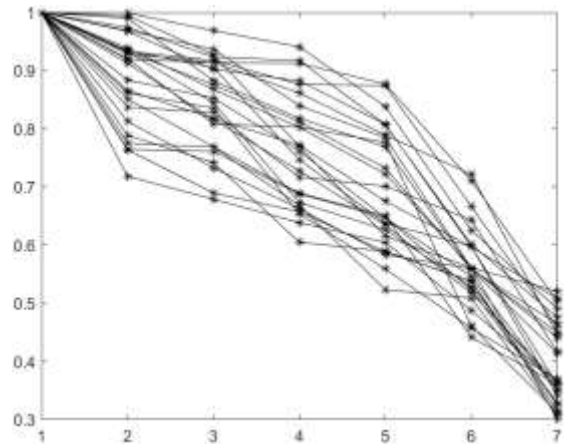

Figure 16. The figure of weeks with monotonically decreasing days from Monday to Sunday (x-axis represents days of the week, the y-axis represents the ratio of each day to Monday).

maximum shipment demands in 88 weeks (%58.3), Tuesday in 26 weeks (%17.2), Wednesday in 24 weeks (%15.9), Thursday in 11 weeks (%7.3), and Friday in 2 weeks (%1.3). The weeks with maximum shipment demands on Friday were the 63rd and 66th weeks. In the 63rd week, the demands on weekdays were generally similar to each other. The ratio of Friday's demand to Monday's demand was calculated as 1.1, indicating a negligible difference. In the 66th week, Friday was April 10th. On the night between April 10th and 11th, a two-day nationwide lockdown was announced due to **Covid-19**, and there was a reduction in operations related to bread-making machines in the company. **Covid-19** is an unexpected event that created a shock effect. In Figure 17, the demand figure for the 14 days from Monday of Week 66 to Sunday of Week 67 is
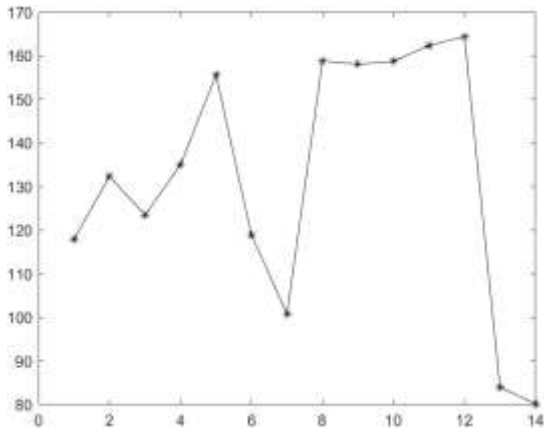
Figure 17. *Weeks 66 and 67: Effect of Covid-19*

depicted. The 2-day lockdown corresponds to the weekend (x=6,7), and it is evident that there is a significant increase in demand in the week following the lockdown (x=8,9,10,11,12). This indicates that the response to the shock lasts longer than a typical weekend response. The ratio of the number of weeks where maximum demand occurs on Tuesday to the number of weeks where maximum demand occurs on Monday is 29.5%, and similarly, the ratio of the number of weeks where maximum demand occurs on Wednesday to the number of weeks where maximum demand occurs on Monday is 27.3%. The difference between Tuesday and Wednesday is not substantial. Therefore, it can be inferred that the backlog of shipment demands over the weekend does not significantly impact the pattern on Tuesday.
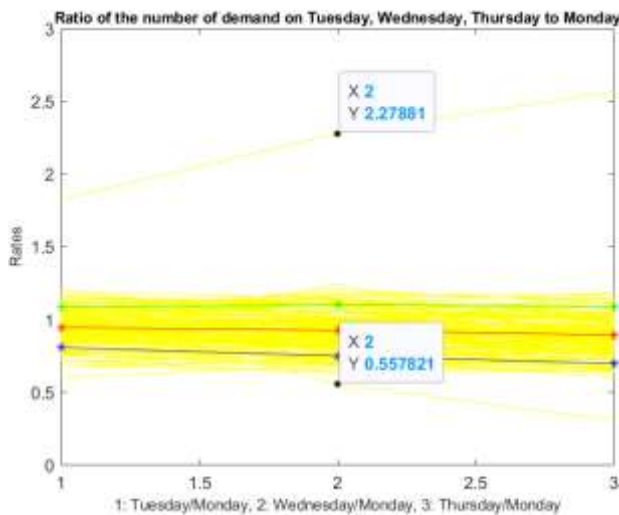
Figure 18. *Yellow: ratios, Red: mean, Green: mean + standard deviation, Blue: mean - standard deviation.*

The ratios of Tuesday, Wednesday, and Thursday to Monday are shown in Figure 18, highlighted in yellow. Additionally, the average of the ratios is depicted in red, the sum of the average and standard deviation of the ratios is shown in green, and the difference between the average and standard deviation of the ratios is represented in blue. The weeks where Wednesday deviates from the general pattern, with ratios of 0.56 and 2.28 to Monday, are weeks 49 and 51, respectively. In week 49, Monday and Tuesday have higher delivery demands compared to other days, resulting in a difference in the ratios. In Week 50, Monday's delivery demand is high, leading to lower ratios for other days. However, there is a general decrease in delivery demand compared to other weeks, and this decline in demand is also present on Monday of Week 51. The dates with low demand are between December 11th and 23rd, 2019. The reason for the low demand during this period is adverse weather conditions such as fog and snowfall. In Week 51, the effect of the shock continues, and the delivery demand is lower compared to other days of the week. Apart from weeks 49 and 51, the ratios of other days to Monday are not significantly different.
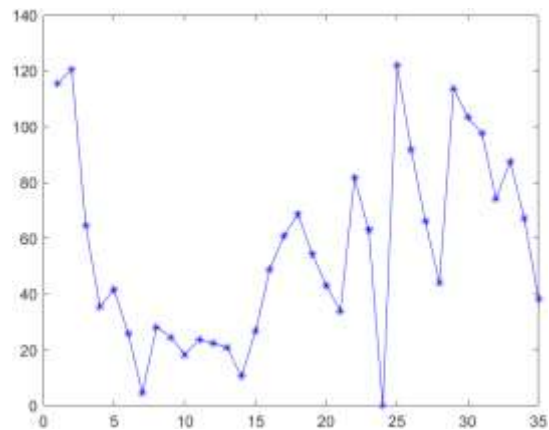

Figure 19. *Weeks 49, 50, 51, 52, and 53: Effect of Fog and Snowfall*

In Figure 19, 35 days is plotted, including weeks 49, 50, and 51, as well as the subsequent weeks 52 and 53, along with the corresponding changes in demand. The decline during weeks 49, 50, and 51 is evident, especially with the fog and snow warning. In Week 52, there is a significant drop on Wednesday due to the New Year holiday, and the impact is strongly observed on the following day. The effect of the New Year holiday was extensively examined in Section 2. After the manifestation of the New Year effect in week 52, demand continued to follow its normal trend in Week 53.

5. Conclusion

November is a period when discounts and fluctuations in demand occur each year. Demand is

low one day before the announcement of the discounts and significantly increases after the discounts begin. Several major campaigns are held throughout November, creating a distinct pattern for this month. Official holidays result in a decrease in demand on a respective day and an increase in demand on the following day, thus forming a 'V' pattern for one-day official holidays. On the first day of religious holidays, there is a decrease in demand, followed by an increase in demand on the second day and onwards. Exceptional events that do not recur in the same period each year, such as Covid-19 and adverse weather conditions, also have a disruptive effect on the overall demand pattern. Additionally, the data analysis clearly shows the increase in e-commerce due to the emergence of Covid-19.

As a result of this study, demand fluctuations in response to special days and unexpected circumstances have been identified. In cases where the increase in demand exceeds the capacity of existing vehicles, daily rental vehicles can be arranged from companies that provide such services to solve the problem. Extracting the demand model for special days and unexpected shocks will enable operational preparedness and prevent process slowdowns. The impact of the Covid-19 shock has lasted longer compared to other shocks. This is due to the influence of extraordinary human behavior driven by the idea of stockpiling food and supplies in response to the crisis.

Author Statements:

- **Ethical approval:** The conducted research is not related to either human or animal use.
- **Conflict of interest:** The authors declare that they have no known competing financial interests or personal relationships that could have appeared to influence the work reported in this paper
- **Acknowledgement:** This publication has been created by utilizing TUBITAK-2244 Industrial Doctorate Program (Project No: 119C147). However, all responsibility for the publication belongs to the owners of the publication. Financial support from TUBITAK does not constitute an endorsement by TUBITAK of the scientific content of the publication. I would also like to thank the logistics company that provided data support for this study.
- **Author contributions:** The authors declare that they have equal right on this paper.
- **Funding information:** The authors declare that there is no funding to be acknowledged.

- **Data availability statement:** The data that support the findings of this study are available on request from the corresponding author. The data are not publicly available due to privacy or ethical restrictions.

References

[1] Gbatu, A. P., Wang, Z., Wesseh Jr, P. K., & Tutdel, I. Y. R. (2017). The impacts of oil price shocks on small oil-importing economies: Time series evidence for Liberia. *Energy*, *139*; 975-990. DOI: 10.1016/j.energy.2017.08.047

[2] Rambachan, A., & Shephard, N. (2019). Econometric analysis of potential outcomes time series: instruments, shocks, linearity, and the causal response function. *arXiv preprint arXiv:1903.01637*.

[3] Leduc, S., & Liu, Z. (2016). Uncertainty shocks are aggregate demand shocks. *Journal of Monetary Economics*, *82*; 20-35. DOI: 10.1016/j.jmoneco.2016.07.002

[4] Albuquerque, P., & Bronnenberg, B. J. (2012). Measuring the impact of negative demand shocks on car dealer networks. *Marketing Science*, 31(1); 4-23. DOI: 10.2139/ssrn.1273017

[5] Cooley, J. W., & Tukey, J. W. (1965). An algorithm for the machine calculation of complex Fourier series. *Mathematics of computation*, 19(90); 297-301.

[6] Tran, L. T. T. (2021). Managing the effectiveness of e-commerce platforms in a pandemic. *Journal of Retailing and Consumer Services*, *58*; 102287. DOI: 10.1016/j.jretconser.2020.102287

[7] Galhotra, B., & Dewan, A. (2020, October). Impact of COVID-19 on digital platforms and change in E-commerce shopping trends. In *2020 Fourth International Conference on I-SMAC (IoT in Social, Mobile, Analytics, and Cloud)(I-SMAC)* (pp. 861-866). IEEE.
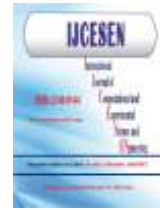
Determining the Drying Rates of Fabrics with Different Knit Structures by Fuzzy Logic Method

Feyza Akarslan KODALOĞLU[1]*, Murat KODALOĞLU[2]

[1]Suleyman Demirel University, Engineering Faculty, Textile Enginering Department, 32200, Isparta-Turkey
* **Corresponding Author** : **Email:** feyzaakarslan@sdu.edu.tr - **ORCID:** 0000-0002-7855-8616

[2]Isparta University of Applied Sciences, Vocational School of Technical Sciences, 32200, Isparta-Turkey,
Email: muratkodaloglu@isparta.edu.tr - **ORCID:** 0000-0001-6644-8068

Abstract:

Drying is a process applied to reduce the amount of water in a product or to reduce it to very low levels. The constantly changing conditions during the drying process make it difficult to determine the most suitable operating conditions to perform the drying process, such as drying time, energy consumption and product structural characteristics. In terms of a suitable drying, it is important to be able to control the factors affecting the drying depending on the characteristics of the product. Among these factors, the drying method and the pre-treatments that can be applied are also effective on drying. The high temperatures applied during drying and other conditions that are not chosen correctly can cause negative results in both the appearance of the product. The drying process in the textile industry is an expensive and laborious process that requires a lot of energy. The main purpose of the drying process is to provide maximum energy saving and energy efficiency at minimum time and cost without compromising the quality and structural properties of the material used. In this study, four fuzzy models were created depending on fabric fiber blend ratios and knitting structure in order to determine the effect on drying speed depending on time and temperature by using fuzzy logic method, which is one of the artificial intelligence methods. Average values in 100% cotton and 50% pes-cotton blend ratios; at 50 °C, the drying rate reaches the highest value of 1.9 over time, from 0.5 at the beginning, and 0.8 at the end of drying. At 60 °C, the drying rate starts at 1.2, reaches the highest value of 1.8, and completes at 1.1 at the end of drying. While the drying rate at 70 °C is 1.3 at the beginning, it reaches its highest value at 2.3 and completes it at 1.4 at the end of drying.

1. Introduction

Drying process is carried out in many areas of industry and various dryers are used. One of these areas is the textile industry. The most important factor to be considered in the drying process is the use of minimum energy consumption and maximum possible drying speed in order to obtain the material with the required and desired properties. In order to achieve a more effective drying, it is necessary to know the operating principles of the dryers used in the industry, their forms, the characteristics of the products to be dried, and the capacity. Other factors affecting the drying process are; type of material, structure, ambient conditions, quality and speed of air. The main function in the drying process is to control the parameters that affect the drying or the

removal of moisture. In this respect, fuzzy logic, which is one of the artificial intelligence methods, is the most useful method in the drying process.

Artificial intelligence methods are successfully applied in many areas. In most and even almost all of the studies, artificial intelligence methods are used in parameter estimation, evaluation of certain data, monitoring of a certain situation, diagnosis, classification, grading, detection, control, selection, optimization, etc. is used. Since all artificial intelligence methods are based on data, the developed artificial intelligence methods produce results in the data range in which they were developed, and at the same time, the output or result is tried to be estimated depending on the known variable parameters with these methods. One of the most important abilities bestowed on human beings

by the creator is the ability to predict. In other words, human beings can make very successful predictions in the face of situations that are different from these examples, but similar to these examples, based on many examples they have experienced for the same or a similar job. This is called experience in real life. The fuzzy logic method, one of the artificial intelligence methods, is an artificial intelligence method created based on the fuzzy inferences expressed as a result of the ability of human beings to make predictions. The fuzzy set concept, which was introduced by Lütfi Zadeh [1,2] in 1965, was developed by Mamdani [3-5] and many other researchers, and the fuzzy logic method took its current form. In the fuzzy logic method, the process flow is from the input parameters to the output as in other artificial intelligence methods. In other words, the current algorithm of the fuzzy logic method is estimation and classification, etc., rather than design. enables such studies. Recently, modern methods have found application in the textile industry [6-9]. Expert systems are among the leading techniques [10]. Fuzzy logic, which is the basis of expert systems, is best known for allowing systems based on common sense assumptions or using expert data to be modeled mathematically [11-13]. Therefore, the main use is in system control [14,15]. With these systems, energy consumption is reduced without compromising the quality of the product [16]. In this study, four fuzzy models were created depending on fabric fiber blend ratios and knitting structure in order to determine the effect on drying speed depending on time and temperature by using fuzzy logic method, which is one of the artificial intelligence methods. When the studies in the literature were examined, no study was found in which the temperature and time parameters and artificial intelligence programming method were used together in the drying process of yarn mixture ratios in knitted fabrics. The textile sector is one of the most developed sectors in Turkey and the detection of measurement results with artificial intelligence methods comes to the fore [17,18].

2. Material and Methods

In the drying process, 30x30 fabric samples with different properties such as yarn raw material (fiber type), density, fabric weight, and weaving construction were used. The properties of the materials used are given in Table 1. Fabric samples were first conditioned for 24 hours under laboratory conditions. (65% humidity, 20±2 °C). The conditioned fabric samples were weighed in the ambient humidity measured with a hygrometer and their weight in the ambient humidity was determined. Dry weights were found by weighing at

Table 1. Fabrics with different knit structures.

Sample	Weight (g/m²)	Raw materials	Weaving and Knitting Structure
1	290	%100 Cotton	Lacoste
2	354	%50 Cotton %50 PES	1x1 Rib
3	500	%100 Cotton	Supreme
4	276	%50 Cotton %50 PES	interlock

certain intervals in the oven. After the samples were wetted with distilled water so that the entire surface was evenly moistened, they were mechanically dried and pre-drying was carried out. The total moisture weight was determined by weighing again. In the meantime, the dryer was brought to the temperature conditions foreseen for the experiment and placed in the desired regime. The image of the dryer used in the study is given in Figure 1. For the drying experiments, fabrics with 4 different properties were selected and the experiments were carried out at 5 different temperatures (50 °C, 55°C, 60 °C, 65 °C and 70 °C). For the precision of the test results, the experiments were repeated three times to confirm the accuracy of the results. Since the drying air speed is constant in the textile industry, the examination has been made depending on the temperature and the change in the properties of the fabric products. Considering that the test conditions predicted did not change during the drying process, attention was paid to keep the temperature and air velocity constant.

Figure 1. The dryer used in the study

3. Results and Discussions

The fuzzy logic model created in this study was created using the MATLAB program, and the

resulting data were examined. With the fuzzy logic module of the MATLAB program, the Mamdani model with two inputs and one output has been established. This model is based on the center of gravity method. The first of the input membership function sets is the 'Temperature' parameter. As seen in Figure 2 below, the values are processed into the fuzzy logic module of the MATLAB program. The second of the input membership function sets is 'duration'. As seen in Figure 3 below, the values are processed into the fuzzy logic module of the MATLAB program. The 'drying rate' was chosen as the set of the output membership function. As seen in Figure 4 below, the values are processed into the fuzzy logic module of the MATLAB program.
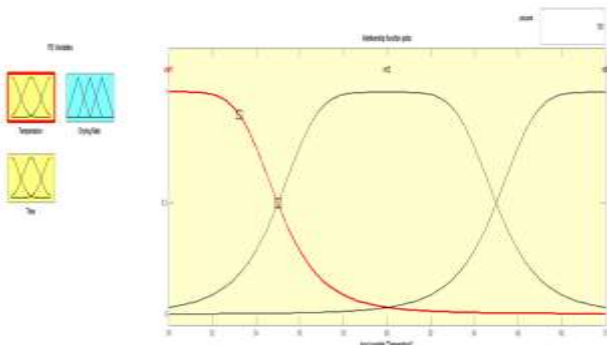
Figure 2. *Temperature membership functions, which is the first set of inputs.*
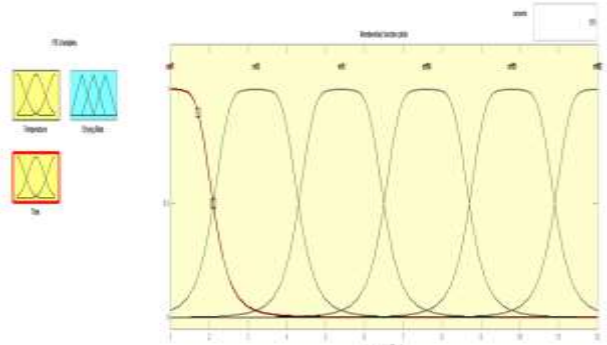
Figure 3. *Time membership functions, the second set of inputs*
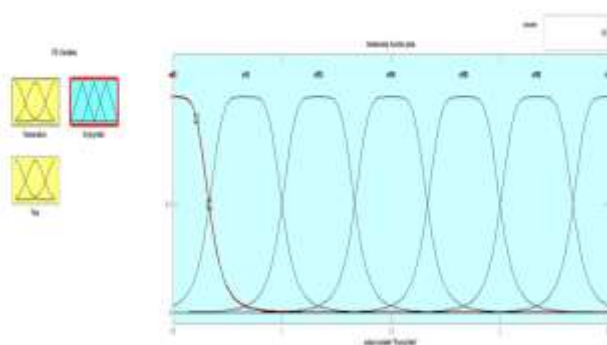

Figure 4. *Drying rate membership functions as output set*

In the study, the gbellmf method was chosen in the type of membership functions used in the input and output sets. Thus, a trapezoidal shape, which is a geometric shape, was obtained. In this way, approximate values are obtained within the framework of fuzzy logic rules. A total of two hundred fuzzy rules were created and used for the output graphs. The created Fuzzy Logic Method and the rule table are given in Figure 5 and Figure 6.
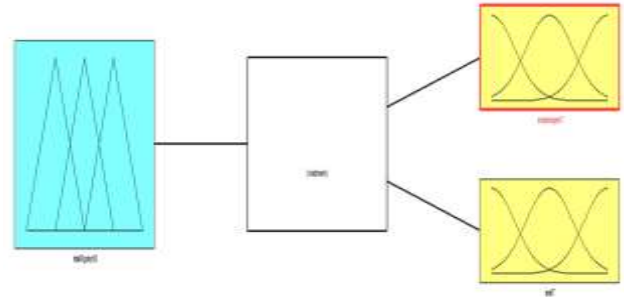

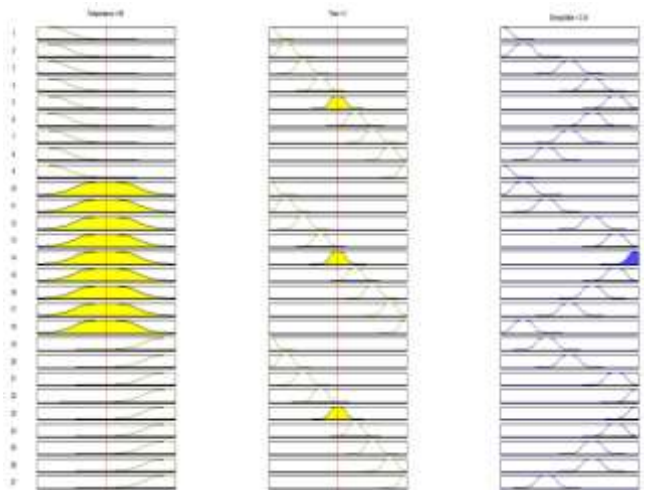**Figure 5.** *Fuzzy logic model*

Figure 6. *Rule table*

After the membership functions are entered in the MATLAB fuzzy logic editor, the values of the membership function are also entered in the rule editor. After the rule entries were completed, the results were monitored with the rule viewer. During the creation of the results, the center of gravity method was chosen as the clarification method.

Measurement results obtained from each experiment as a result of experimental studies The system, which was simulated with the MATLAB program after processing all the data, gave the following results for the drying speed of the fabric with 100% cotton and lacoste knit structure. As can be seen in Figure 7, the drying rates increased depending on the time as the drying temperature increased. At 50 °C, the drying rate reaches 1.2 at the beginning, to the highest value of 1.4 over time, and to 1.2 at the end of the period. At 55°C, it reaches the highest value of 1.6 from 1.4 at the start of the time and completes it at 1.2 at
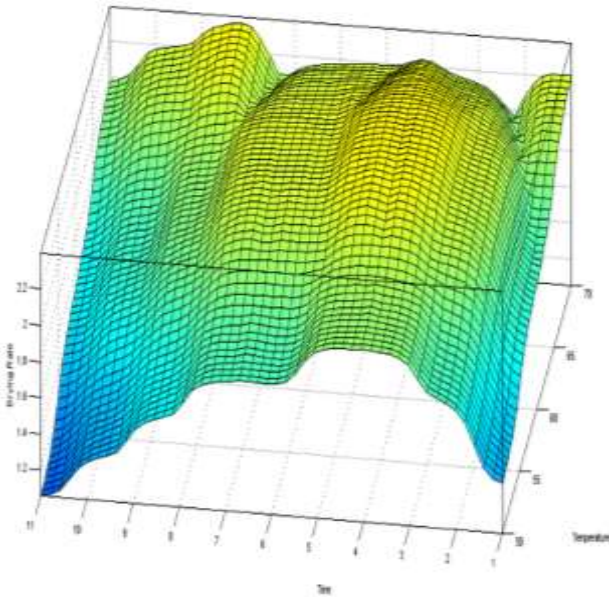
Figure 7. *Data obtained with MATLAB program for 100% cotton and lacoste knitting*
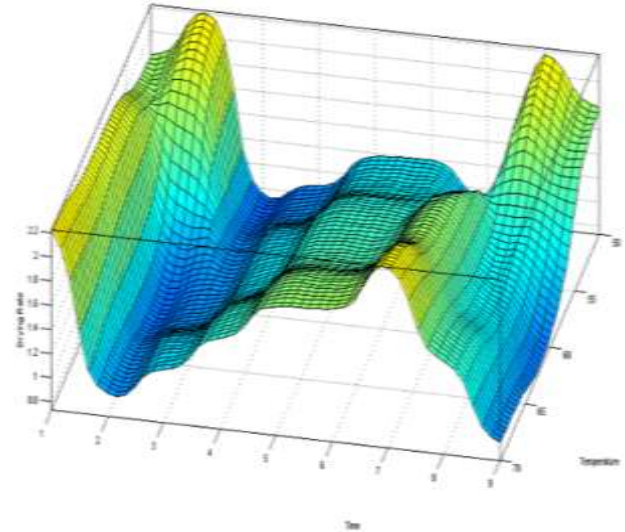
the end of the time. It starts at 1.6 at the beginning of 60°C time, reaches the highest value of 1.8, and completes at 1.4 at the end of the time. At 65 °C, it reaches the value of 2 at the beginning of the time and completes it at the value of 1.8 at the end of the time. At 70 °C, it reaches the value of 2.2 at the beginning, and the highest value of 2,4, and completes the value of 2 at the end of the time.

The drying speed of the fabric, which has a 100% cotton and single jersey knit structure, is given in the system simulated with the MATLAB program.
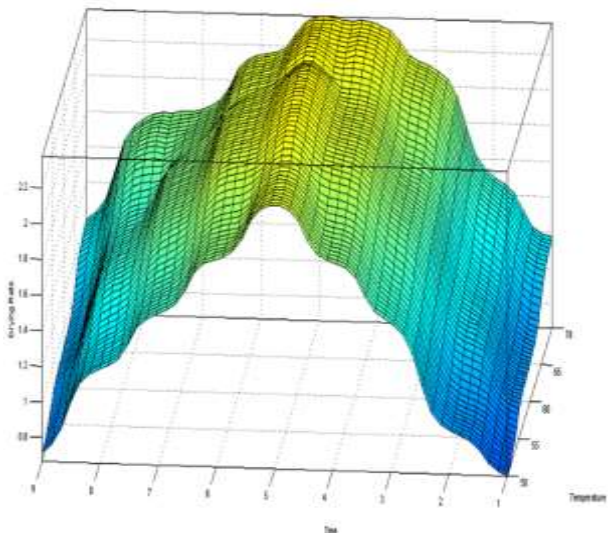
Figure 8. *Data obtained with MATLAB program for 100% cotton and single jersey knitting*

As seen in Figure 8, at 50 °C, the drying rate is 0.5 at the beginning and reaches the highest value of 1.4 over time and 0.6 at the end of the period. At 55°C, it reaches the highest value of 1.6 from 0.8 at the start of the time and completes it at 0.8 at the end of the

time. It starts at 1 at the start of 60°C time, reaches the highest value of 1.8, and completes at 1.2 at the end of the time. At 65 °C, it reaches 1.2 at the beginning of the time and reaches the highest value of 2, and then completes it at the value of 1 at the end of the time. At 70 °C, it reaches the highest value of 1.4 at the beginning, and the highest value of 2.4, and completes it at the value of 1.2 at the end of the time. The system simulated with the MATLAB program is 50% cotton - 50% PES and the drying speed of the fabric with interlock knit structure is given.

Figure 9. *Data obtained with MATLAB program for 50% cotton - 50% PES and interlock knitting*

As seen in Figure 9, at 50 °C, the drying rate reaches the highest value of 2.2 over time, from 1.8 at the beginning, and 1.8 at the end of the period. At 55°C, it reaches the highest value of 1.8 from 2 at the start of the time and completes it at 1.2 at the end of the time. It starts at 1.8 at the start of 60°C time, reaches the highest value of 2, and completes at 1.2 at the end of the time. After reaching the value of 1 at the beginning of the 65 °C period and reaching the highest value of 2, it completes at the value of 1 at the end of the time. At 70 °C, it reaches the value of 2.2 at the beginning, and completes it at the value of 0.8 at the end of the time.

The system simulated with the MATLAB program is 50% cotton - 50% PES and the drying speed of the fabric with rib knit structure is given. As seen in Figure 10, at 50 °C, the drying rate reaches 2 at the beginning and 1.6 at the end of the period. At 55°C, it reaches the value of 2.2 at the start of the time and completes it at the value of 2 at the end of the time. It starts at 1.4 at the start of 60°C time and completes at 2 at the end of the time. At 65 °C it reaches the value of 1.6 at the beginning of the time and completes it at the value of 2 at the end of the time. At 70 °C, it is at the value of 1.5 at the beginning and at the end of the time it is at the value of 2.
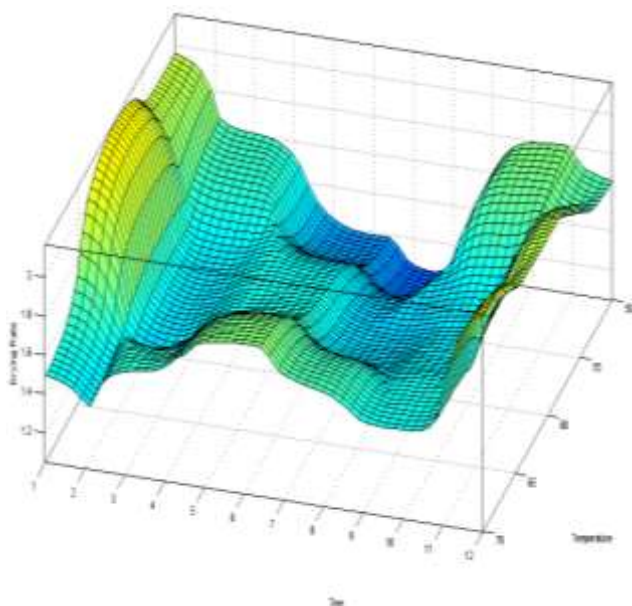
***Figure 10.** MATLAB program is 50% cotton - 50% PES and the drying speed of the fabric with rib knit structure*

4. Conclusions

In this study, the drying efficiency of various fabrics with different properties was researched. The drying rate-time graphs of four samples with different parameters for drying temperatures at 50 °C, 55°C, 60 °C, 65°C and 70 °C were evaluated. It has been observed that the slightest change in fabric parameters has a great effect on the drying efficiency. The drying rates in the experiments performed at different temperatures showed similar characteristics, and the drying rates increased as the temperature increased.

The developed fuzzy logic models can be used safely by integrating them into package programs that can make artificial intelligence-based design and strength calculations, either in their current form or by further development. The drying process will be carried out with the contribution of different technological developments with minimum energy consumption and maximum drying speed by determining the properties of the material to be dried. In this study, it has been successfully presented that fuzzy logic is a powerful and alternative method in both estimation and design with its use on numerical data.

Since it is one of the most energy-consuming processes in the industry, more research should be done in order to develop technologies in the field of drying and to obtain higher quality products. One of the key approaches to increasing the energy efficiency of many industrial operations is the application of fuzzy logic control. Published studies have proven that using the fuzzy logic method allows the determination of the parameters that are effective in reducing the drying time.

Author Statements:

References

[1]Şen, Z. (2010). Rapid visual earthquake hazard evaluation of existing buildings by fuzzy logic modeling. *Expert systems with Applications*, 37(8); 5653-5660.

[2]Şen, Z. (2011). Supervised fuzzy logic modeling for building earthquake hazard assessment. *Expert systems with applications*, 38(12);14564-14573.

[3]Zadeh, L. A. (1973). Outline of a new approach to the analysis of complex systems and decision processes. *IEEE Transactions on systems, Man and Cybernetics,* (1), 28-44. https://doi.org/10.1109/TSMC.1973.5408575

[4]Zadeh, L. A. (1975). The concept of a linguistic variable and its application to approximate reasoning-III. *Information Siences*, 9(1);43-80. https://doi.org/10.1016/0020-0255(75)90036-5

[5]Mamdani, E. H. (1976). Advances in the linguistic synthesis of fuzzy controllers. *International Journal of Man-Machine Studies,* 8(6); 669-678.

[6]Hosseinpour, S., & Martynenko, A. (2022). Application of fuzzy logic in drying: A review. *Drying Technology,* 40(5); 797-826.

[7]Arief, U. M., Nugroho, F., Purbawanto, S.,Setyaningsih, D. N., Suryono, N. (2018). Analysis of Maizena Drying System Using Temperature Control Based Fuzzy Logic Method. AIP Conference Proceedings; *AIP Publishing LLC*, , March; 1941(1);020005.

[8]Heriansyah, H.; Istiqphara, I.; Adliani, N. (2019). Optimization of Herbal Dryer System Based on Smart Fuzzy and Internet of Thing (IOT). *Int. J.Eng. Sci. Appl.*, 6; 104–110

[9] Nadian, M. H.; Abbaspour-Fard, M. H.;Martynenko, A.; Golzarian, M. R. (2017). An Intelligent Integrated Control of Hybrid Hot Air-Infrared Dryer Based on Fuzzy Logic and Computer VisionSystem. *Comput. Electron.* Agric.,137;138–149.

[10] Sourveloudis, N. C.; Kiralakis, L. (2005). Rotary Drying ofOlive Stones: Fuzzy Modeling and Control.*WSEASTrans. Syst.*,4; 2361–2368.

[11] Atthajariyakul, S.; Leephakpreeda, T. (2006). Fluidized Bed Paddy Drying in Optimal Conditions via Adaptive Fuzzy Logic Control. *J. Food Eng.,*75;104–114.

[12] Khodabakhsh Aghdam, S. H.; Yousefi, A. R.;Mohebbi, M.; Razavi, S. M. A.; Orooji, A.;Akbarzadeh-Totonchi, M. R. (2015). Modeling for Drying Kinetics of Papaya Fruit Using Fuzzy Logic Table Look-up Scheme.Int. *Food Res.* 22;1234–1239.

[13] Bagheri, N.; Nazilla, T.; Javadikia, H. (2015). Developmentand Evaluation of an Adaptive Neuro FuzzyInterface Models to Predict Performance of a SolarDryer.Agric. *Eng. Int. CIGR*, 17;112–121.

[14] Jafari, S. M.; Ganje, M.; Dehnad, D. (2016). Ghanbari, V.Mathematical, Fuzzy Logic and Artificial Neural Network Modeling Techniques to Predict Drying Kinetics of Onion. J. *Food Process. Preserv.,*40;329–339.

[15] Abdenouri, N., Zoukit, A., Salhi, I., & Doubabi, S. (2022). Model identification and fuzzy control of the temperature inside an active hybrid solar indirect dryer. *Solar Energy*, 231; 328-342.

[16] Júnior, M. P., da Silva, M. T., Guimarães, F. G., & Euzébio, T. A. (2022). Energy savings in a rotary dryer due to a fuzzy multivariable control application. *Drying Technology*, 40(6); 1196-1209.

[17] Majumdar, A., & Ghosh, A. (2008). Yarn strength modelling using fuzzy expert system. *Journal of Engineered Fibers and Fabrics*, 3(4); 61-68.

[18] Paul, T. K., Jalil, T. I., Parvez, M. S., Repon, M. R., Hossain, I., Alim, M. A., ... & Jalil, M. A. (2022). A Prognostic Based Fuzzy Logic Method to Speculate Yarn Quality Ratio in Jute Spinning Industry. *Textiles*, 2(3); 422-435.

Convolutional Neural Network (CNN) Prediction on Meningioma, Glioma with Tensorflow

Aslı BACAK[1]*, Mustafa ŞENEL[2], Osman GÜNAY[3]

[1] Electrical and Electronical Faculty, Department of Biomedical Engineering, Yıldız Technical University, Turkey
* Corresponding author Email: asli.bacak@std.yildiz.edu.tr - **ORCID:** 0009-0004-3928-2268

[2] Electrical and Electronical Faculty, Department of Biomedical Engineering, Yıldız Technical University, Turkey
Email: mustafa.senel@std.yildiz.edu.tr **- ORCID:** 0009-0007-9892-9449

[3] Electrical and Electronical Faculty, Department of Biomedical Engineering, Yıldız Technical University, Turkey
Email: ogunay@yildiz.edu.tr **- ORCID:** 0000-0003-0760-554X

Abstract:

Brain tumors can significantly affect a patient's life in a variety of ways. Classification of brain tumors is also important. Artificial intelligence (AI) techniques such as machine learning and deep learning can be very beneficial to physicians to classify tumors based on various parameters. In this study, the dataset is comprised of two distinct components which were prepared specifically for testing and training purposes, respectively. TensorFlow software library was used to utilize of Convolutional Neural Network (CNN). Since the most suitable weight values to solve the problem in deep learning are calculated step by step, the performance in the first epochs was low and unstable compared to the progressive values, and the performance increased as the number of epochs increased. However, after a certain step, the learning status of our model decreased considerably. The accuracy of the created model was observed to reach 0,90. As a result, as stated in its intended use, a mechanism that helps physicians and uses time efficiently has been successfully developed.

1. Introduction

Brain tumors are abnormal growths of cells in the brain or surrounding tissues. Brain tumors can significantly impact a patient's life in various ways, depending on the type, size, and location of the tumor, as well as the individual's overall health and other factors. Some common effects of brain tumors on a patient's life may include headaches, seizures, cognitive and memory problems, speech difficulties, vision and hearing changes, fatigue, and emotional or psychological distress. Treatment options such as surgery, radiation therapy, chemotherapy, and supportive care may also have their own effects and impact on the patient's quality of life [1]. According to the American Brain Tumor Association, it is estimated that over 87,000 people in the United States will be diagnosed with a primary brain tumor in 2022 [2].

Diagnosis of a brain tumor typically involves imaging tests such as MRI or CT scans, followed by a biopsy or other tests to determine the type and grade of the tumor. Furthermore, classification of brain tumors is also important for several reasons. Firstly, it helps to determine the type and grade of the tumor, which can guide treatment decisions and prognosis. Secondly, it allows for more accurate and consistent diagnosis, which can help improve patient outcomes. Thirdly, classification can aid in the development of personalized treatment plans and targeted therapies. Finally, it enables researchers to study and better understand the biology and behavior of different types of brain tumors, which could lead to the development of new treatments and improved patient care [3,4].

Artificial intelligence (AI) techniques such as machine learning and deep learning can be used to classify tumors based on various parameters such as tumor size, shape, texture, and other features extracted from medical images or clinical data.

One common approach is to use convolutional neural networks (CNNs), a type of deep learning algorithm that has been shown to be highly effective in image classification tasks. CNNs can be trained

on large datasets of medical images such as CT scans, MRIs, or mammograms, to learn to distinguish between different types of tumors based on their features.

Another approach is to use decision trees or support vector machines (SVMs) to classify tumors based on clinical data such as patient demographics, medical history, and lab results. These algorithms can learn to identify patterns and correlations between different factors and predict the likelihood of a tumor being malignant or benign. AI-based tumor classification systems can provide doctors with valuable insights into the nature and severity of tumors, helping them to make more informed decisions about treatment options and improve patient outcomes. However, it is important to note that AI should be used as a complementary tool to human expertise and not as a replacement for it. Doctors should always make the final decision based on their clinical judgment and experience.

There are some potential disadvantages to physicians classifying brain tumors on their own without any AI algorithm which help physicians to distinguish. Here are a few examples:

- Misdiagnosis
- Treatment variability
- Lack of standardization
- Limited predictive value

It is important for physicians to carefully consider all available information when classifying brain tumors and to use classification systems as tools to guide treatment decisions, rather than relying solely on them.

Misdiagnosis: Brain tumors can be challenging to diagnose because symptoms can vary widely, and different types of tumors may appear similar on imaging tests. If a physician relies too heavily on a particular classification system, they may misdiagnose a tumor or overlook important features that could affect treatment decisions. A study published in the Journal of Neurosurgery found that the accuracy of brain tumor diagnosis varied widely among physicians, with some cases being misdiagnosed as much as 40% of the time [5]. This highlights the potential risk of misdiagnosis, particularly when relying solely on classification systems. Treatment variability: Different types of brain tumors may require different treatments, and misclassification can result in inappropriate treatment decisions.

A study published in the Journal of Neuro-Oncology found that incorrect classification of gliomas led to inappropriate treatment decisions in nearly 20% of cases [6]. Lack of standardization: There are several different classification systems for brain tumors, and different physicians may use different criteria or terminology. This can make it challenging to compare research findings or treatment outcomes across different studies or institutions. A review article in the Journal of Neuropathology and Experimental Neurology notes that the World Health Organization's classification system for brain tumors has undergone several revisions, which can make it difficult to compare data across studies [7]. Limited predictive value: While classification systems can be helpful in guiding treatment decisions, they are not always predictive of patient outcomes. A study published in the Journal of Clinical Oncology found that histological classification of gliomas had limited prognostic value, with clinical factors such as age and performance status being more predictive of survival [8]. The three specific types of tumors studied in this article are pituitary tumor, malignant tumor, and meningioma tumor. Pituitary tumor is the mass formation as a result of uncontrolled division of the cells forming the pituitary gland tissue for some reasons; It is called a pituitary adenoma. This tumor type represents 12% of all tumors [9]. Most pituitary tumors are benign tumors that do not spread beyond the skull. Even if these tumors are not considered cancerous, it is inconvenient to leave them there without intervention, as their location is close to the brain and can affect the hormonal level of the body. Malignant tumors, on the other hand, are considered cancerous and they become life-threatening by metastasizing in the area where they are located. Examination and prompt initiation of treatment are very important. Meningioma tumors are slow-growing and mostly benign tumors that surround the meninges and constitute 15-20% of all intracranial tumors and are seen at a higher rate in women than in men [10].

2. Material and Methods

In this study, the dataset utilized was procured through a search conducted on the Kaggle platform [11]. The dataset is comprised of two distinct components which were prepared specifically for testing and training purposes, respectively. Each of these sections comprises a total of 3264 Magnetic Resonance Imaging (MRI) images encompassing three different tumor types, namely meningioma (fig 1), glioma (fig 2) and pituitary tumors, alongside tumor-free subcategories. This dataset contains 394 MR images for testing and 2870 MR images for training (Table 1). The tabulated information below presents the distribution of MR images across various categories, including tumor-free images, glioma tumors, meningioma tumors, and pituitary tumors.
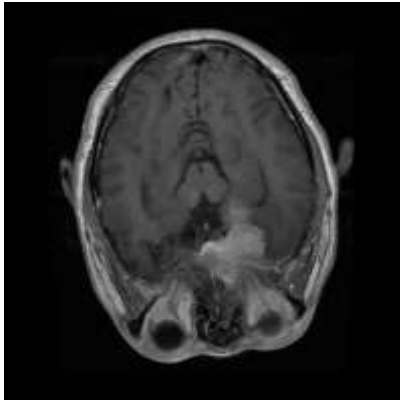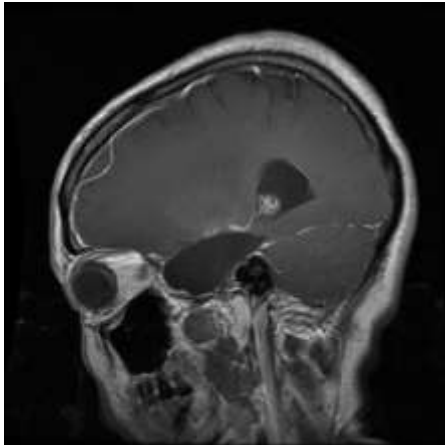
Figure 1. MR Image with Meningioma Tumor

Figure 2: MR Image with Glioma Tumor

Table 1*. Distribution of MR images*

MR Images	Testing	Training
Tumor-free	105	395
Glioma tumors	100	826
Meningioma tumors	115	822
Pituitary tumors	74	827

In the field of machine learning, neural networks have shown remarkable success in a wide range of areas such as computer vision[12], natural language processing[13], and bioinformatics[14]. These models also have enormous potential to promote data analysis and modeling for various problems in educational and behavioral sciences given their flexibility and scalability as universal function approximator[15]. The Convolutional Neural Network (CNN) operates on a mechanism inspired by the functioning of neurons in the human brain. It is a deep learning algorithm that has proven to be highly effective in various computer vision tasks, including image classification, object detection, and image segmentation. (fig 3) The underlying principles of CNN involve the extraction and analysis of hierarchical features from input images, allowing for accurate identification and understanding of the visual content.

CNN learns by comparing and contrasting the unique properties and patterns present within the input data. When presented with images, it aims to discern and differentiate various objects or classes by leveraging the spatial relationships and local correlations present in the data.

This process of feature extraction occurs through the utilization of convolutional layers and filters (fig 4) within the CNN architecture. These layers perform convolution operations on the input images, capturing local information and detecting low-level
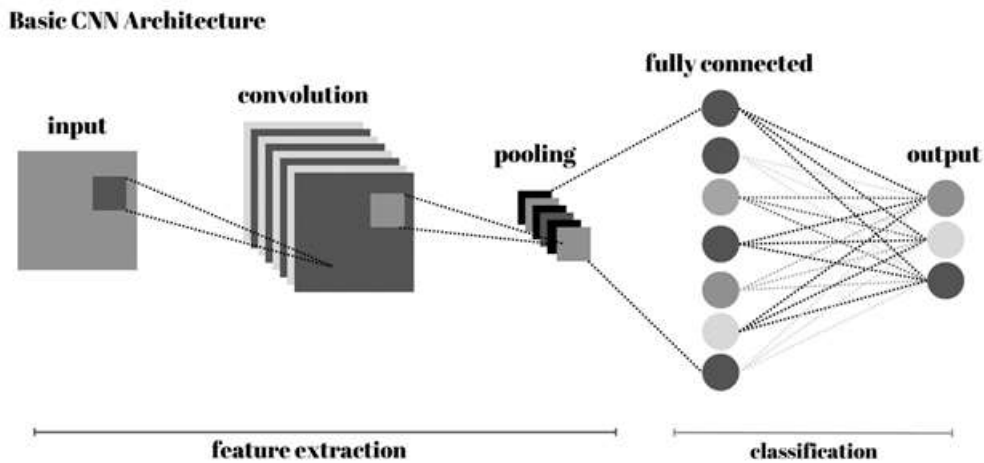

Figure 3. Basic CNN Architecture

features such as curves, edges, and textures. By incorporating multiple layers, CNN can hierarchically learn more complex and abstract representations, combining the detected low-level features to form higher-level concepts. Furthermore, CNN employs pooling layers to downsample the extracted features, reducing the dimensionality of the representations while retaining the most salient information. This enables the network to focus on important features and discard redundant or less informative details. Additionally, the activation functions applied after each convolutional or pooling layer introduce non-linearities, facilitating the network's ability to capture and model complex relationships between features. By iteratively training on a large labeled dataset, CNN learns to optimize its internal parameters (weights and biases) through a process known as backpropagation. Backpropagation involves the computation of gradients, which are used to update the network's parameters based on the error between the predicted output and the ground truth labels. This iterative training process allows CNN to gradually refine its feature representations, improving its ability to accurately classify and recognize objects in new, unseen images. In summary, the Convolutional Neural Network (CNN) paradigm draws inspiration from the biological structure and functioning of the human brain. Through the extraction of hierarchical features and the application of convolution, pooling, and activation operations, CNN effectively learns to distinguish and classify objects within images. The iterative training process further enhances its performance by optimizing the network's internal parameters. As a result, CNN has emerged as a powerful tool in computer vision, enabling a wide range of applications in fields such as medical imaging, autonomous driving, and image understanding. In our study, the Python programming language was used to implement our algorithm, given its versatility and extensive support within the data science community. Also we aim to harness the potential of Convolutional Neural Network (CNN) methodology (fig 4). To accomplish this, we utilized the TensorFlow software library, developed by the Google Brain Team, which stands as a popular choice for artificial intelligence and machine learning. TensorFlow is a flexible and scalable software library for numerical
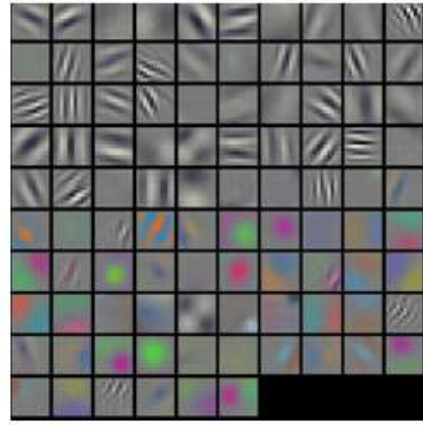
Figure 4. *Example of some of filters used in CNN*

computations using dataflow graphs. It is a powerful tool that helps in the rapid and efficient development of projects in the field of artificial intelligence and deep learning, providing many functions and tools for building and training neural networks that are widely used in deep learning projects; and it is also compatible with Python language and has a large ecosystem. This library and related tools enable users to efficiently program and train neural network and other machine learning models and deploy them to production. TensorFlow operates using multidimensional arrays called tensors. These tensors allow Python to complete more complicated computations that are needed when working with machine learning. This format of holding information is used to save much more complicated information in a tensor than in a typical one dimensional array [16]. It provides high performance computing by effectively using hardware accelerators such as GPU (Graphics Processing Unit) and TPU (Tensor Processing Unit). It offers optimization techniques to accelerate large-scale data processing and training processes.

In our approach, we embarked on a multi-step process to effectively leverage the CNN architecture. Initially, we focused on the "Training" section of the dataset, containing MRI images, and performed a classification task. The goal was to categorize the images into four distinct groups: non-tumor, meningioma tumor, malignant tumor, and pituitary tumor. By organizing the data in this manner, we established a foundation for the subsequent steps of our algorithm. To facilitate the learning process, we associated the MRI images from each tumor type with their corresponding labeled folders. This step

involved providing the artificial intelligence model with a dedicated set of images for each tumor category, thereby enabling it to learn and recognize the unique visual features associated with each specific tumor type. Through the application of the CNN methodology, the model underwent a series of data processing operations, including convolution and pooling, to extract meaningful patterns and distinctive characteristics from the input images. As the model iteratively processed and analyzed the images, it gradually acquired the ability to discriminate and differentiate between the different tumor types based on their visual attributes. By undertaking numerous repetitions and combinations, the model honed its capacity to learn and accurately identify the presence of a specific tumor type within an individual MRI image. This training process was crucial in enabling the CNN model to progressively enhance its discriminatory capabilities. The model's ability to recognize subtle variations and intricate patterns within the images improved with each iteration. As the CNN architecture learned to extract and associate low-level features, such as edges and curves, it gradually built more abstract and higher-level representations of the tumor types present in the images. This hierarchical learning allowed the model to capture increasingly complex relationships between features, leading to more accurate classification outcomes.

In summary, our study leveraged the CNN methodology through the TensorFlow software library to train an artificial intelligence model for the classification of MRI images. The iterative learning process, aided by the CNN architecture, enabled the model to discern and identify the unique features associated with different tumor types. By processing and analyzing the images repetitively, the model acquired the ability to make accurate tumor type classifications based on the distinctive visual patterns observed within the input data. After that, we designated a separate set of images for testing purposes to evaluate the performance of the trained artificial intelligence model and further improve the accuracy of its predictions. By explicitly associating each test image with its corresponding tumor type, we enabled the model to conduct a comparative analysis based on its acquired knowledge and reference information.

In this evaluation phase, the artificial intelligence model first leveraged its learned representations to assess the test images against the previously encountered tumor types. By scrutinizing the distinctive features extracted from the test images, the model made comparisons with the established reference information. Through repeated iterations of this comparative process, the model progressively refined its ability to discern and differentiate the characteristic traits of the various tumor types, ultimately leading to a higher accuracy rate.

By engaging in this iterative evaluation and refinement cycle, the artificial intelligence model further fine-tuned its discriminatory capabilities. The repetitive exposure to diverse test images allowed the model to strengthen its understanding of the subtle visual cues specific to each tumor type, resulting in heightened accuracy when predicting the tumor type of an unseen image.

3. Results

Our study employed a distinct set of test images to assess the performance of the trained artificial intelligence model. Through iterative comparisons with learned representations and reference information, the model refined its ability to differentiate between tumor types. This iterative process contributed to achieving a higher accuracy rate by enhancing the model's capacity to recognize and discern the unique characteristics associated with different tumor types (fig 5).

The model was trained with the training set and the weights were updated again. This process was repeated at each training step to calculate the most appropriate weight values for the model. Each of these training steps is called an "epoch".

While the model is being trained, not all of the data are included in the training at the same time. They take part in education in a certain number of parts. The first piece is trained, the performance of the model is tested, and the weights are updated according to the success with backpropagation. Then the model is retrained with the new training set and the weights are updated again.

Since the most suitable weight values to solve the problem in deep learning are calculated step by step, the performance in the first epochs was low and unstable compared to the progressive values, and the performance increased as the number of epochs increased. However, after a certain step, the learning status of our model decreased considerably.

The accuracy, macro average and weighted average values for all tumor types are shown below as 0 refers to Glioma Tumor, 1 refers to No Tumor, 2 refers to Meningioma Tumor and 3 refers to Pituitary Tumor (fig 6). Finally, the values obtained for each training round (epoch) are given in the Fig 7.

4. Conclusions

In this study, a mechanism that can help physicians in the classification of glioma, meningioma and pituitary gland tumors, which are the three most common types of brain tumors, and that uses time efficiently has been studied. It is aimed to examine the brain cross-section images obtained by using an MRI device, to understand which type of brain tumor it corresponds to, and thus to diagnose the patient's condition correctly and in the shortest possible time, and to start the treatment as soon as possible. In addition, it was aimed to expand the size of this study by adding a tumor-free image class. It has been prioritized that the obtained classification mechanism has a high accuracy rate. For these purposes, a CNN model was created with TensorFlow and the model was evaluated by considering the success rate on the basis of various parameters. As a result of the examinations, it was determined that the accuracy rate of the model created was close to 0.90 and slightly above. As stated in the aim of the study, a mechanism that helps physicians and uses time efficiently has been successfully developed. When other studies are examined, it is seen that the accuracy rate obtained is quite close to some successful studies. Due to the fact that the study is open to development, more efficient results can be obtained in the future. For this, the data set used in the study can be expanded to ensure that the learning models work more effectively. After the data set is enlarged, the cross-section images can be grouped based on various desired criteria and the models can be trained in this way, and the effect on the classification result can be observed.

Author Statements:

- **Ethical approval:** The conducted research is not related to either human or animal use.

Figure 5. *Accuracy Outputs*

Figure 6. *Accuracy, Macro Avg. and Weighted Avg. Values*

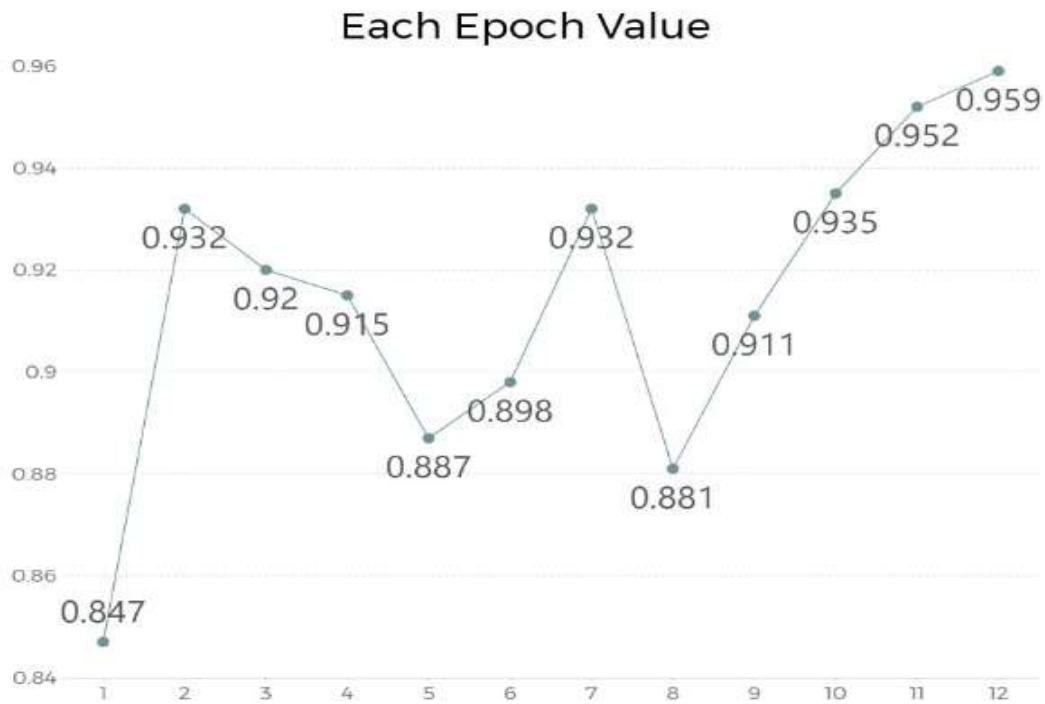|	precision	recall	f1-score	support
0	0.91	0.94	0.92	93
1	0.98	0.84	0.91	51
2	0.92	0.98	0.95	96
3	1.00	0.98	0.99	87
accuracy			0.94	327
macro avg	0.95	0.93	0.94	327
weighted avg	0.95	0.94	0.94	327

***Figure 7.** Each Epoch Value*

- **Conflict of interest:** The authors declare that they have no known competing financial interests or personal relationships that could have appeared to influence the work reported in this paper

- **Acknowledgement:** The authors declare that they have nobody or no-company to acknowledge.

- **Author contributions:** The authors declare that they have equal right on this paper.

- **Funding information:** The authors declare that there is no funding to be acknowledged.

- **Data availability statement:** The data that support the findings of this study are available on request from the corresponding author. The data are not publicly available due to privacy or ethical restrictions.

References

[1] Lin, N. U., Lee, E. Q., & Aoyama, H. (2015). Challenges relating to solid tumour brain metastases in clinical trials, part 1: patient population, response, and progression. A report from the RANO group. *The Lancet Oncology,* 16(10);e419-e426. doi: 10.1016/s1470-2045(15)00096-2

[2] https://www.abta.org/brain-tumor-facts-statistics/

[3] Louis, David N., et al. (2021). The 2021 WHO Classification of Tumors of the Central Nervous System: a summary. *Neuro-Oncology*, 23(8);1231-1251, https://doi.org/10.1093/neuonc/noab064.

[4] Ghafoorian, Mohsen, et al. (2018). Deep Learning-Based Classification of Diffuse Gliomas Using MR Imaging. *Radiology*, 281(3);907-918, https://doi.org/10.1148/radiol.2018181748.

[5] Mandonnet, E., Duffau, H., Bauchet, L., & Almairac, F. (2010). Misdiagnosis of brain tumors: incidence and guidelines for avoidance. *Journal of Neurosurgery*, 112(2);467-473.

[6] Shin, J. Y., Kim, E. H., Cho, B. K., & Kim, S. H. (2015). Inappropriate treatment decisions for gliomas due to misclassification of tumor grade. *Journal of Neuro-Oncology*, 121(1); 85-92.

[7] Louis, D. N., Perry, A., Reifenberger, G., von Deimling, A., Figarella-Branger, D., Cavenee, W. K., ... & Ellison, D. W. (2014). The 2016 World Health Organization classification of tumors of the central nervous system: a summary. *Acta Neuropathologica*, 131(6);803-820.

[8] Weller, M., van den Bent, M., Tonn, J. C., Stupp, R., Preusser, M., Cohen-Jonathan-Moyal, E., ... & Reifenberger, G. (2015). European Association for Neuro-Oncology (EANO) guideline on the diagnosis and treatment of adult astrocytic and oligodendroglial gliomas. *Journal of Clinical Oncology*, 33(25);2930-2936.

[9] Cancer Treatment Centers of America (n.d.). Types of Brain Cancer. https://www.cancercenter.com/cancer-types/brain-cancer/types, retrieved: 29.09.2020.

[10] Lopes MBS, Randenberg SR. Central nervous system. In Fletcher CDM, ed. Diagnostic Histopathology of Tumors. London: *Livingstone*, 2000:1607.

[11] Sartaj Bhuvaji, Ankita Kadam, Prajakta Bhumkar, Sameer Dedge, & Swati Kanchan. (2020). Brain Tumor Classification (MRI) [Data et]. *Kaggle* https://doi.org/10.34740/KAGGLE/DSV/1183165

[12] Hinton, G. E., Srivastava, N., Krizhevsky, A., Sutskever, I., & Salakhutdinov, R. R. (2012). Improving neural networks by preventing co-adaptation of feature detectors. arXiv preprint arXiv:1207.0580.

[13] Weston, J., Ratle, F., & Collobert, R. (2008, July). Deep learning via semi-supervised embedding. *In Proceedings of the 25th international conference on Machine learning* (pp. 1168-1175).

[14] Shin, S. H., Bae, Y. E., Moon, H. K., Kim, J., Choi, S. H., Kim, Y., ... & Nah, J. (2017). Formation of triboelectric series via atomic-level surface functionalization for triboelectric energy harvesting. *ACS nano,* 11(6); 6131-6138.

[15] Bo Pang, Erik Nijkamp, Ying Nian Wu, (2020). Deep Learning With TensorFlow: A Review, *UCLA*

[16] Kiran Seetala, William Birdsong, Yenumula B. Reddy, Image Classification Using TensorFlow, *16th International Conference on Information Technology-New Generations (ITNG 2019)*, 2019, Volume 800, ISBN : 978-3-030-14069-4.